



HAL
open science

Observations and quantifications of precipitation signatures from C-band dual-polarized SAR measurements

Yuan Zhao

► **To cite this version:**

Yuan Zhao. Observations and quantifications of precipitation signatures from C-band dual-polarized SAR measurements. Signal and Image Processing. Ecole nationale supérieure Mines-Télécom Atlantique, 2021. English. NNT : 2021IMTA0284 . tel-03601164

HAL Id: tel-03601164

<https://theses.hal.science/tel-03601164>

Submitted on 8 Mar 2022

HAL is a multi-disciplinary open access archive for the deposit and dissemination of scientific research documents, whether they are published or not. The documents may come from teaching and research institutions in France or abroad, or from public or private research centers.

L'archive ouverte pluridisciplinaire **HAL**, est destinée au dépôt et à la diffusion de documents scientifiques de niveau recherche, publiés ou non, émanant des établissements d'enseignement et de recherche français ou étrangers, des laboratoires publics ou privés.

THESE DE DOCTORAT DE

L'ÉCOLE NATIONALE SUPERIEURE MINES-TELECOM ATLANTIQUE
BRETAGNE PAYS DE LA LOIRE - IMT ATLANTIQUE

ÉCOLE DOCTORALE N° 598
Sciences de la Mer et du littoral
Spécialité : Océanographie, Physique et Environnement

Par

Yuan ZHAO

Observations and Quantifications of Precipitation Signatures from C-band dual-polarized SAR measurements

Thèse présentée et soutenue à Plouzané, le 6 Décembre, 2021

Unité de recherche : LabSTICC

Thèse N° : 2021IMTA0284

Rapporteurs avant soutenance :

Paco López-Dekker Professor, Delft University of Technology

Wenming Lin Professor, Nanjing University of Information Science and Technology

Composition du Jury :

Président : René Garello Professor, IMT Atlantique

Examineurs : Paco López-Dekker Professor, Delft University of Technology

Wenming Lin Professor, Nanjing University of Information Science and Technology

Werner Alpers Professor, University of Hamburg

Dir. de thèse : Ronan Fablet Professor, IMT Atlantique

Co-enc. de thèse: Bertrand Chapron Researcher, IFREMER

Invité:

Alexis Mouche Researcher, IFREMER

L'école National Supérieure Mines-Télécom Atlantique Bretagne Pays de la Loire

IMT Atlantique

**Observations and Quantifications of
High Precipitation Signatures from
C-band dual-polarized SAR
Measurements**

Thèse de Doctorat

Présentée par: ZHAO Yuan

Département: Signal et Communications

Laboratoire: LabSTICC

Directeur de thèse: FABLET Ronan

Co-encadrants de thèse: CHAPRON Bertrand

Invité: MOUCHE Alexis

Acknowledgements

First, I really appreciate the China Scholarship Council (CSC) for giving me the opportunity to pursue my PhD at Ifremer, France. Then my deepest thanks go to my PhD advisors, Dr. Bertrand Chapron and Dr. Alexis Mouche for providing me the opportunity to conduct PhD study and accepting me as a member of the Lops-siam, Ifremer. I would like to thank you for your inspirational guidance and warm encouragement, your patience and dedication in the studies. Your immense knowledge and scientific curiosity have motivated me to expand and pursue my study interests. Your guidance has helped me conduct the studies and finish this thesis in this period. It is a pleasant and invaluable experience for me to work with you.

I would like to thank Dr. Jean Tournadre in cooperating the study in atmospheric models and doing a serious and detailed modification on this manuscript. Your active participation in the study encourages me to go through the tough time.

In addition, I would like to thank Dr. Ronan Fablet for his assistance in completing the doctoral processes. I am grateful for his kind support, particularly every time I seek for help.

Many thanks to all staff members in Lops-siam for all the efforts after I joined the lab, and for the assistance in accessing to the laboratory and research facilities. Without their precious support it would not be possible to conduct this research here. I thank my fellow labmates in Lops-siam for all the fun we have had in the last four years.

I am grateful to all the Chinese friends in Brest for keeping me company as getting through the hard time and having some fun in exploring different cities and getting the ski skills.

Last, but certainly not least, I am extremely grateful to my beloved family, especially my parents, for their unwavering faith in me and unconditional love, support, and understanding. This thesis is dedicated to them.

Although with difficulties and setbacks, my Ph.D. journey was also full of growths and gains for both my knowledge and my personality. These four years are the most meaningful time for me to become an independent person, not only in research but also in social life. For that, I will always be grateful for the time I spent and the people I met at Ifremer and France.

Publications

1. Zhao, Y., Long  p  , N., Mouche, A., & Husson, R. (2021). Automated Rain Detection by Dual-Polarization Sentinel-1 Data. *Remote Sensing*, 13(16), 3155.
2. Zhao, Y., Tournadre, J., Mouche, A., Alpers, W., & Chapron B.. A Numerical Model to Assess the Impact of Precipitation on C-band SAR Observation over coastal area, in preparation.
3. Alpers, W., Zhao, Y., Mouche, A. A., & Chan, P. W. (2021). A note on radar signatures of hydrometeors in the melting layer as inferred from Sentinel-1 SAR data acquired over the ocean. *Remote Sensing of Environment*, 253, 112177.
4. Combot, C., Mouche, A., Knaff, J., Zhao, Y., Zhao, Y., Vinour, L., Quilfen, Y. and Chapron, B., 2020. Extensive High-Resolution Synthetic Aperture Radar (SAR) Data Analysis of Tropical Cyclones: Comparisons with SFMR Flights and Best Track. *Monthly Weather Review*, 148(11), pp.4545-4563.

Abstract

Spaceborne Synthetic Aperture Radar (SAR) is a good tool to observe atmospheric and oceanic phenomena due to its high resolution and its independence of weather and light. The precipitation is one of the common phenomenon observed in SAR images, depending on the instrumental configuration, rain rate and sea surface state. Previous studies on precipitation signatures in C-band SAR images present conflicting views about the sensitivity of the radar backscatter to rain rate and the proposed models of rain impact can not always be effectively applied to SAR images. In addition, when retrieving sea surface wind from SAR images, the impact of precipitation on the signal can give rise to large errors. These uncertainties and limitations point to the necessity of a finer and quantitative analysis of the precipitation phenomena in SAR images. This study takes benefit of the dual-polarization Sentinel-1 mission that has the capability of monitoring sea surface in both co- and cross-polarization and of the significant numbers of data now routinely acquired in coastal areas. Meantime, the weather radar networks in the U.S. and Japan provide continuous measurements of rain rate, which can be collocated with each SAR data. Benefiting from the large collocated SAR/rain dataset, this study aims to evaluate and identify the rain signatures in C-band SAR images. A numerical model is then proposed to analyze the mechanisms of precipitation signatures. The dataset statistical analysis shows that the measured backscatter increases with rain rate in co- and cross-polarizations, but is also dependent on the incidence angle and the surrounding sea state. Impacted by these factors, rainbands in tropical cyclones are characterized by dark or bright patches with increasing distance from the center of tropical cyclones(TCs) center. The bright and dark patches are strongly associated with the volume scattering and attenuation from hydrometers in the atmosphere. Furthermore, new algorithms are proposed to detect the rain cells and rainbands in SAR images based on the datasets. In particular, detected rainbands are then used to provide new insights to describe and understand the TC wind structures, further compared with in situ Dropsondes, SAR detected wind streaks and high-resolution numerical simulations.

Contents

1	Introduction	1
2	Background	5
2.1	Rain signatures in SAR observation	5
2.1.1	Satellite observation on tropical rain cells	5
2.1.2	Satellite observation of tropical cyclones	9
2.2	Mechanisms for precipitation modulation on radar signal	13
2.2.1	Atmospheric transmission	13
2.2.2	Backscattering on the sea surface	15
2.2.2.1	Ring waves and splash products	15
2.2.2.2	Wave damping	18
2.2.3	Gust front	19
2.3	Radar cross section under different rain rates	21
2.4	Precipitation Flag	24
3	Dataset	25
3.1	SAR data (Sentinel-1 and RadarSAT-2)	25
3.2	Weather radars	26
3.2.1	NEXRAD	26
3.2.2	Hong Kong weather radar	27
3.2.3	JMA rain radar	28
3.3	ECMWF data	29
3.4	Collocation between the datasets	29
4	Observation of rainfall effects on SAR images	31
4.1	Observation on rain signatures in SAR images	31
4.1.1	Case Study	31
4.1.2	Statistical Results	34

4.1.3	Bright signatures in SAR images	39
4.2	The impact of precipitation on cyclone cases	46
4.2.1	Eyewall	47
4.2.2	Spiral Rainband	50
4.2.3	Radial Profile of Rain Rate	54
4.3	Summary	56
5	Model explanation for the rain impacts	58
5.1	Transfer Model through rain cell	58
5.1.1	Transfer model through the atmosphere	58
5.1.2	SAR data rain model	63
5.2	Evaluation of the impact of different rain rate and incidence angle	66
5.2.1	Geometry of simulated radar backscatter	66
5.2.2	Sea surface backscatter	67
5.2.3	Wind speed	69
5.2.4	Radar pulse length	69
5.3	Validation	70
5.3.1	Case 1	70
5.3.2	Case 2	76
5.3.3	Case 3	77
5.4	The impact of time shift of rain data on simulation	79
5.5	Summary	83
6	Precipitation detection on SAR images	84
6.1	Dual polarization filter for rain detection in SAR images	84
6.1.1	Local Gradient Method	85
6.1.2	Optimization of dual-pol resolutions	86
6.1.3	Validation	89
6.2	Rainband Filter in tropical cyclones	93
6.2.1	NRCS Difference map	94
6.2.2	Non-local mean filter	98
6.2.3	ROC curve	99
6.2.4	Validation	101

6.3	Summary	105
7	Inflow angle of tropical cyclone cases	107
7.1	Inflow angle from spiral rainbands	107
7.1.1	rainband shape	108
7.1.2	Inflow angle estimation	109
7.1.3	Inflow angle distribution	110
7.2	Inflow angle comparison for TC Michael	116
7.2.1	Translations of dropsondes and HWRF data	116
7.2.2	Wind directions compared with dropsondes	118
7.2.3	Comparison between wind streaks and rainbands	120
7.2.4	Comparison between HWRF data and rainbands	121
7.2.5	Comparison between wind streaks and HWRF data	123
7.3	Summary	125
8	Conclusions	126
8.1	Conclusions	126
8.2	Future work	128
	References	130

List of Figures

2.1	SIR-C/X-SAR images of the same scene in the Gulf of Mexico acquired at different radar frequencies and polarizations on April 18, 1994. Reproduced from Melsheimer et al. (1998) ©IEEE	7
2.2	Examples of C-band SAR images with rain signatures reported by Alpers et al. (2016).(a) 23:53 UTC on 9 June 2015 acquired by Sentinel-1 at VV images. Rain signatures in the west of the Philippine island.(b) ENVISAT/ASAR at VV polarization at 02:27 UTC on 18 August 2011 close to Hong Kong. (c) ENVISAT/ASAR VV-pol image at 14:18 UTC on 6 August 2008 over the South China Sea off the coast of Hong Kong.(d) ENVISAT/ASAR HH-pol image at 21:18 UTC on 9 December 2011 over the southern North Sea. ©Elsevier	8
2.3	(a) Radar reflectivity in Northern Hemisphere tropical cyclone with a double eyewall from Houze Jr (2010) (b)Schematic illustration of tropical cyclone structure including eyewall and rainband from X. Li et al. (2013). ©AMS	10
2.4	Different rainband patterns observed in TC captured by RadarSAT-2 reported by X. Li et al. (2013). ©AMS	11
2.5	SIR-C/X-SAR images acquired over the Andaman Sea near the Malaysian coast at 1847:18 UTC on 17 April 1994 from Melsheimer et al. (1998)	19
3.1	Location of NEXRAD (a) and JMA (b) weather radar stations and number of collocated SAR images for each stations. The grey areas represent the radar coverage.	28
3.2	(a) Histogram of base reflectivity for collocated data over US coastal area. (b)2D histogram with the collocation number falling within the bins of base reflectivity (x axis) and ECMWF wind speed (y axis) in the US. (c) and (d) show the same histograms with (a) and (b) but for the collocation around Japan. reflectivity and wind speed.	30
4.1	(a)(b) SAR images at VV and VH polarization acquired at 23:19 UTC on June 13 2017. (c) Base reflectivity at the same time from the NEXRAD station. (d) (e) NRCS (red or green lines) and base reflectivity (blue line) along the Transect 1 (red line on (a)) and Transect 2 (green line on (a)). (f) Mean VV and VH NRCS as a function of base reflectivity. . . .	33

4.2	Same as 4.1, but the SAR acquisition time is 23:53 UTC 1 Sep 2017.	34
4.3	Same as 4.1, but the SAR acquisition time is 0010UTC 31 Aug 2017.	35
4.4	Example of NRCS ratio computation (a) SAR image at VV polarization. The red star marks a single pixel for calculation of NRCS ratio. The red rectangle covers the calculation area for the pixel, with a width of 0.5° incidence angle range and the length of 50 km in the azimuth direction. The blue area in the left panel denotes the area without rain (Base reflectivity <20 dBZ). (b) the base reflectivity measured by NEXRAD at the same time. (c) NRCS ratio calculation result for all the pixels under rain (Base reflectivity >20 dBZ).	36
4.5	Statistics of $NRCS_{ratio}$ with respect to base reflectivity for VV polarization (a - Top) and VH polarization (b - Bottom). The legend in each sub figure stands for the NRCS in rain-free area, suggesting different wind regimes (0-4 m/s, 4-8 m/s, 8-16 m/s, and ≥ 16 m/s) as approximately derived with CMOD-5 model. Above histogram denotes the data amount for lines at each base reflectivity bin.	38
4.6	The latitude distribution of the bright patches.	40
4.7	The incidence angle distribution for bright patches.	40
4.8	The distribution of base reflectivity for bright patches.	41
4.9	A Sentinel-1 VV (a) and VH (b) images acquired on 13 June 2017 23:20 UTC and corresponding base reflectivity obtained at 23:14 d), 23:18 (e) and 23:23 (f) UTC on the same day. The black, blue and purple contours in (a) and (b) indicate the 40 dBZ base reflectivity from the three sequential observations times. The ECMWF wind field is presented in (c).	41
4.10	The distribution of wind speed for bright patches.	42
4.11	Examples of NEXRAD hydrometeor classifications for three cases of rain cells.	43
4.12	The distribution of wind speed for bright patches.	43
4.13	The NRCS distribution for bright patches compared to GMFs at wind speed of 5 m/s, 7 m/s and 10 m/s. Top panels VV NRCS, bottom panels VH NRCS	44
4.14	A case acquired on 12 Apr 2017 at VV (a) and VH (b). (c)(d) Reflectivity and RHI provided by the Hong Kong Observatory. RHI depicts the reflectivity along the purple transect in panels a and b. The white line inside denotes the height of 3km. (e)(f) VV, VH and reflectivity along the Purple and Green transects of panels a and b.	45

4.15	The panels from top to bottom show TC Sally on 15 Sep 2020 at 23:53UTC at cat-1, Florence on 13 Sep 2018 at 10:58UTC at cat-3 and Michael on 10 Oct 2018 at 23:46UTC at cat-4. The first and second columns are for S-1 image at VV and VH polarizations. The third column shows the base reflectivity from NEXRAD in colocation with each S-1 example. The last column displays the variation of NRCS along the red transect associated with base reflectivity. Each transect is taken at the same incidence angle.	48
4.16	Left panels: The $NRCS_{diff}$ of the inner rainbands close to the center for the cases in Fig. 4.15. Middle panels, statistics of The $NRCS_{diff}$ with respect to base reflectivity for the zoom area in left panel. Right panels: the histogram of $NRCS_{diff}$ as base reflectivity is over 20 dBZ. These analysis is based on VV-pol S-1 data.	49
4.17	Same analysis with Fig. 4.16 but for VH polarization.	50
4.18	TC Michael captured by S-1 at VV (a) and VH (b) polarizations on Oct 09, 2018 at 23:44UTC. (c) Base Reflectivity from NEXRAD KTLH, KTBW, KBYX stations. The dash lines mark the maximum detection range (480 km) for each station. (d) Wind field retrieved from dual-pol SAR images.	52
4.19	VV- and VH-pol NRCS and base reflectivity for the 3 areas marked in Fig. 4.18.	53
4.20	The plots of VV- and VH-NRCS together with base reflectivity and ECMWF wind speed along the transects red, blue and purple inserted in Fig.4.19.	54
4.21	Laura captured by Sentinel-1 in (a) VV and (b) VH polarizations at 00:10 UTC 27 Aug 2020. The light purple and grey contours inside stand for the base reflectivity of 35dBZ and 20 dBZ respectively. (c) Base reflectivity from NEXRAD KLCH station. The dash line marks the largest detection range of radar. The mean radial profiles of NRCS in VV (d) and VH (e) are shown together with the profiles of $NRCS_{diff}$ (f), wind speed (g) and base reflectivity (h).	55
4.22	(a) the probability histogram of the radial location of maximum precipitation relative to RMW. The x axis of R^* stands for the radial distance over RMW. (b) R^* with categories against RMW.	56
5.1	The radiation transfer across a cylinder filled with precipitation	59
5.2	Attenuation coefficient with respect to rain rate at C-, X-, and Ku-band	60
5.3	Coefficient η from raindrops and ice particles.	61

5.4	Geometry of the radar pulse in the model. The colored zones represent the rain cell. θ is incidence angle. c is the speed of light and t is the radar pulse length. $R_r = ct/2$ and L is the tilted path length, i.e. the points with the rain cloud with the same range as the surface.	64
5.5	Geometry for a 6km-height rain cell with an incidence angle of 30° . (d)(e)(f) take the $\sigma_{0,surf}$ as -20, -15 and -5 dB.	67
5.6	The ratio of $\sigma_{0,m}$ to $\sigma_{0,surf}$ for the incidence angles of 32° (upper), 38° (middle), 46° (lower). For each incidence angle, the $\sigma_{0,m}$ in left and middle panels is chosen as the maximum and minimum of the simulated value corresponding to the sea surface backscatter. The right panel takes the $\sigma_{0,m}$ in the middle of the rain cell.	68
5.7	The ratio of $\sigma_{0,m}$ to $\sigma_{0,surf}$ at different wind speeds. The $\sigma_{0,surf}$ is estimated using CMOD5. The values of $\sigma_{0,m}$ in left and middle panel refer to the maximum and minimum in each simulation. And the right panel includes $\sigma_{0,m}$ received from the middle of rain cell.	70
5.8	Attenuation, emission and simulated $\sigma_{0,m}$ across a 6-km-height rain cell. The volume length L for the left and right panels are 3 km and 7 km respectively.	71
5.9	(a) Copol (VV) SAR image acquired at 23:27 UTC on 25 May 2017. (b) base reflectivity and (c) rain rate from NEXRAD.(d) copol SAR image and 10 and 20 mm/hr rain rate contours.	71
5.10	Attenuation (a) and emission (b) in dB. (c) $\sigma_{0,surf}$ by smoothing copol σ_0 in Fig. 5.9(a1). (d) Simulated $\sigma_{0,m}$.	72
5.11	(From top to bottom) measured copol σ_0 , rain rate, attenuation and emission calculated from the model, surface σ_0 and simulated σ_0 along the transect inserted in Fig. 5.10	73
5.12	Scatterplot of measured and simulated $\sigma_{0,m}$ for rain rate (a)less than and (b) larger than 1mm/h. The correlation coefficient for each plot are included.	74
5.13	Upper panels: sea surface backscatter smoothed by mean(a1), median(b1) and Gaussian (c1) filters. Lower panels: corresponding simulated $\sigma_{0,m}$.	74
5.14	(From top to bottom) VV-pol measured $\sigma_{0,m}$, rain rate, smoothed $\sigma_{0,surf}$ and simulated $\sigma_{0,m}$ along the transect inserted in Fig. 5.13.	75
5.15	(a) Copol SAR image acquired at 11:17 UTC on the 15 th Sep 2018, (b), (c) base reflectivity and rain rate from NEXRAD,(d) co-pol SAR image with the red and green rain rate contour of 10 mm/hr and 35 mm/hr.	76
5.16	Same with Fig. 5.10 but for case 2.	77

5.17	(a) Simulated $\sigma_{0,m}$. (b) Measured and simulated $\sigma_{0,m}$ along the yellow transect. (c) Rain rate along the yellow transect.	78
5.18	Subplots of (a) rain rate, (b) measured $\sigma_{0,m}$ and (c) simulated $\sigma_{0,m}$, (d) base reflectivity as well as (e) correlation between copol σ_0 and rain rate, (f) correlation between copol σ_0 and the simulated $\sigma_{0,m}$	79
5.19	(a) Copol SAR image of tropical cyclone Michael obtained by Sentinel-1 at 11:50 UTC on 10 Oct 2018. (b) and (c) base reflectivity and rain rate at 11:50 UTC provided by NEXRAD. (d) co-pol σ_0 overlaid with rain rate contours.	80
5.20	Same as Fig. 5.10 for Case 3.	80
5.21	Scatterplot of copol σ_0 and $\sigma_{0,m}$ for different rain rate ranges.	81
5.22	(a1) Detail of Copol SAR images of case 3 and NEXRAD rain rates at 11:47 (b1), 11:50 (c1) and 11:52 UTC (d1). (b2),(c2),(d2) simulated $\sigma_{0,m}$ using the (b1) (c1) and (d1) rain rate fields. The green line represents the transect usde for fine comparison.	81
5.23	Copol σ_0 , smoothed $\sigma_{0,surf}$, simulated $\sigma_{0,m}$, attenuation, emission and rain rate along the green transect in Fig. 5.23. The three panels are from the simulations using the NEXRAD rain rate fields at 11:47 UTC, 11:50 UTC and 11:52 UTC respectively.	82
6.1	Illustration of a ROC applied on VV at 400 meters resolution for a set of minimum reflectivity values	87
6.2	Performance of Koch filters at different resolution/polarization with dual-pol filters on the left, and single-pol filter on the right.	88
6.3	True positive rate of rain detection percentage as a function of rain rate for different wind speed regimes with respect to the polarization channels considered. (a) VV-generated filter, (b) VH-generated filter and (c) dual-pol filter.	89
6.4	True positive rate of rain detection percentage as function of incidence angle for the polarization channels considered with respect to different rain rates. The first bin at 32 degree is affected by artefacts linked to recurrent invalid data at near range.	90
6.5	The first and second columns show the Koch filters generated with VV (400 m) and VH (800 m) channels respectively for the three cases in Figs. 4.1 ~ 4.3. The last column shows the proposed dual-pol filters correspondingly. The blue and purple contours mark the base reflectivity of 20 dBZ and 40 dBZ respectively.	91

6.6	(a) and (b) Sentinel-1 VV and VH SAR images at 21: 08 UTC on 3 Sep 2019. (c) Wind speed and direction from ECMWF. (d) Rain rate provided by JMA. (e) (f) Transect of VV and VH NRCS and rain rate along the red and green lines of (a) and (b). (g) (h) (i) Masks generated only by single-pol VV/VH and by our proposed algorithm. The two rectangles overlaid on (a),(b),(d) outline the 2 areas with heavy rain.	92
6.7	Tropical cyclone Laura captured by Sentinel-1 at 00:10 UTC at 27 Aug 2020.(a)(b) VV-pol and VH-pol images.(c) Base Reflectivity provided by NEXRAD at the same time. (d)(e) (f) VV, VH and dual (VV and VH) pol filter)	94
6.8	VV-pol image of TC Laura at multiple resolutions, i.e., 1km, 3km, 5km, 10km,20km, 40km (top panels) with $\sigma_{0,diff}$ combining different resolutions (middle and bottom panels). . . .	95
6.9	Same with Fig. 6.8 but for VH.	96
6.10	Pdf of $\sigma_{0,diff}$ between 5 km and 20 km with respect to base reflectivity in (a)VV and (b) VH.	97
6.11	(a) $\sigma_{0,diff}$ between 5 km and 20 km. (b)Absolute value of $\sigma_{0,diff}$ of (a). (c) Final result after Non-Local Mean filter applied on (b).	98
6.12	ROC curves for VV polarization at different resolution combinations.	99
6.13	Same with Fig. 6.12 but for VH.	100
6.14	The detection percentage at different combination of <i>res1</i> and <i>res2</i>	100
6.15	top panel: Typhoon Maysak captured by Sentinel-1 at VV and VH polarizations and the together with rain rate from JMA. Middle panel: The rain masks from Koch method at VV and VH respectively and the dual-pol filter we proposed. Bottom panel: rain masks from VV- and VH-pol $\sigma_{0,diff}$ along with our developed method.	102
6.16	Rain detection from (a) VV-generated filter, (b) VH-generated filter, (c) dual-pol filter and (d) our developed filter as a function of rain rate for different wind speed regimes.	103
6.17	The upper panels show a zoom of cyclone Maysak case presented in Fig. 6.15. The lower panels are for Malakas on 19 Sep 2016 at 21:21 UTC.	104
6.18	Rain detection as a function of incidence angles.	105
7.1	(a) TC Michael captured by Sentinel-1 at 9 Oct 2018 at 23:45. (b) Mask generated from dual-pol SAR images based on the method proposed in Section 6.2. The shape of rainbands are shown by colored lines.	108

7.2	To the derivation of the streamline equation. α is the inflow angle and <i>iscomplementaryto</i>	
	α . The bold dashed curve is the streamline; solid curves designate p and p-p isobars (p is the pressure, Δp is the pressure change between isobars); V is the wind speed in point S; u and v are tangential and radial components of the wind speed V at point S, respectively; and θ is the polar angle of radius vector r counted off from arbitrary selected point S_0 . . .	110
7.3	(a) the mask for each rainband along with the fitted streamline by equation 7.5. (b) The normalized radial distance (R^*) with respect to the relative angle φ_r for each rainband. Inflow angles for each rainband associated with φ_r (c) and R^* (d).	111
7.4	The histograms of maximum wind speed (V_{max}), the radius of V_{max} (RMW) and storm translation speed (V_s). V_{max} and RMW are extracted from SAR images.	112
7.5	The radius of maximum wind as a function of maximum wind speed.	112
7.6	(a) The distribution of Inflow angle (α) with respect to the normalized radial distance (R^*). The black line shows the mean of α with errorbars.(b) The histograms of α at different radial distance ranges.	113
7.7	Inflow angle (α) versus R^* with maximum wind speed (V_{max}) stronger and weaker than 52 m/s (a), storm translation speed lower and higher than 5 m/s (b), RMW larger and smaller than 25 km (c).	114
7.8	The scatter of Inflow angle (α) with respect to sea surface wind speed at 10 m (U_{10}). The mean and standard deviation α of are shown by the black lines.	114
7.9	Inflow angle (α) against V_{max} under different normalized radial distance ranges. a and b are coefficients in linear regression $\alpha = a \times V_{max} + b$	115
7.10	The dropsonde location before (a) and after translation (b). The orange dash line shows the TC track location at close times from best track. The time difference between dropsondes and SAR acquisition time is shown in the right table. T Inflow angle (α) with storm translation speed lower and higher than 5 m/s.	116
7.11	The contour of atmosphere pressure from HWRF before and after shift. The TC center distance between HWRF and SAR is 7 km.	117

7.12	Base reflectivity from three NEXRAD stations, KEVX, KTBW and KBYX. The measurements were at 23:45 on 9 Oct 2018 and on 0 UTC on 10 Oct 2018 respectively. The dash line denotes the maximum detection range for each weather radar station. Colored lines are the extracted streamlines for each rainband. The black lines with arrows were intended for the estimating the degree of rotation.	118
7.13	Left panel shows the wind direction from in situ dropsondes (bold blue arrow), wind streaks (thin red arrow) and HWRF data (thin blue arrow) at a height of 150 m. The colored lines denoted the streamlines of flagged rainbands in Fig. 7.3. The right panel compares inflow angle (α) and wind direction from HWRF data and wind streaks with dropsondes.	119
7.14	(a) Inflow angle (α) from SAR wind streaks are compared with that from the streamlines of rainbands. (b) wind direction comparison between SAR wind streaks and rainbands.	121
7.15	The correlation coefficient and bias of wind direction between SAR rainband streamlines and HWRF data at different heights are shown before (solid) and after (dash) HWRF data shift and rotation.	122
7.16	Inflow angle (left panel) and wind direction (right panel) from SAR rainbands are compared with HWRF data at three heights, 10 m, 500 m, and 1 km.	123
7.17	(a) The histogram of wind direction difference between HWRF (10 m) and wind streaks. (b) the wind direction difference against incidence angle. The dash red line is the regression fit on the scatter points. The green line marks the location of TC center. The orange line denotes the location of difference equal to 0. (c) The correlation coefficient and bias between SAR wind streaks and HWRF data are shown at increasing heights before (solid) and after (dash) HWRF data shift and rotation	124

Chapter 1

Introduction

Spaceborne synthetic aperture radar (SAR) has the capability of capturing various oceanic and atmospheric phenomena, including tropical rain cells and rainbands in tropical cyclones (TCs). In 1978, Seasat documented the first signatures of tropical rain cells and TCs in SAR images. Since then, many efforts have been devoted to understand the mechanisms of rain signatures in SAR images. However, there are still conflicting views and limitation on research regarding how largely rain impacts the radar backscatter and how to recognize those rain signatures in SAR images as well as how the wind direction distributes around the rainbands in TCs. Such uncertainties are mainly due to the limited datasets available and large spatial resolutions in the past. This research aims to uncover and explain the modification by rainfall on C-band radar backscatter and to propose improved algorithms to detect the rain signatures in SAR images under various wind regimes. In particular, to detect the signatures of rainbands in TCs could help to understand the wind structures in relation to atmosphere boundary rolls in TCs. This chapter will provide an introduction to the study by first discussing the background and context, followed by the research problem, the research objectives and significance as well as the overall organization of this thesis.

The signatures of precipitation in SAR images depend on the SAR instrumental configuration (incidence angle, polarization, frequency), on the sea surface modification by rain (ring waves, splash products and wave damping) as well as the atmospheric effects (volume scattering and attenuation). Melsheimer et al. (1998) showed that the rain signatures were frequency dependent using data from the Spaceborne Imaging Radar-C/X-band SAR (SIR-C/X-SAR) mission in 1994. They compared the rain signatures simultaneously at L-, X-, and C-bands based on SIR-C/X-SAR data. The precipitation signatures at C-band are the most complicated to interpret of the three frequencies because the radar backscatter can be enhanced or reduced at this frequency, resulting from the intertwined effects of surface modification and atmospheric effects. Many researchers concentrated on the rain-induced surface structures to understand the mechanisms of rain signatures, since the surface structures (ring waves, splash products) are commonly observed and can be readily created in laboratory. Those structures apparently change the sea surface roughness, and also be the potential scatterers of incident microwaves.

As for the atmospheric effects, the raindrops can scatter and absorb the incident microwaves. Attenuation and scattering are quite significant at high frequency (e.g., Ku band, X band) but can not be considered as negligible at C band especially in heavy precipitation.

The existing studies on rain signatures in C-band SAR images indicate that radar backscatter in rain area is a result of multiple factors. Given the complex mechanisms involved, it is difficult to evaluate how the Normalized Radar Cross Section (NRCS) responds to rainfall rate and to separate the contributions from the different processes. Upon this, a few studies focused on case studies or explanatory conceptual model of rain impact. However, their results present conflicting views about the sensitivity of NRCS to rain rate and the models can not always be qualitatively applied to SAR images. For instance, Lin et al., 2014 showed that VV-pol NRCS significantly increases with rain rate even under light rain whereas Liu et al. (2016) found that the NRCS increases with base reflectivity up to 45 dBZ and then decreases gradually. As for the proposed models, the factors included differ which make it difficult to understand the mechanisms involved.

The detection/recognition of rain signatures in SAR images has not been widely studied mainly because of the lack of coincident collocated rainfall rate measurements. Instead, many algorithms have been proposed for the heterogeneity detection in SAR images, either in the spectral or the spatial domain. These methods shows efficiency in object detection yet with a defect in rain signature recognition. With the benefits of dual-polarization information from Sentinel-1, it can be expected to greatly serve for the development of rain signature detection, in particular the recognition of rainbands in TCs that could not only help to remove the rain contaminated area, but also to reveal the cyclone structure and its potential development.

Given the conflicting views and limitation on the precipitation impact on radar backscatter, this study aims to evaluate and identify the rain signatures in C-band SAR images. To be more specific, the objectives for this study are:

- 1) To quantify the impact of rainfall rate on C-band radar backscatter under different wind regimes and the difference between co- and cross-polarization.
- 2) To propose a model to evaluate the contribution from volume scattering and attenuation on radar backscatter in heavy rainfall.
- 3) To propose the methods for recognizing the rain cell clusters and rainbands in TCs.
- 4) To evaluate the inflow angle and wind direction derived from TC rainbands, wind streaks and different models.

This study aims to better understand the modification of radar backscatter by precipitation, benefiting

from a large collocated dataset between C-band SAR and weather radar. This unique dataset could extensively be used for further precipitation studies, and/or as ancillary data to support more investigation on atmospheric or oceanic topics. However, although the dataset is significantly large, the observation of TCs is still limited because of the limited occurrence of TCs. Thus, the algorithm for rainband detection will still require further validation using more TC cases. The inflow angles around rainbands in TCs provide a unique attention on the cyclone structures. Due to the limited number of TCs, a more comprehensive analysis on inflow angles is necessary to reveal the variation of surface winds. In addition, as the model proposed in this study focuses on atmospheric transmission, it has good potentials to be integrated in more complicated models in the future.

This dissertation is organized into 8 chapters. In Chapter One, the background and context of the study are introduced. Also it introduces the research objectives and followed questions. At the same time, we propose the values of such research and some limitations.

Chapter Two summarizes the existing literature concerning the observation of precipitation in SAR data and some laboratory experiments conducted to understand the rain-induced structures and atmospheric transmission as precipitation occurs. Some method of image processing such as targets detection (local gradient and thresholding methods) already used for the analysis of SAR images are presented.

Chapter Three described in details the different datasets used in this study, including SAR images, weather radar precipitation measurement, the European Centre for Medium-Range Weather Forecasts (ECMWF) wind product. The colocation strategy between these different datasets is also presented.

In Chapter Four, the statistics of VV-and VH-polarization NRCS are given with increasing incidence angles and wind speeds in case of tropical rain cells. The mechanisms for high backscatter are discussed. In addition, the signatures of precipitation on rainbands are analyzed in terms of inner rainband and outer rainband respectively.

Chapter Five presents a numerical model which has the capability of simulating the radar backscatter under different rain rates. Within this mode, the attenuation and backscattering by the raindrops are taken into account and simultaneously the surface effects are neglected.

In Chapter Six, two methodologies with the capability of filtering rain cells and rainbands in TCs in SAR images are presented. The new filters are developed using the data collocated over US coastal areas and are then validated independently using the data collocated over the Japan archipelago.

In Chapter Seven, the inflow angles and the wind directions derived from the rainbands, in situ dropsondes, wind streaks, and HWRF data are analysed in TC Michael.

The conclusions of this study are given in last chapter, where the perspectives of this subject and its potential application on model development are also discussed.

Chapter 2

Background

Contents

2.1	Rain signatures in SAR observation	5
2.1.1	Satellite observation on tropical rain cells	5
2.1.2	Satellite observation of tropical cyclones	9
2.2	Mechanisms for precipitation modulation on radar signal	13
2.2.1	Atmospheric transmission	13
2.2.2	Backscattering on the sea surface	15
2.2.3	Gust front	19
2.3	Radar cross section under different rain rates	21
2.4	Precipitation Flag	24

2.1 Rain signatures in SAR observation

2.1.1 Satellite observation on tropical rain cells

The Seasat satellite launched in 1978 was the pioneering Earth observation mission of NASA carrying the first spaceborne SAR instrument. This L-band SAR captured a lot of images with different atmospheric and oceanographic phenomenons, including the footprints of rain cells. Similar patterns were hereafter repeatedly reported in studies by multi-frequency SARs, i.e., L-band ALOS-1/2, X-band TerraSAR-X/TanDEM-X, C-band ENVISAT/ASAR and ERS-1/2.

L-band SAR missions have been launched continuously after Seasat, i.e., JERS-1 (1992–1998), ALOS (2006–2011), ALOS-2 (2014–present), and SAOCOM-1 (2017–present). The rain effects on L-band was shown to be generally dark patterns sometimes associated with surrounding bright clusters related to gust fronts. This kind of signatures where rain cells in tropical regions are usually observed as dark spots along with bright patches in L-band SAR images. As observed in Fu and Holt (1982), rain cells have a echo-free hole about 5×7 km because the rainfall smooth the capillary/gravity waves. Surrounding the holes, high radar return zones with a roughly elliptically shape are observed due to the wind squalls. The

structures suggest that rain happened in the center while the induced gust front radially moves away from the rain cell center.

Clusters of rain cells such as squall lines could have similar appearance. A squall line usually consists of clusters of thunderstorms forming along or ahead of a cold front. Squall lines in Fu and Holt (1982) appeared as two bright and curvilinear strips with some rain-induced dark spots. The bright strips were caused by the spatially variable local winds between 5-9 m/s after referring to the Seasat scatterometer data. Melsheimer et al. (1998) presented similar patterns in L-band SAR imagery but also revealed that signatures of rain cells at L-band could only appear as dark patches (Fig. 2.1). Furthermore, the L-band SAR images show very low backscatter in rain-contaminated area no matter the co-pol or cross-pol polarization. Due to the long wavelength at L band, the impact of hydrometeors on the microwave transmission in the atmosphere is negligible so that the contribution from sea surface is dominant. The dampening of Bragg waves by rain-enhanced turbulence leads to the radar backscatter reduction. This was also reported in a study of JERS-1 satellites (Iguchi et al., 1995). Overall, the rain signatures at L-band is mainly associated with the damping of short gravity waves or the variation of local winds on the water surface and independent of the absorption or scattering in the atmosphere due to its long wavelength.

At X-band, rain cells in SAR images appears as bright patches at near range followed by long dark shadows, as observed by TerraSAR-X, SIR-C/X and Shuttle Radar Topography Mission(SRTM) (Dankmayer et al., 2009). The case observed by SIR-C/X shows that kind of signature (Fig. 2.1). The VV-pol backscattering in bright region associated with rain is around 4-5 dB above that unaffected by precipitation. This enhancement is attributable to the backscattering from hydrometeors. By comparison, the backscatter in the shadow is 10 dB lower than that of rain-free region resulting from the attenuation in the atmosphere. As a result, the atmospheric effects are dominant on the backscatter at X-band.

The signatures at C-band consists of concurrent bright and dark patches but in different location from X-band and L-band. As seen in Fig. 2.1, the rain signatures mostly appear as bright patches adjacent to small dark regions in VV/HH. Furthermore, the signatures differ in co- and cross-polarizations. In VV/HH, rain appears to be associated with bright more or less surrounded by dark areas. However, almost only bright patches are observed in HV polarization even where dark patches appear in VV/HH polarization. The backscatter in bright patches increases by 4-5 dB in VV/HH compared to rain-free areas whereas the increase can exceed 10 dB in HV. However, the reduction of radar backscatter is about 5-8 dB in HH/VV but almost no reduction in HV.

Alpers et al. (2016) summarized the different kinds of signatures of rain cells at C-band under different

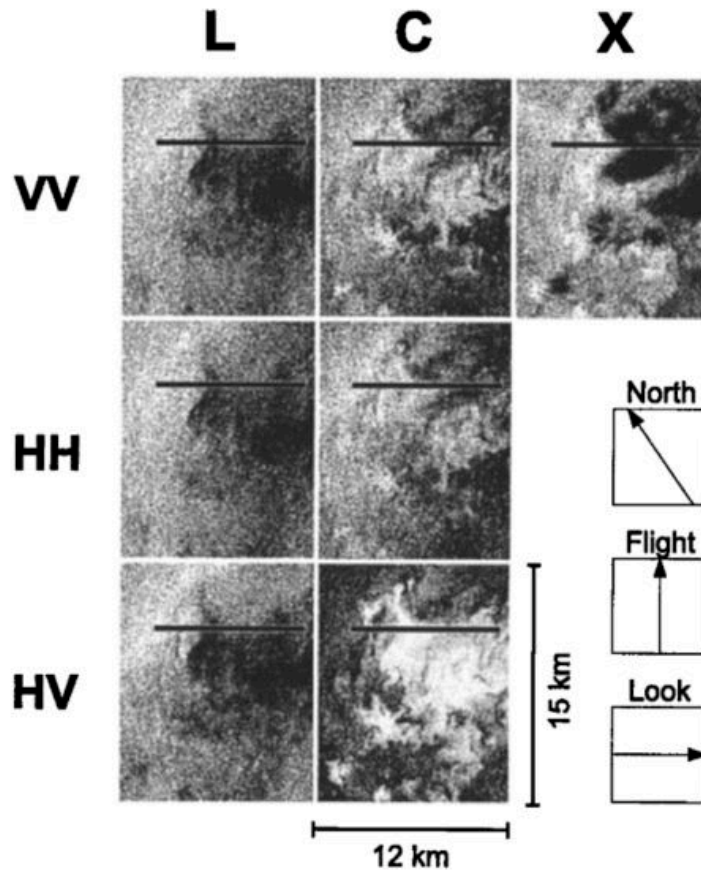


Figure 2.1: SIR-C/X-SAR images of the same scene in the Gulf of Mexico acquired at different radar frequencies and polarizations on April 18, 1994. Reproduced from Melsheimer et al. (1998) ©IEEE

wind and rain conditions as shown in Fig. 2.2. Fig. 2.2(a) is a VV-pol image captured by Sentinel-1 at 23:53 UTC on 9 June 2015. Apparently there is no dark hole in the center but only a bright patch, which could result from the scattering from hydrometers or the ring waves or splash products on the surface. Moreover, the less bright area in the surrounding of the cell is due to the downdrafts. The wind speed in no-rain area is around 2.5 m/s although no rain rate was reported. Fig. 2.2(b) presents a rainband as the dark hollow where the rain rate is up to 50 mm/h. The rainband moved westward at a speed of approximately 9.2 m/s and the wind speed from NCEP model was blowing to west with about 2-4 m/s. Fig. 2.2(c) shows a similar pattern as Fig. 2.2(b), but with a strong ambient wind speed of 12-14 m/s and a rain rate of 30-75 mm/h. However, a dark strip was observed as seen in Fig. 2.2(c), in relation to the ambient wind speed. However, a squall line reported by Lin et al. (2001) and observed in ERS-2/SAR images and colocated with weather radar appears as a bright line only (not shown here).

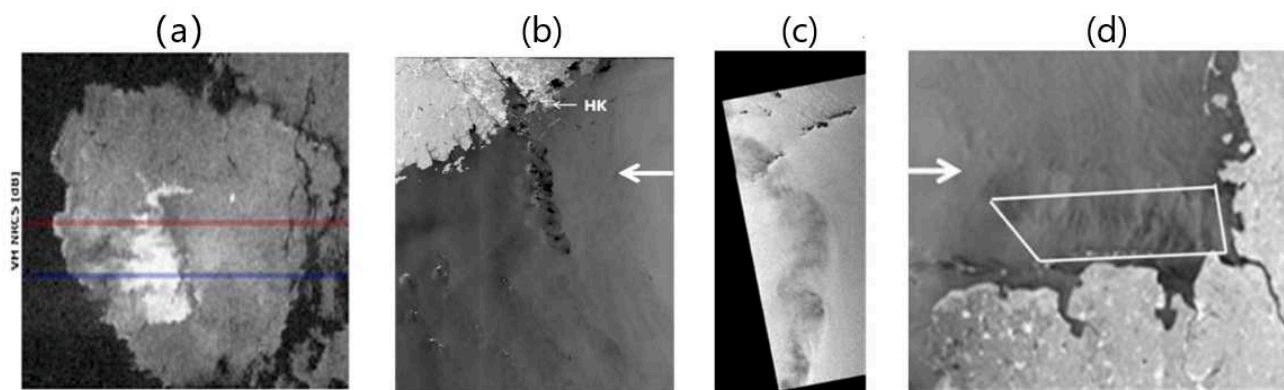


Figure 2.2: Examples of C-band SAR images with rain signatures reported by Alpers et al. (2016). (a) 23:53 UTC on 9 June 2015 acquired by Sentinel-1 at VV images. Rain signatures in the west of the Philippine island. (b) ENVISAT/ASAR at VV polarization at 02:27 UTC on 18 August 2011 close to Hong Kong. (c) ENVISAT/ASAR VV-pol image at 14:18 UTC on 6 August 2008 over the South China Sea off the coast of Hong Kong. (d) ENVISAT/ASAR HH-pol image at 21:18 UTC on 9 December 2011 over the southern North Sea. ©Elsevier

Fig. 2.2(d) is an example of stratiform rain shown as shallow footprint in the HH-pol SAR image. The rain rate is between 1 and 5 mm/hr and the wind speeds blows from northwest at a speed of 12-14 m/s.

The atmosphere transmission for C-band can be neglected in light to moderate rain but can be dominant in heavy rainfall (Danklmayer et al., 2009). Meanwhile, the rain-induced structures on the sea surface including ring waves, splashes, stalks can effectively modify the sea surface roughness. Therefore, the bright patches at C-band can be attributed to the scattering from hydrometeors in the atmosphere or to the rain induced increase of sea surface roughness. The dark areas can result from the attenuation in the atmosphere or to the wave damping due to the enhanced turbulence beneath the sea surface. Because of these multiple factors contributing to the signature of rain cells, the C-band backscatter lies in a region of transition between enhancement and reduction and for each case both attenuation and enhancement resulting from atmospheric and/or surface processes can be observed.

Overall, the patterns of rain signatures in C-band SAR images are more complicated to interpret than that in L- and C-band imagery. This complexity has been primarily shown to be related to rain rate and wind conditions but still no general laws have been given.

2.1.2 Satellite observation of tropical cyclones

Precipitations in tropical cyclone (TC) are organized in bands spiralling towards the center or eye (Maynard, 1945; Wexler, 1947). The rainbands in TC can be classified into eyewalls, principal rainbands, secondary rainbands and distant rainbands (Willoughby et al., 1984; Willoughby, 1988; Houze, 2010) or be categorized by their distance to the TC center: 1) eyewall region, 2) inner rainband region and 3) outer rainband region (Molinari et al., 1999). The principal rainbands and secondary rainbands are in the inner rainband region and the distant rainbands are formed in the outer rainband region. A schematic of those rainbands is illustrated in Fig. 2.4(a).

Wexler (1947) was the first to document the cyclone structure using weather radar. The observed quasi-circular bands around the center showed asymmetry in their distribution. Marks (1985) tracked the hurricane Allen in 1980 during 6 consecutive days and gave a first quantitative description of the radar reflectivity in cyclone rainbands. The heaviest rainfall happened around the eyewall with reflectivity around 42-45 dBZ where the precipitation pattern is mainly a quasi-circular ring. Black et al. (1996) and Dodge et al. (1999) hereafter reported that the reflectivity in the eyewall region generally exceeds 40 dBZ. Hence and Houze (2011) collected TRMM reflectivity data of storms from 1998 to 2007 for different intensity categories and differentiated the reflectivity characteristics from convective and stratiform precipitations in the eyewall region. Below 5 km altitude, the convective precipitation mostly concentrated between 40-45 dBZ whereas the stratiform precipitation had a peak around 30 dBZ. Above 5 km both reflectivities sharply decreased and centered around 22 dBZ due to the concentration of ice at height between 5 and 9 km. In some mature TCs, two eyewalls can form where the reflectivities are observed over 40 dBZ, even to 48 dBZ in the two eyewalls (Jorgensen, 1984; Dodge et al., 1999).

The principal rainband is stationary relative to the TC center and extends outwards from the inner core. The closer to the center the rainband, the more tangential it becomes to the eyewall. The vertical cross section of the reflectivity shows an elongated sloping cell with high reflectivity, which is surrounded by stratiform precipitation sometimes with a bright band in the melting layer (Houze, 2014; Senn and Hiser, 1959). The radial slope of high reflectivity is in the same direction as the eyewall cloud. However, compared to the eyewall, the high reflectivities in the principal rainband is confined below 8-10 km since the radial outflow from the eyewall dominates the flow at that height Hence and Houze (2011).

Observations of the secondary rainbands are very limited. Willoughby et al. (1984) described the secondary rainband from aircraft observation during the RAINEX campaign. Secondary rainbands are often transient and smaller than the principal one. They are located inward of the principal rainband in the

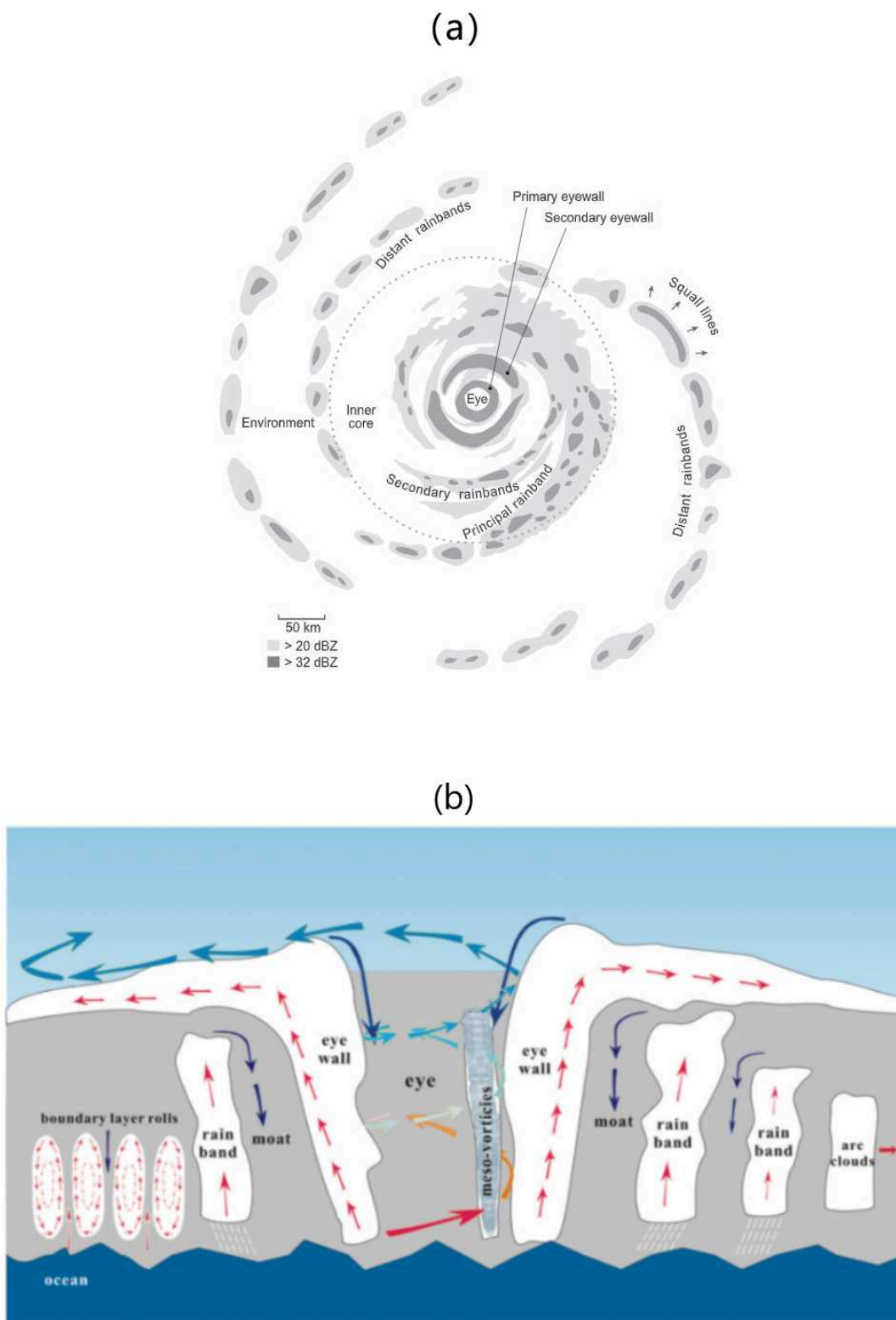


Figure 2.3: (a) Radar reflectivity in Northern Hemisphere tropical cyclone with a double eyewall from Houze (2010) (b) Schematic illustration of tropical cyclone structure including eyewall and rainband from Li et al. (2013). ©AMS

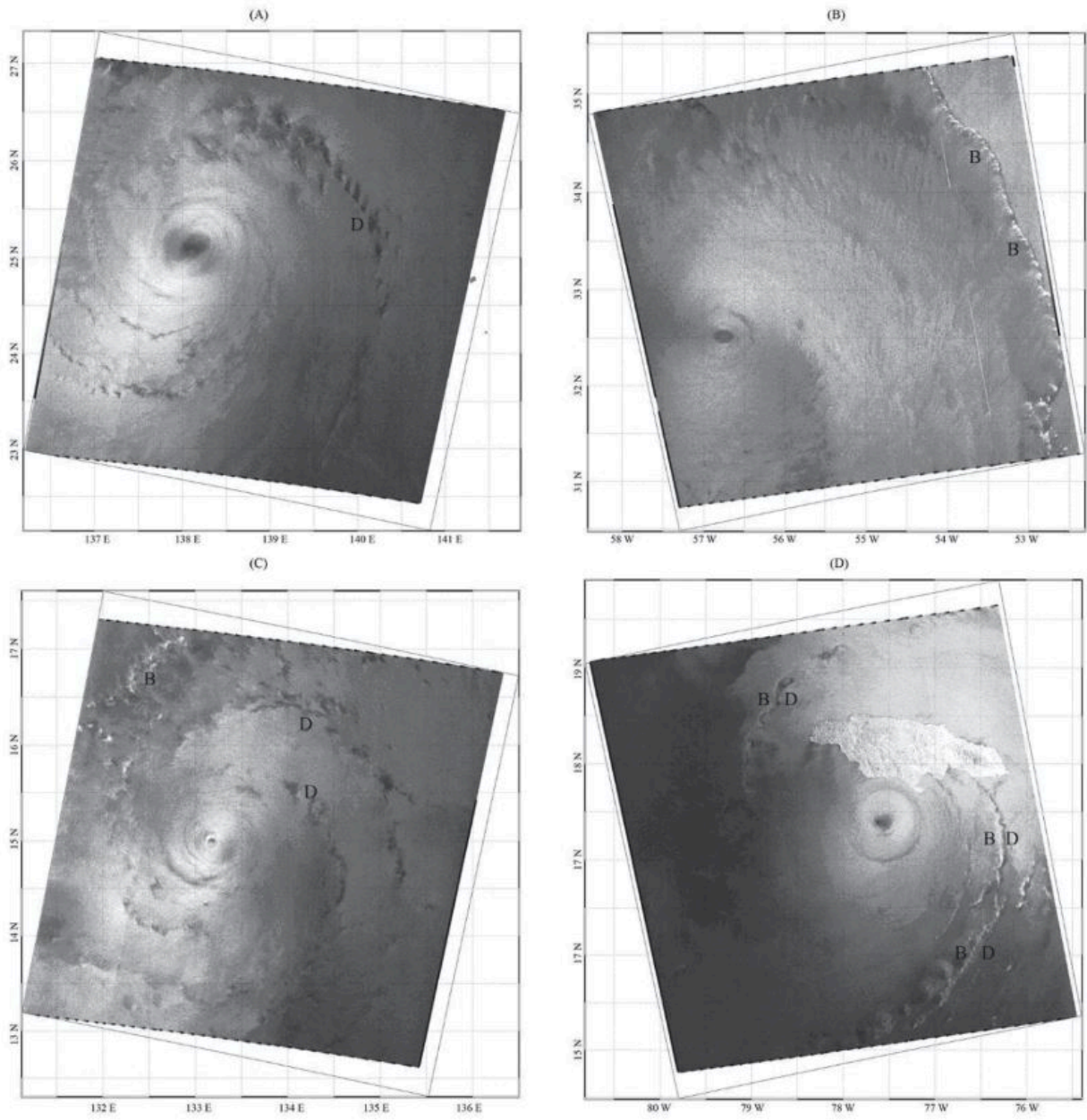


Figure 2.4: Different rainband patterns observed in TC captured by RadarSAT-2 reported by Li et al. (2013). ©AMS

inner core, generally at a distance from the center of three times the radius of maximum wind (e.g., Allison et al., 1974; Fett and Brand, 1975). It often merges between eyewall and principal rainbands. They have a smaller size and rotate cyclonically around the center at a slower speed than the tangential flow. Xiao et al. (2019) compared the difference between the secondary and principal rainbands in convective structures. They pointed out that the mechanism for secondary rainband is closely in relation to the mid-level convergence whereas the principal rainband is convective in the upwind to mid-wind section. An updraft in secondary rainband goes slant in 1-2km height and then keeps almost updraft between 2.5km and 8km in comparison to the nearly upright below 8 km in principal rainband.

The distant rainbands are located far from the TC center with a possible formation of squall lines, where convective rain cells are embedded by stratiform. Hence and Houze (2011) demonstrated that the reflectivity in distant rainbands has a distribution than the eyewall and principal rainbands, i.e, higher proportion in the low reflectivity ranges. Also the reflectivity peak lies between 20 and 30 dBZ below 5 km whereas it is around 32dBZ in the eyewall and inner rainbands. In their study, the reflectivity contours in distant rainbands extend to greater heights (10-12 km) than that in the inner rainbands (8-9km). It was thereby concluded that the convection in distant rainbands is unconstrained by the inner-core vortex.

The arc-shaped distant rainbands indicates a strong downdraft spreading out below the convective cells. The presence of downdraft often lead to a sharp gradient of reflectivity at the inner edge of the distant rainbands (Cheng and Li, 2020)

Thanks to the development of Earth Observation from space, TC images have been collected in multi-frequencies (visible, IR, radar), which help monitor and study the TC movement and rainbands evolution. The rainbands in SAR images were observed as different patterns, manifested by the enhancement or reduction of radar cross section, in relation to storm intensity and wind structures (Dvorak, 1975; Li et al., 2013).

Jameson et al. (1997) described the precipitation in rain storms acquired by SIR-C/X-SAR at nadir and slant geometries. They showed that rain can induce large variations of the signal at incidence angles from 30° to 50° . Fu and Holt (1982) reported that Seasat sampled hurricane Iva (Cat-1) in the eastern Pacific Ocean and a tropical storm near the Gulf of California. In Iva, one spiral arm shown as connected dark and bright patches was located at about 50 km from the center. Another arm was observed as bright strips extending from the west to the east south of the center. These two spiral arms were in relation to the rainbands as depicted by the infrared images from GOES. For the storm, the rainbands were shown as a cyclonic dark area around the center. Katsaros et al. (2002) reported that hurricane Mitch captured by RADARSAT-1 was characterized by low radar signals close to the center in a strong rain area. Li

et al. (2013) summarized the different eye shapes and rainband patterns in tropical cyclones. Four types of rainband patterns were reported: 1) dark, 2) bright, 3) dark in inner rainband and bright in outer rainband, 4) half dark and half bright as shown sequentially in Fig. 2.4. However, due to the lack of rain data, no explanations was given for the appearance of these different rainband patterns.

2.2 Mechanisms for precipitation modulation on radar signal

As space-born SAR looks downward in case of precipitation. There are 3 physical process responsible for modulating the received backscatter radar signal 1) scattering and attenuation by hydrometeors as radar pulse penetrates the atmosphere, 2) scattering by rain-induced structures, i.e., ring waves, splash products (craters, stalks, crowns and bouncing-upward raindrop) on the sea surface as well as wave damping due to the turbulence in the sea upper layer enhanced by impinging raindrops, 3) sea surface roughness increased by the downdraft winds associated with raincells.

2.2.1 Atmospheric transmission

In radar meteorology, scattering and attenuation by hydrometeors (i.e., raindrops, ice crystals, hail....) has been extensively studied since the 1960s. Weather radars can measure the precipitation intensities due to their scattering properties [e.g., Doviak and Zrníc, 1993; Sauvageot, 1991]. The attenuation results from two processes as an electromagnetic wave propagates through a precipitation region. One part of the energy is absorbed by the different hydrometeors while another part is scattered in all directions. These two mechanisms are strongly related to the dielectric properties of the hydrometeors. The effect of volume scattering and attenuation is also strongly in relation to the radar frequency and the rainfall rate. With higher radar frequency or heavier rainfall rate, stronger scattering and attenuation happens on the hydrometeors. Most weather radars operate at S-band or C-band and provide estimates of the rainfall rate from the reflectivity, which is a function of the particle density and diameters in one unit volume.

Raindrops have the diameter between 0.6 mm and 4 mm. The attenuation by raindrops of radar signal has been widely studied since the 60's and the Marshall-Palmer (Marshall, J. S., and W. McK. Palmer, 1948: The distribution of raindrops with size. *J. Meteor.*, 5, 165–166.) Olsen et al. (1978) $A = aR^b$ relationship is now widely used, . The a and b coefficients are frequency dependant and estiamtes are available for the frequency between 1GHZ and 100GHZ. The relation was computed assuming that the dropsize distribution in widespread and convective rain cells follows the Laws and Parsons, Marshall and Palmer, and Joss et al distributions. Battan (1971) estimated that radar attenuation by wet ice spheres.

The inside volume of very small and very large ice spheres produces relatively little attenuation because the former has a small radar cross section and the latter has a very low concentration. Compared to dry hail, water-coated ice spheres cause more attenuation. For C-band, the two-way attenuation could be 6 dB/km given the hailstone has a size of 2.89 cm with a water coat of 0.05 cm. The attenuation by dry snow in the microwave region is less than that by rain of the same intensity. However, snow attenuation may be increasingly important for shorter wavelengths.

The scattering behavior on hydrometeors is often associated with Rayleigh or Mie scattering regime. These approximations depend on the frequencies and the electrical size of the particle, x defined by the size parameter $x = 2\pi r/\lambda$, where the r is the radius of the particle sphere and λ is the electromagnetic wave wavelength ; For $x \ll 1$, the wavelength is much larger than the particle and hence all parts of the particle experience nearly the same electric field. Thus the Rayleigh approximation can be applied to scattering problems with low size parameter. Given the frequency below 10 GHz and the raindrop size, the backscattering can be approximated by Rayleigh scattering. It depends on frequency, refractive index and reflectivity.

Different from weather radars that look upward from the ground, SARs look downward from space, thereby penetrating the hydrometeors in the atmosphere in which the volume scattering and attenuation can not be simply neglected especially at X- and C-bands. The SIR-C/X-SAR mission launched in 1994 with X- and C-band radars operated under two observation geometries; nadir and side-looking observations and slant using a rolling antenna (Jameson et al., 1997; Melsheimer et al., 1998). At nadir observation, profiling measurements could be carried out, i.e., radar backscatter measurements as a function of height. At slant geometry, rain areas were shown as brighter than surrounding, which reached -10 dB at C-band and X-band. It was subject to the backscattering under heavy precipitation. However, the rain cells over Amazon forest were shown as dark areas with bright patches at the leading edges at X-band and only dark areas at C-band. (Melsheimer et al., 1998) presented several cases acquired simultaneously at C-band and X-band, where more bright areas were shown at C-band than at X-band in Fig. 2.1. These studies illustrated that the scattering and attenuation can both dominate the radar backscatter. Apart from that, the scattering at X-band is stronger than C-band due to its shorter wavelength.

Strong backscatter at cross-polarization was first noticed by Jameson et al. (1997) in the melting level where the wet crystals act like randomly oriented wet dipoles in the nadir geometry where contamination of the rain echoes from the sea surface is largely eliminated. When the melting is completed, the cross-polarized signals disappear with the formation of the raindrops. Likewise, already as early as 1952, Browne and Robinson (1952) have carried out cross-polarization measurements with a ground-based radar

operating at a 3.2cm wavelength. They found that the 'melting-band' produce backscattered radiation with a greater cross-polarized component than that given by the rain below and the snow above the freezing-level. For some cases, the melting-band could be detected at cross-polarization, but not at co-polarization. D'Amico et al. (1998) have developed an anisotropic model, which is able to describe this depolarization effect. In their model, the melting layer consists of melting hydrometeors of differing shapes and concentrations. The melting particles are assumed to have a spheroidal shape with axial ratio $r = a/b$, which varies with the melted fraction. At the top of the melting layer the ellipticity of the particles is supposed to be maximum (i.e., the particles are more distorted), and it decreases to the standard value for rain at the bottom of the melting layer. They could show that their model results agree reasonably well with observations. In their model, the melting particles can cause the depolarization, which is defined as linear depolarization ratio (LDR) in radar meteorology. It was observed that LDR can increase by 10 dB at the melting layer, whereas co-pol radar signatures can even increase by around 20 dB.

2.2.2 Backscattering on the sea surface

2.2.2.1 Ring waves and splash products

Before Worthington (1908), few people paid attention to the rain-striking structures in nature and would to record the fantastic phenomena. His study on these structures benefiting from the development of photographic systems showed that a series of process in millisecond precision. He made the raindrop by a water drop slipping from a glass. By controlling the time intervals in the continuous droplets of the same size, Worthington (1908) obtained a series of photos showing the successive process of the splash, such as "ring wave", "crown", "stalk". His study inspired many people who focused on the rain processes using modern high-speed flash photography and provided a precious material for study. Of course these photographs provided more than just the form of the structures but also after analysis of the images some volume information. The structures appeared in the images time sequence, and their dimensions seemed to be related to the water drop diameter. This dependence is strong for low rain rates but becomes weaker as the rain rate increases. However, at a certain azimuth angle, the radar cross section increases with rain rate.

Wetzel (1990) was the first to study the variation of the rain-induced splash products and ring waves along time. A crown gave rise to a height of 1D (D diameter of the drop) and a diameter of 3-4 D with irregular upper boundary. It lasted about 50 ms from its initial formation to the decay. Then the crown subsided down to the floor, leading to the ring waves spreading away and an additional cylinder formed

at the center named 'stalk'. The stalk can reach a height of 4-8D with a diameter $3/4 D$. The lifetime of this process is around 100 to 200 ms. The water ball on top of the stalks may squeeze off splitting into several small drops. The "mesa" relaxes into a second annular wave that propagates outward in pursuit of the original "crown" wave, the whole thing is preceded by what appears to be a set of weak waves of very small wavelength (parasitic capillaries). If secondary droplets have been squeezed off in the stalk, they fall back to form much weaker systems of secondary "ring waves". Variations in the detail "ring wave" of the splash process are probably due to variations in such parameters such as the surface and drop temperatures, surface cleanliness, drop size and velocity. For example, in the case of large, high-speed drops, the walls of the "crown" are seen to meet over the top of the initial crater to form a "bubble," with no evidence of a central stalk.

The formation of these structures is in relation to the raindrop size and terminal velocities. The terminal velocity of raindrops can reach 4 m/s for a diameter of 1 mm, and 8 m/s for 3 mm raindrops, dependent on pressures and temperature (Foote and Du Toit, 1969).

Rodriguez and Mesler (1985) observed that the drops could strike the splash but instead the drops coalesce with the pool forming a vortex ring. Only a series of rings was generated as drops fell from 1.32 m height and reached a velocity of 0.51 m/s. Comparatively, the splash were produced by drops falling from 18.72 m with a terminal velocity of 1.92 m/s even though the drop diameter was kept at the same diameter of 2.8 mm. This experiment shows that when the raindrop falling speed is low (like 0.6 m/s) it is certainly like the raindrop floating on the surface. However, if the raindrop velocity is over 2.4 m/s, the splash could be intrigue by raindrops with diameter larger than 1 mm. It is also mentioned by Yikun, 1988 that the splash could occur for various drop sizes as falling speed reaches 1 m/s. Yet the crater diameter was in relation to the falling height of the drop. It increases rapidly as the falling height increases and the time for the crater to grow to its maximum size increases as well. Craeye et al. (1999) observed that the energy of ring waves has a strong dependence on the drop size with a wavenumber around $0.2mm^{-1}$.

Ring waves were identified as a major contributor to the radar backscatter under rain by Bliven and Giovanangeli (1993). A further experiment was conducted by Bliven, P. W. Sobieski, et al. (1997) during which rain rates ranging from 5 to 200 mm/hr were simulated by needles of various diameters. They showed that the surface roughness increased with increasing rain rates, but that the mean slope decreased. The frequency spectra of the sea surface elevation is the largest between 3.25 to 12 HZ representing almost 90 % in the total surface variance. More significantly, the amplitude of the frequency spectra increased with increasing rain rate but kept a similar shape. That is the maximum of the spectrum remained around

the same frequency. Corresponding, the wavelength of ring waves ranged from 2 to 15 cm with a peak around 5.3 cm. The VV normalized radar cross section at incidence angle of 30° grows with increasing rain rate, and followed in a power law model. Craeye and Piotr W Sobieski (1995) analyzed the signature of ring waves as a function of incidence angle. However this response decreases rapidly when increasing incidence. Lemaire et al. (2002) studied the impact of the raindrop size distribution on the ring waves spectra. The study showed that the ring wave spectra remains constant as rain rate increases for a given drop size, and the amplitude of spectrum increases with increasing rain rate. For a given rain rate, the peak frequency decreases as the raindrop size becomes larger whereas the ring wave energy increases.

Sobieski and Bliven (1995) suggested that ring waves might be the largest contributor to the radar backscatter due to its long duration by recording the rain-induced structures including crown, craters, stalks and ring wave in consecutive time series using high speed digital camera. The rain simulator was positioned at 13 m above the water surface to insure that the raindrops reach the terminal velocity during the experiment. The crown was initially recorded 18 ms after the raindrop reached the surface. Then crater appeared at 50 ms following the crown subsidence. Later a mixed of craters and stalks occurred at 90 ms. Ring waves propagating outward were the last feature recorded 270 ms after the beginning of the event. The radar backscatter at 13.5 GHz and 36 GHz showed obvious enhancement during the rain events at an incidence angle of 30° . Notably, craters and stalks could induce higher backscatter than ring waves but due to their shorter lifetime their total contribution to the measurements at both frequencies could be smaller. Besides, the lifetime of ring waves observed at 13.5 GHz was longer than the other waves. It showed that at both frequencies. But the long duration of ring waves make itself contribute more than splash products finally. Moreover, the lower frequency radar detected the ring wave propagation at a longer time than high frequency.

Braun and Gade (2006) conducted a field and laboratory experiments at S-, X-, C-band. By comparing the Doppler spectra before and during rain event (35 mm/h), they showed that the VV-pol Doppler spectra at C-band had a maxima at 6.4GHz with incidence angle of 35° and wind speed of 6.5 m/s, coincident with its resonant Bragg frequencies. They confirmed that the ring waves can contribute to the radar backscatter at co-polarization under natural conditions at steep incidence angles on the condition of middle wind speed and heavy rainfall rate. In their laboratory experiment, the cross-polarization was also investigated which showed that a broad maximum in Doppler spectra developed under a heavy rainfall rate of 35 mm/hr, whereas two peaks appeared at co-polarization. This indicated two possible contributions: one from the development of splash products and the other from wind-waves superimposing with ring waves on the sea surface.

2.2.2.2 Wave damping

Seafarers have the common experience that rainfall can calm the sea surface waves and the surface breaking. In Cavaleri et al. (2015), the white caps on the sea surface are smoothed during the rainfall at a rate of 32 mm/h. The wave height is 1.4 m and the wind speed is about 14 m/.

As early as 1875, Reynolds (1875) reported that the raindrops can increase the turbulence in the upper layer along with the generation of a vortex ring. Rain has an obvious damping effect on short-wavelength gravity waves like an oil film in the absence of wind. This damping effect smooths the sea surface roughness owing to the enhanced turbulence in the upper layer and the dissipation caused by small-scale wave breaking (Tsimplis and Thorpe, 1989). Thereby the momentum transferred to long waves is diminished. The mixing of the turbulence layer is dependent on the size of raindrops, rain rate and time. Green and Houk (1979) estimated the mixing layer depth by generating warm artificial rain falling on the cold water. They found that the turbulence layer has a depth of 10-30 cm in fresh water and 5-10 cm in salt water 20 min fter rainfall happened.

Nystuen (1990) illustrated that the damping can not be ignored at low to high wind conditions. For light winds, wave damping is significant for short gravity waves higher than that no-rain situation. In moderate to high winds, the damping effects on short wavelengths is still increased even thought the wind stress still generates the waves.

The wave damping dominates the radar backscatter at L-band. Atlas (1994) and Melsheimer et al. (1998) evidenced the damping by the evolution and interaction of convective rain cells. The echo-free holes within SAR images were well colocated with precipitation regions recorded by weather radars, which evidenced the hypothesis that the holes resulted from wave damping. The damping effect by falling rainfall lasted for about 1 hour. The low backscatter in rain area appeared where the rain rate was very high with existing intense damping effects before the damping effects offseted by the sea surface winds.

The damping effect is also observed at C-band. Braun and Gade (2006) calculated the ratios of the relative radar cross-sections under rain and wind to that under wind only at VV polarization. The ratio at C-band presents both positive and negative values, resulting from wave generation and wave damping effects respectively. The rainfall rate is 12 mm/h. And the transition wavenumber is around $100\text{rad}/\text{m}$, corresponding to a wavelength of 6.3 cm.

An increasing drop size in turn causes a decreasing frequency of the spectral peak of the rain-induced ring waves (Houk and Green 1976, Lemaire et al. 2002). The intensity of wave damping and roughness enhancement is affected by increasing wind speeds (Braun et al. 2002), but can still be observable even

under strong wind conditions as images of rain bands in hurricanes show (Katsaros et al. 2000).

2.2.3 Gust front

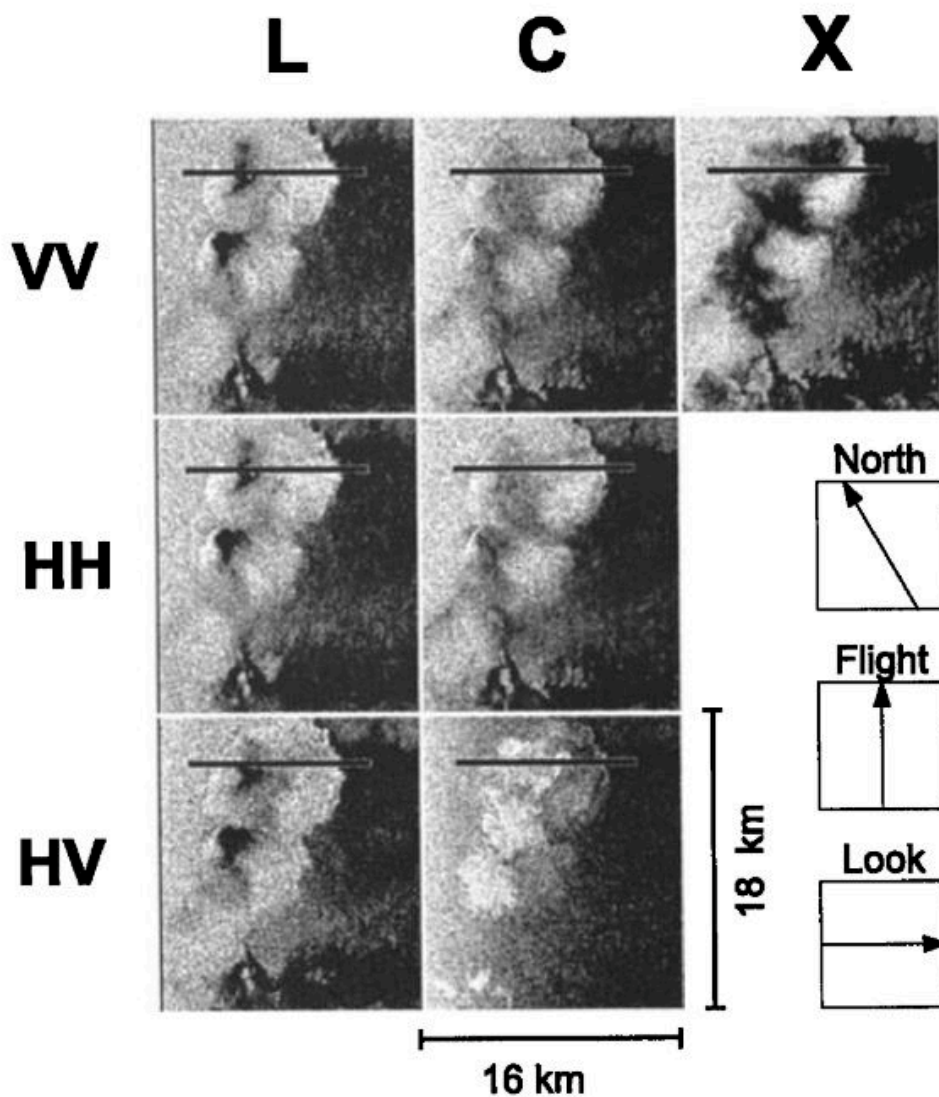


Figure 2.5: SIR-C/X-SAR images acquired over the Andaman Sea near the Malaysian coast at 1847:18 UTC on 17 April 1994 from Melsheimer et al. (1998).

The cool air from the rain storm hits the ground and then spreads in all directions, named as a downdraft. If the air moves very fast, it can create a gust front also called the outflow boundary. It is a line of dangerously gusty winds. In weather radar maps, the gust front can be mapped out when an insects echo is visible. Because the cool air in the leading edge of the gust front moves forward and the

air in the front gets thus lifted blowing up insects that are captured by the radar.

Gust fronts are characterized by high radar backscatter because the increase of local wind enhances the sea surface roughness. They have typical patterns in SAR images: 1) a circle or elliptical shape of bright area with a sharp edge, 2) a bright area with a arc boundary ahead of the rain cells in the moving direction. A gust front is in general visible when the ambient wind field is not too strong and does not resist the airflow in the downdraft. The weaker the surrounding wind speed is, the more obvious the gust front appears. Thus, the signatures of gust fronts are more pronounced in the case of low wind conditions in subtropical/tropical regions as reported by Fu and Holt (1982), Atlas (1994), Melsheimer et al. (1998), Lin et al. (2001), and Alpers et al. (2016). The rain areas are usually shown as dark area with a bright spot in the middle and surrounded by bright clusters (downdraft). The radially spreading downdraft can get distorted if a strong wind field surrounds the rain cells, leading to an irregular signatures in SAR images. In this situation, the bright signatures are located in the downwind direction because the local winds are superimposed to the downdraft. By comparison, a dark area is probably shown in the upwind due to the counterbalance between downdraft and the ambient wind field. The appearance of gust fronts facilitates the identification of rain cells in SAR images.

The radar signatures of gust fronts look quite similar at L-, X- and C-band for the co- and cross-polarizations even though the downdraft patterns are not exactly the same. It is interpreted as a differential increase of the sea surface roughness, in particular, the Bragg waves, at the three frequencies. The dark areas in X- and L-band are different due to the difference of wave damping and atmosphere attenuation. The relaxation time for the Bragg waves (from 3 cm to 30 cm) to the state before precipitation happens at most on the tens of seconds.

Another factor impacting the presence of downdraft is the azimuth angle between the radar looking direction and the wind direction. The dependence of NRCS on azimuth angles is in general stronger in co-polarizations than at cross-polarization. However, the similar patterns of the gust fronts in VV/HH/HV confirm that the main mechanisms for the increased radar backscatter have little dependence on azimuth angles. The simulation by Mitnik (1992) on open convective cells further showed that the ambient wind direction and the ratio of the ambient wind speed to the horizontally-spreading radial wind speed associated with the convective cell are the dominant factors determining the shape and orientation of rain cells signatures in SAR images. That explains the reasons why the strong contrast of radar backscatter between the inside and outside of rain cells in the case little or no ambient wind is almost not sensitive to the wind direction relative to the radar look direction.

2.3 Radar cross section under different rain rates

All the aforementioned processes are involved in the modulation of the radar backscatter under rain. Both ring waves and splash products can increase the water surface variance when the sea is calm. Moore et al. (1979) and Bliven and Giovanangeli (1993) investigated the impact of rain fall on the development of ring waves and splash products under increasing wind speed.

Moore et al. (1979) made a first attempt to investigate the modulation by raindrops of the radar backscatter measured by a 14 GHz FM radar indicating that rain rate and wind speed could significantly modulate the radar backscatter. In their experiment, all measurements were made at the same incidence angle of 40° and distance so that they compared the backscatter power at different rain rates under a certain wind speed between 3 m/s and 20 m/s with that only perturbed by wind. Even though only six cases of rain rates (3, 9, 13, 20, 25, 120 mm/h) were tested and the artificial rain might not reach the terminal velocity falling only from 3 m, they first revealed that the interaction between the rain-induced structures and the wind-driven gravity waves were in relation to wind speed and rain rate. For rain rates lower than 3 mm/h, the rain effect on radar backscatter can be neglected. For rain rates from 3 mm/h to 25 mm/h, radar backscatter under rain is higher than that without rain as wind speed increases up to 9 m/s. However, the very heavy rain at 120 mm/h has been over that with wind from 3 m/s to 15 m/s.

Another similar experiment conducted by Bliven and Giovanangeli (1993) measured the radar cross section by scatterometer at 36 GHz at an incidence angle of 30° and VV polarizations. As the raindrop fell from 1.5 km above the water surface, its striking speed onto the surface only reaches half the terminal velocity. Compared with Moore et al. (1979), they measured the radar cross section in three different conditions, i.e., light wind, light rain and combination of light rain and wind conditions respectively. Typical ring waves and vertical stalks were observed and the radar backscatter showed an obvious increases with rain rate increasing with constant low wind. Furthermore, the measurements for a mixed raindrop size (1.2, 2.8 mm) was higher than that with a fixed diameter of 2.8 mm. It can be inferred that in heavy rainfall, the measurements get increased probably because more large diameter of raindrops occurs (Best, 1950). Another phenomenon in this study was revealed that the radar cross section under lightest rain is comparable to that for the light winds.

Some studies took into account one/multiple mechanisms to simulate the radar cross section. Wetzel (1990) established the electromagnetic scattering model on splash products and ring waves, where the former two are modeled as dielectric cylinders and the last one is treated as a perturbation approximation. The model results described the behaviours of the splash and ring waves well. It predicted that the radar

cross section was on the same order of the magnitude but received no further experimental evidence.

The scattering and attenuation at C-band can not be neglected for heavy rain. Ulaby et al. (1981) described the theory of attenuation and emission by raindrops and snow. Following this theory, Melsheimer et al. (1998) proposed a conceptual model where the radar cross section is composed of the backscatter from sea surface, attenuation and emission by raindrops in the atmosphere. Hereafter, Tournadre and Quilfen (2003) made more consideration of a transfer model for inhomogenous rain cells targeted on Ku-band scatterometer where the backscatter from sea surface was assumed constant ignoring the sea surface roughness modulation by rainfall. The scatterometer pixel size of 25 km is in general much larger than the characteristic length scale of the precipitation variability, which has thus to be considered. This might not be the case for high resolution SAR images. They showed that the atmospheric effects at C-band can lead to strong modification of the measured backscatter and to an overestimation of wind speed for low sea surface backscatter and an underestimation at high backscatter.

Bliven and Giovanangeli (1993) proposed a rain and wind model for backscatter from scatterometer in which the backscatter from wind and rain are two separate terms. Instead of modelling the rain-induced structures, they readily approximated the radar backscatter from rain as a least-square linear model as a function of rain rate where the coefficient was evaluated by the Ku-band scatterometer measurements at incidence angle of 30° and VV polarization. The radar backscatter from wind was described by the model provided by Ulaby et al. (1981). Although the model was not employed to be compared to real measurements under rain, radar cross section showed an increase with rain rate at each azimuth angle. Reppucci et al. (2007) compared the NRCS across hurricane Katrina acquired by ENVISAT ON 28 Aug 2005 to the simulated one using Holland model. The strong signal damping of 2 dB close to the center was interpreted as the attenuation in the atmosphere or the reduction of the sea surface roughness. Yet no further evidence was supported.

Contreras and Plant (2006) established a wave model integrating ring waves and wave damping and validated it by Ku-band observations. In this model the wave damping effect was parameterized by the turbulence using an eddy viscosity. Simulations at C-band showed that rain can increase the backscatter at incidence angles from 25° to 65° for wind speed less than 10 m/s. For a small incidence angle of 15° , the backscatter was decreased due to wave damping.

Draper and Long (2004) proposed a SeaWinds scatterometer model including the surface perturbation and atmosphere transmission where the parameters inside were estimated by the TRMM PR observation and NWP model. They separated wind/rain ranges into three regimes. In first regime (low winds/high rain rate), rain dominates (which provided a possibility to derive rain rate directly). In the second regime

(middle winds/middle rain rate), rain and wind contributed to the signal on the same order. In the third regime (high winds/low rain rate), wind dominates the signal. The three regimes indicated that scatterometer signal is dominated by the surface perturbation in low rain rate but by volume scattering in the atmosphere in high rain rates.

Nie and Long (2007) followed the model proposed by Draper and Long (2004) whereas the surface perturbation was derived from ECMWF and measurements from the ESCAT scatterometer. Particularly they investigated the backscatter at C-band for varying incidence angle from 40° to 57° . The contribution from sea surface under rain was affected by incidence angle and rain rate simultaneously. For low rain rate, the sea surface backscatter decreases with incidence angle but increases at a heavy rainfall. At a moderate rain rate (5.8 mm/h), it almost stayed constant with no dependence on incidence angle. Also they showed that the incidence angle dependence in the three regimes where the thresholds for the three regimes were the same as Draper and Long (2004). With incidence angle increasing, the regime 1 diminished whereas the regime 3 increased, indicating the wind play more dominance at large incidence angles.

Xu et al. (2015) established a model for Ku-, X-, C- band under precipitation incorporating the atmosphere transmission, ring wave spectrum and wind-driven spectra. Their results had a good match with Nie and Long (2007) and also showed a great improvement to the wind-only model. Even though the mean bias in the rain region is greatly balanced in this model, radar backscatter simulated by this model was underestimated in two transects analysis of a case study perhaps because of the low resolution of the rain data and the non consideration of the splash products or the shift of rain cells in space.

Liu et al. (2016) made an experiment of the inclusion of splash products in a new model of sea surface roughness under precipitation. The splash was randomly distributed on the water surface and were considered as the main contributor to the received energy. The correlation between the radar backscatter and the weather radar demonstrated that the reflectivity could affect the radar backscatter significantly, i.e., the radar backscatter increases with reflectivity up to 45 dBZ and then decreases. This conclusion was different from the previous studies conducted by Moore et al. (1979), Contreras and Plant (2006), Draper and Long (2004), and Nie and Long (2007), which supported that the radar backscatter increases monotonously with rain rate.

Zhang et al. (2016) characterized the sea surface scattering including gravity and gravity-capillary wave spectra together with ring wave spectrum and atmospheric effects (scattering and attenuation). They deduced that the reduction of backscatter in case of precipitation is less influenced by atmospheric effects than by wave damping on the sea surface.

Shi et al. (2019) collected the GF-3 SAR images. The effects of rain signature vary with the incidence

angle of the observations, having a damping effect on the SAR radar signal at incidence angles between 15° to 30° while enhancing the radar signal at incidence angles between 30° to 45° and incidence angles smaller than 10° . It was also found that the difference has a ‘V’ relationship with significant wave height at various incidence angles, therefore, including rain effects is important when attempting wave retrieval from SAR images.

2.4 Precipitation Flag

Segmentation algorithms aim to separate objects from the background and to differentiate pixels having nearby values for improving the contrast. Thresholding is a time-saving and memory-efficient segmentation method, the goal is to select one or multiple thresholds to discriminate between specific targets and the background. One common technique for thresholding is based on the analysis of the histogram of a gray-scale image (Sezgin and Sankur, 2004).

The histogram of a gray-scale image is readily generated. If the histogram shows two separate classes with peaks corresponding to targets and background, the threshold is easy to identify. However, in most cases, these two classes can have an partial interaction which requires an additional criteria to decide the threshold. Otsu threshold proposed by Nobuyuki Otsu in 1978 (Otsu, 1979) is one of most widely used, segmenting the targets by minimizing or maximizing the variance between each classes. This method have good results for processing bimodal images. It was successfully applied to SAR images for change detection, flood monitoring, oil spill detection, etc., (Yu et al., 2017; Ban and Yousif, 2016; Phan et al., 2019). However, this method is a global method based on histograms generated from a whole image. For the case with uneven illumination, due to the variability of the background a general threshold will not work and a local threshold technique also called adaptive thresholding has to be used. These thresholding methods

As applied in SAR images, the local gradient proposed by Koch (2004) have been paid much attention. Before operating Sobel operator, the image resolution is reduced to 100m, 200m, 400m. After the reduction and resampling in this smooth, some speckle noises are also removed and features at large-scale are thus reserved. As operating the Sobel operator in x and y directions, a map of 2D gradients is extracted. By computing the quotient of the gradient, they propose 4 parameters to detect the block objects (i.e., land, sea ice), narrow features (internal waves, oil spill) and point targets (ships). This method is widely used in SAR application. Especially all the heterogeneity objects detected by this algorithm needs to be masked before wind inversion.

Chapter 3

Dataset

Contents

3.1 SAR data (Sentinel-1 and RadarSAT-2)	25
3.2 Weather radars	26
3.2.1 NEXRAD	26
3.2.2 Hong Kong weather radar	27
3.2.3 JMA rain radar	28
3.3 ECMWF data	29
3.4 Collocation between the datasets	29

In this chapter, the datasets used in this study are presented, in particular the SAR images data from the Sentinel-1 and RadarSAT-2 satellite, the weather radar precipitation measurements in the US, Japan and Hong Kong coastal area, as well as the ECMWF atmospheric numerical model data. The strategy used to collocate these different data is also introduced at the end of the chapter.

3.1 SAR data (Sentinel-1 and RadarSAT-2)

The Sentinel-1 system is a constellation of two satellites (Sentinel 1A and 1B) carrying C-band SAR sensors that can acquire data day and night and for all weather conditions. Sentinel-1A has been successfully launched in April 2014 and calibrated SAR images are available from the end of 2014. Sentinel-1B was launched in 2016, and share the same orbit plane as Sentinel-1A, with a 180° orbital phasing difference, providing a 6 days repeat cycle. They can operate in four exclusive modes, Interferometric Wide Swath (IW), Extra Wide Swath (EW), StripMap (SM), and Wave (WV). Among these modes, the IW and EW modes use the Terrain Observation with Progressive ScanSAR (TOPSAR) imaging technique that provides large swath widths (250 km for IW and 400 km for EW) and enhanced radiometric performances by reducing the scalloping effect. IW is the main acquisition mode over the coastal and land areas. The IW spatial resolution is 5 m by 20 m and its incidence angle ranges from 29 ° to 46 °. EW has a wider swath of 410 km with a combination of 5 sub-swaths and incidence angle ranging

from 18.9° to 47.0° . The pixel size in EW is $25\text{ m} \times 25\text{ m}$ in range and azimuth direction. In IW/EW, data can be acquired at either single polarization (VV/HH) or dual polarizations (VV+VH/HH+HV). For these ScanSAR modes, Slant-Range Single-Look Complex products (SLC) and Ground Range Detected products (GRD) are available. For the GRDH images two resolution classes are possible: High Resolution (HR) and Medium Resolution (MR).

RADARSAT-2 is the follow-on C-band sensor of RADARSAT-1, launched on 14 December 2007. It is operated by the Canadian Space Agency (CSA). It has the ability of acquiring fully polarimetric (HH + HV + VH + VV) data in a variety of beam modes. The swath width varies from 20 km to 500 km depending on the beam mode. The following Beam modes are available: Standard, Wide Swath, Fine Resolution, Extended Low Incidence, Extended High Incidence, ScanSAR Narrow and ScanSAR Wide. The wide ScanSAR mode has the largest swath width of 500 km, which makes it quite useful to monitor the large scale ocean activities like tropical cyclones. The pixel size in this mode is $50\text{ m} \times 50\text{ m}$ with incidence angles from 20° to 49° . The Wide Swath Beam Mode allows imaging of wider swaths than Standard Beam Mode, but at the expense of slightly coarser spatial resolution. The three Wide Swath beams, W1, W2 and W3, provide coverage of swaths of approximately 170 km, 150 km and 130 km in width respectively, and collectively span a total incidence angle range from 20 degrees to 45 degrees.

3.2 Weather radars

3.2.1 NEXRAD

The NOAA's Next Generation Weather Radar (NEXRAD) network consists of 159 S-band high-resolution weather radars throughout the United States and several oversea locations. Depending on the precipitation state, the radars work in different operation modes (clear air mode and precipitation mode) and scanning strategies involving different elevation angles. The Clear air mode that is the most sensitive, operates for analyzing air movements when there is little or no precipitation activity in the area or at the onset of precipitation. Small objects like atmospheric dust or even light snow can be occasionally detected. The ground clutter (radar echo from the ground) can often be observed in the near range of the radar location as an irregular circular shape that can appear at both clear air mode and precipitation mode. In this study, we used the precipitation measurements from a total of 34 stations deployed in coastal area, as shown in figure 3.1. Different precipitation products in Level 3 are referred to, including base reflectivity ($1\text{ km} / \sim 5\text{ min}$), base velocity ($1\text{ km} / \sim 5\text{ min}$), instantaneous precipitation rate ($0.25\text{ km} / \sim 5\text{ min}$) and hydrometeor classification ($0.25\text{ km} / \sim 5\text{ min}$) (Federal Meteorological Handbook No.

11—Doppler Radar meteorological observations (WSR-88D). Part C: WSR-88D products and algorithms, 2017).

Base reflectivity is a radar centered product with a maximum radius of 460 km. It is the reflectivity at the lowest radar elevation angle of 0.5° above the horizon. The value of reflectivity is provided in unit of dBZ, which ranges from -28 to +28 in clear air mode or from 5 to 75 in precipitation mode. We take 20 dBZ as the start of light rain in this study. Additionally, one should note that the altitude of radar beam increases with increasing distance from the radar location. Although the elevation angle is quite small, the beam altitude can reach 5 km close to the maximum radar coverage.

The hydrometeor classification product gives the most probable dominant scatterer estimation at the lowest scanning elevation. It combines different reflectivity and depolarization parameters that efficiently distinguish rain, snow, ice, and biological objects. Thus, this product is helpful to estimate the scattering types and thereby determine the possible effects on NRCS.

Instantaneous precipitation rate is derived from the lowest elevation ranges by dual polarization quantitative precipitation estimation algorithm. It takes into account different conversion involving hydrometeor types instead of a single Z-R conversion.

3.2.2 Hong Kong weather radar

The Terminal Doppler Weather Radar (TDWR) was originally built to serve the terminal area of the airport. Its mission is to detect windshear and microburst associated with convective storms, so as to enhance the safety of aircraft landing and taking off from the Hong Kong International Airport. There are now two TDWR stations, one at Tai Lam Chung, Tuen Mun near the Marine Police Base and another at Brothers Point, Tuen Mun. Both stations are strategically located at about 12 km northeast of Chek Lap Kok so that the TDWRs have a clear view of the runways, airport approach and departure zones.

The first TDWR was installed in Tai Lam Chung TDWR station in 1996 and the second one in 2014. This one (TDWR2) is now the primary operation radar to support the weather observation. Since both TDWRs operate in the vicinity of the airport, the ground clutter is large and a variety of methods are used to reduce this clutter and to also eliminate the impact of moving targets as such birds, aircraft and automobiles. The rain rate and reflectivity can be provided by Hong Kong Observatory (HKO), where the rain rate is converted by $Z = 200R^{1.6}$.

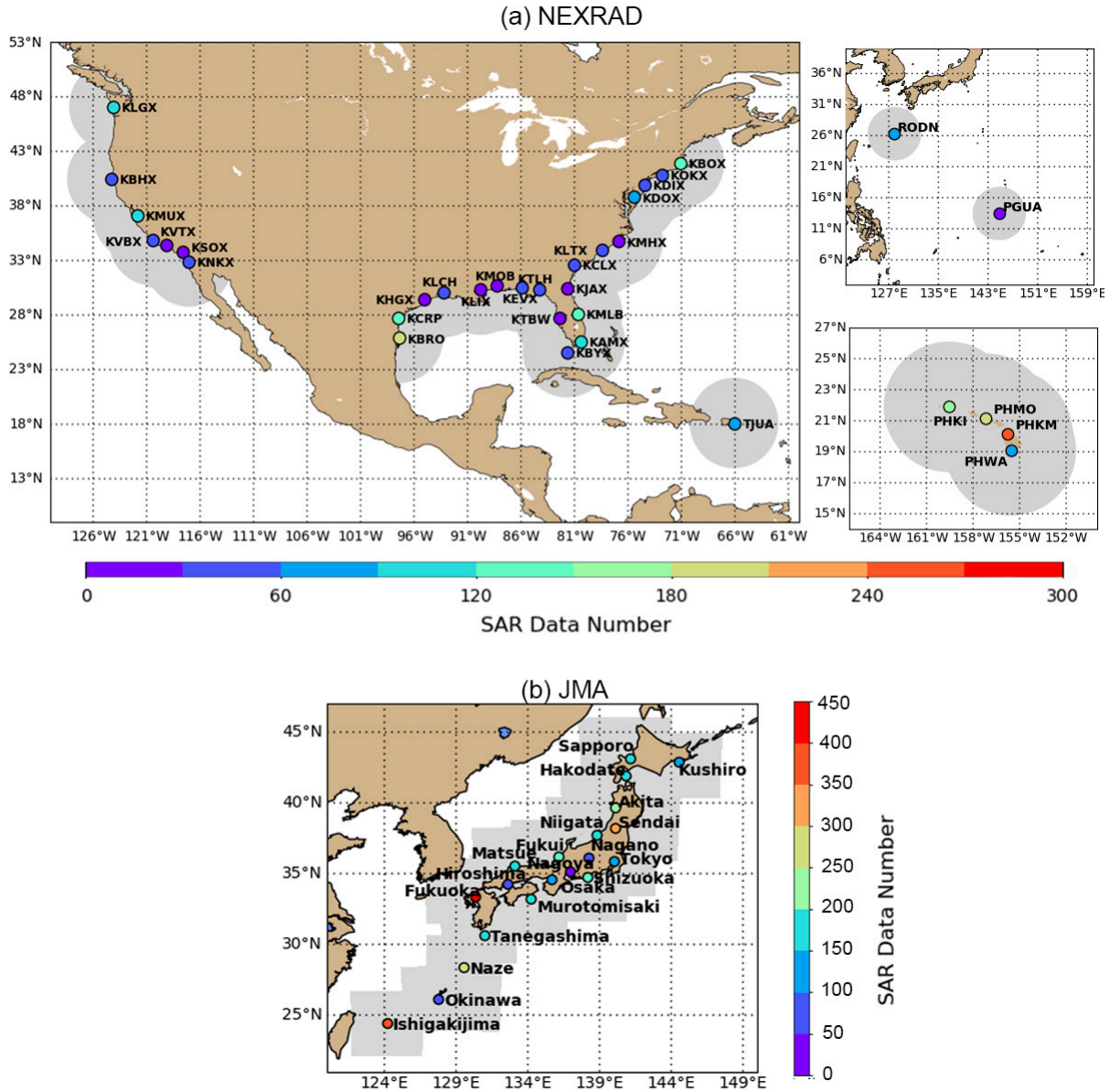


Figure 3.1: Location of NEXRAD (a) and JMA (b) weather radar stations and number of collocated SAR images for each stations. The grey areas represent the radar coverage.

3.2.3 JMA rain radar

The rain data from the Japan Meteorological Agency (JMA) radar network are also used. The rain rate product is updated every 10 mins with a 1-km spatial resolution. The coverage of JMA is depicted in Fig. 3.1. The product is based on constant altitude plan position indicator (CAPPI) reflectivity data at about 2 km altitude from multiple JMA radars. For now, only the rainfall rate product (in mm/hr)

is provided using a reflectivity-rainfall (Z-R) relationship (Marshall and Palmer, 1948). This dataset is accessible from the website (<https://www.jma.go.jp/en/radnowc/>).

3.3 ECMWF data

The ECMWF is one of the world’s leading numerical modelling centres. It operates a set of global models and of data assimilation systems for the dynamics, thermodynamics and composition of the Earth’s fluid envelope and interacting parts of the Earth-system. The data assimilation systems bring observations from ground stations, radiosondes, satellites and many other sources in balance with the meteorological equations to form a physically valid state of the atmosphere. This data is used as initial condition for the various forecast model sets.

3.4 Collocation between the datasets

The collocation is necessary for the following analysis because these data have different temporal and geographic coverage. Firstly, Sentinel-1 data needs to match up with NEXRAD locations spatially. Secondly, for every Sentinel-1 case, we select nearest weather radar observations in time. The maximum temporal difference between the satellite and weather radar is set to 5 min. Finally, the rain data at 1 km resolution are mapped on the same grid as Sentinel-1 products by searching the nearest neighbor in weather radar map.

After collocation, we narrow the match-up data pairs to rainy cases based on base reflectivity maps. Additionally, considering that winds have the direct influence on sea surface roughness, we also take into account the hourly forecast wind product provided by European Centre for Medium-Range Weather Forecasts (ECMWF). They are available on a spatial grid of 0.125° ensuring a maximum time difference between SAR data and the forecast product of less than 0.5 hours. Finally we got over collocated 2393 cases in US coastal area and 4311 cases in Japan.

Fig. 3.2 (a)(c) show the histograms of base reflectivity in US and rain rate in Japan. It can be seen that the base reflectivity has a normal distribution ranging from -20 dBZ to 55 dBZ with a maximum around 18 dBZ. The negative value only happens when the ground clutter or very light snow/drizzle are detected in clear air mode (for which the maximum value is around 30 dBZ). According to a traditional Marshall-Palmer relationship $Z = 200R^{1.6}$, 20 dBZ stands for a rain rate of 0.01 mm/hr, which can be neglected as rain-free in most studies. Therefore, in the following we consider the areas with reflectivity lower than 20 dBZ as rain-free. The distribution of rain rate in Japan fits a lognormal distribution, over

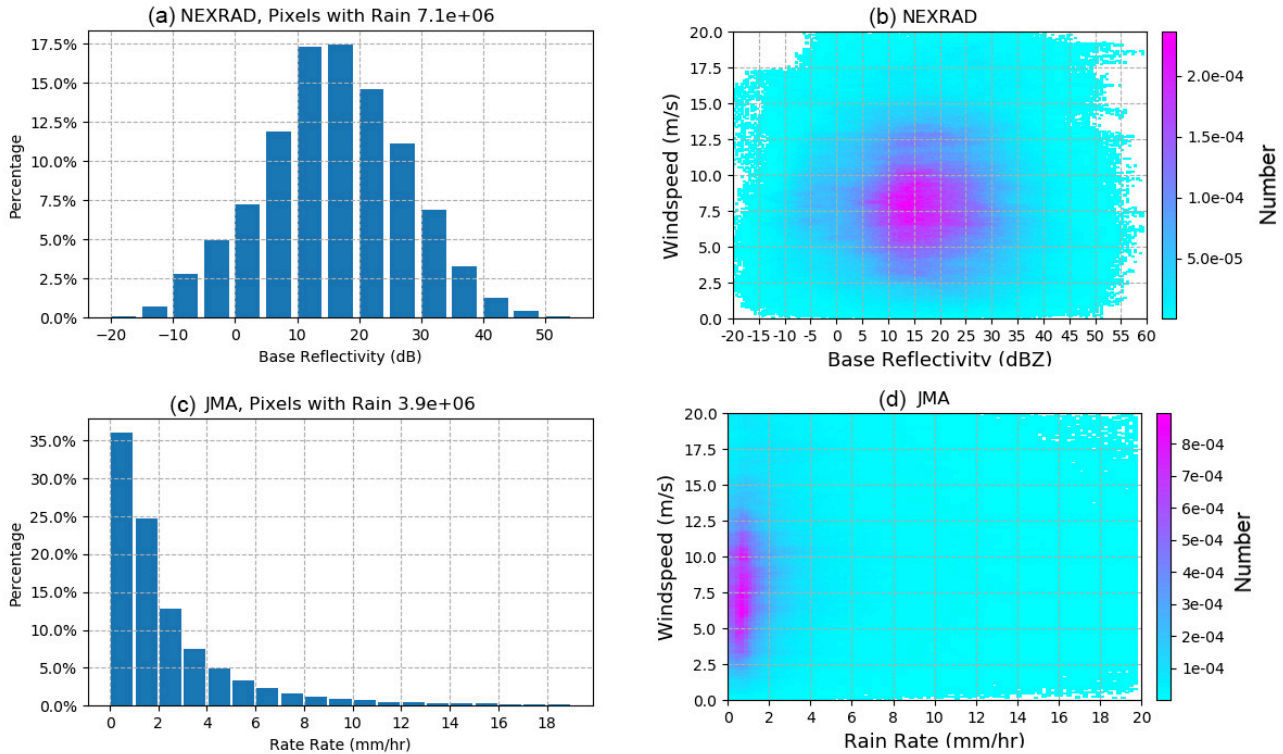


Figure 3.2: (a) Histogram of base reflectivity for collocated data over US coastal area. (b) 2D histogram with the collocation number falling within the bins of base reflectivity (x axis) and ECMWF wind speed (y axis) in the US. (c) and (d) show the same histograms with (a) and (b) but for the collocation around Japan. reflectivity and wind speed.

90 % of which are in rain rate lower than 10 mm/hr.

The right panel of Fig.3.2 shows match-up between wind speed and rain intensity. As observed, the most data concentrates in wind speed ranges from 2.5m/s to 12.5 m/s, in line with the general observation of wind over the ocean. The collocated data provides us with a very base to investigate the impact of rain on radar signal (SAR images) under different wind regimes.

Observation of rainfall effects on SAR images

Contents

4.1	Observation on rain signatures in SAR images	31
4.1.1	Case Study	31
4.1.2	Statistical Results	34
4.1.3	Bright signatures in SAR images	39
4.2	The impact of precipitation on cyclone cases	46
4.2.1	Eyewall	47
4.2.2	Spiral Rainband	50
4.2.3	Radial Profile of Rain Rate	54
4.3	Summary	56

This chapter is organized in two parts. The first part investigates the impact of precipitation on radar backscatter under different rain rate and wind speed excepted for TCs. Inside the case studies with different kinds of rain signatures are first given and a statistics of NRCS at co- and cross-polarizations from Sentinel-1 is analyzed. Then bright patches are analyzed in terms of base reflectivity, wind speed, hydrometeor classification, NRCS and possible mechanisms for its appearance. The second part focuses on precipitation signatures in TCs collected from both Sentinel-1 and Radarsat-2, revealing the radar backscatter variation in eyewall and spiral rainbands. Also the radial location of maximum precipitation is investigated along with the location of maximum wind speed (RMW).

4.1 Observation on rain signatures in SAR images

4.1.1 Case Study

Different rain signatures on C-band SAR images was preliminary investigated in Alpers et al. (2016), which shows that their patterns are related to different rain rate and wind speed in variant rain forms,

e.g. rain cells and squall lines, but no quantitative estimation was given for these cases. Liu et al. (2016) showed that the mean NRCS in VV increases with base reflectivity up to 45 dBZ and then decreases gradually but only for a single rain cell. Thus in this section, we show three different kinds of rain signatures in dual-pol SAR images, with collocated base reflectivity and wind vectors. Additionally, the mean of NRCS were computed with respect to base reflectivity for the three cases in order to compare with the results presented in Liu et al. (2016).

Fig. 4.1 (a) and (b) show a case with two rain cells shown as bright patches surrounded by dark ones. Here the ECMWF surface winds are about 3 m/s while a wind gust can clearly be observed around the two rain cells. Despite some noise in VH polarization, the location and shape of the bright signatures in SAR images clearly collocate well with the base reflectivity over 40 dBZ while the dark patches are associated with relatively low reflectivities of less than 40 dBZ. To better show the relations between the NRCS and reflectivity, two transects with the same incidence angles are analyzed. They both show that the NRCS strongly increases with increasing rain rate over 40 dBZ. To be more specific, the transect 1 (red) in Fig. 4.1 (d) shows a VV-pol NRCS increase of 8 dB whereas the VH-pol NRCS increases by 10 dB. The second transect (green) shows a slightly different situation where the NRCS shows strong attenuation (decrease) at the edges of the rain cell and a strong increase at the center of the cell. The statistics of NRCS against base reflectivity confirms that both the mean VV and VH NRCS increases gradually with increasing base reflectivity after 35 dBZ (Figure 4.1 (f)). The decrease of NRCS observed after 50 dBZ is not significant and result from a slight mismatch between the SAR and NEXRAD data.

Figure 4.2 (a) and (b) present another kind of rain signature, showing only bright patches in both VV and VH images. Different from the case above, there is no gust front and dark patches observed around the bright ones. This case was acquired at 23:53 UTC on 1 September 2017 over the Gulf of Mexico. In this case, we notice a good match between bright patches observed in both VV-pol and VH-pol images and the high base reflectivity as well (see Fig. 4.2 (c)). More interestingly, NRCS in VV and VH along transect 1 (red) shows two peaks apparently associated with the large increase of base reflectivity. Likewise, the VV-pol and VH-pol NRCS along the transect 2 (green) also shows the similar trend with the transect 1. And in Fig.4.2(f), the mean of NRCS increase gradually with base reflectivity increasing. The reason for the pure bright rain signatures is possibly due to the form of stratiform rain induced by a stationary front in the north (confirmed by the weather chart from National Centers for Environmental Information (NCEI)), which is often measured with lower vertical air velocity than convective rain (REF).

The last case in Fig. 4.3 (a) and (b), acquired at 00:10 UTC on 31 August 2017, displays dark patches in VV and adjacent bright and dark patches in VH. The ambient wind is stronger than that of the two

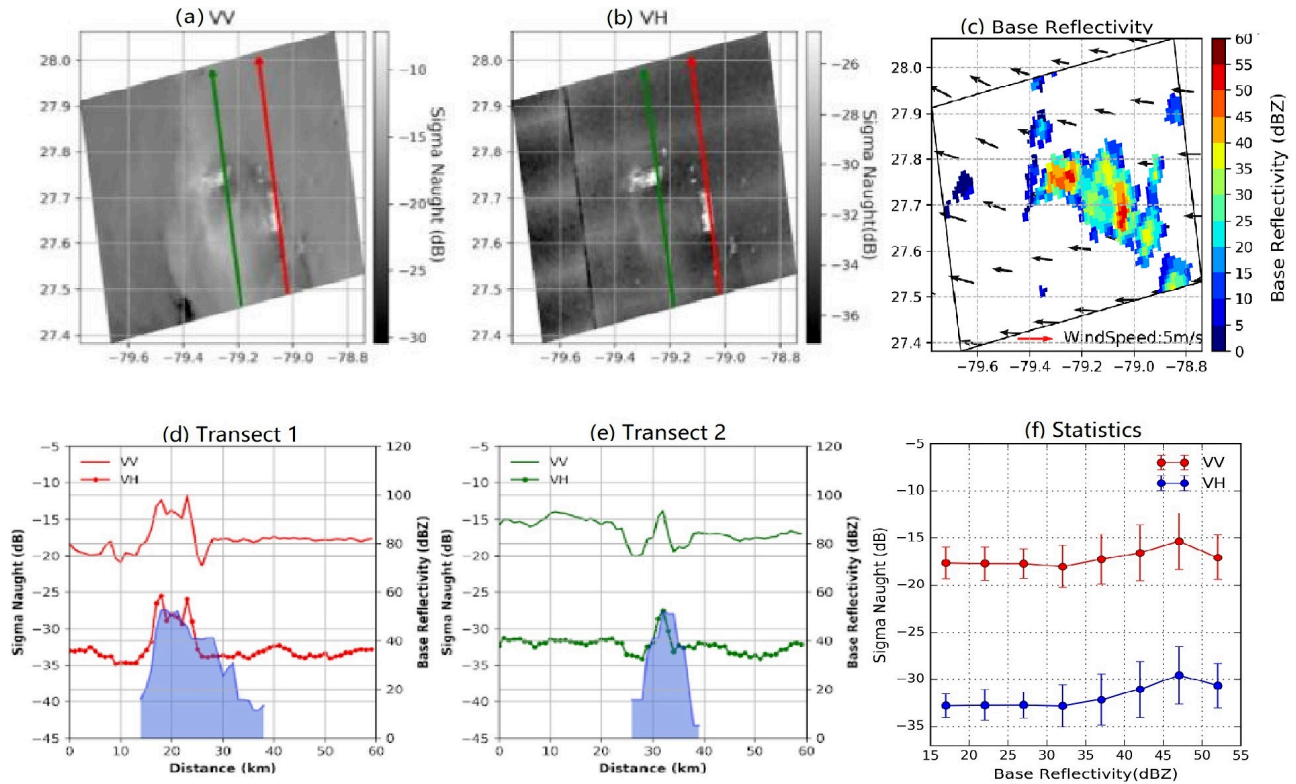


Figure 4.1: (a)(b) SAR images at VV and VH polarization acquired at 23:19 UTC on June 13 2017. (c) Base reflectivity at the same time from the NEXRAD station. (d) (e) NRCS (red or green lines) and base reflectivity (blue line) along the Transect 1 (red line on (a)) and Transect 2 (green line on (a)). (f) Mean VV and VH NRCS as a function of base reflectivity.

previous cases, about 13 m/s from the ECMWF. To show the NRCS variation under rain, two transects (red and green) with constant incidence angles are considered. For transect 1 (red), NRCS in VV shows a slight increases as first crossing the rain and then decreases until the right border of rain cell. For transect 2, VV-pol NRCS shows an attenuation at the borders of the rain cell with a slight increase in the middle. However, the maximum of NRCS in rain region is very close to that in surrounding rain-free area, which makes the signatures difficult to recognize. For VH, NRCS along the transect 1 (red) and transect 2 (green) both show a large increase, even though the increment is less than that along the transects in above cases. In Fig. 4.3(f), the mean of NRCS in VV almost keeps stable with base reflectivity. Comparatively, the NRCS in VH starts to increases from 30 dBZ and then decreases over 45 dBZ, similar to that in Fig. 4.3(f). This case indicates that the rain footprint in SAR images may be easier to identify in VH than VV.

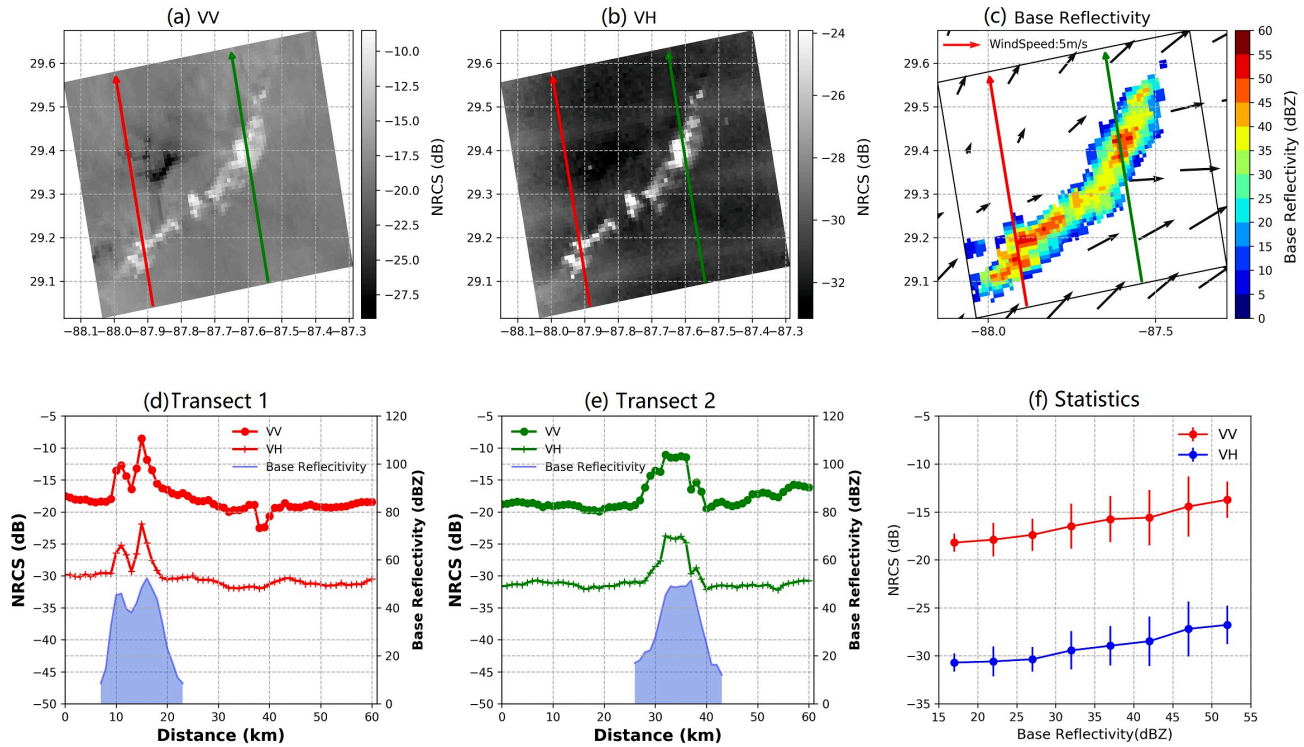


Figure 4.2: Same as 4.1, but the SAR acquisition time is 23:53 UTC 1 Sep 2017.

As shown by the above cases, rain signatures in C-band SAR images do not always present bright or dark patches and they can obviously differ in VV and VH polarizations. The statistics of NRCS for the 3 cases indicate that NRCS can increase or decrease under high rain intensity and its variation is not only associated with rain intensity, but also certainly to local winds, i.e. surrounding surface backscatter.

4.1.2 Statistical Results

As described above, wind is a critical parameter influencing the nature and structure of rain signatures. Thus, in order to better examine the impact of rain rate on radar backscattering, we calculate NRCS ratio in order to remove the contribution from various sea state. The NRCS ratio is calculated by equation 4.1. It is the ratio of NRCS under rain to NRCS in rain-free area. The value of NRCS ratio indicates how much the NRCS is increased or decreased by rainfall in comparison to rain-free area. If the NRCS ratio is positive, it means that radar backscattering is increased due to rainfall and vice versa. Note that the NRCS ratio here is given in dB. For this computation the SAR and NEXRAD data have to be sampled

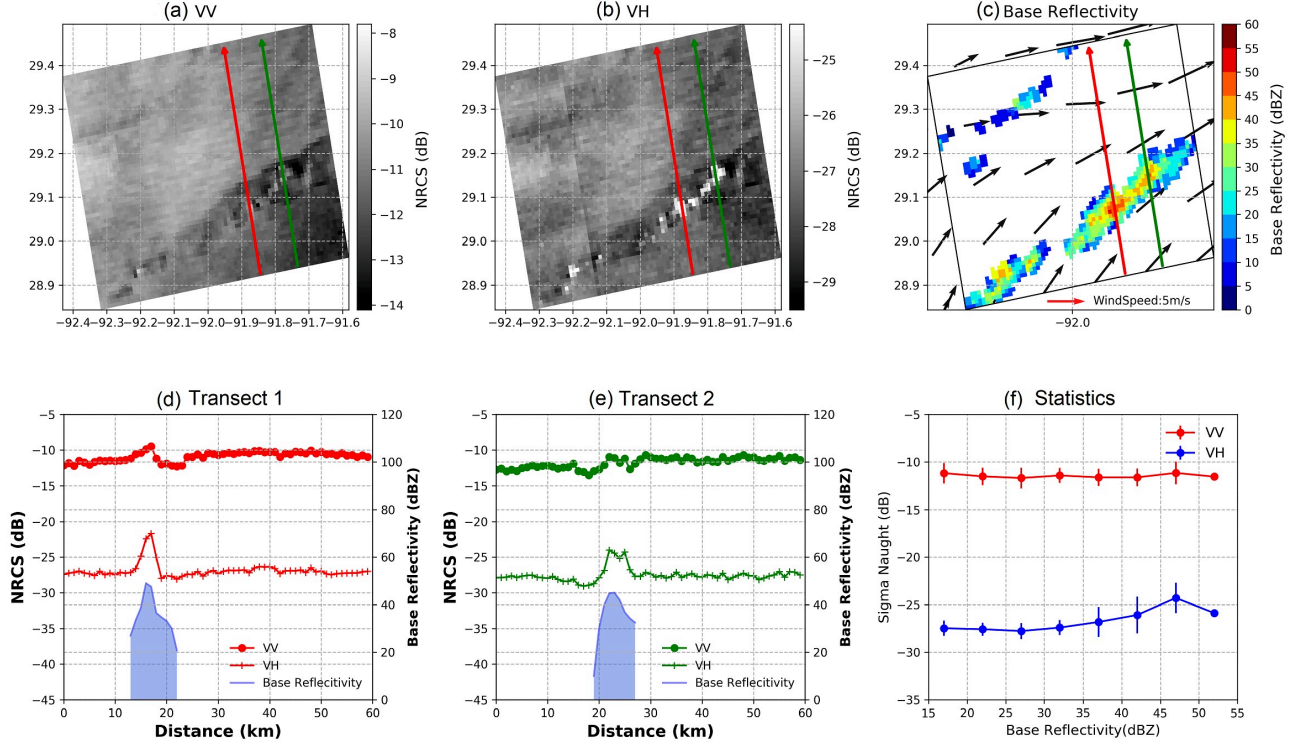


Figure 4.3: Same as 4.1, but the SAR acquisition time is 0010UTC 31 Aug 2017.

or resampled on the same grid.

$$NRCS \text{ ratio} = 10 \log_{10} \frac{NRCS_{rain}}{NRCS_{rain-free}} \quad (4.1)$$

The calculation is shown by an example in Fig. 4.4. Based on the pixelwise collocations between the SAR images and NEXRAD data, all the rainy pixels can be readily identified. Generally, a base reflectivity of 20 dBZ is typically the point at which light rain begins. Thus in this study, the pixels with base reflectivity higher than 20 dBZ are considered as rainy. In Fig. 4.4 (a), the base reflectivity at the pixel marked by a red star is 48.3 dBZ where the NRCS is -9.8 dB. We search for all the rain-free pixels around this given pixel over an area of 50 km along azimuth direction and 0.5° incidence angle range (marked as red rectangle). Within this area, all pixels with a base reflectivity less than 20 dBZ are considered as rain-free, depicted by the blue region in the left panels of Fig.4.4. For the given single pixel, the mean of the rain-free NRCS in the rain-free area is -19.6 dB and thereby the NRCS ratio is 9.8 dB by referring to equation (4.1). Accordingly, for all the rainy pixels(i.e. with base reflectivity larger than 20 dBZ) the NRCS ratio can be estimated using this process, as shown in Fig. 4.4(c). NRCS ratio helps

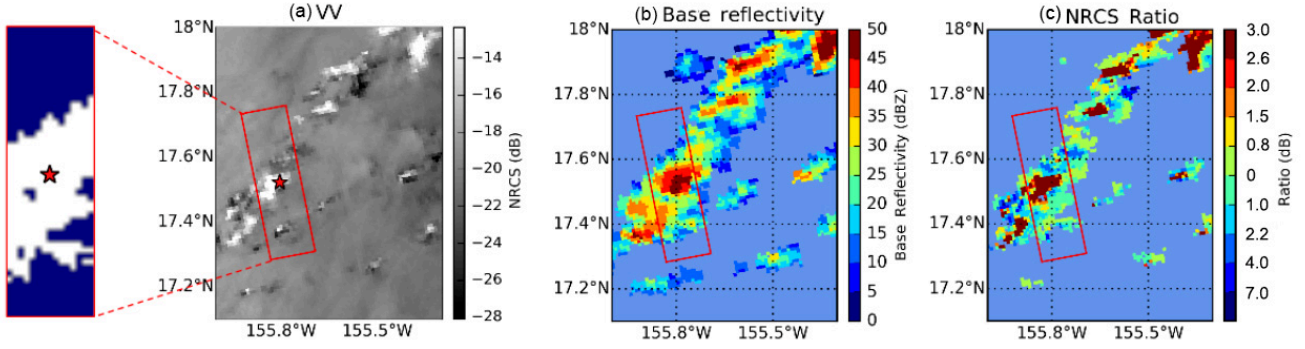


Figure 4.4: Example of NRCS ratio computation (a) SAR image at VV polarization. The red star marks a single pixel for calculation of NRCS ratio. The red rectangle covers the calculation area for the pixel, with a width of 0.5° incidence angle range and the length of 50 km in the azimuth direction. The blue area in the left panel denotes the area without rain (Base reflectivity < 20 dBZ). (b) the base reflectivity measured by NEXRAD at the same time. (c) NRCS ratio calculation result for all the pixels under rain (Base reflectivity > 20 dBZ).

to focus on the rain effects on the NRCS by normalizing the influence of surface backscatter.

We first get the statistics of NRCS ratio at VV polarization. Considering the NRCS dependence on incidence angles, the NRCS ratios are gathered into four incidence angle bins: $29^\circ - 33^\circ$, $33^\circ - 37^\circ$, $37^\circ - 41^\circ$ and $41^\circ - 46^\circ$. Fig. 4.5 displays the statistics of VV NRCS ratio relative to base reflectivity with 5 dBZ bins. Moreover, since local winds is critical for influencing the NRCS as described above, the NRCS ratio is averaged in four rain-free NRCS ranges respectively, corresponding to the ambient wind speeds of 0-4 m/s, 4-8 m/s, 8-16 m/s, and > 16 m/s (shown by four color lines in Fig. 4.5). And the histogram above each sub-figure denotes the data amount at each rain-free NRCS range, marked with the same colors with lines as reference.

In general, at low to moderate winds (< 16 m/s), the NRCS ratio statistics at all incidence angles show an increasing trend with intensifying rain excepted for the wind speed larger than 12 m/s with an incidence angle lower than 33° . This is in agreement with previous studies based both on observations (Moore et al., 1979; Lin et al., 2014) and simulations (Contreras and Plant, 2006; Nie and Long, 2007; Xu et al., 2015). However, the mean of NRCS ratios at low wind (black lines) are negative at base reflectivity lower than 25 dBZ (see figure 4.4 (a1) to (a3)). It is different from the results of ASCAT NRCS statistical analysis presented by Lin et al. (2014), which shows a significant increase even at very light rain. However, the NRCS from ASCAT has a resolution of 25 km, much larger than the resolution of 1 km adopted in this study. Negative ratio could possibly indicate the non-negligible impact of rain damping

on Bragg waves at light rain, whereas this fine-scale rain signature could be smoothed and difficult to identify at a lower resolution.

Besides, at winds higher than 16 m/s, the NRCS ratio is somewhat quite constant, even with a slight decrease at incidence angle from 29° to 37° . By contrast, NRCS ratio at light winds (0-4 m/s) shows the greatest enhancement at same base reflectivity bin, indicating a significant contribution from the sea surface or atmosphere. As simulated in laboratory by Moore et al. (1979), rain could readily roughen the sea surface even at light winds, leading to higher increase of NRCS. Yet at very high winds, excessive wave breaking and foam are usually apparent on the sea surface. The rain-induced structures, i.e., ring waves and splash products, hardly enhance the sea surface roughness and even probably attribute a reduction effect. As for the backscattering from hydrometeors, it can not be ignored at heavy precipitation. However, the main mechanism for inferred to have more contribution to the NRCS at large incidence angles.

Overall, above statistics indicate that increasing rain rate could indeed enhance NRCS at VV for low to moderate winds. While for very high winds, the NRCS is hardly impacted by rain. So it is necessary to consider wind speed when discovering the rain impact on sea surface. One should note that the statistics are obtained for base reflectivity from 20 dBZ to 55 dBZ. High base reflectivity (especially >40 dBZ) usually indicates strong confections and much aggregation of hydrometeors in the atmosphere.

Compared to co-polarization, there are only a few studies concerning the rain signatures at cross-polarization. The cases presented by Melsheimer et al. (1998) show that the rain signatures at cross-polarization might be more pronounced than that at co-polarization. The two cases in Fig. 4.1,4.2 present rain signatures that appear quite similar in VV and VH, whereas in Fig. 4.3 the bright patches in VH are more pronounced than in VV. Similar to VV, the statistics of NRCS ratio computed in VH are shown in Fig. 4.5(b1)-(b4). It is noted that NRCS ratio is around 0 dB under light rain, up to 5.4 mm/h. This is probably due to the high noise floor for the VH polarization. Because our ability to get NRCS ratio at cross-polarization for light wind speeds is strongly related to the NESZ of Sentinel-1. Most cases in VH are with a backscatter around or lower than NESZ in IW mode. This may also explain why possible wave damping effect observed in co-polarization are not visible in cross-polarization.

In addition, like co-polarization, we observe a significant increase of NRCS ratio under high base reflectivity and the NRCS ratio at low winds is greater than at high winds. The remarkable increase is due to the presence of very bright patches at VH, similar to VV. Likewise, Radarsat-2 also observes the very bright patches induced by rain at VV and VH (see for example the Fig. 8 in Alpers et al. (2016)), where the NRCS at VH increase by about 6 - 8dB. Also it is worthy of notice that the ratio at cross-polarization for the same wind and base reflectivity seems a little higher than at co-polarization. As

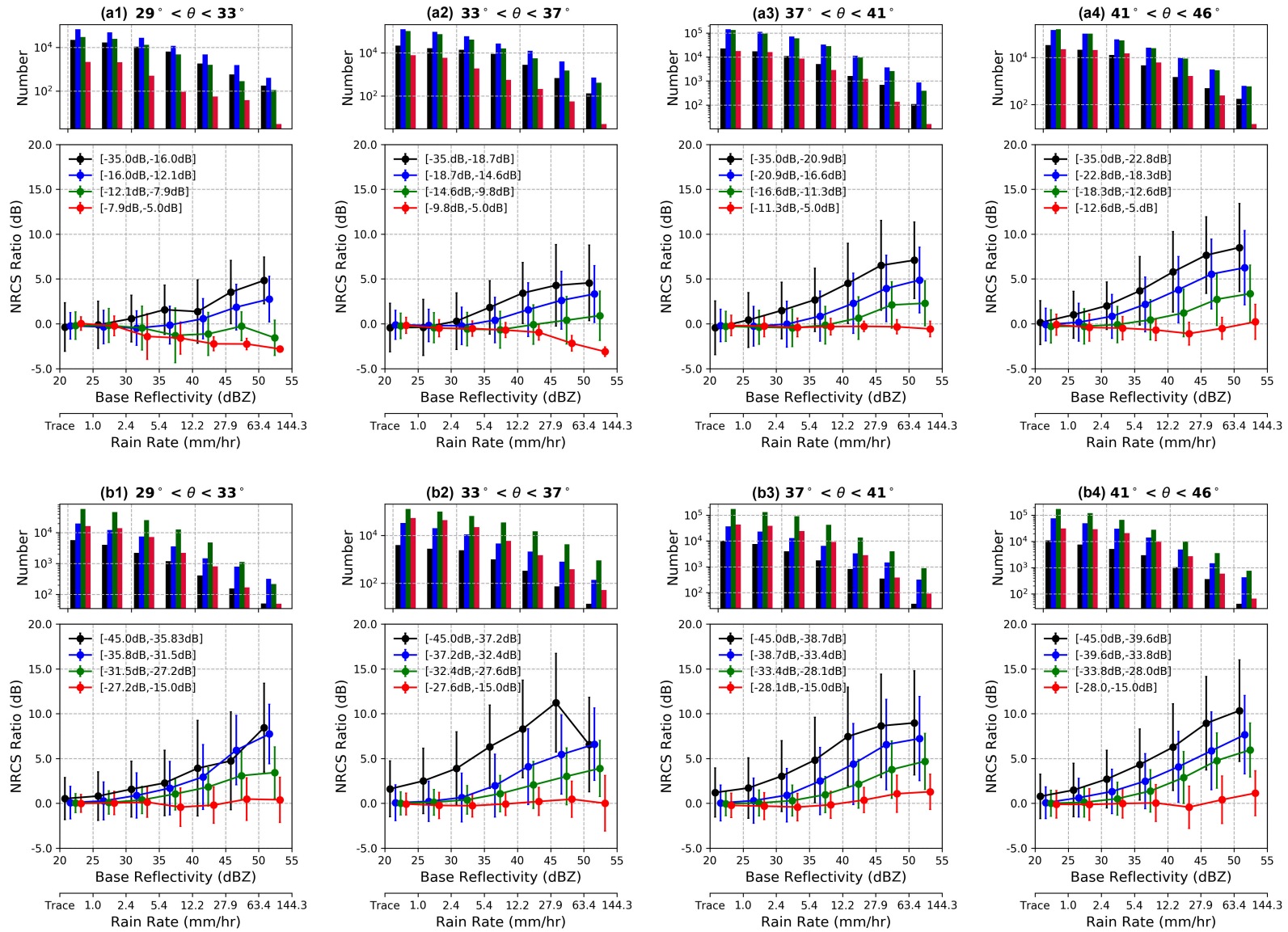


Figure 4.5: Statistics of $NRCS_{ratio}$ with respect to base reflectivity for VV polarization (a - Top) and VH polarization (b - Bottom). The legend in each sub figure stands for the NRCS in rain-free area, suggesting different wind regimes (0-4 m/s, 4-8 m/s, 8-16 m/s, and ≥ 16 m/s) as approximately derived with CMOD-5 model. Above histogram denotes the data amount for lines at each base reflectivity bin.

explained by Braun and Gade (2006), the increase at co- and cross-polarization is thought to be related to ring waves and splash products respectively. But due to the limited observing height in their experiment, the volume scattering and attenuation in the atmosphere is not taken into account. Especially in heavy precipitation, the concentration and melting of the ice particles could strongly reflect the radar signal, which was noticed by Jameson et al. (1997) where the radar backscatter observed a strong signal around melting layer only at cross-polarization. So the large increase of NRCS at VH largely results from the combined effect of the reflection in the atmosphere and the backscatter from the sea surface. Overall, the NRCS at cross-polarization is also affected by the rain intensity, especially for low wind regime. But the noise makes it difficult to observe the wave damping effect like VV.

4.1.3 Bright signatures in SAR images

Rain is often associated to bright patches in SAR images when the rain rate is very high as shown in Figs. 4.1~4.3. In this subsection, we analyze the distribution of latitude, incidence angle, base reflectivity, wind speed as well as hydrometeor classification when bright patches are observed. Besides, the statistics of NRCS for bright patches in VV and VH are shown in comparison to the GMFs at certain wind speeds. Note, bright patches here are referred to the pixels with NRCS ratio in VV and VH both larger than 3 dB.

- Latitude

As shown in Fig. 4.6, the bright patches distribute from 15°N to 46° N. Here, the values on y-axis refer to the proportion of pixels associated with bright patches relative to the total number of observations available at each latitude bin. This normalization is applied due to the fact that more radar stations are equipped in subtropical regions. As observed, more bright patches are found in the latitude band between 22-34°N. We also note a significant amount of bright patches near the equator (below 20°N) and between 36-44°N.

- Incidence Angle

As shown in Fig. 4.7, more bright patches are observed at large incidence angles, as shown in statistics of Fig. 4.5. Indeed, we selected the data with NRCS ratio larger than 3 dB in VV and VH whereas it should be incident angle dependent. As a matter of fact, Fig. 4.5 in above subsection illustrates that the NRCS ratio is higher at large incidence angles than at low incidence angles for the same wind regime. Higher NRCS ratio means the bright patches are easier to identify. This suggests that the occurrence of bright patches will be larger for large incidence angles.

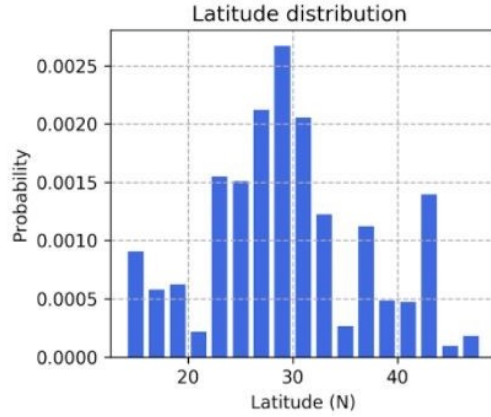


Figure 4.6: The latitude distribution of the bright patches.

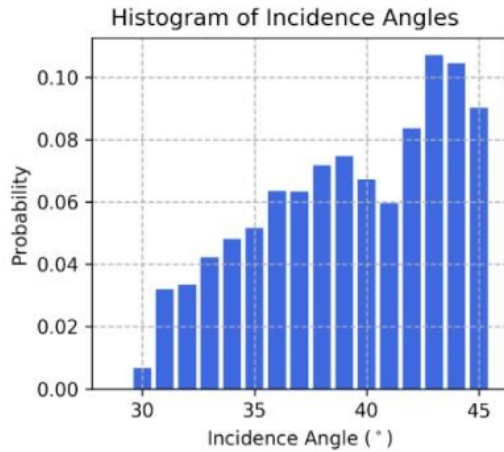


Figure 4.7: The incidence angle distribution for bright patches.

- Rain intensity

Fig. 4.8 shows that bright patches are prone to appear in the cases where we observe high values of reflectivity in the ground-based radar. The data in low reflectivity with bright patches can be explained by the shift between rain cells and bright patches. Fig. 4.9 displays an example where the largest bright patch in the red box is shifted with respect to the location of the 40 dBZ base reflectivity. Note that even though we used the “continuous” NEXRAD observations, there is still a 2 min difference here. From the time sequence of base reflectivity, it seems that the temporal shift between the two data cannot explain the difference observed between SAR and NEXRAD signatures. Here, this shift may be explained by the different observation geometry between NEXRAD (observation from ground) and SAR (observation from air).

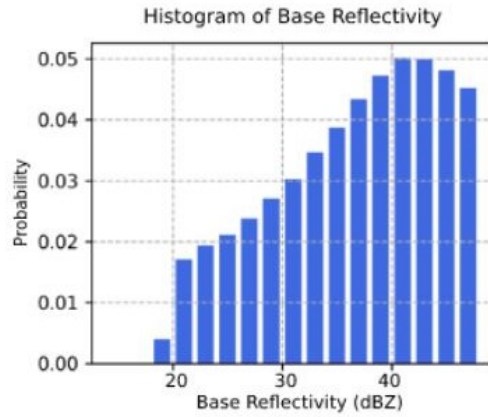


Figure 4.8: The distribution of base reflectivity for bright patches.

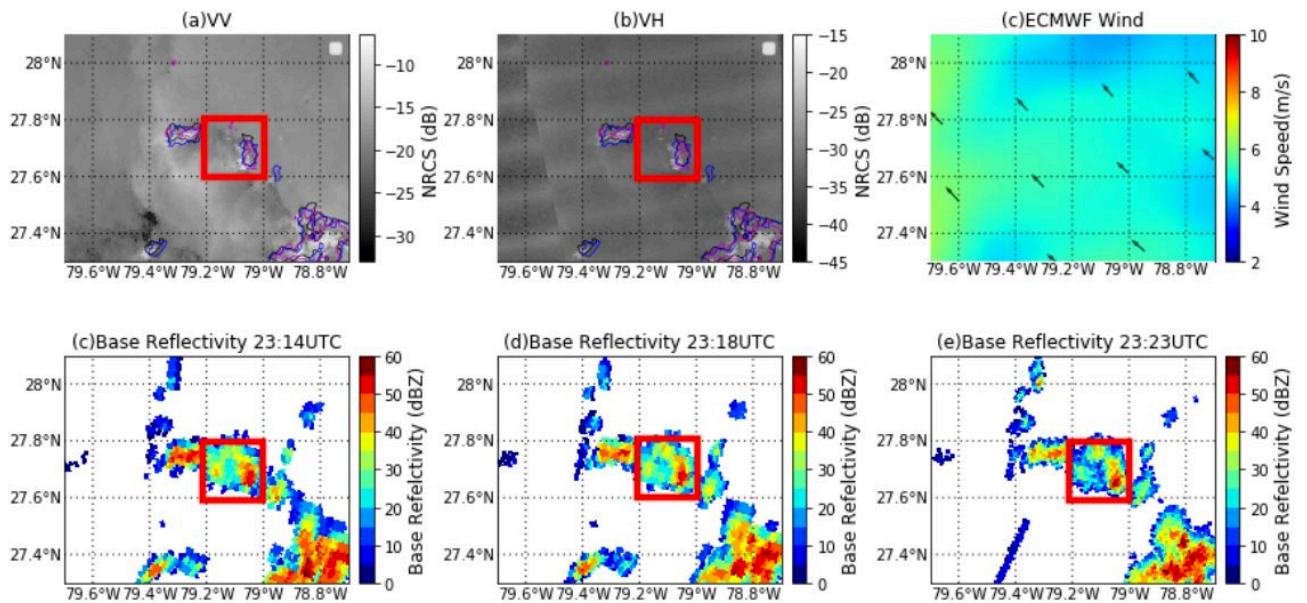


Figure 4.9: A Sentinel-1 VV (a) and VH (b) images acquired on 13 June 2017 23:20 UTC and corresponding base reflectivity obtained at 23:14 d), 23:18 (e) and 23:23 (f) UTC on the same day. The black, blue and purple contours in (a) and (b) indicate the 40 dBZ base reflectivity from the three sequential observations times. The ECMWF wind field is presented in (c).

- Wind speed

Fig. 4.10 shows the probability of bright patches as well as the total number of data amount for wind speed classes of 2 m/s. It can be clearly seen that more bright patches are observed in wind regimes lower than 6 m/s and that the probability decreases at wind speed between 2 m/s and 12 m/s. It makes sense because the rain-enhanced backscatter is easier to identify when the background

NRCS is relatively low. Comparatively, the probability obtained between 12 m/s and 18 m/s wind speed is relatively low but shows a slight increase. Even though it might be biased by the low data number, the possibility of observation on bright patches for high winds can not be ignored. Overall we conclude that, most of the detected bright patches appear in wind speed regimes lower than 10 m/s.

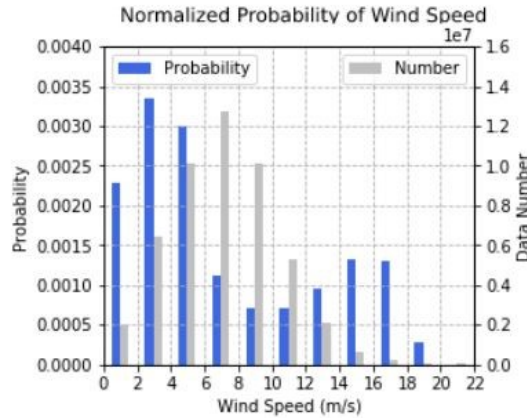


Figure 4.10: The distribution of wind speed for bright patches.

- Hydrometeor Classification

NEXRAD developed an algorithm for hydrometeor classification based on a fuzzy logic algorithm. The classification has the capability of distinguishing the diverse targets (graupels, rain, hail, biological targets, etc.) in one scanning volume, which helps to certificate the presence of melting layer and reveals the convection process in rain cell. For the three cases in subsection 4.1.1, the hydrometeors classification at lowest elevation angle 0.5° for the 3 cases is shown in Fig.4.11. It can be seen that graupel, big raindrop even with small hail appear in the bright area in above 3 cases. The graupel and big raindrops are usually present in the melting layer where solid-phase graupel melts into big size raindrop.

However, due to the strong updraft in the rain storm, the updraft in convection mixes the different phase hydrometers. Thus we collect the hydrometeor classification associated with the bright patches within different height ranges, i.e., 0-3km, 3-5.5km, 5.5-7km, > 7 km. The probability of bright patches to be in one given class for two different wind conditions is presented on Fig. 4.12. Below 3 km (in blue), the types of light/moderate rain and heavy rain are dominant for both wind conditions. The proportion of heavy rain increases for wind speed over 10 m/s. Between 3.5 km and 5.5 km (in

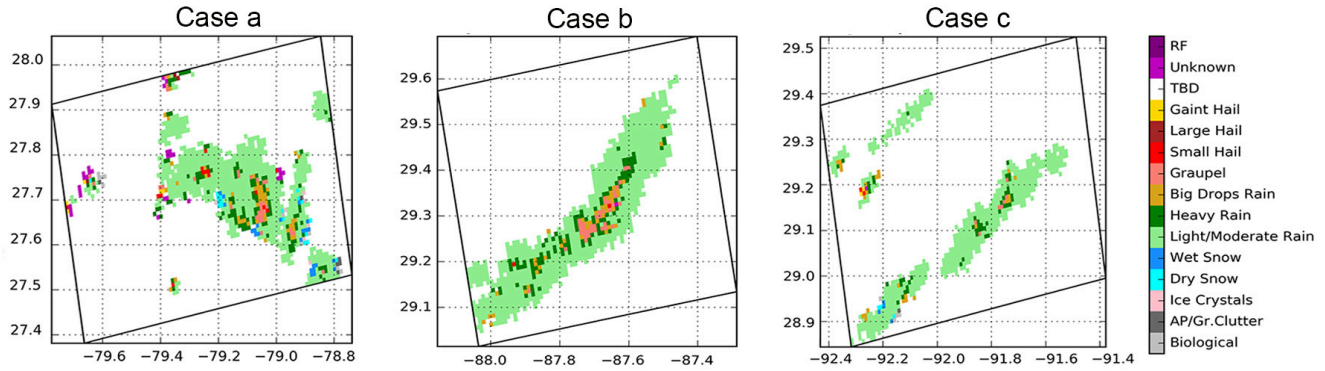


Figure 4.11: Examples of NEXRAD hydrometeor classifications for three cases of rain cells.

orange), we note that the percentage of dry snow becomes significant (>0.28) and is higher in the high wind speed regime. At this height light/moderate rain and dry snow seems to dominate the probability. The percentage of graupel is the third largest value. Above 5.5 km (cyan and pink), the percentage of Light/Moderate rain significantly decreases to become the same order of magnitude as the graupel for the low wind speed regime, but is clearly lower for the high wind speed regime. Dry snow now dominates whatever the wind regime. This illustrates that the bright patches observed in case of strong winds are associated with a high concentration of dry snow, graupel and to a lesser extent with rain droplets.

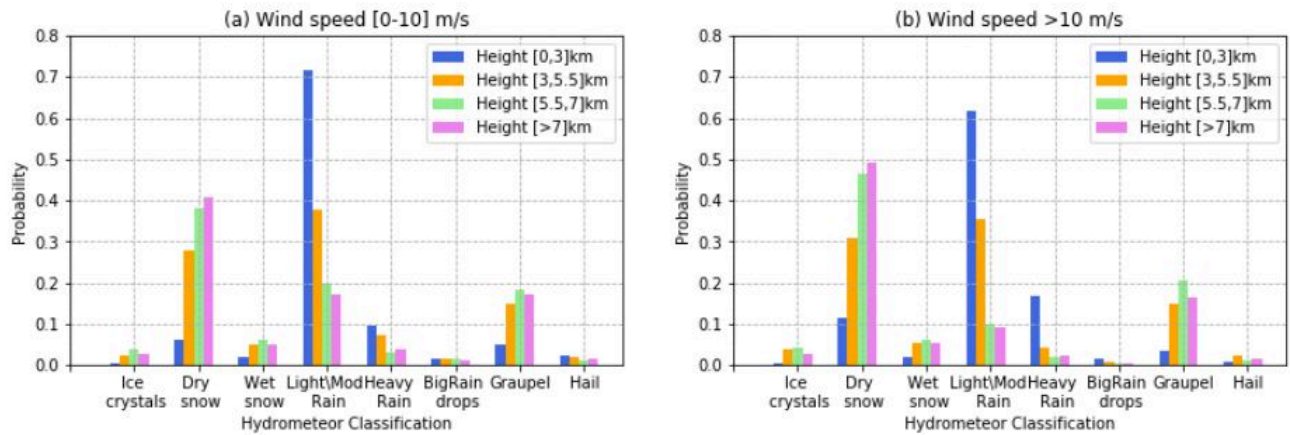


Figure 4.12: The distribution of wind speed for bright patches.

- NRCS

We regroup the NRCS associated with bright patches into three ranges by wind speed, i.e., 0-5 m/s, 5-7 m/s, 7-10 m/s, under different base reflectivity conditions. Fig. 4.13 shows the mean NRCS in

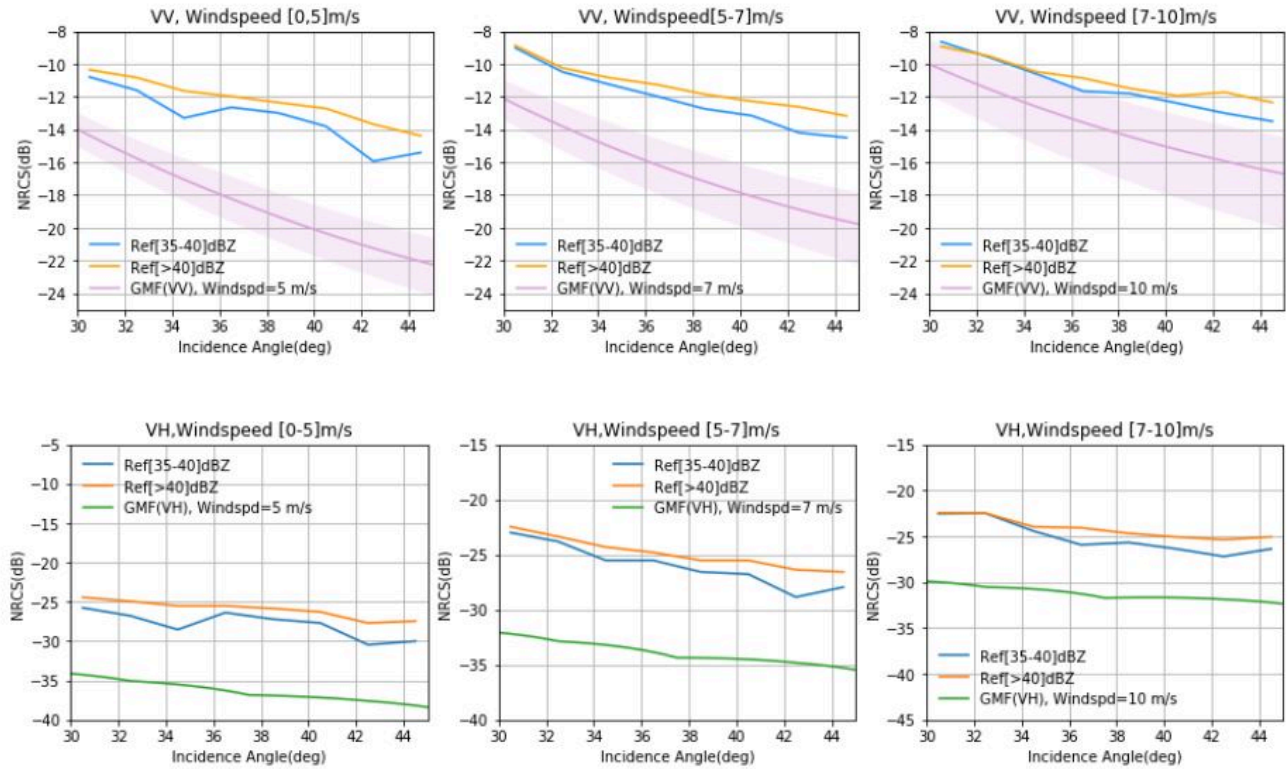


Figure 4.13: The NRCS distribution for bright patches compared to GMFs at wind speed of 5 m/s, 7 m/s and 10 m/s. Top panels VV NRCS, bottom panels VH NRCS

the three wind speed groups, together with the NRCS estimated by GMFs at different wind speeds (5m/s, 7 m/s and 10 m/s). The GMFs used is the CMOD5n for the VV polarization and H14E for the VH polarization. The upper and lower boundaries of the VV GMF shadow denote the values obtained for upwind and crosswind respectively.

For VV, the NRCS associated with bright patches is clearly higher than that without rain. However, their difference becomes smaller with wind speed increasing. Besides, we note that in the same wind condition, NRCS is larger for large values of base reflectivity. That is reasonable because more raindrops and other hydrometeors are involved at high rain rates, which could have more contribution to backscatter.

For VH, the mean NRCS is higher than the GMF values no matter the wind speed. Even at wind speed between 7 and 10 m/s, NRCS is still 5 dB larger than GMF. The NRCS difference found in VH is greater than in VV for the same wind condition. It is consistent with the case study where the bright patches are more apparently observed in VH than in VV (Please see Fig.4.13).

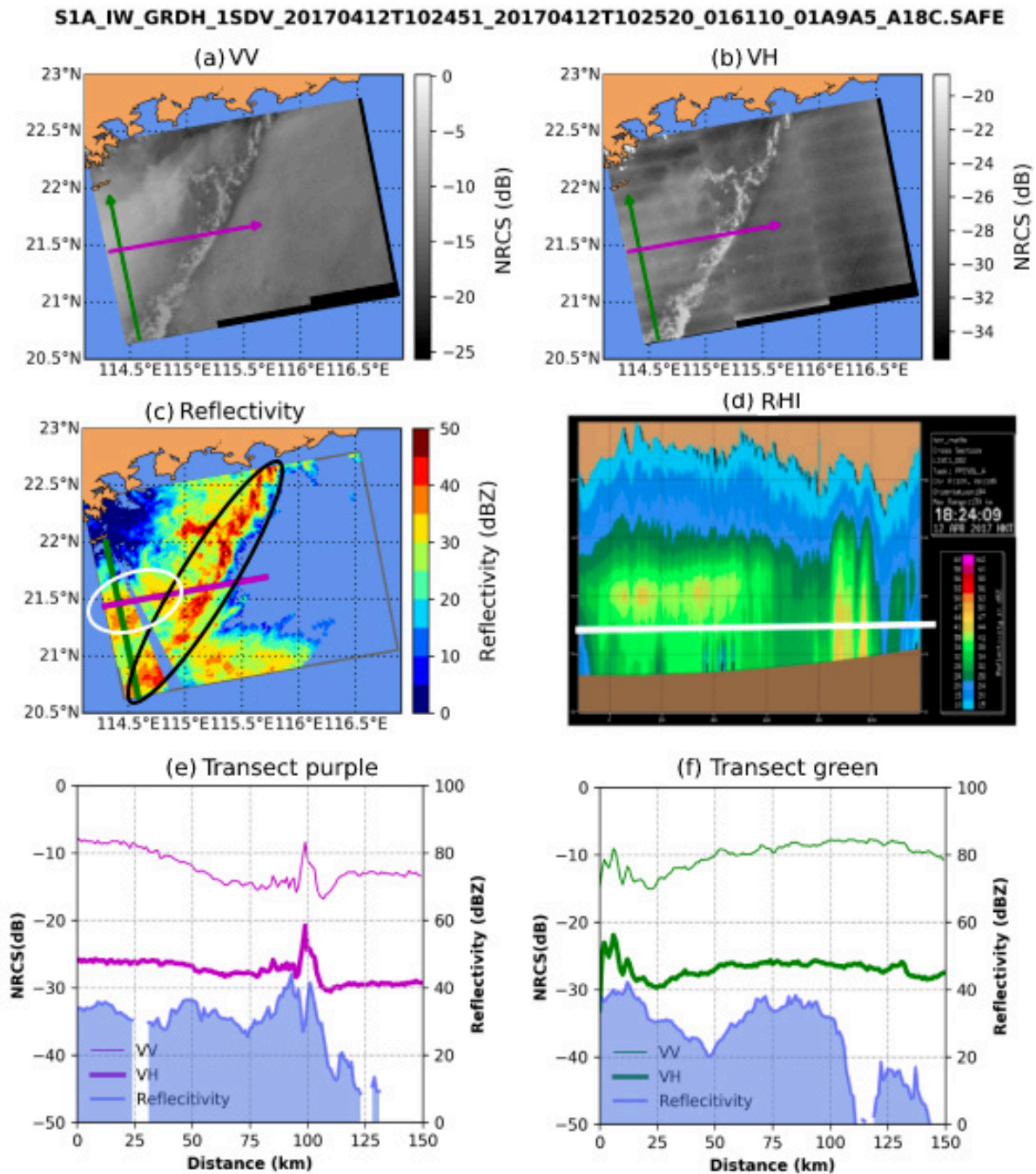


Figure 4.14: A case acquired on 12 Apr 2017 at VV (a) and VH (b). (c)(d) Reflectivity and RHI provided by the Hong Kong Observatory. RHI depicts the reflectivity along the purple transect in panels a and b. The white line inside denotes the height of 3km. (e)(f) VV, VH and reflectivity along the Purple and Green transects of panels a and b.

- Mechanism for bright patches

In the case of SAR side-looking geometry, the radar backscatter from rain cells attributes to 1) attenuation and emission from hydrometeors in the atmosphere, 2) the modulated sea surface roughness by rain-induced ring waves, splash products and wave damping. The wave damping can decrease the sea surface backscatter but its effect can be almost neglected. The ring waves and splash products are measured to increase the sea surface roughness largely. In particular, the stalks in splash products can reach 23 mm from experiment conducted by Liu et al. (2016). Supposing that large increase at VH is mainly attributed to surface scattering, the increment in VH is supposed to be less than VV, opposed to be the above cases observation. Therefore, we speculate that the very bright patches at VV and VH are more attributable to emission from mixed hydrometers in the atmosphere.

From statistical analysis on base reflectivity and hydrometeor classification, the bright patches are prone observed in high base reflectivity with high concentration of raindrops, graupels and dry snow. A case near Hong Kong also illustrates this point. Fig. 4.14(c) shows 2 areas with intense rain (high reflectivity), contoured with white and black ellipses. The rainfall in the 2 areas is different: stratiform and convective forms respectively from the RHI analysis along the transect purple (Fig. 4.14(d)). In stratiform rain, we can clearly see the melting layer at around 4-km height. In transect purple, we can see that NRCS shows an obvious increase in the convective region and only a slight increase in the stratiform region. But the latter could also result from a small incidence angle increase or surrounding wind speed increase. Thus we consider another transect green at a fixed incidence angle. We can note there is an apparent increase of NRCS in both VV and VH associated with convective rain at the start of this transect. Yet between 20 km and 100 km NRCS in VV and VH show a slight increase and then almost keep constant, whereas the base reflectivity decreases first and then increases up to 38 dBZ. This difference in the signal variation proves that the slight increase of NRCS in the stratiform rain area is due to increased wind speed not rain. Rain-induced bright patches are visible in convective rain area but not in the stratiform rain. Thus we can infer that all the hydrometeors in the rain volume are responsible for the appearance of bright patches.

4.2 The impact of precipitation on cyclone cases

TCs carry great amount of precipitation often leading to destructive natural hazards like flood. Precipitation in TCs within eyewall and spiral rainbands show different signatures, which are obtained

the first attention in Seasat mission. These signatures indicate the intensities of TCs but also give rise to larger errors in sea surface wind inversion. In this section, we describe the rainband signatures associated with TC category in co- and cross-polarizations, in particular, for eyewall and spiral rainbands. Besides, the location of the heaviest precipitation in eyewall is further investigated with the RMW.

4.2.1 Eyewall

Eyewall is one of primary structures in TCs, which wraps a ring of heavy precipitation and high winds around the center. The precipitation in TCs is typically convective, where the reflectivity can be as high as 55 dBZ (~ 100 mm/h). Fig. 4.15 shows TC Sally on 15 Sep 2020, Florence on 13 Sep 2018, Michael on 10 Oct 2018 at category-1, -3 and -4 respectively. As observed, the dark circle closest to the center is associated with heavy precipitation in eyewall. More specifically, the transects of NRCS in co- and cross-polarizations both show decreases where a sharp increase in base reflectivity is observed. This reduction of radar backscatter obviously results from heavy rainfall because the transects are made at the same incidence angles for each case. This feature indicates that the dark area closest to the cyclone eye observed in a VV/VH image is an good indicator of heaviest precipitation in the eyewall.

For the 3 cases at different categories, base reflectivity is more than 40 dBZ in some areas. Thus a further question appears that if the radar backscatter under the same intense precipitation has an same reduction attenuation at similar amplitude under the same base reflectivity. To answer this question, a statistics of NRCS_{diff} has been made at VV and VH separately for each case. Here, $\text{NRCS}_{diff} = 10\log_{10}(\text{NRCS}_{1\text{km}}/\text{NRCS}_{40\text{km}})$. NRCS_{diff} takes advantages of S-1 data on multiple resolutions to manifest increment or reduction of local signals with respect to the surrounding. Positive means the increment of signals and vice versa. To note, the statistics of NRCS_{diff} in Fig. 4.16 and Fig. 4.17 are made based on the zoom area presented in each case.

Fig. 4.16 displays the map of NRCS_{diff} , as well as its statistics and histogram at VV polarization. It is clearly observed that the precipitation area in eyewall is shown with negative NRCS_{diff} . Particularly, NRCS_{diff} is less than -1 dB in some areas as base reflectivity exceeds 40 dBZ (purple contour). The mean NRCS_{diff} for the 3 cases is further computed in a base reflectivity bin of 5 dBZ. It can be seen that the mean NRCS_{diff} decreases with base reflectivity after 35 dBZ, indicating that heavier rainfall leads to more attenuation of radar backscatter.

The mean NRCS_{diff} for the 3 cases are then compared in the same base reflectivity ranges. As base reflectivity over 45 dBZ, the mean NRCS_{diff} is about -0.6, -0.8 and -1.1 for Sally (category-1), Florence (category-3) and Micheal (category-4) respectively. The histogram of NRCS_{diff} with base reflectivity

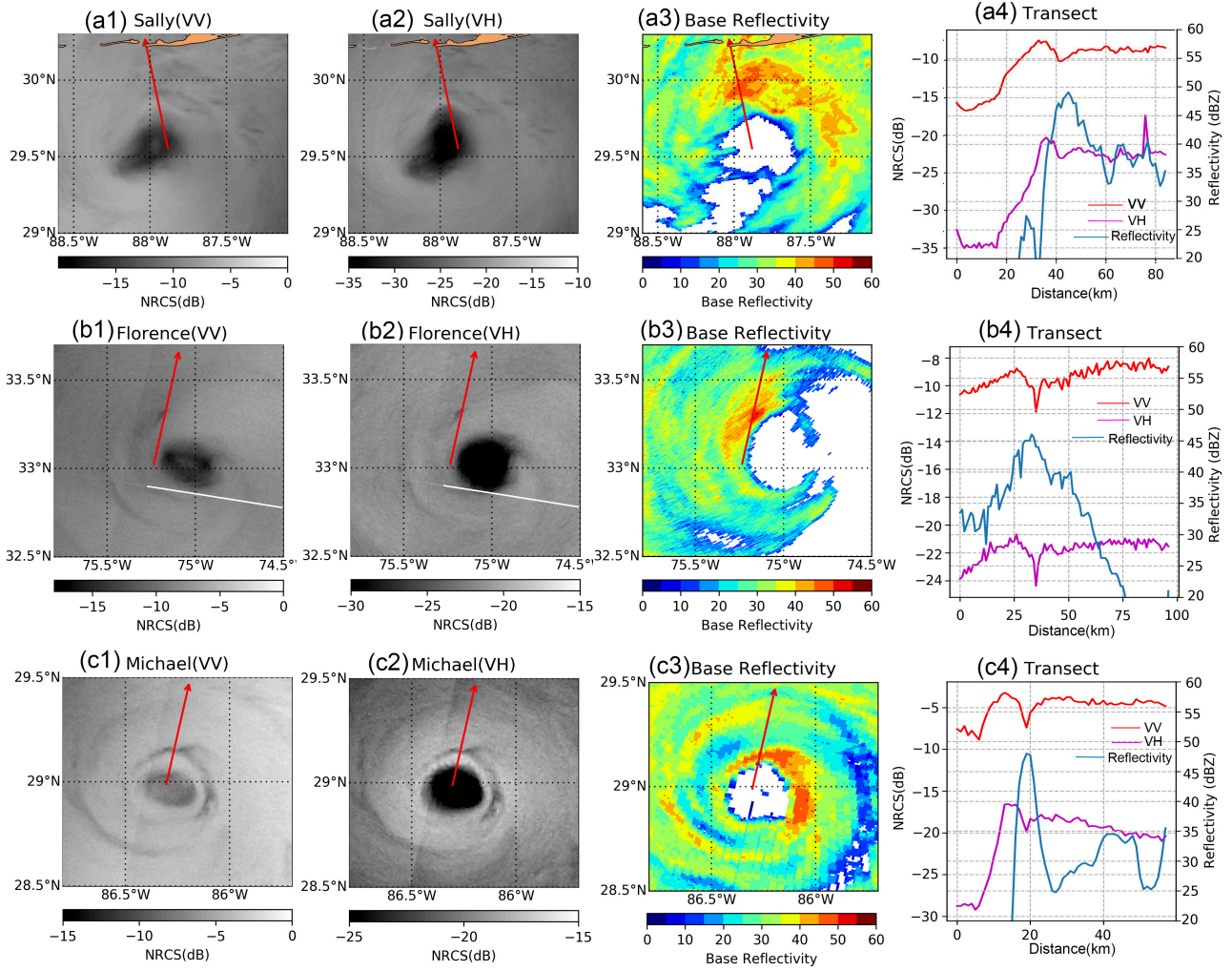


Figure 4.15: The panels from top to bottom show TC Sally on 15 Sep 2020 at 23:53UTC at cat-1, Florence on 13 Sep 2018 at 10:58UTC at cat-3 and Michael on 10 Oct 2018 at 23:46UTC at cat-4. The first and second columns are for S-1 image at VV and VH polarizations. The third column shows the base reflectivity from NEXRAD in colocation with each S-1 example. The last column displays the variation of NRCS along the red transect associated with base reflectivity. Each transect is taken at the same incidence angle.

over 40 dBZ also shows a larger probability in negative $NRCS_{diff}$ bins. The peaks in the histogram are about -0.6 for Florence and Micheal, lower than Sally. And the proportion of values less than -1dB also increases. Above indicates that rainfall can make strong attenuation on VV-pol radar backscatter in eyewall and this effect becomes more significant at high-category TC.

In VH, the mean $NRCS_{diff}$ for the 3 cases decreases with base reflectivity after 35 dBZ, similar to

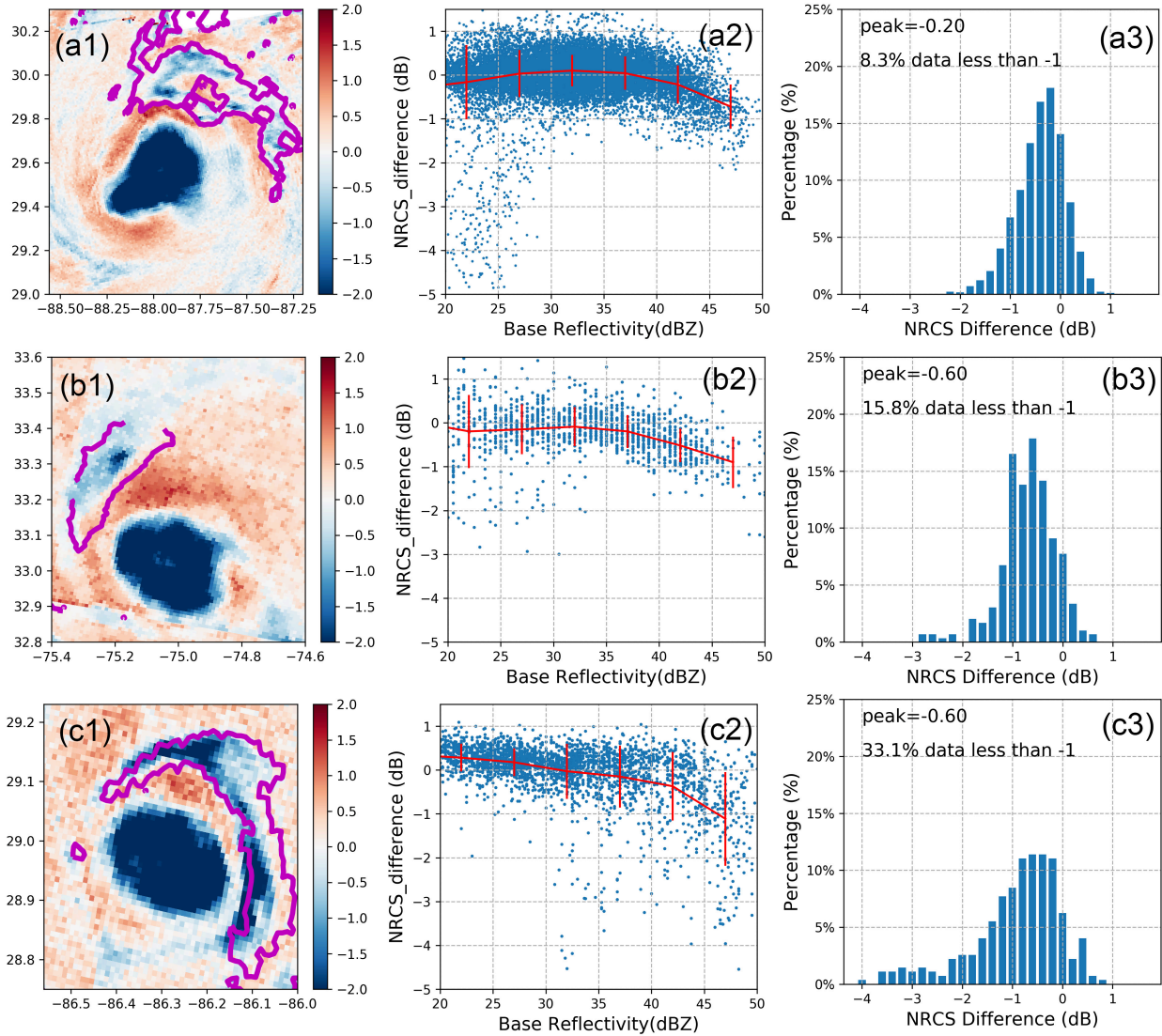


Figure 4.16: Left panels: The $NRCS_{diff}$ of the inner rainbands close to the center for the cases in Fig. 4.15. Middle panels, statistics of The $NRCS_{diff}$ with respect to base reflectivity for the zoom area in left panel. Right panels: the histogram of $NRCS_{diff}$ as base reflectivity is over 20 dBZ. These analysis is based on VV-pol S-1 data.

VV. However, $NRCS_{diff}$ in VH has less negative values in base reflectivity of 40 dBZ (purple contour). The mean $NRCS_{diff}$ over 45 dBZ is -0.2, -0.4, -0.65 for Sally, Florence and Micheal respectively, slightly larger than VV. Also, the histograms of $NRCS_{diff}$ in the last column show that the probability of negative values of $NRCS_{diff}$ is lower than VV, indicating the less attenuation in VH. In addition, the histogram of Michael shows the 16.9% data less than -1, whereas Sally and Florence have 10.4% and 6.9%. It further means that in VH the proportion of low $NRCS_{diff}$ is not sensitive to increasing category, which suggests

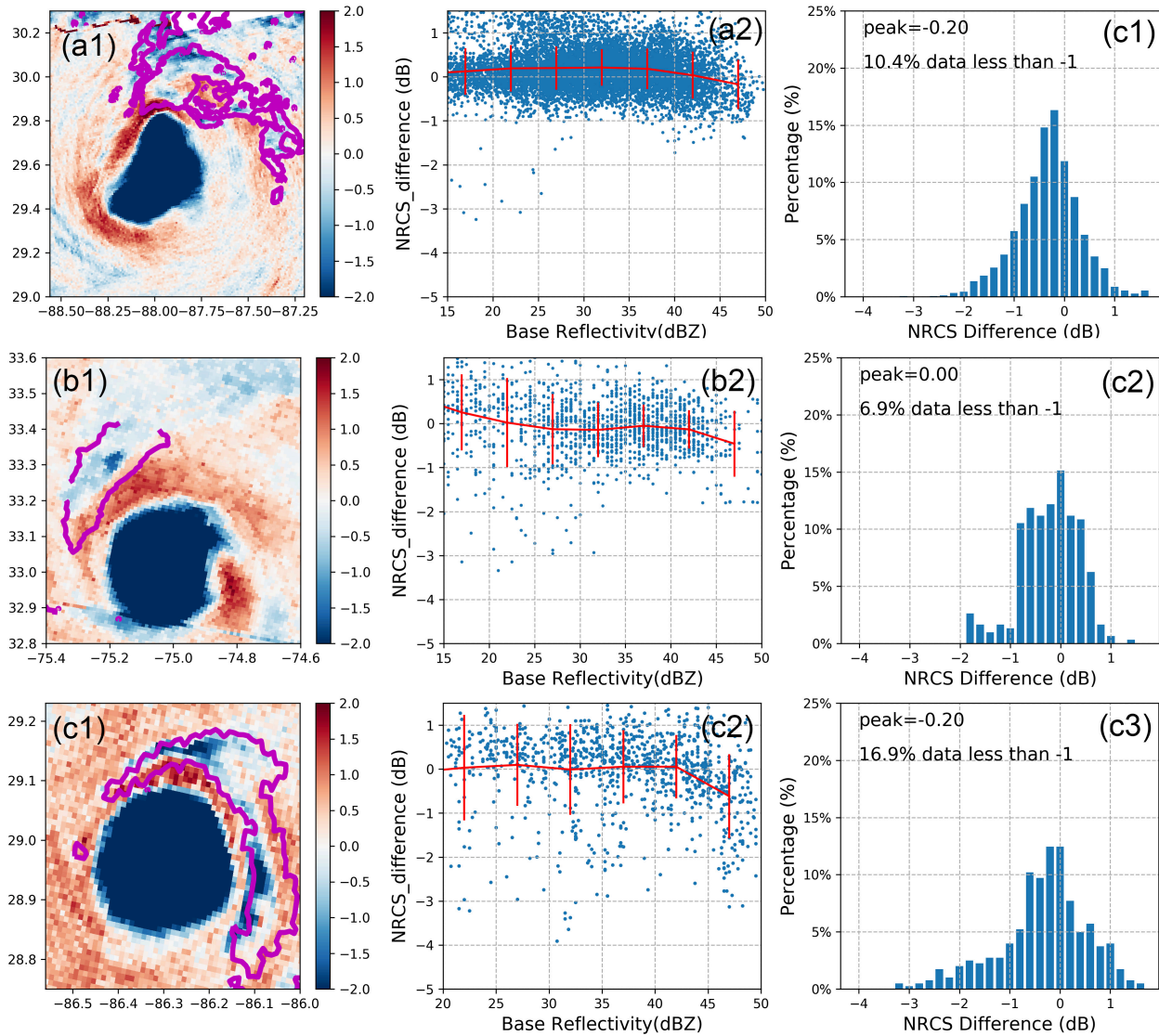


Figure 4.17: Same analysis with Fig. 4.16 but for VH polarization.

a more contribution from atmosphere instead of ocean surface. Although only 3 cases are analyzed in this section, we can see that the precipitation in the eyewall can lead to strong attenuation on radar backscatter in VV and VH polarizations. And in both polarizations, the attenuation becomes more significant at high-category TC even at same rain rate.

4.2.2 Spiral Rainband

According to the analysis in above subsection, the eyewall with heavy rainfall is always observed as dark area close to the center. Yet as for the spiral rainbands outside of the eyewall, the signatures shows more different features. As reported in Li et al. (2013), the signatures of rainbands were observed

as purely dark, purely bright, half bright and half dark. Since no rain rate data was provided, they did not focus on the relation between the rainband signatures and rain rate. Although limited TC cases are collected with collocated weather radar in our study, it gives a good opportunity to investigation this relation and factors impacting the rainband signatures.

Spiral rainbands in Florence (category-3) and Michael(category-4) in Fig. 4.15 shows dark strips around the eyewall associated with base reflectivity over 35 dBZ. Fig. 4.18 shows another example of Michael at category-3 captured by VV- and VH-polarization S-1 images at 23: 44 UTC on 9 Oct 2018. In this case, rainbands with significant signatures in good colocation with base reflectivity in Fig. 4.18(c). Note that the base reflectivity combines measurements from three coastal stations, KTLH, KTBW, and KBYX. Thus, for one region in the reach of multiple radars, base reflectivity in this map takes the largest value among them. Because the base reflectivity can be greatly underestimated as close to the maximum detection range. Fig. 4.18(d) shows the sea surface wind by a dual-pol wind retrieval algorithm from VV and VH-polarization images. This algorithm has better capabilities of wind speed estimation than ECMWF winds for high-category TC (Mouche et al., 2017).

Here we compare the spiral rainbands in three areas (marked by color box) in Fig. 4.18, which are shown in Fig. 4.19. In area 1, the rainband is observed as dark in VV but bright in VH, the difference of which is seldom reported before. In comparison, the rainbands close to the center are observed as dark in both VV and VH and in the other 2 zoom areas rainbands shows many bright patches in both polarizations. The transect of NRCS (red transect) in area 1 clearly shows a decrease of 2 dB in VV but a increase of about 3 dB in VH (Fig. 4.20), associated with base reflectivity up to 45 dBZ.

In area 2 (green box), the rainband is observed as bright surrounded by some dark shadows in both polarizations. The pronounced signatures are similar to the features of rain cells presented in Section 4.1.1, where volume scattering from hydrometeor is more dominant than attenuation. With the base reflectivity over 42 dBZ, NRCS in VH increases by 3 dB, close to the increment at transect red. This can be explained by similar surrounding wind condition since the inversed wind speed for the two transects (red and blue) is about 17 m/s and the VH-pol NRCS for the two transects is around -26 dB in light-rain area. However, as for VV, we observe a sharp increase in transect blue opposite to the decrease in transect red probably due to a larger incidence angle. As shown in the statistics for rain cells (Fig. 4.16), the rain signatures in VV is largely impacted by the incidence angles, where NRCS shows a large increase at incidence angles higher than 41° but keeps close to or less than that without rain at low incidence angles under the same wind speeds. Thus due to large incidence angles, volume scattering in area 2 plays a more important role whereas attenuation is dominant in area 1 at VV polarization. In transect blue, there is a sharp decrease

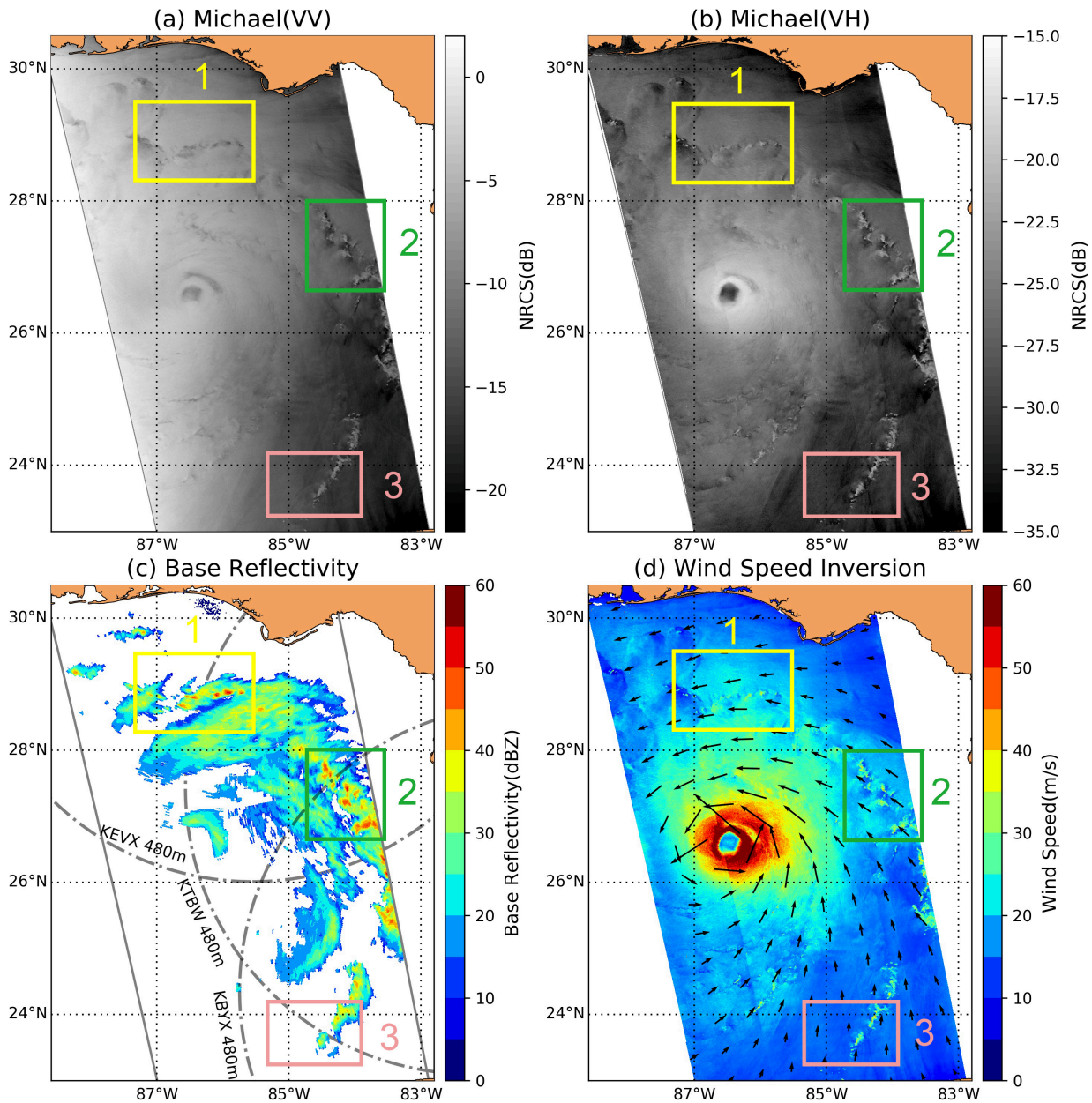


Figure 4.18: TC Michael captured by S-1 at VV (a) and VH (b) polarizations on Oct 09, 2018 at 23:44UTC. (c) Base Reflectivity from NEXRAD KTLH, KTBW, KBYX stations. The dash lines mark the maximum detection range (480 km) for each station. (d) Wind field retrieved from dual-pol SAR images.

before increase in both polarizations. It is supposed to be caused by contrary between gust front and surface winds because the wind direction is towards the rainband (Fig. 4.18(d)).

In area 3 (pink box), the rainband is shown as bright patches in both polarizations. NRCS along

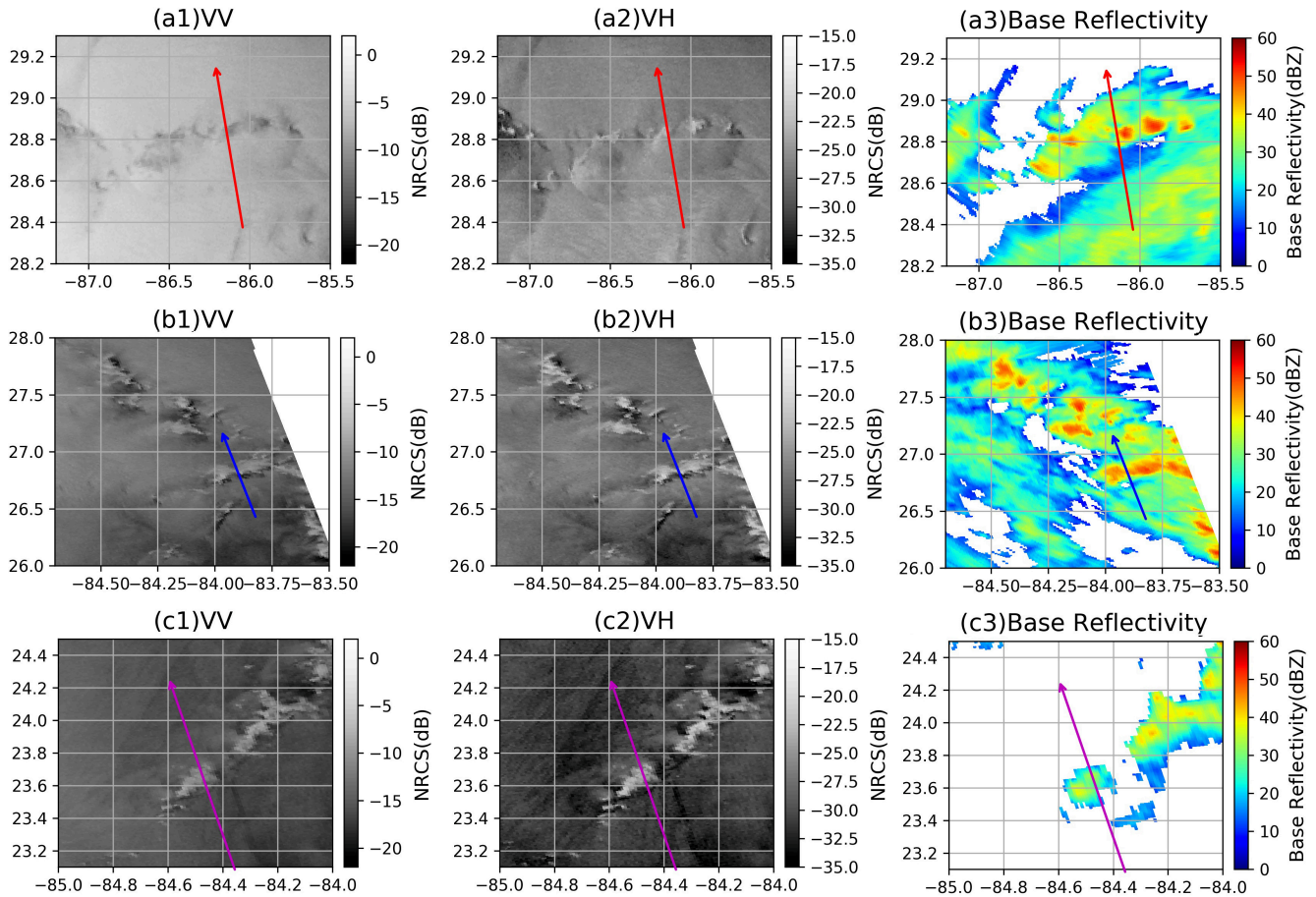


Figure 4.19: VV- and VH-pol NRCS and base reflectivity for the 3 areas marked in Fig. 4.18.

the transect purple increases more than 5 dB in VV and VH where base reflectivity goes up to 35 dBZ. Even though the base reflectivity might be underestimated, the increment of NRCS on transect purple is still larger than transect blue, owing to a lower wind speed in the surrounding area. Overall, the variant signatures of rainbands in SAR images depend on rain rate, surrounding wind speed and incidence angles. For one TC, the eyewall and rainbands close to center are often observed as dark area with heavy rainfall whereas rainbands far from the center are shown with different signatures, probably differing in co- and cross-polarizations. Especially the distant rainband developed from individual rain cells, whose vertical structure is relatively unaffected by the vortex dynamics of inner core leading to a similar signatures to convective rain cells or thunderstorms.

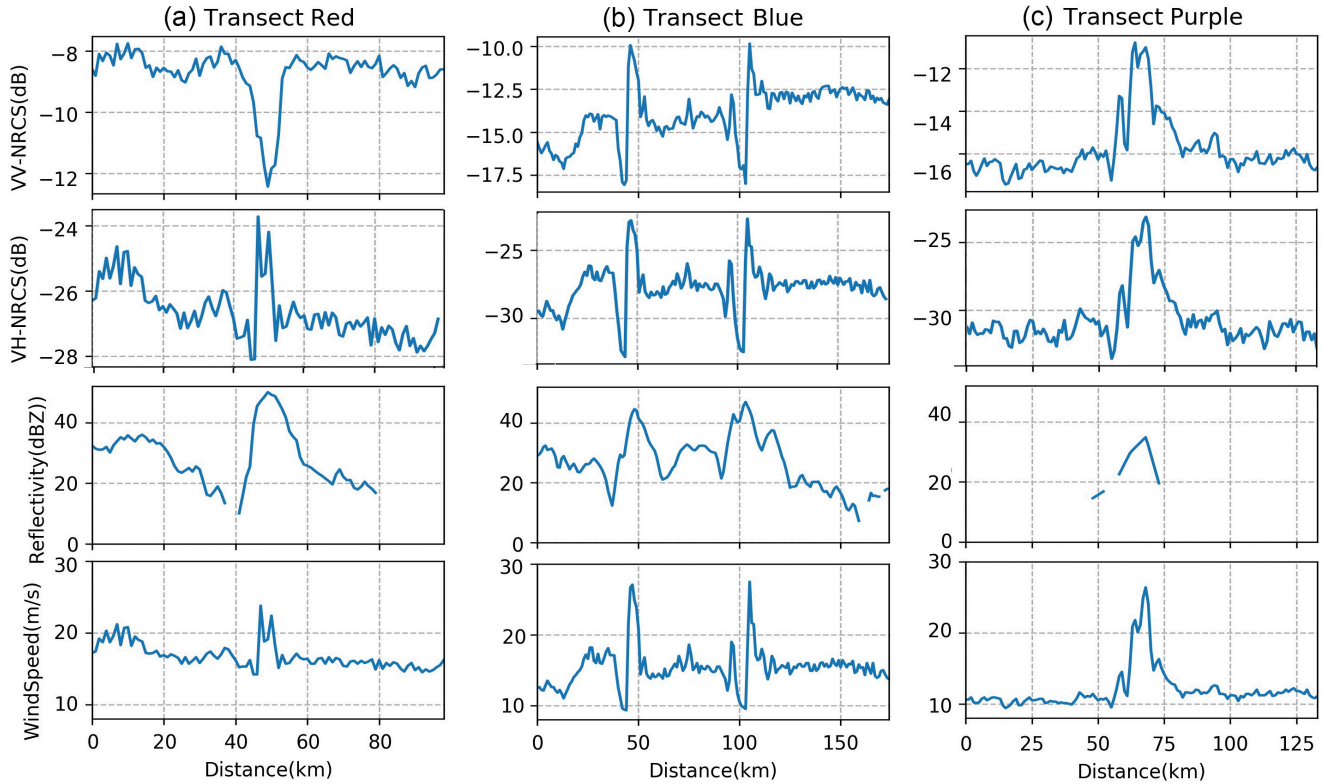


Figure 4.20: The plots of VV- and VH-NRCS together with base reflectivity and ECMWF wind speed along the transects red, blue and purple inserted in Fig.4.19.

4.2.3 Radial Profile of Rain Rate

From the weather radar, eyewall is readily recognized as a uniform ring of intense radar reflectivity where precipitation particles are generated rapidly to produce heavy rainfall. In the past, the radial profiles of wind and rain rate were paid much attention individually for TC analysis, yet less focus on the RMW and the radius of maximum rainfall rate (RMRR). According to the analysis above, precipitation in eyewall can lead to strong attenuation on NRCS, appearing as dark semi-circle around the TC center. It gives an opportunity to investigate the radial location of RMRR relative to RMW in SAR images without the weather radar data. (Foerster et al., 2014) showed the most intense precipitation in TCs usually happens in the region of eyewall, defined at 0.75-1.5 RMW. Here we collected 53 cases to further investigate it, especially on the relations between the relative location and category. These cases are selected with apparent attenuation close to center which we believe it related to rainfall, also with eye fully captured by Sentinel-1 from 2015 to 2020.

Fig. 4.21 shows an example of Laura to get the RMW and RMRR. The SAR images are captured at

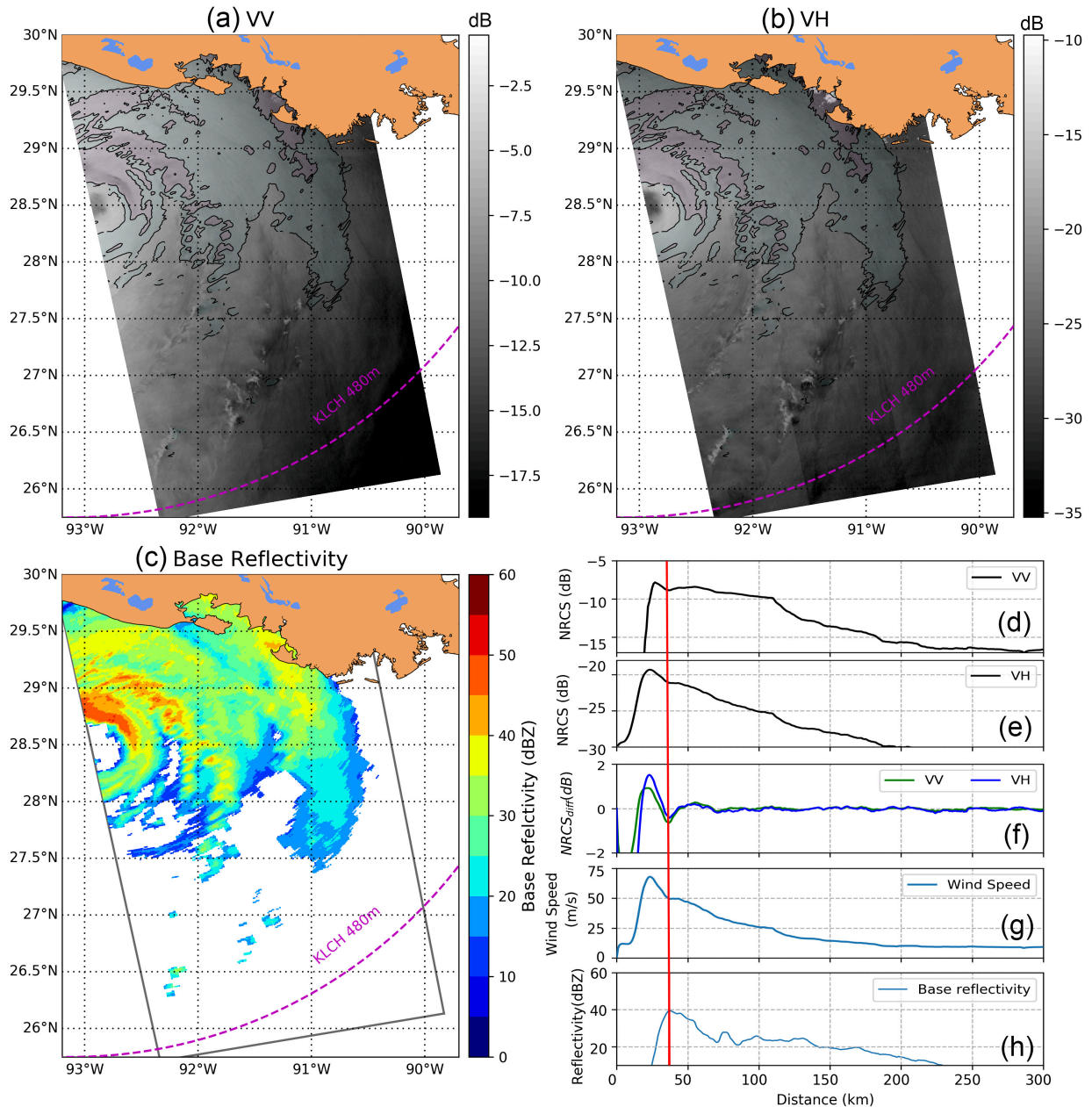


Figure 4.21: Laura captured by Sentinel-1 in (a) VV and (b) VH polarizations at 00:10 UTC 27 Aug 2020. The light purple and grey contours inside stand for the base reflectivity of 35dBZ and 20 dBZ respectively. (c) Base reflectivity from NEXRAD KLCH station. The dash line marks the largest detection range of radar. The mean radial profiles of NRCS in VV (d) and VH (e) are shown together with the profiles of $NRCS_{diff}$ (f), wind speed (g) and base reflectivity (h).

27 Aug 2018 at 00:10UTC, when Laura is at the stage of category-4. The collocated base reflectivity from NEXRAD is over 45 dBZ as observed. The dark semi-circle in VV and VH close to the center is well

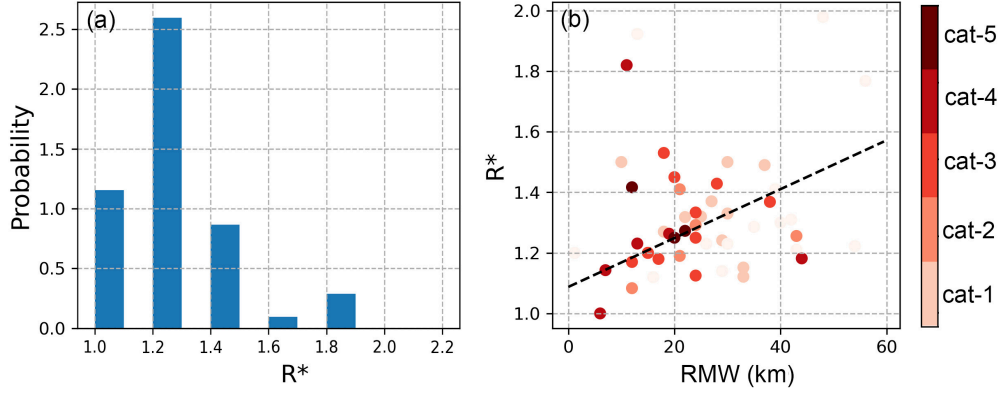


Figure 4.22: (a) the probability histogram of the radial location of maximum precipitation relative to RMW. The x axis of R^* stands for the radial distance over RMW. (b) R^* with categories against RMW.

colocated with the contour of 35 dBZ. In radial profiles of VV- and VH-polarization NRCS in Fig. 4.21(d) and (e), a decrease behind the NRCS peak is observed at the location of maximum base reflectivity. Also the radial profile of NRCS_{diff} in Fig. 4.21(f) clearly show an decrease of -0.5 dB behind an abrupt increase in both polarizations, illustrating an attenuation due to heavy rains. To get the RMW, a radial profile of wind speed is given in Fig. 4.21(f), where the wind speed is derived from the SAR images. Then the radial location of RMRR is readily compared with RMW. For Laura, RMW is at 23 km and RMRR is at about 30 km h, about 1.3 RMW.

Similar to Laura, we get RMW from the radial profile of retrieved wind speed for all the 53 cases. And RMRR is derived from the minimum of NRCS_{diff} at VV and VH polarizations. The histogram of RMRR in Fig. 4.22(a) reveals that RMRR locates at 1-2 RMW, with the maximum around 1.2 RMW. This is different from the results by (Foerster et al., 2014) probably since RMW from meteorology is mostly derived at 2 km whereas we extract RMW from sea surface. In addition, we observe a increase of RMRR with the increasing RMW. Generally the mature TCs at high category with heavy rainfall and wind speed carry a smaller eye. The RMRR shifting away from RMW suggests a dispersion of precipitation, and also weakening process of TCs. However, there is no clear correlation between category and the RMRR observed only based on the 53 cases. More cases are necessary to dig into the precipitation distribution and the development associated with RMW and V_{max} .

4.3 Summary

This chapter takes advantage the collocation dataset to document the rain impact on the backscattered signal for the two polarization channels. On average, the radar backscatter under precipitation increases

with rain rate from light to moderate winds regime, although the rainfall signatures on C-band SAR images is very complex with concurrent bright and dark patches (Atlas, 1994; Melsheimer et al., 1998; Alpers et al., 2016). The shift of rain cells and the changing elevation of radar beam result into the large variability around the mean trend. In addition, this sensitivity to rain rate is found to be more pronounced for higher incidence angles in the case of VV polarization but not in VH polarization. For the strongest wind conditions analyzed here, the radar backscatter is lower than the surrounding at incidence angles less than 33° . Comparatively, VH at the same incidence angles is higher than VV. This illustrates the advantage of cross-polarization for precipitation recognition, especially at low incidence angles and high winds. To note, in the case of cross-polarization, the low signal-to-noise ratio observed for low wind speed regimes may have impacted our analysis. Improvements in future mission performances will certainly allow to refine this analysis.

The observation on TCs are analyzed in terms of eyewall and spiral rainbands. The precipitation in eyewall induces a strong attenuation on radar backscatter, shown as a dark strip around the center. In comparison, the spiral rainbands are shown as different patterns with increasing distance from the center. For rainbands close to eyewall, it is observed with dark region in VV and VH whereas rainbands far from the center can be observed as dark in VV and bright in VH, or the bright with dark patches in the surrounding in both polarizations. The signatures of precipitation in TCs is also dependent on rain rate, wind speed and incidence angles, similar to the rain cell cases. Particularly, the attenuation in eyewall is related with improvement of category in VV. In addition, the maximum precipitation is found to locate in 1-2 RWM. And with RMW increasing, the RMRR goes away from RMW, indicating a dispersion of precipitation and weakening process of TCs.

Model explanation for the rain impacts

Contents

5.1	Transfer Model through rain cell	58
5.1.1	Transfer model through the atmosphere	58
5.1.2	SAR data rain model	63
5.2	Evaluation of the impact of different rain rate and incidence angle	66
5.2.1	Geometry of simulated radar backscatter	66
5.2.2	Sea surface backscatter	67
5.2.3	Wind speed	69
5.2.4	Radar pulse length	69
5.3	Validation	70
5.3.1	Case 1	70
5.3.2	Case 2	76
5.3.3	Case 3	77
5.4	The impact of time shift of rain data on simulation	79
5.5	Summary	83

One method to analyze the signature of rain in SAR images is to compute the impact of rain using a numerical model based on the transfer equation of electro-magnetic wave through the atmosphere. Based on previous works on the impact of rain on SAR data by Melsheimer et al. (2001) and scatterometer data by Tournadre and Quilfen (2003), we developed a numerical model simulating the impact of rain on SAR data.

5.1 Transfer Model through rain cell

5.1.1 Transfer model through the atmosphere

During the transit through the atmosphere microwave signals experience scattering and attenuation by aerosols and/or hydrometeor particles. The variation of signals under different rain conditions in this

process is strongly dependent on frequencies and can be evaluated by models (Tournadre and Quilfen, 2003; Xu et al., 2015; Contreras and Plant, 2006). If a volume is filled with homogeneous rain, the radiative transfer equations in atmosphere can be described by Eq. (5.1), where the axis of z points towards the ground and θ is the incidence angle (Fig. 5.1) (Tournadre and Quilfen, 2003). $I_+(r)$ and $I_-(r)$ refer to the downward and upward power transferring respectively.

$$\begin{aligned} dI_+(z) &= -k_a I_+(z) dz \sec(\theta) \\ dI_-(z) &= -\eta I_+(z) dz \sec(\theta) + k_a I_-(z) dz \sec(\theta) \end{aligned} \quad (5.1)$$

where k_a and η stand for the atmospheric attenuation and volume scattering coefficients of hydrometeors

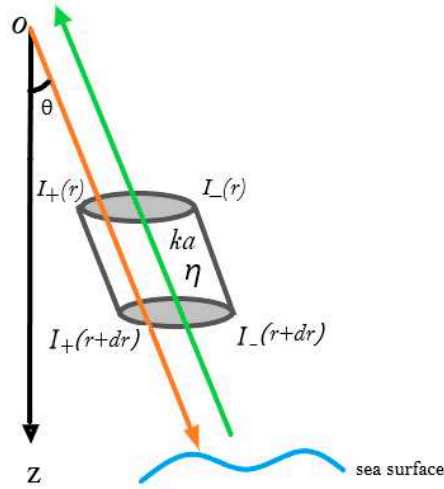


Figure 5.1: The radiation transfer across a cylinder filled with precipitation

(e.g., raindrops, ice particles) respectively. Marshall and Palmer (1948) proposed the following relationship between the attenuation by raindrops at a given frequency (k_a) is in relation and the rain rate,

$$k_a = aR^b \quad (5.2)$$

where R is the rain rate in mm/hr and the a and b are frequency dependent coefficients. At C band, $a = 1.06 \times 10^{-3}$ and $b = 1.393$ (Olsen et al., 1978). At Ku-band, a and b are 0.0314 and 1.14 respectively (Slack et al., 1994), whereas $a = 0.008$ and $b = 0.95$ for X band. Figure 5.2 shows the k_a coefficient at different frequencies. As shown, rain can cause significant attenuation on radar signal at high frequencies

like Ku band due to strong Rayleigh scattering. At C band, attenuation is almost negligible at low rain rate, but it becomes significant at high rain rate especially for rain rate exceeding 40 mm/hr. Although ice crystals and water vapor can also be present during precipitation event, they contribute much less to attenuation compared to raindrops and can be regarded as negligible in a first order approximation (Oguchi, 1983). Thus, Tournadre and Quilfen (2003) only take into account the attenuation and emission by raindrops.

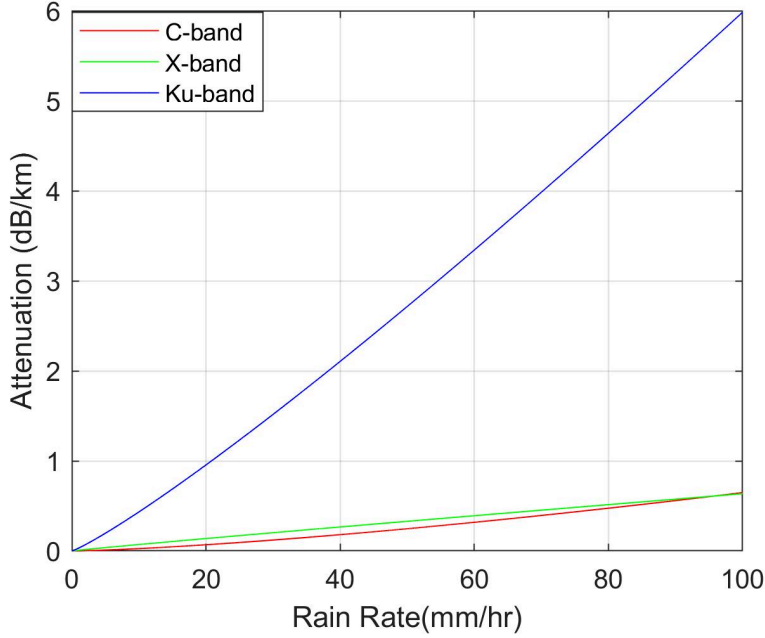


Figure 5.2: Attenuation coefficient with respect to rain rate at C-, X-, and Ku-band

In Eq. (5.1) η is referred to as the volume scattering coefficient by Rayleigh approximation. It is an algebraic sum of the backscattering cross section of the individual spherical particles. For a microwave signal of frequency f , the normalized backscattering cross section ξ_b of a given particle of radius r is given by

$$\xi_b = \frac{64\pi^4}{\lambda^4} r^4 |K|^2 \quad (5.3)$$

where λ is radar wavelength. K is a complex quantity, dependent on the refractive index n of hydrometers, defined as

$$K = \frac{n^2 - 1}{n^2 + 2} \quad (5.4)$$

K is equal to 0.94 for raindrops, and 0.19 for ice particles (Melsheimer et al., 2001). Summing up all the

particles in an unit volume, the total volume backscattering coefficient η becomes

$$\begin{aligned}\eta &= \sum_{i=1}^N \pi r_i^2 \xi_b \\ &= \frac{64\pi^5}{\lambda^4} |K|^2 \sum_{i=1}^N r_i^6\end{aligned}\quad (5.5)$$

Weather radars measure in general the reflectivity Z , defined as

$$Z = \sum_{i=1}^N d_i^6 \quad (5.6)$$

where $d_i = 2r_i$ is the diameter of the i th particle. Then, Eq. (5.5) can be rewritten as

$$\eta = \frac{\pi^5}{\lambda^4} |K|^2 Z \quad (5.7)$$

After changing the unit of Z from m^6 per m^3 to mm^6 per m^3 , η is expressed by

$$\eta = 10^{-18} \frac{\pi^5}{\lambda^4} |K|^2 Z \quad (5.8)$$

The value of η is thus dependent on the rain intensity, the incident wavelength and the refraction index of the hydrometeor. Fig. 5.3 shows that the volume scattering by raindrops is much larger than that of ice particles because of a higher refraction index. It is thus reasonable to neglect in a first order approximation the volume scattering from ice in the model.

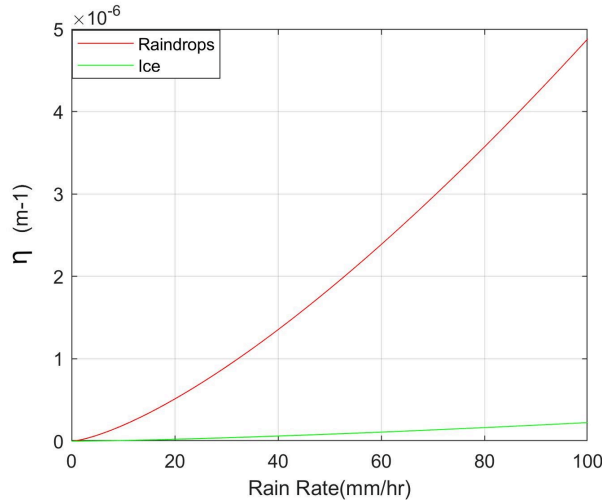


Figure 5.3: Coefficient η from raindrops and ice particles.

Assuming that the rain rate is constant within the elementary volume of figure 5.1, k_a and η are

constant according to Eqs. (5.2), (5.8). Thus, the solutions of I_+ and I_- is derived as follows,

$$\begin{aligned} I_+(z) &= I_+(0)e^{-k_a z \sec(\theta)} \\ I_-(z) &= I_-(z)e^{k_a(z-d)\sec(\theta)} + \int_d^z \eta I_+(0)e^{2k_a z' \sec(\theta)} \sec(\theta) dz' \end{aligned} \quad (5.9)$$

where the d refers to the lower boundary of the transfer path (here the sea surface). If the sea surface backscattering coefficient is σ_0 and the top height of rain is H , the power I_+ and I_- at the lower boundary can be expressed as:

$$I_+(d) = I_+(0)e^{-k_a H \sec(\theta)} \quad (5.10)$$

$$I_-(d) = \sigma_0 I_+(d) = \sigma_0 I_+(0)e^{-k_a H \sec(\theta)} \quad (5.11)$$

Combining these two equations, $I_-(0)$ can be inferred from $I_+(0)$, as shown in Eq. (5.12). Thereby the rain-modified radar backscatter $\tilde{\sigma}_0$ defined as the ratio of $I_-(0)$ to $I_+(0)$, can be calculated from the surface backscattering coefficient σ_0 , the attenuation coefficient k_a , the height of rain column H and the emission coefficient η , by Eq. (5.13).

$$I_-(0) = I_+(0)\sigma_0 e^{-2k_a H \sec(\theta)} + \eta I_+(0) \frac{1}{2k_a} \left(1 - e^{-2k_a H \sec(\theta)}\right) \quad (5.12)$$

$$\tilde{\sigma}_0 = \frac{I_-(0)}{I_+(0)} = \sigma_0 e^{-2k_a H \sec \theta} + \eta \frac{1}{2k_a} \left(1 - e^{-2k_a H \sec \theta}\right) \quad (5.13)$$

The above equations are all derived assuming a uniform rain rate in the volume. In reality, the situation is more complex since the rain distributes non-uniformly in space. Moreover, depending on the rain type, the thickness of the rain cloud changes as well. For a convective rain storm, the cloud top height can exceed 10 km, whereas for stratiform rain cloud top are generally lower than 5 km. Thus, for integrating attenuation by the inhomogeneous rain along the ray path, we define the atmospheric transmission τ between $z = 0$ and $z = s$ as

$$\tau(0, s) = \int_0^s k_a(z) dz \quad (5.14)$$

τ is thus a function of the distance of radar beam s . Then, equation (5.13) can be generalized as

$$\tilde{\sigma}_0 = \sigma_0 e^{-2\tau(0,s)} + \int_0^s \eta(z) \{e\}^{-2\tau(0,s)} dz \quad (5.15)$$

5.1.2 SAR data rain model

The above model is applicable to all frequencies and to all type of active microwave sensors. However, for scatterometer or altimeter, the measurement cell can be quite large (~ 25 km) and certainly much larger than typical rain cells (a few km). The measurement cell can thus be only partially filled by rain. For Sentinel-1 SAR, the pixel size in GRDH IW mode is $10 \text{ m} \times 10 \text{ m}$. In this study, we use the level-1 product averaged at a 1 km resolution. This resolution is close to weather radar commonly providing rain rate or reflectivity products at 1 km resolution. The measurement cell can thus reasonably be assumed to be filled with rain that is constant horizontally.

The conceptual model presented by Melsheimer et al. (2001) considered homogeneous rain cells for modelling the SAR radar backscatter. In this model, the rain cell boundary is irregular. When computing the measured backscatter power, all the hydrometeors with the same range to the sensor as the sea surface (in $z = 0$) need to be taken into account. For a given point $M(x, y)$, the NRCS can be calculated by,

$$\begin{aligned} \tilde{\sigma}_0(x, y) = & \sigma_0(x, y) \exp \left[-2 \int_0^{f(y)} k_a(u) du \right] + \sin \theta \int_0^{l(y)} \eta(s) \\ & \cdot \exp \left[-2 \int_0^{f_y(s)} k_a(u) du \right] ds \end{aligned} \quad (5.16)$$

where y is the ground-range coordinate, $l(y)$ is the length of the rain-filled tilted column contributing to the NRCS, $f_y(s)$ is the boundary of the rain cell as a function of the s coordinate of the tilted column with the origin at y , and $f(y)$ is the path length of radar signal at range y . For computation of $\tilde{\sigma}_0$, the f, l, f_y, k_a, η need to be known. If the rain rate is also known in the each point (x, y) , Eq. (5.16) can then be numerically integrated.

It should be noted that the model provided by Melsheimer et al. (2001) is only in bidimensional. They consider the point y along the looking direction without a size. Moreover, the radar pulse length t is assumed a quasi Dirac. For S-1 IW mode, t is between $5 \mu\text{s}$ and $100 \mu\text{s}$. The interval between the front and the rear of the radar pulse is of the order of several kilometers. This volume will contribute to the volume emission.

Assuming a cylindrical rain cell of height H and a radar pulse length of t , the geometry of the sampling of the sea surface is depicted in Fig. 5.4. The power measured by a SAR is composed of both the signal backscattered by the surface and by the atmospheric hydrometeors within the rain cell. The volume of scattering hydrometeors within the rain cell depends of the distance from nadir of the considered SAR pixel. For pixels in region 1 (Fig. 5.4), the power backscattered from the ground is not attenuated by rain and the hydrometeors within the yellow zone backscatter some power to the sensor (Fig.5.4). For region

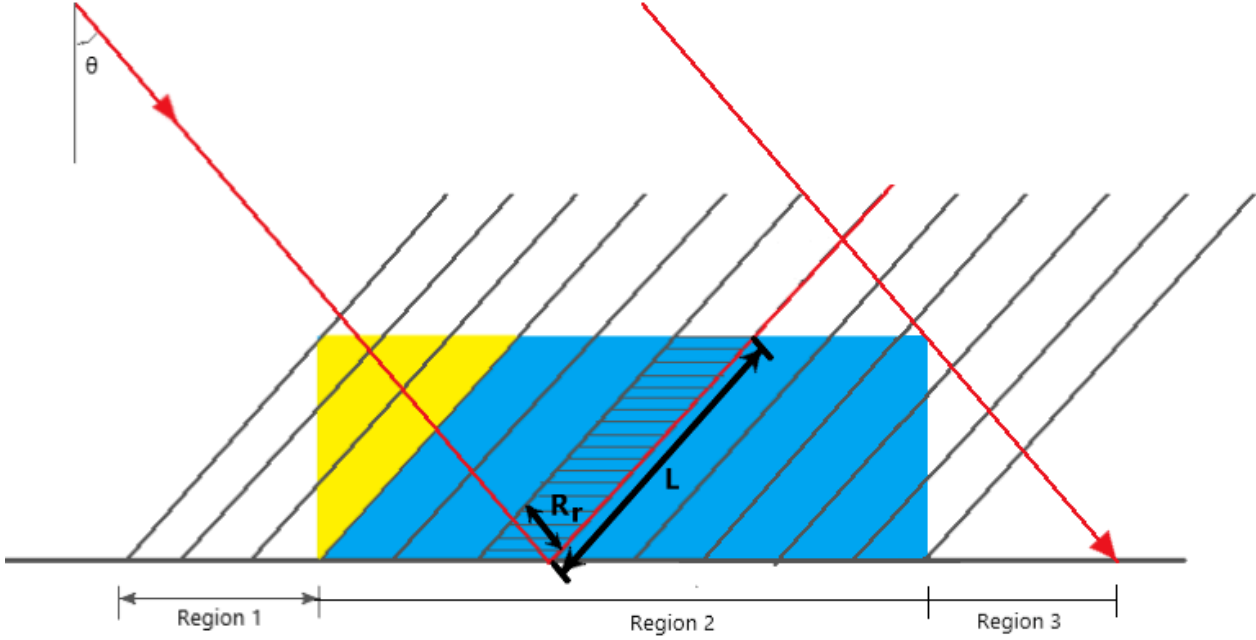


Figure 5.4: Geometry of the radar pulse in the model. The colored zones represent the rain cell. θ is incidence angle. c is the speed of light and t is the radar pulse length. $R_r = ct/2$ and L is the titled path length, i.e. the points with the rain cloud with the same range as the surface.

2, the surface backscatter is attenuated along its travels within the rain cell (blue and yellow zones) while the emission by the rain volume covered during the pulse length (in blue) contributes to the received power. Thus in one volume of radar pulse the attenuation and volume scattering both contribute to the received backscatter. Comparatively, in region 3 the radar pulse is still attenuated by rain but there is no more emission by volume scattering.

In this study, the pixel size is 1km by 1km for S-1 data. Thus it is more reasonable to consider the attenuation and volume scattering in a 3D volume above the 1km-by-1km pixel. More generally, the received power for SAR can thus be written as

$$P_{\text{meas}} = P_{\text{surf}} + P_{\text{rain}} \quad (5.17)$$

where the P_{meas} stands for the received power and the P_{surf} and P_{rain} correspond to the powers backscatter by the surface and the hydrometeors (i.e; the first and second terms in Eq. (5.21)) respectively. x, y are the SAR across and along look directions.

If the ocean surface backscatter coefficient is $\sigma_{0,\text{surf}}$, and the atmospheric transmission is $\tau(0, s)$, P_{surf}

can be estimated by

$$P_{\text{surf}} = A_R P_o \sigma_{0,\text{surf}} e^{-2\tau(0,\infty)} \quad (5.18)$$

where $A_R = R_x R_y$ is the ground resolution and P_o is the emitted power. R_x and R_y are the azimuth and range resolutions respectively.

The contribution from volume scattering is dependent on the volume size (volume length L and width R_r), related to the geometry and the radar pulse length t . $R_r = ct/2$ where c is light speed. If the backscatter from hydrometeor in one unit volume is η , the total backscatter P_{rain} from hydrometeor is

$$P_{\text{rain}} = P_o R_x \int_0^{R_r} \int_0^L \eta(z, s) \{e\}^{-2\tau(z,\infty)} dz ds \quad (5.19)$$

Accordingly, the measured NRCS $\sigma_{0,m}$ can be written as

$$\sigma_{0,m} = \frac{P_{\text{meas}}}{A_R P_o} = \sigma_{0,\text{surf}} e^{-2\tau(0,\infty)} + \frac{1}{R_y} \int_0^{R_r} \int_0^L \eta(z, s) \{e\}^{-2\tau(z,\infty)} dz ds \quad (5.20)$$

For simplicity, Eq. (5.20) can be written into

$$\sigma_{0,m} = A \sigma_{0,\text{surf}} + E \quad (5.21)$$

where A and E are the attenuation and emission terms.

$$A = e^{-2\tau(0,\infty)} \quad E = \frac{1}{R_y} \int_0^{R_r} \int_0^L \eta(z, s) \{e\}^{-2\tau(z,\infty)} dz ds \quad (5.22)$$

Eq. (5.21) makes the model in a simple form to understand. It is clear that the radar received backscatter is composed of the surface backscatter $\sigma_{0,\text{surf}}$, the attenuation term A and the emission term E . As the rain rate increases, the value of A decreases and E increases. The measured backscatter contains thus less and less information on the surface for increasing rain rates. Emission from hydrometers can become dominant in the measured total radar backscatter.

The model proposed by Melsheimer et al. (2001) was mainly theoretical and was not designed to numerically model SAR signal in presence of rain while the Tournadre and Quilfen (2003) was designed for scatterometer with very large ground resolution and pulse length. Our model based on this two model includes the pulse length and the high ground resolution achieved by SAR processing. In Eq.(5.16), they do not consider pulse length so that all the volumes before the one given point are integrated. If the radar operates at short pulse length, this integration certainly overestimates the volume scattering. However, for altimeter or scatterometer, it can be ignored because they work in a short pulse length.

The $\sigma_{0,m}$ is strongly related to rain intensity because the attenuation and emission terms depend on rain rate. In this model, because of the rain data available, we hypothesise that the rain rate is constant

with altitude from the surface to the cloud top. If 3D rain rate fields are available, the model works and can simulated more accurately the $\sigma_{0,m}$. So far it is still quite challenging to estimate an accurate 3D rain rate field especially over the open ocean. That is the main reason for taking a homogeneous rain rate in height by most models.

5.2 Evaluation of the impact of different rain rate and incidence angle

Within the model, $\sigma_{0,m}$ is related to rain rate, sea surface backscatter, pulse length as well as the geometry between incidence rays and the rain cell. To show the $\sigma_{0,m}$ variation across a rain area, we assume a cylinder rain cell in height of 6 km, located between 120 km and 140 km with respect to nadir. The incidence angle is constant as 30 °. The analysis in the following is based on the single rain cell. Also the radar pulse length is 2.3 μ s in subsection 5.2.1 ~ 5.2.4.

5.2.1 Geometry of simulated radar backscatter

Fig. 5.5 shows the attenuation, emission and simulated $\sigma_{0,m}$ when radar rays cross the rain cell. The background colored in pink, yellow and grey corresponds to region 1, 2 and 3 in Fig. 5.4 respectively. As described before, attenuation is initially observed in region 2 and increases to a maximum. Then it decreases gradually in region 3. The value of attenuation is estimated on two-way, which can reach 4 dB at 50 mm/hr. But for rain rate less than 30 mm/hr, the signal losses less than 2 dB. It coincides with the previous studies that the attenuation by raindrops can be neglected at C-band, excepted for cyclone cases or severe rain storm.

For emission, it increases in region 1 and reach its maximum in region 2. Before reaching the right border of region 2, it decrease gradually until region 3. The maximum is -24.4 dB, -19 dB, -15.1 dB and -12.5 dB for rain rates of 6 mm/hr, 15 mm/hr, 30 mm/hr and 50 mm/hr.

Therefore, with the attenuation and emission, the simulation shows an strong dependency on the sea surface backscatter and rain rate. When the sea surface backscatter is -20 dB (Fig. 5.5(d)), the simulated $\sigma_{0,m}$ is larger than the sea surface backscatter and increases with rain rate as observed, indicating the dominance of emission. For a higher sea surface backscatter of -15 dB, it shows a similar trend but with an obvious attenuation in region 3. It suggests that the emission is dominant before and across the rain cell but behind the rain cell high rain rate can induce an attenuation. As for high sea surface backscatter, rain attenuates significantly the signal in region 2 and 3. It clearly shows the alternative dominance between emission and attenuation under different wind conditions and geometry.

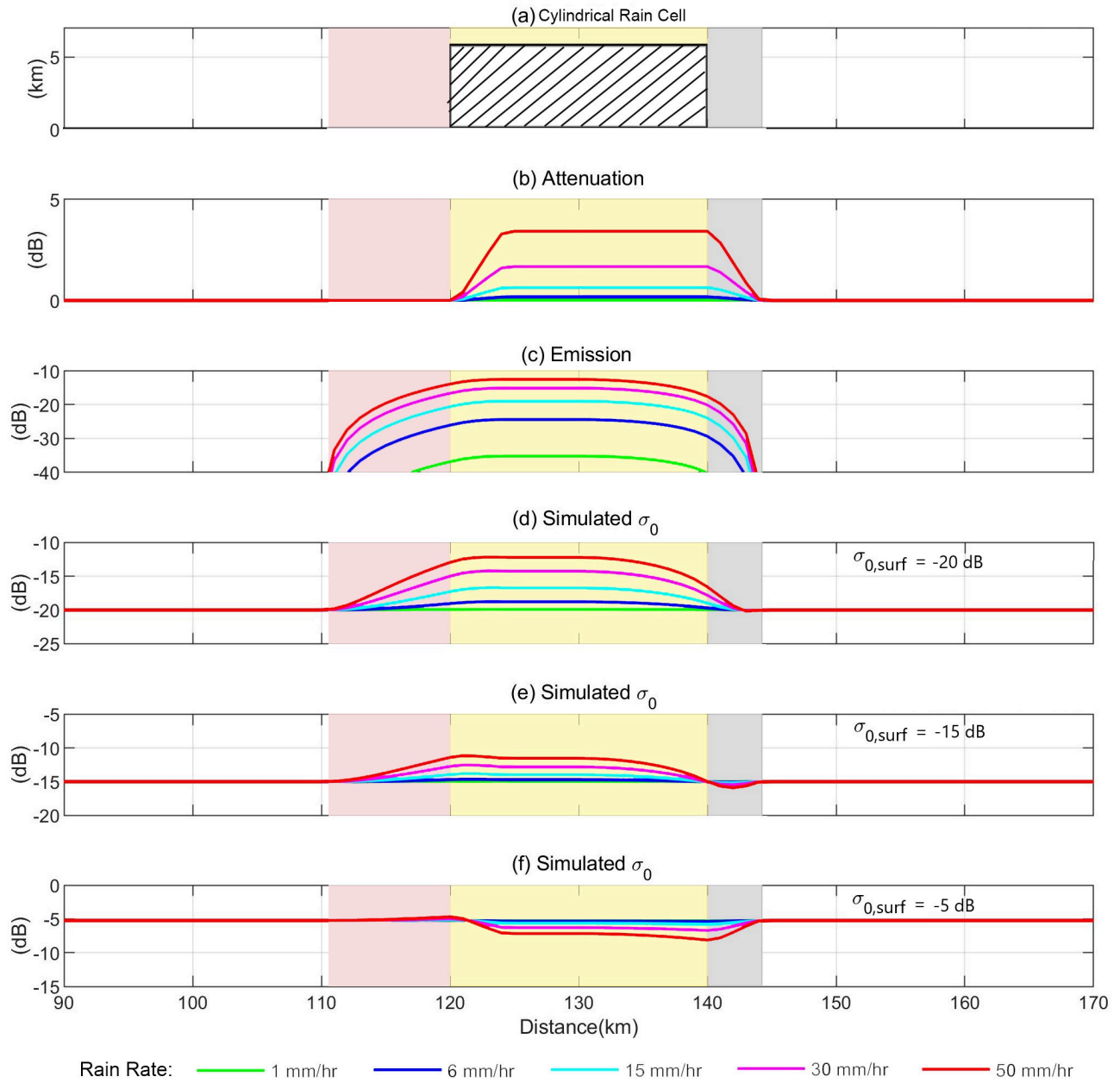


Figure 5.5: Geometry for a 6km-height rain cell with an incidence angle of 30° . (d)(e)(f) take the $\sigma_{0,surf}$ as -20, -15 and -5 dB.

5.2.2 Sea surface backscatter

As shown in Fig. 5.5, the simulated $\sigma_{0,m}$ shows variation along the distance with a maximum and a minimum. To better show the $\sigma_{0,m}$ variation with respect to $\sigma_{0,surf}$, the ratio of $\sigma_{0,m}$ to $\sigma_{0,surf}$ is plotted in Fig. 5.6. Inside, the $\sigma_{0,m}$ in the left and the middle panel takes the maximum and minimum

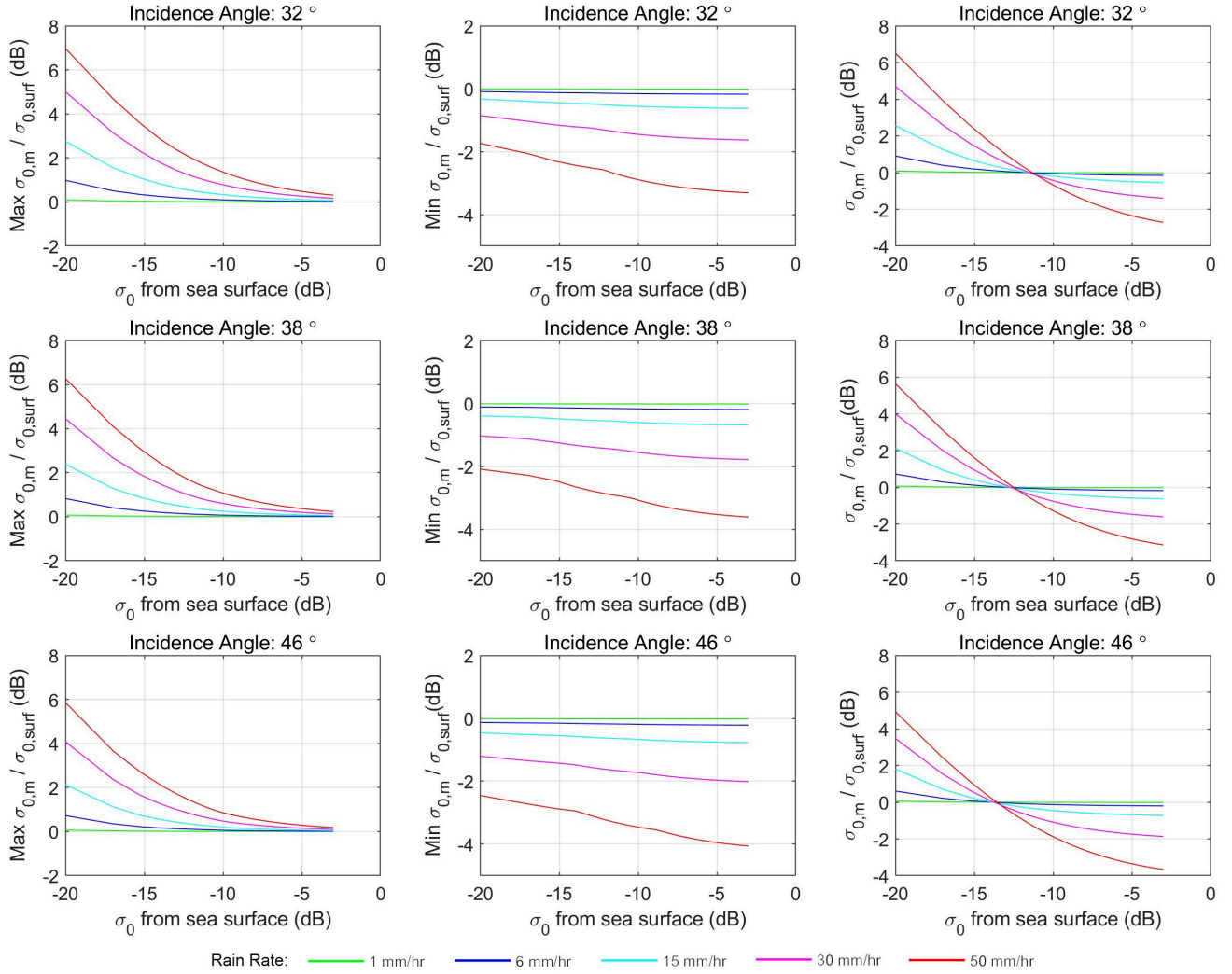


Figure 5.6: The ratio of $\sigma_{0,m}$ to $\sigma_{0,surf}$ for the incidence angles of 32° (upper), 38°(middle), 46°(lower). For each incidence angle, the $\sigma_{0,m}$ in left and middle panels is chosen as the maximum and minimum of the simulated value corresponding to the sea surface backscatter. The right panel takes the $\sigma_{0,m}$ in the middle of the rain cell.

in each simulation respectively. Their corresponding ratios are referred as max ratio and min ratio in the following. And $\sigma_{0,m}$ in the right panel refers to the value received from the middle of rain cell (130km in Fig. 5.5) for each simulation so that the derived ratio is named by mean ratio hereafter.

As observed, the max ratio decreases with the $\sigma_{0,surf}$ but remains always positive. Moreover, the max ratio takes higher values at large rain rates and low $\sigma_{0,surf}$. The higher the max ratio, the more obvious the bright patches will be (in statistics, the NRCS ratio is greater in large incidence angle). When $\sigma_{0,surf}$ exceeds -5 dB, the ratio is close to 0, indicating that rain signatures can be hardly observed.

In terms of min ratio, it is observed as negative for all rain rates excepted for 1 mm/hr, suggesting the dominance of attenuation in region 3. As expected, the attenuation becomes larger with increasing rain rate.

The mean ratio clearly shows the alternate dominance of attenuation and emission contributing to the total backscatter with increasing sea surface backscatter. Moreover, for a given incidence angle, the no variation threshold is independent of the rain rate. With incidence angle increasing, this threshold moves towards lower sea surface $\sigma_{0,surf}$. Therefore, at a large incidence angle, it is more probable that the emission dominates the total backscatter if the sea surface $\sigma_{0,surf}$ keeps the same.

5.2.3 Wind speed

In reality, the sea surface $\sigma_{0,surf}$ decreases with decreasing incidence angle for the same wind regime at co-polarization. In order to show the modulation of rain on the $\sigma_{0,m}$ at different incidence angles, we estimated the sea surface backscatter $\sigma_{0,surf}$ using the geophysical model function CMOD5 for different wind speeds. In Fig. 5.7, the ratio of $\sigma_{0,m}$ to $\sigma_{0,surf}$ shows an increase along with the incidence angle. That is in coincidence with observation displayed by Fig. 4.5 in Section 4. Also, the emission at low winds dominates the radar backscatter whereas the attenuation is more important at high winds. With increasing rain rate, the variation of ratio becomes larger. It is notable that at rain rate of 50 mm/hr and wind speed of 15 m/s, the ratio becomes negative at all incidence angles. This explains why the rainbands in tropical cyclone are often shown as dark area, especially near the cyclone center.

5.2.4 Radar pulse length

The radar pulse length, also sometimes referred as pulse width, is the duration of a single transmitted radar pulse, typically in microseconds. The longer the pulse length the larger the volume width R_r , and thereby the stronger the contribution from emission to the measured signal. Since the emission is strongly dependent on the rain cell geometry, Fig. 5.8 shows the values of emission and simulated $\sigma_{0,m}$ located at distance of 130 km in the above Fig. 5.5 with respect to a range of pulse length. The incidence angle is 40° and the rain rate is 50 mm/hr. Apparently the emission increases with pulse length up to $4 \mu s$ and then keeps constant limited by the rain cell height (i.e. once the pulse length corresponds to the height of the rain cell). Correspondingly, the simulated $\sigma_{0,m}$ follows the same variation with emission since the attenuation keeps constant at the location.

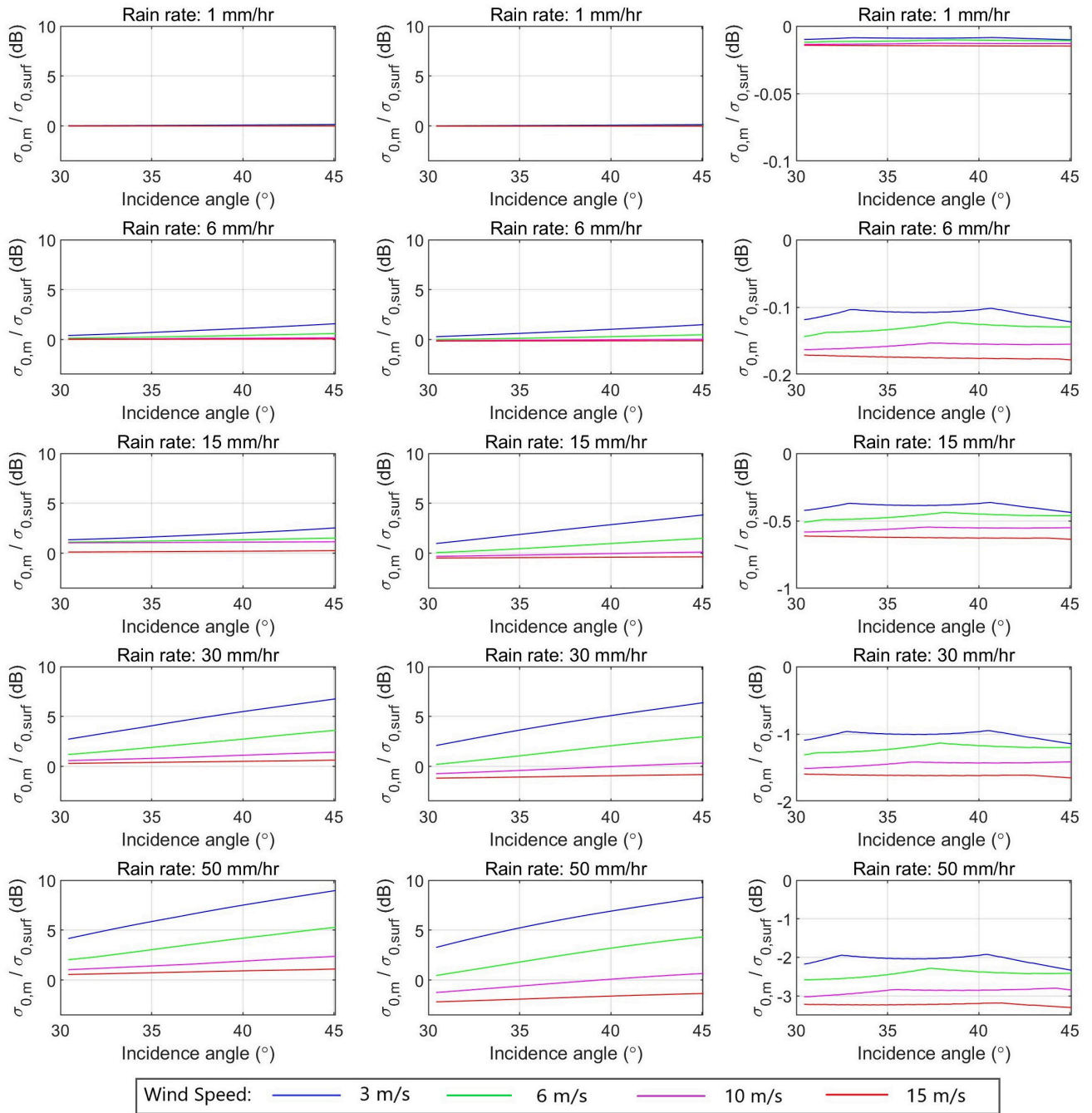


Figure 5.7: The ratio of $\sigma_{0,m}$ to $\sigma_{0,surf}$ at different wind speeds. The $\sigma_{0,surf}$ is estimated using CMOD5. The values of $\sigma_{0,m}$ in left and middle panel refer to the maximum and minimum in each simulation. And the right panel includes $\sigma_{0,m}$ received from the middle of rain cell.

5.3 Validation

5.3.1 Case 1

The VV SAR image presented in Fig. 5.9(a), acquired at 23:27 UTC on 25th of May 2017, exhibits several bright patches of high backscatter. The coincident NEXRAD base reflectivity and rain rate in

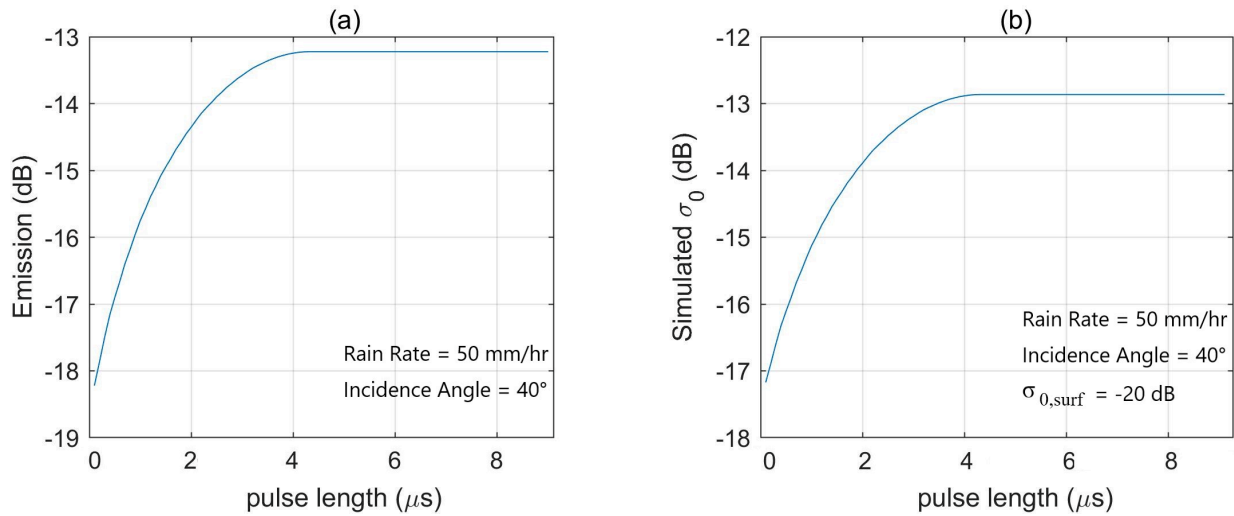


Figure 5.8: Attenuation, emission and simulated $\sigma_{0,m}$ across a 6-km-height rain cell. The volume length L for the left and right panels are 3 km and 7 km respectively.

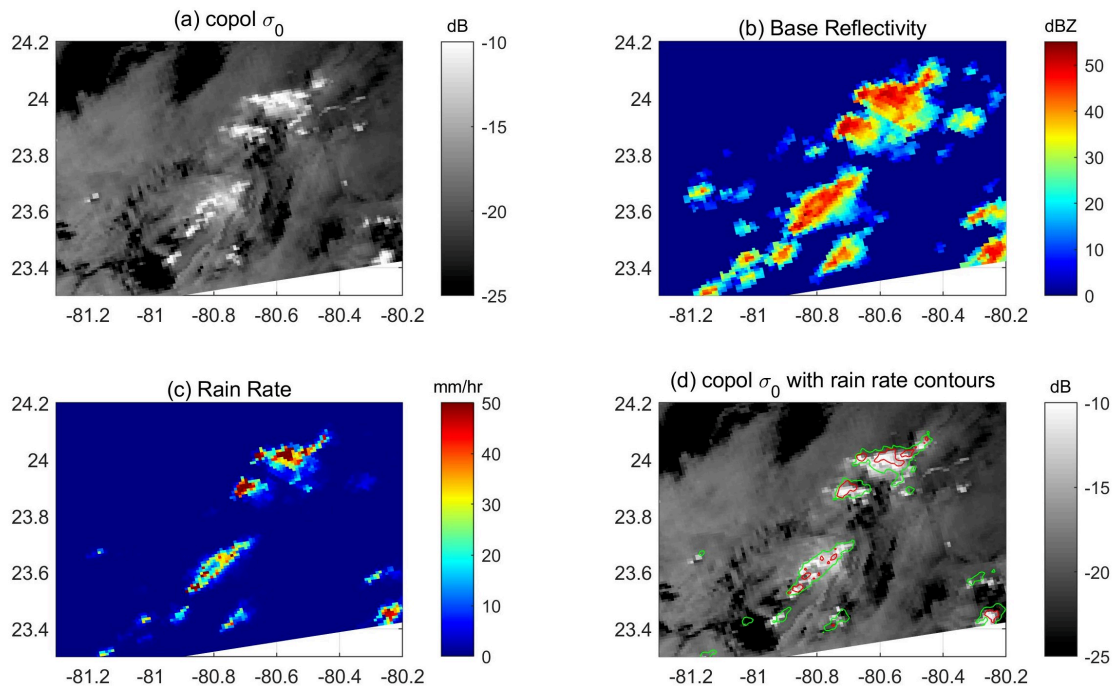


Figure 5.9: (a) Copol (VV) SAR image acquired at 23:27 UTC on 25 May 2017. (b) base reflectivity and (c) rain rate from NEXRAD.(d) copol SAR image and 10 and 20 mm/hr rain rate contours.

Fig. 5.9(b)(c) show that the bright patches were clearly associated with the two rain clusters. The contours of 10 mm/hr and 20 mm/hr overlaid on VV image (Fig. 5.9(d)) displays the bright patches observed in the rain rate of 10mm/hr and even 20 mm/hr. Wind speed from ECWMF is about 3 m/s, accounting for

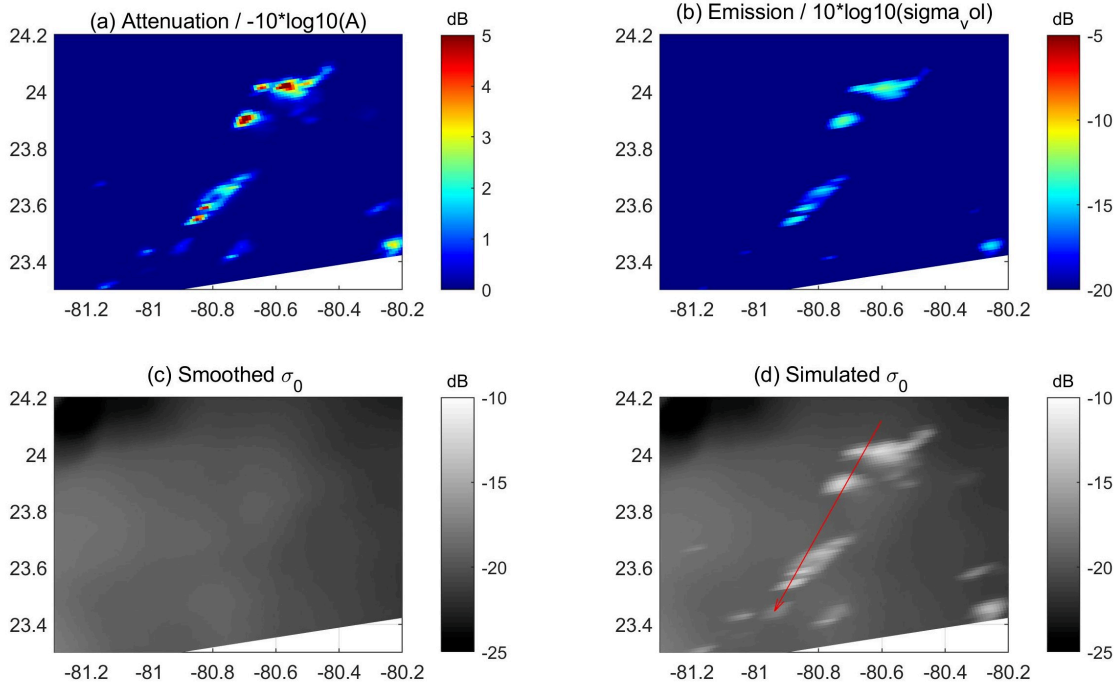


Figure 5.10: Attenuation (a) and emission (b) in dB. (c) $\sigma_{0,surf}$ by smoothing copol σ_0 in Fig. 5.9(a1). (d) Simulated $\sigma_{0,m}$.

the low backscatter in rain-free area.

Before doing the simulation, it is necessary to know the sea surface backscatter $\sigma_{0,surf}$ and the pulse length t . From the annotation file, t is between $5.2 \times 10^{-5}s$ and $6.3 \times 10^{-5}s$. So R_r in Eq. (5.20) is 7.8 km at the minimum. After involving rain rate, the attenuation and emission terms can be estimated by Eq. (5.22). The emission and attenuation in Fig. 5.10(a)(b) take the absolute value in dB. The emission in the north of the rain cell can reach -15 dB and whilst the attenuation exceeds 5 dB.

An accurate $\sigma_{0,surf}$ is almost impossible to estimate because the sea surface roughness is modified by several factors like ring waves, splash products as well as downdraft instantly as raindrops impinge onto the sea surface. Thus we choose to approximate $\sigma_{0,surf}$ in line with the ambient one without rain contamination, by smoothing the measured $\sigma_{0,m}$. Many filters can be applied to smooth, e.g. median and Gaussian filters. In Fig. 5.10(c), the median filter is adopted with a window size of 40 pixels. The simulated $\sigma_{0,m}$, presented in Fig. 5.10(d), shows very similar patterns as the rain cells visible on the co-pol SAR image.

A more specific evaluation of this simulation is shown in Fig. 5.11, which compares the simulated and measured $\sigma_{0,m}$ along the transect inserted in Fig. 5.10(d). It can be seen that the enhancement of

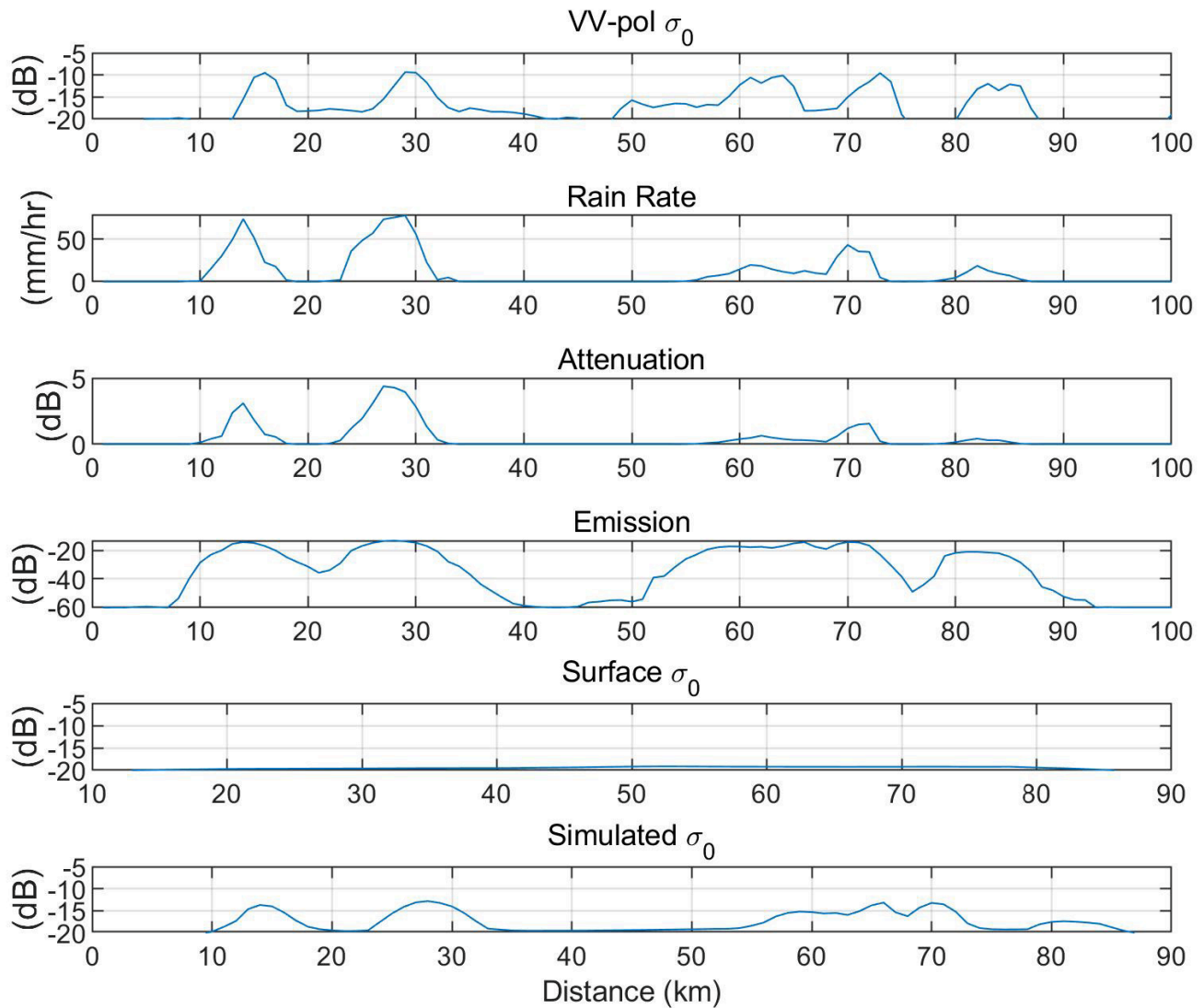


Figure 5.11: (From top to bottom) measured copol σ_0 , rain rate, attenuation and emission calculated from the model, surface σ_0 and simulated σ_0 along the transect inserted in Fig. 5.10

the VV-pol σ_0 is well colocated with the increase of base reflectivity. Based on the model, attenuation and emission are generated and thus we get the simulated $\sigma_{0,m}$. A shift on maximum location is noticed between the simulated and measured of $\sigma_{0,m}$. It is reasonable due to the acquisition time difference between NEXRAD and S-1 data. Compared to the smoothed $\sigma_{0,surf}$, the simulated values show an improved agreement with the observation (Fig, 5.12). Even though there is an offset of about 2-4 dB when σ_0 larger than -15 dB, it still explains why the very bright signatures in the SAR images result from the emission by hydrometeors within the rain cells.

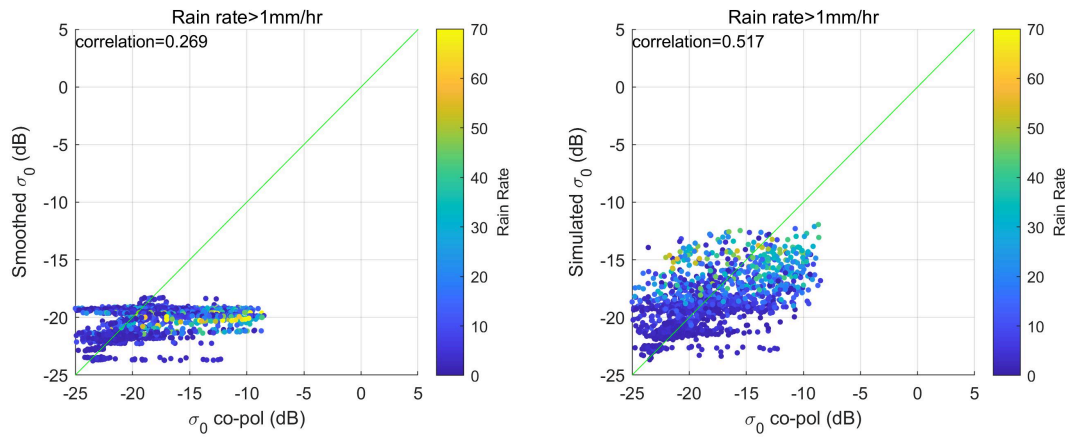


Figure 5.12: Scatterplot of measured and simulated $\sigma_{0,m}$ for rain rate (a) less than and (b) larger than 1mm/h. The correlation coefficient for each plot are included.

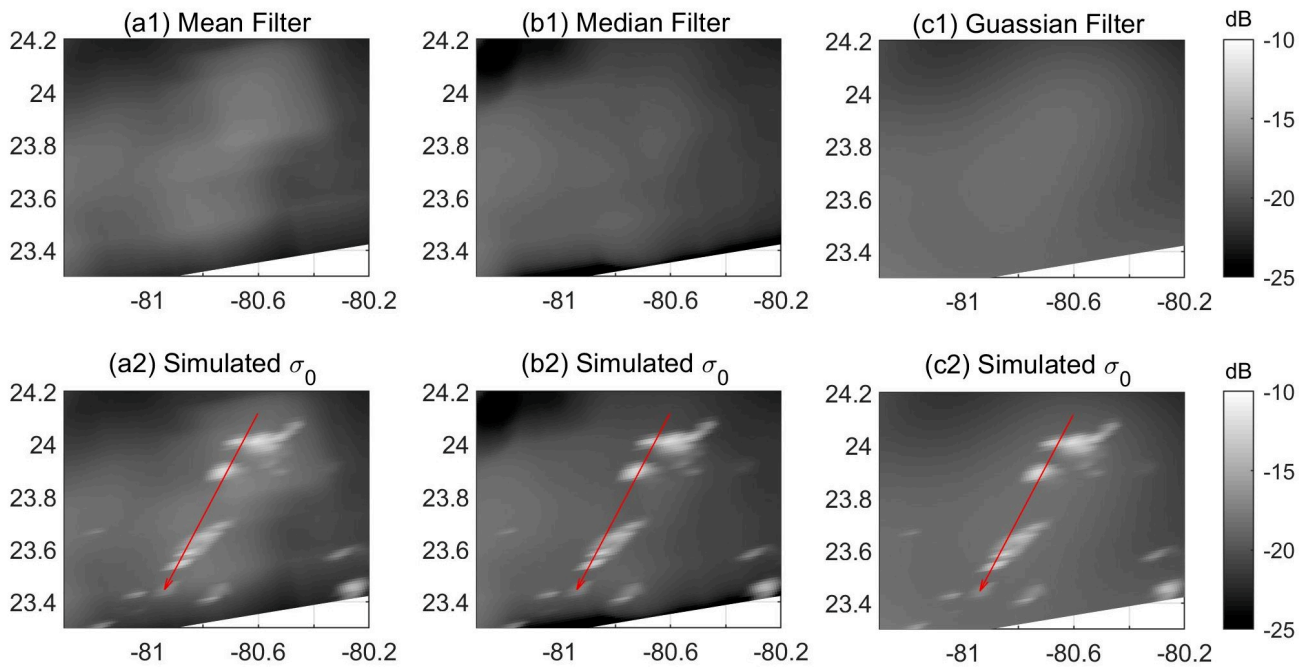


Figure 5.13: Upper panels: sea surface backscatter smoothed by mean(a1), median(b1) and Gaussian (c1) filters. Lower panels: corresponding simulated $\sigma_{0,m}$.

As indicated before, rain impinges on sea surface, generating ring waves, splash products and enhances the turbulence beneath the surface. It is hard to simulate the sea surface backscatter, given the too complex factors involved. Also we focus on the atmosphere transmission in this study and thus simply hypothesize that the sea surface roughness in rain area is similar to that without rain. To this end, many

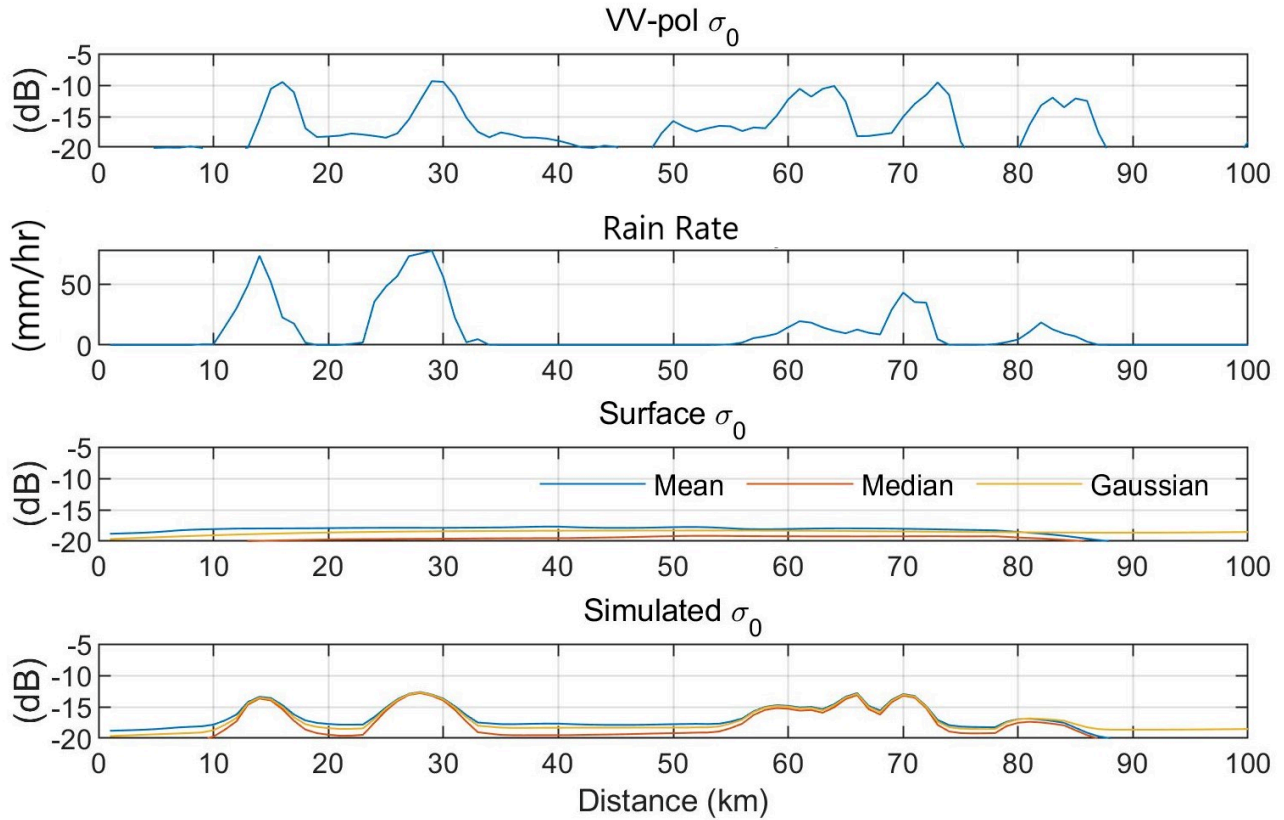


Figure 5.14: (From top to bottom) VV-pol measured $\sigma_{0,m}$, rain rate, smoothed $\sigma_{0,surf}$ and simulated $\sigma_{0,m}$ along the transect inserted in Fig. 5.13.

filters can be adapted to remove the rain contamination, i.e., median, mean and Gaussian filters.

Fig. 5.13 (a1)(b1) shows the sea surface backscatter generated by mean and median filters individually at a neighbour size of 40 pixels. Fig. 5.13(c1) applies the Gaussian filter with the neighbour size of 20 pixels. The lower panel presents the simulated $\sigma_{0,m}$ corresponding to these filters. Besides, the simulation based on the three filters is compared along a transect. Apparently, the simulation all shows the similar bright patches to observation no matter the filters. But sea surface roughness produced by mean filter is slightly higher than the other so that the simulated $\sigma_{0,m}$ is higher as rain rate is not high. However, they produce almost the same value corresponding to the peak in the rain rate. Additionally, we can see that the very dark area in the SAR images outside the rain cells are due to very low winds. This area is better simulated when applying the mean and median filters but not for Gaussian filter. It suggests that for the quite variable sea surface, median filter is better than the other ones.

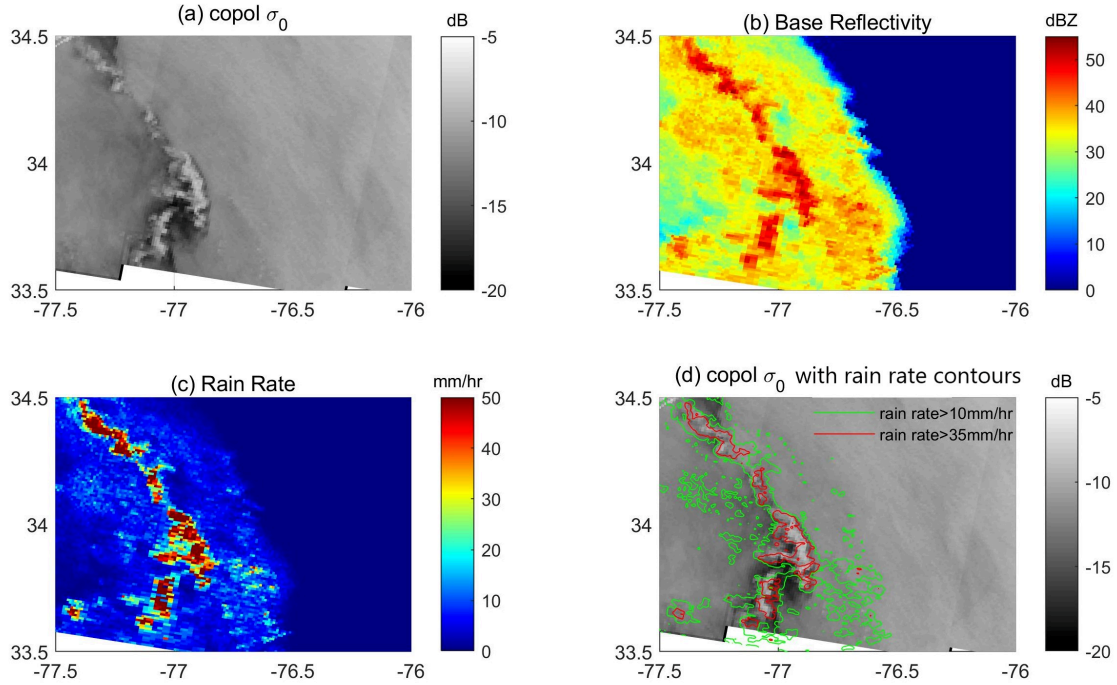


Figure 5.15: (a) Copol SAR image acquired at 11:17 UTC on the 15th Sep 2018, (b), (c) base reflectivity and rain rate from NEXRAD, (d) co-pol SAR image with the red and green rain rate contour of 10 mm/hr and 35 mm/hr.

5.3.2 Case 2

Another case presented in Fig. 5.15 shows apparent bright signatures located at incidence angles between 40° and 43° . The bright patches are well collocated with the 35 mm/hr rain rate contour, where the maximum rain rate is over 50 mm/hr. The surrounding wind speed is about 10 m/s. The attenuation and emission estimated using our model are shown in Fig. 5.16(a) and (b) respectively. The smoothed $\sigma_{0,surf}$ is produced by applying a median filter in a window size 10×10 pixels. Accordingly, the simulated $\sigma_{0,m}$ shows similar patterns of bright patches as the observation. This indicates the dominance of volume scattering at incidence angles over 40° under a rain rate of 50 mm/hr, which is also presented in Fig. 5.7. Besides, we can note that the dark zones located behind the bright patches, which is different from observation where the dark area is present both in the front of and behind bright patches. The dissimilarity is possibly because of the reduction of local winds around the rain cells, which are certainly not well represented by the smoothed $\sigma_{0,surf}$.

In order to evaluate the model more precisely, we consider a transect across the bright patches as shown in Fig. 5.17(a). The increase of $\sigma_{0,m}$ along the yellow transect is apparently caused by high rain

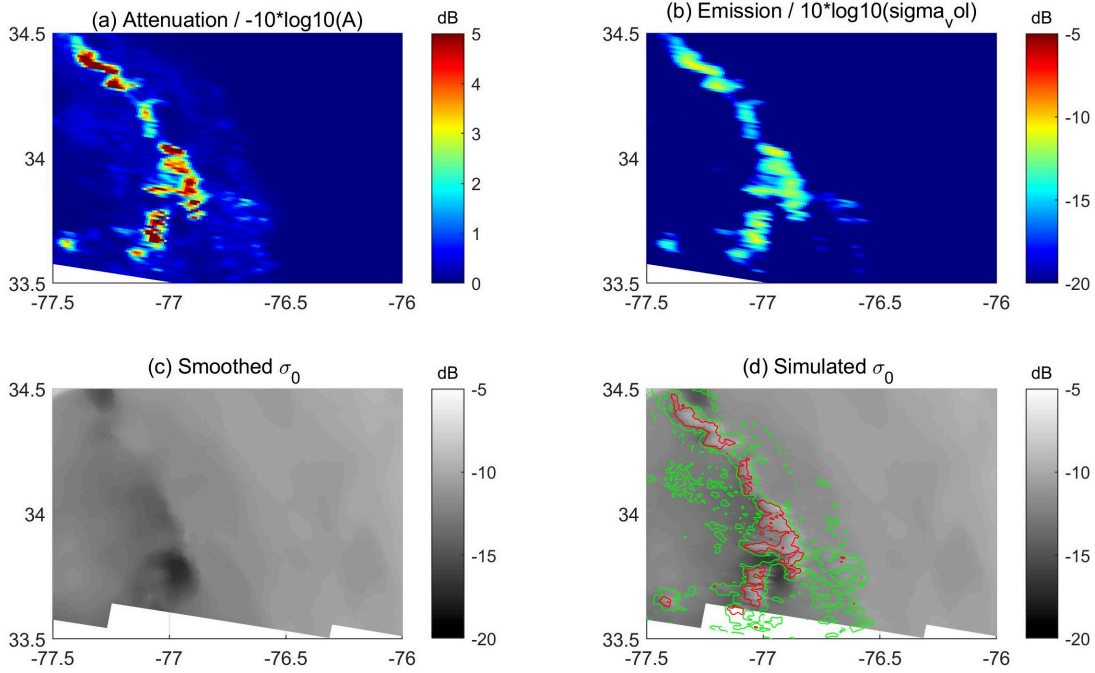


Figure 5.16: Same with Fig. 5.10 but for case 2.

rate. The difference between measured and simulated $\sigma_{0,m}$ is of the order of 1 dB. But the location of maximum simulated $\sigma_{0,m}$ is in a shift with observation. This is further illustrated by the correlation in Fig. 5.18. When zooming in the bright patches, it is clear that the simulation is a little different from observation in shape and location. That is reasonable because the contour of 35 mm/hr in rain rate does not exactly match up with observed bright patches. Thus the correlation coefficient between simulated and observed $\sigma_{0,m}$ presents positive and negative values simultaneously in Fig. 5.18(e)(f). The correlation coefficient is calculated pixel by pixel by taking the mean correlation in a 5×5 pixels window. The high positive correlation indicates the good performances of the model where the rain rate field is well colocated with the measured σ_0 . However we need to note that a shift of rain rate vs sigma0 can result in a difference of about 1 dB between the simulated and measured σ_0 .

5.3.3 Case 3

Different from regular cases, heavy rainfall are commonly observed in tropical cyclones where the rainbands are organized as spiral streamlines around the center especially at high category. Fig. 5.19 shows the cyclone Michael at category-4 at 11:50 UTC on Oct 10th 2018. Rainbands are evident in the base reflectivity and rain rate fields from NEXRAD, where the region with rain rate over 10 mm/hr has a

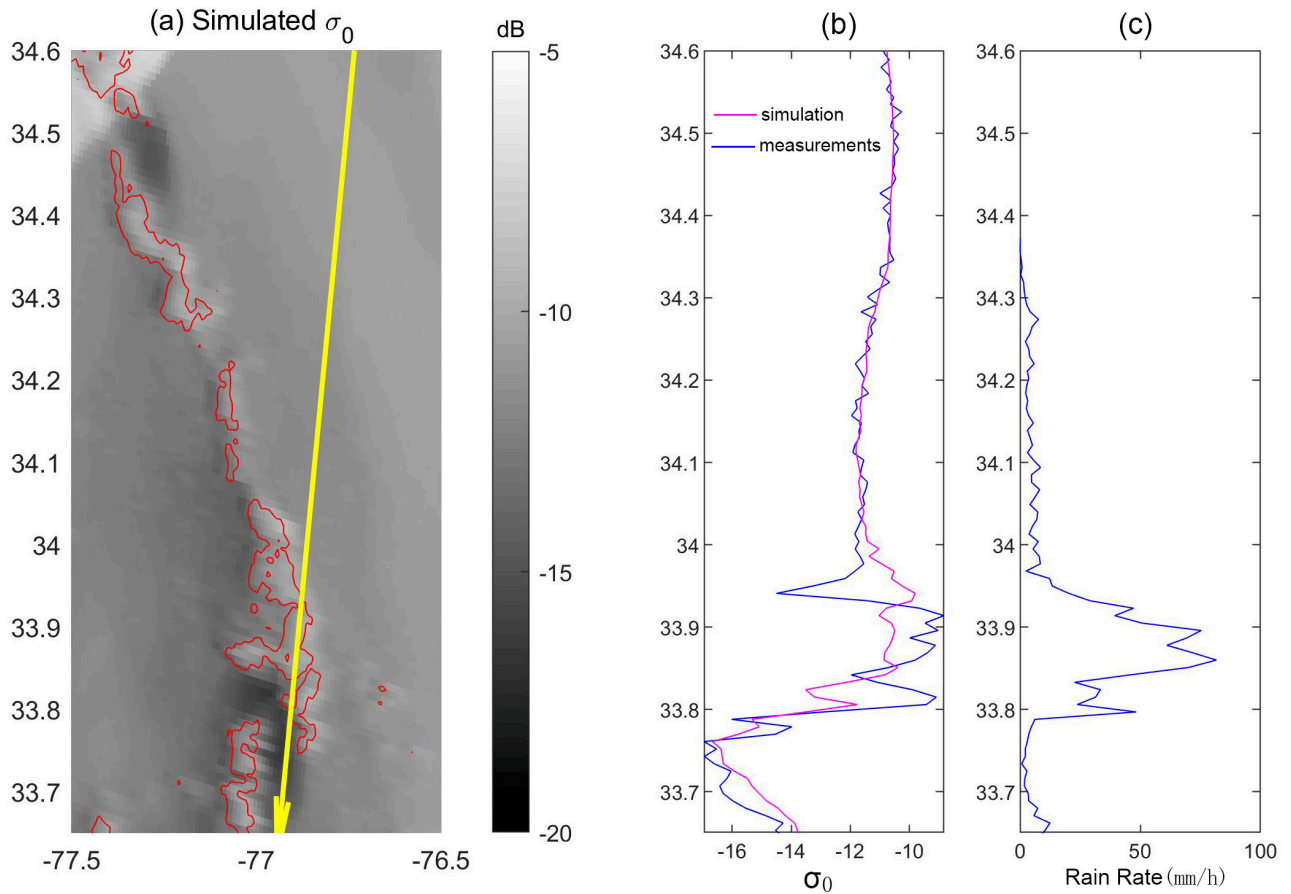


Figure 5.17: (a) Simulated $\sigma_{0,m}$. (b) Measured and simulated $\sigma_{0,m}$ along the yellow transect. (c) Rain rate along the yellow transect.

good collocation with the dark area in SAR images as can be seen in Fig. 5.19(d). Notably the rainband regions closest to the center where the rain rate is over 50 mm/hr, whereas the rainbands farther away show a rain rate larger than 20 mm/hr.

As seen in Fig. 5.20, the attenuation can be up to 5 dB in areas with rain rate of 50 mm/hr. By comparison, the emission shows the most contribution from the closest rainband to the center, up to -14 dB. The simulated $\sigma_{0,m}$ is generated a smoothed $\sigma_{0,surf}$ as the sea surface backscatter. Clearly, the simulated $\sigma_{0,m}$ displays a very similar signatures as the observation in Fig. 5.19(a), where the rainbands appear as dark stripes.

It should be considered that the rain-generated products may smooth the sea surface as a large amount of wave breaking happens at extreme wind conditions. The smoothed σ_0 referred may be larger than that in reality. Nevertheless, the simulated values show a very high correlation with the observations at different rain rates. In Fig. 5.21. the correlation is over 0.9 as rain rate over 5 mm/hr and up to 0.94

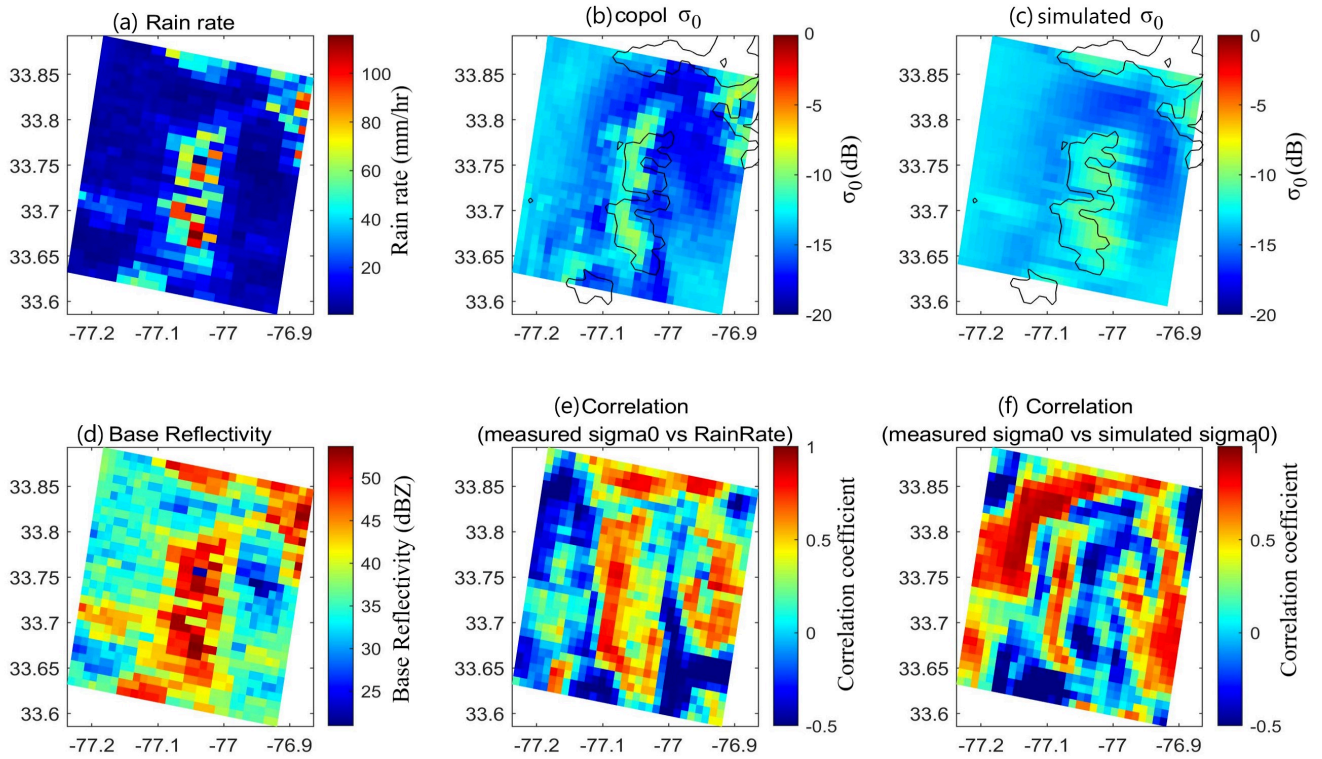


Figure 5.18: Subplots of (a) rain rate, (b) measured $\sigma_{0,m}$ and (c) simulated $\sigma_{0,m}$, (d) base reflectivity as well as (e) correlation between copol σ_0 and rain rate, (f) correlation between copol σ_0 and the simulated $\sigma_{0,m}$.

as rain rate larger than 20 mm/hr. This high correlation indicates the good performance of our model in cyclone cases. Moreover, it also suggest that the rain modulation of the sea surface roughness might be small since our model only considers the attenuation and scattering in the atmosphere. As discussed in the last section, the signal across the atmosphere gets more attenuation than emission at high rain rate and wind speed.

5.4 The impact of time shift of rain data on simulation

It should be noted that the simulation accuracy is strongly dependent on the temporal resolution of collocated precipitation products. Especially when the surrounding wind speed is relatively high, the rainbands can move significantly even in a couple of minutes. Thus the selection of rain products at the appropriate time is crucial to the simulation. In this study, the NEXRAD products used are provided very frequently, which is beneficial to check the feasibility of the model simulation. However, the shift of rain

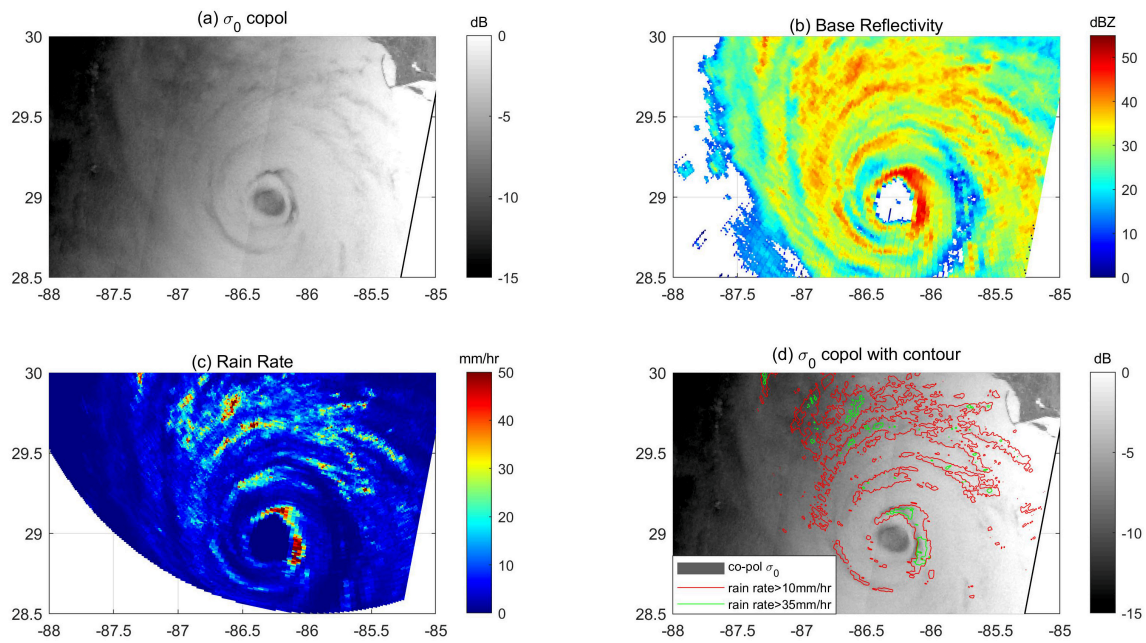


Figure 5.19: (a) Copol SAR image of tropical cyclone Michael obtained by Sentinel-1 at 11:50 UTC on 10 Oct 2018. (b) and (c) base reflectivity and rain rate at 11:50 UTC provided by NEXRAD. (d) co-pol σ_0 overlaid with rain rate contours.

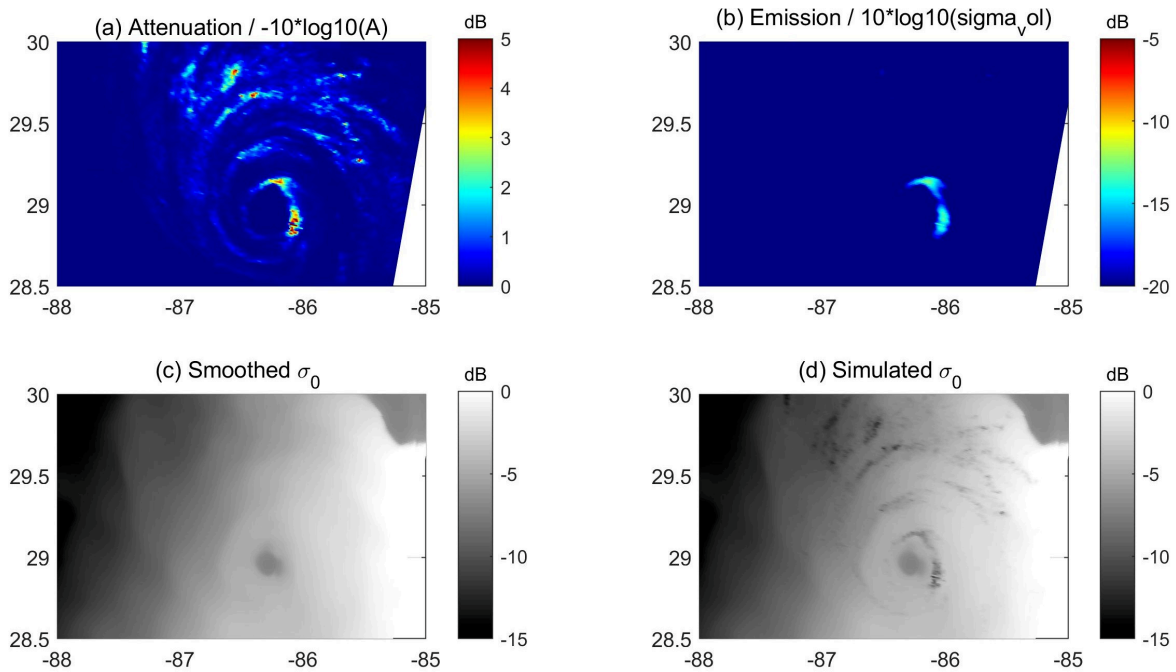


Figure 5.20: Same as Fig. 5.10 for Case 3.

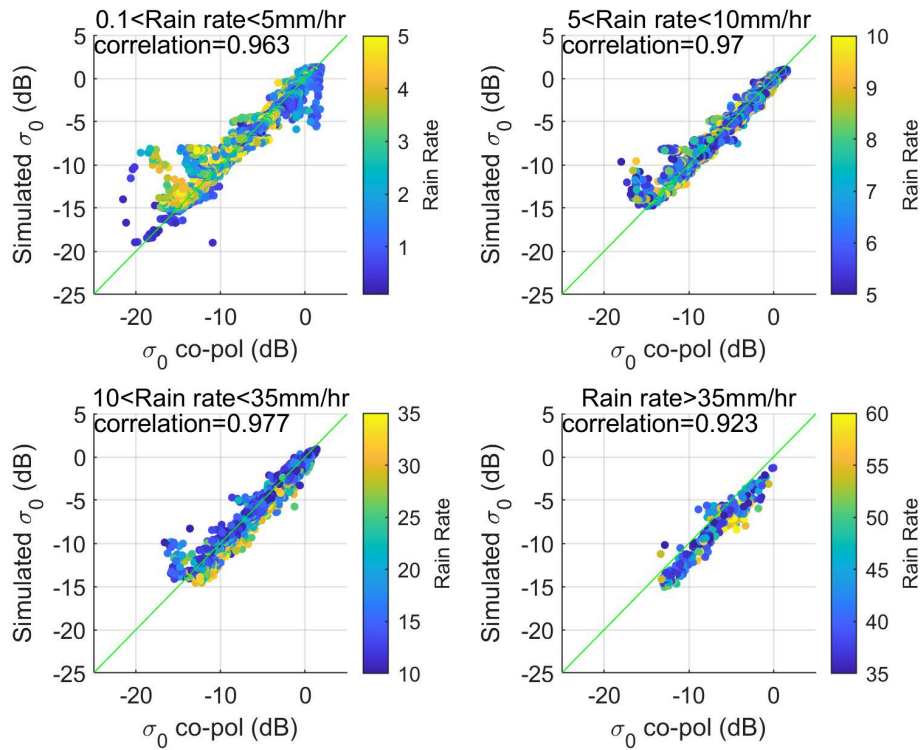


Figure 5.21: Scatterplot of copol σ_0 and $\sigma_{0,m}$ for different rain rate ranges.

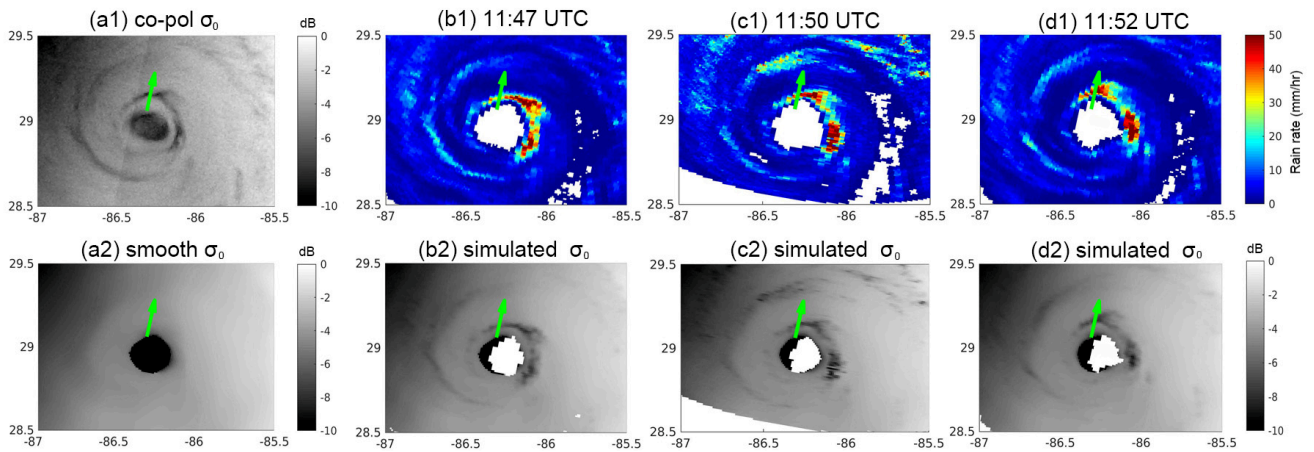


Figure 5.22: (a1) Detail of Copol SAR images of case 3 and NEXRAD rain rates at 11:47 (b1), 11:50 (c1) and 11:52 UTC (d1). (b2),(c2),(d2) simulated $\sigma_{0,m}$ using the (b1) (c1) and (d1) rain rate fields. The green line represents the transect used for fine comparison.

cells in the couple of minutes can still be noticeable, thereby inducing an offset between the simulation and measurements. The consecutive NEXRAD rain rate fields at 11:47 UTC, 11:50 UTC and 11:52 UTC

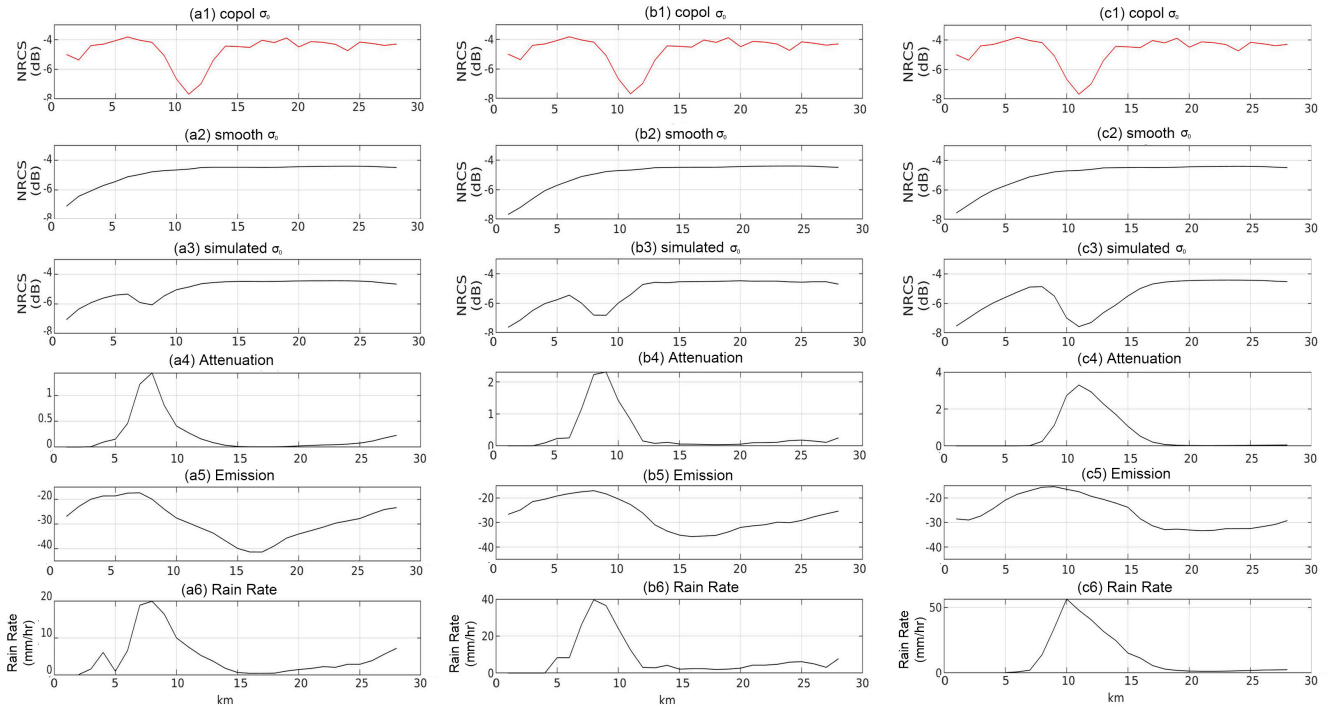


Figure 5.23: Copol σ_0 , smoothed $\sigma_{0,surf}$, simulated $\sigma_{0,m}$, attenuation, emission and rain rate along the green transect in Fig. 5.23. The three panels are from the simulations using the NEXRAD rain rate fields at 11:47 UTC, 11:50 UTC and 11:52 UTC respectively.

respectively presented in Fig. 5.22 show that the rainbands closest to the TC center experienced significant rotations in 5 min. SAR acquisition time is from 11:50 UTC to 11:51 UTC. One transect is inserted across the rainband to better check the agreement among the results during the rainbands shifting.

Fig. 5.23 shows the co-pol σ_0 , smoothed surface backscatter $\sigma_{0,surf}$ and simulated $\sigma_{0,m}$ along the green transect from the simulations involving the three NEXRAD observation times. Besides, the attenuation and emission terms as well as the rain rate are also shown at the same time. It can be seen that the maximum rain rate increases over time and its location shows shift as well. Also, the minimum of copol σ_0 locates between the simulation at 11:50 UTC and 11:52 UTC but closer to the latter. The comparison between simulation at different times suggests that it is best for close rainband to take the more approaching rain rate product. Given a large time difference between SAR and weather radar time, it can make a large difference to the simulation accuracy.

5.5 Summary

This chapter propose a atmospheric model which mainly focuses on the backscattering and attenuation of raindrops on electromagnetic waves. It is based on the transfer equation of electromagnetic wave through the atmosphere, with the capability of simulating radar backscatter under different rain rate. The radar backscatter simulated by this model has a good agreement with observation, and give a further certification that the bright patches of precipitation in SAR images mainly results from the volume scattering raindrops. The validation on this model greatly benefits from the short time gap between SAR data and weather radar measurements, since rain cells or rainbands can have a significant shift within minutes, The simulation on tropical rain cells and TCs shows its potential to be integrated in more complicated models in the further.

Precipitation detection on SAR images

Contents

6.1	Dual polarization filter for rain detection in SAR images	84
6.1.1	Local Gradient Method	85
6.1.2	Optimization of dual-pol resolutions	86
6.1.3	Validation	89
6.2	Rainband Filter in tropical cyclones	93
6.2.1	NRCS Difference map	94
6.2.2	Non-local mean filter	98
6.2.3	ROC curve	99
6.2.4	Validation	101
6.3	Summary	105

The complicated rain signatures is helpful to reveal the rain-contaminated region in the ocean but its appearance is an obstacle to retrieve wind information accurately from SAR images. The analysis of SAR images in Chapter4 and the model of Chapter 5 shows that rain, especially heavy ones, can have a significant impact on the measured radar backscatter. For heavy rain cells, the emission term can exceed the surface backscatter precluding the retrieval of surface roughness and wind speed. It is thus necessary for a better interpretation of SAR image and for a pertinent wind retrieval to precisely detect the rain affected pixel and if possible to estimate the degree of contamination of the σ_0 .

6.1 Dual polarization filter for rain detection in SAR images

The local gradient method proposed by Koch (2004) has the capability of detecting heterogeneity across SAR images such as land, front, rain, oil spill, ships, even under nonuniform illumination. However, this method does not work effectively as applied on the single-polarization SAR image. According to the investigation in above section, rain signatures in VH can be more obvious than in VV, which provides a new insight that including the cross-polarization information can be helpful for rain detection. Therefore,

a dual-pol filter is proposed for rain detection by combining the VV- and VH-polarization filter produced by local gradient method. This section introduces the local gradient method, the new dual-pol filter and its validation successively.

6.1.1 Local Gradient Method

This method is based on the Sobel gradient operator, widely used in image processing to detect objects contours. To detect the rain signatures, small-scale ocean features and speckle noise in SAR images need to be first filtered out. Indeed, speckle noise is inherent to SAR images because of the coherent processing of radar signals. Although Ground detected SAR image generally includes multilooking processing decreasing this speckle noise, the Equivalent Number of Look for Sentinel-1 IW GRDH is 4.4. This indicates the need for additional speckle filtering. In addition, SAR images acquired over sea surface may include small-scale features imaged at metric or decametric scale (e.g. waves, ...) which are out of the scope of this study. Three resolutions (200 m, 400 m and 800 m) have been hence chosen in this study to compute NRCS images in co- and cross-polarization channels to be used hereafter. In Koch (2004), four parameters (denoted P_i) are actually computed:

- P_1 is the ratio between the standard deviation and the average computed for each pixel using a sliding bounding box of the smoothed/reduced image. It is computed using a convolutive averaging bounding box over the amplitude (square root of NRCS) and its second moment. This parameter is particularly useful to decipher open water surface from other extended areas (land, tidal zones, sea ice..)
- P_2 is built on a Laplace pyramid filter with the difference between images at adjacent levels in the pyramid. It is based on the squared ratio of the high-pass filtered image and its local average. It "[...] detects the interior of narrow image features, as slicks, internal waves, or fronts." Koch (2004)
- P_3 is the ratio of the magnitude of the squared local Sobel-based gradient and its local average. A Sobel operator is basically involved to do spatial gradient measurement on 2-dimensional images. It is generally adapted to detect edges and point targets.
- P_4 is the ratio between the reduced/smoothed version of the squared local gradient and its absolute squared gradient: it can be considered as a measure of directional coherence. It should detect the edges such as "slicks, internal waves, or fronts." Koch (2004)

These 4 P_i parameters are studied via a histogram analysis to optimize the separability between wind and non-wind related features (here generally mentioned as heterogeneous areas) in Koch (2004). They are linearly scaled between 0 and 1, leading to the parameters f_i . In this study, an attempt to revisit the scaling factors has been carried out. Nonetheless, as proposed by Koch (2004) the scaling factors were found adequate even though they were originally calculated from ERS-1/-2 images. Also, they perform equally well for co- and cross-polarization channels. The squared average of the linearly scaled f_i parameters is then computed, leading to a single F parameter ranging from 0 and 1.

$$F = \sqrt{\frac{1}{4} \sum_{i=1}^4 f_i^2} \quad (6.1)$$

6.1.2 Optimization of dual-pol resolutions

In the original study, a 0.6 threshold was applied on F to binarize the heterogeneity filter. This mask based on the a single-pol image performs differently at the different resolutions. Thus in this study, we apply the local gradient at 3 different resolutions r ($r = \{200, 400, 800\}$) and for the two polarization channels p ($p = \{VV, VH\}$) respectively, here after noted as ${}^p_r F$.

Several quantitative indices/criteria can be employed to assess the goodness-of-fit between the rainy area provided by the reference rain mask and the ${}^p_r F$ parameter. Applying a specific threshold ${}^p_r F > {}^p_r \nu$ with ${}^p_r \nu = [0, 1[$ would enable a direct comparison between two binary masks with Dice coefficient or Intersection over Union (IoU) indices. An analysis based on Receiver Operating Characteristic (ROC) curve is outlined in Fig. 6.1 with $r = 400$ and $p = VV$. The ROC is based on the analysis of True Positive Rate (TPR) and False Positive Rate (FPR) for varying ${}^p_r \nu = [0, 1[$. We recall TPR is the proportion of S-1 heterogeneous observations that are correctly predicted out of all heterogeneous observations (based on a given rain flag reference from NEXRAD). Similarly, FPR is the proportion of S-1 observations that are incorrectly predicted as heterogeneous out of all homogeneous observations.

$$\begin{aligned} \text{TPR}({}^p_r \nu) &= \frac{|{}^p_r F > {}^p_r \nu| \cap |Z > Z_0|}{|Z > Z_0|} \\ \text{FPR}({}^p_r \nu) &= \frac{|{}^p_r F > {}^p_r \nu| - |{}^p_r F > {}^p_r \nu| \cap |Z > Z_0|}{|Z > Z_0|} \end{aligned}$$

where $|\cdot|$ indicates the cardinality of a given set, here considered as the number of pixels of the set in the database.

Fig. 6.1 shows that Koch filter improves with rain rate. It is remarkable that TPR reaches 90% with low FPR of 20% when considering $Z_0 = 45$ dBZ region (eq. 24 mm/hr). In the contrary, for the same value of TPR, FPR increases up to 70% when rain rate decreases below 30 dBZ (eq. 1 mm/hr) are considered. It is expected as co-polarized SAR images show bright patches for base reflectivity exceeding 40 dBZ (see previous section) whereas the backscatter is dominated by sea surface winds especially at light rain.

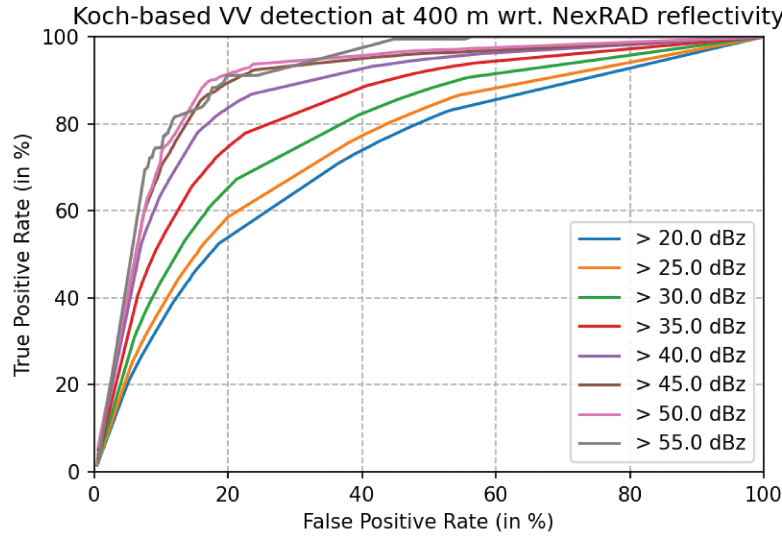


Figure 6.1: Illustration of a ROC applied on VV at 400 meters resolution for a set of minimum reflectivity values

To consider the best trade-off between FPR and TPR (and hence the optimal $\frac{p}{r}\nu^{opt}$), the minimum distance from the ROC curve to the top left corner is considered (see by Tilbury et al. (2000) - an alternative would be the maximum of the Youden index (J) (Youden, 1950)).

$$\frac{p}{r}\nu^{opt} = \frac{p}{r}\nu\sqrt{(1 - \text{TPR})^2\text{FPR}^2} \quad (6.2)$$

For $r = 400$ and $p = \text{VV}$, $\frac{\text{VV}}{400}\nu^{opt}$ is found to be equal to about 0.72 independently on Z_0 value. Beyond this first analysis, it is also of interest to investigate the potential to combine different resolutions and/or polarization channels. To this end, the same assessment based on ROC curves is extended where the final heterogeneity mask is the intersection of each individual heterogeneity mask. All the possible pairs of processing ($r = \{200, 400, 800\}$ and $p = \{\text{VV}, \text{VH}\}$) are combined with a joint optimization of the two individual thresholds $\frac{p_1}{r_1}\nu^{opt}$ and $\frac{p_2}{r_2}\nu^{opt}$.

In Fig. 6.2, the minimum distance to the Top Left corner is retained as criteria (similar results are obtained with Youden Index – not shown here) and estimated for 5 ranges of rain rates (Z from 20 to 55 dBZ). The following comments can be outlined. As obtained, the filters based on co-polarized NRCS are significantly better than the ones based on cross-polarized channel. One explanation could be the low signal-to-noise ratio in cross-polarization. Indeed, this can prevent to detect the texture modification in some cases. A striking example of the noise impact in the case of two storm cells observed by Sentinel-1A C-band SAR is presented on Figure 5 and 7 in Alpers et al. (2016). As observed, several storm cell related features are not present in cross-polarization but in co-polarization. ${}_{400}^{VV}F$ filter provides the best agreement when only one filter is chosen. Combining dual-polarized information improves the detection performances. Among all the possibilities, the joint $({}_{400}^{VV}F; {}_{800}^{VH}F)$ filter exhibits the best agreement. The optimized thresholds are then ${}_{400}^{VV}\nu^{opt} = 0.78$ and ${}_{800}^{VH}\nu^{opt} = 0.71$. We refer to the filter obtained by combining both co- and cross- polarization channels as dual-pol filter hereafter.

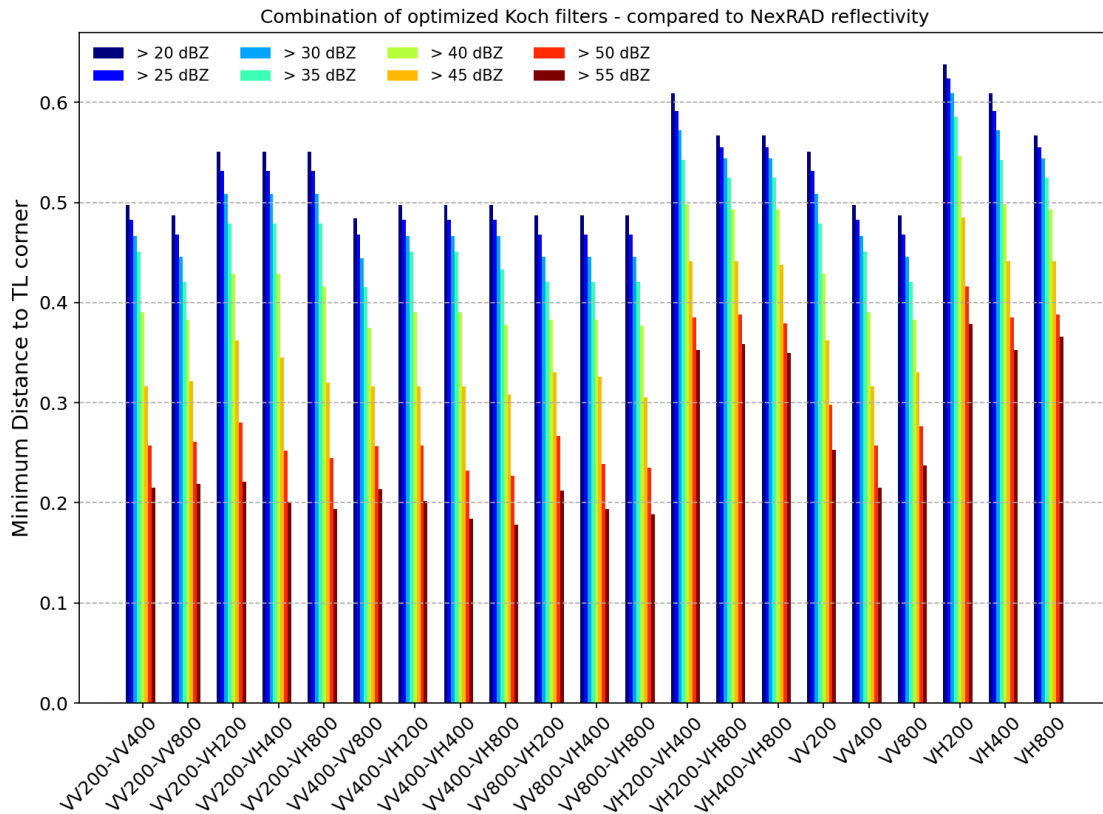


Figure 6.2: Performance of Koch filters at different resolution/polarization with dual-pol filters on the left, and single-pol filter on the right.

6.1.3 Validation

The filter has then been applied to all the available Sentinel-1 data collocated with JMA rain measurements to assess the rain detection performance with respect to the choice of polarization channels, incidence angle and wind speed. Wind speed is used here as a proxy of the local sea state. Three different polarization configurations are considered : the joint (${}_{400}^{VV}F; {}_{800}^{VH}F$) filter and one for each polarization channel the ${}_{400}^{VV}F$ and ${}_{800}^{VH}F$ filters.

Figure 6.3 presents the rain detection percentage as a function of rain rate for different wind speed regimes with respect to the polarization channels considered for the detection. As observed, no matter the polarization configuration, rain is more likely detected for cases corresponding to high rain rates. For all rain rate regimes, the background sea state is found to have an impact on the detection. At a given rain rate, the higher the wind speed values, the less we can detect rain in the signal. In particular, for rain rate larger than 10 mm/hr, the detection rate increases significantly when wind speed decreases. Also, the benefit of merging the two polarization channels for the detection is clear as the percentage of rain detected pixels increase from about 20 – 50 % to up to 70 % when both co- and cross- polarization channels are combined.

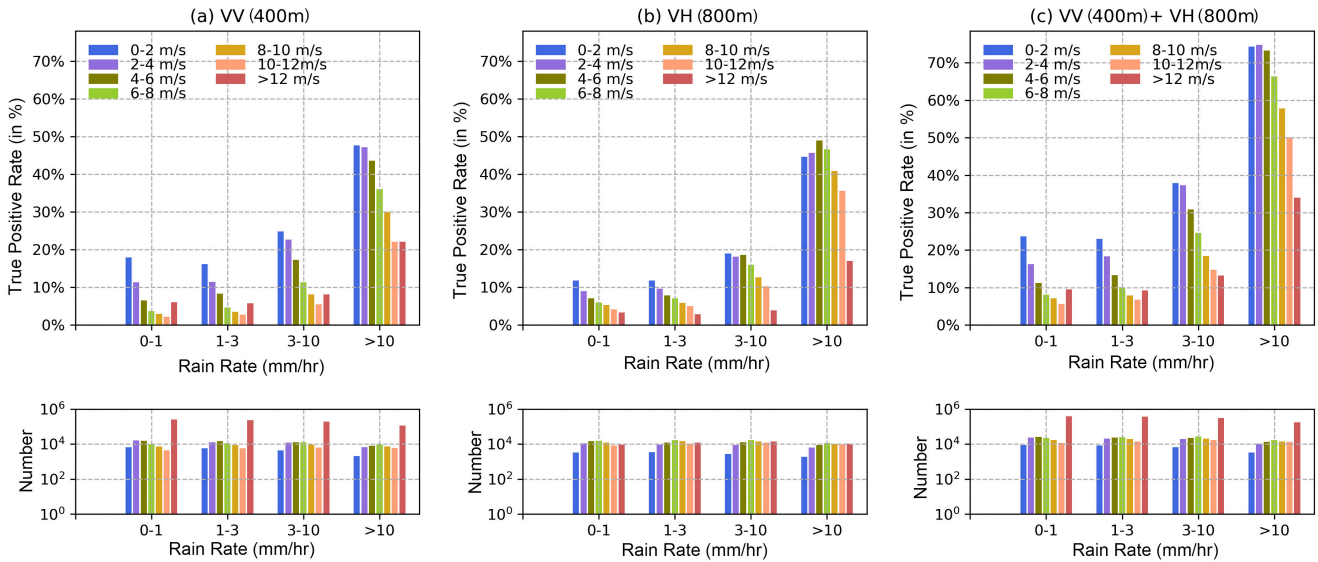


Figure 6.3: True positive rate of rain detection percentage as a function of rain rate for different wind speed regimes with respect to the polarization channels considered. (a) VV-generated filter, (b) VH-generated filter and (c) dual-pol filter.

The detection rate is also analyzed with respect to incidence angle for different rain rates on Figure 6.4.

As observed the rain detection increases with incidence angle, no matter the heterogeneity filter considered. These results confirm that C-band SAR measurements are more sensitive to rain when incidence angles increase as documented in section 4.

In general, the higher detection rate of rain obtained when the two polarization are combined show their complementary and to some extent suggest that their sensitivity may be due to different scattering mechanisms.

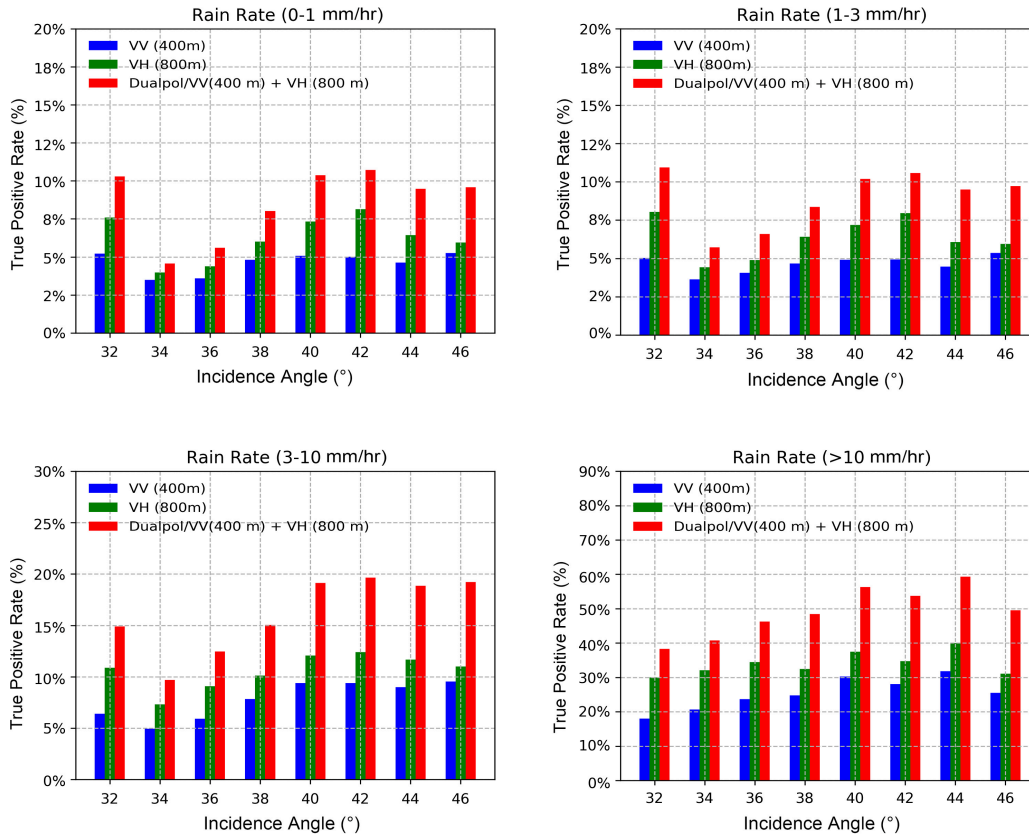


Figure 6.4: True positive rate of rain detection percentage as function of incidence angle for the polarization channels considered with respect to different rain rates. The first bin at 32 degree is affected by artefacts linked to recurrent invalid data at near range.

The application of the dual-pol filter on the three cases in Section 4.1.1 is shown in Fig. 6.5, where the filters generated with VV (400m), VH (800m) and dual-polarizations channels are included. Here the blue and purple contours indicate the base reflectivity of 20 dBZ and 40 dBZ as given by the NEXRAD weather radar. In these cases, the dual-pol filter clearly shows a better agreement with NEXRAD data, in particular as reflectivity is larger than 40 dBZ. As shown for the first case, it seems that the VH filter is more sensitive to noise than the VV and dual-pol filters as evidenced by the subswath jump and

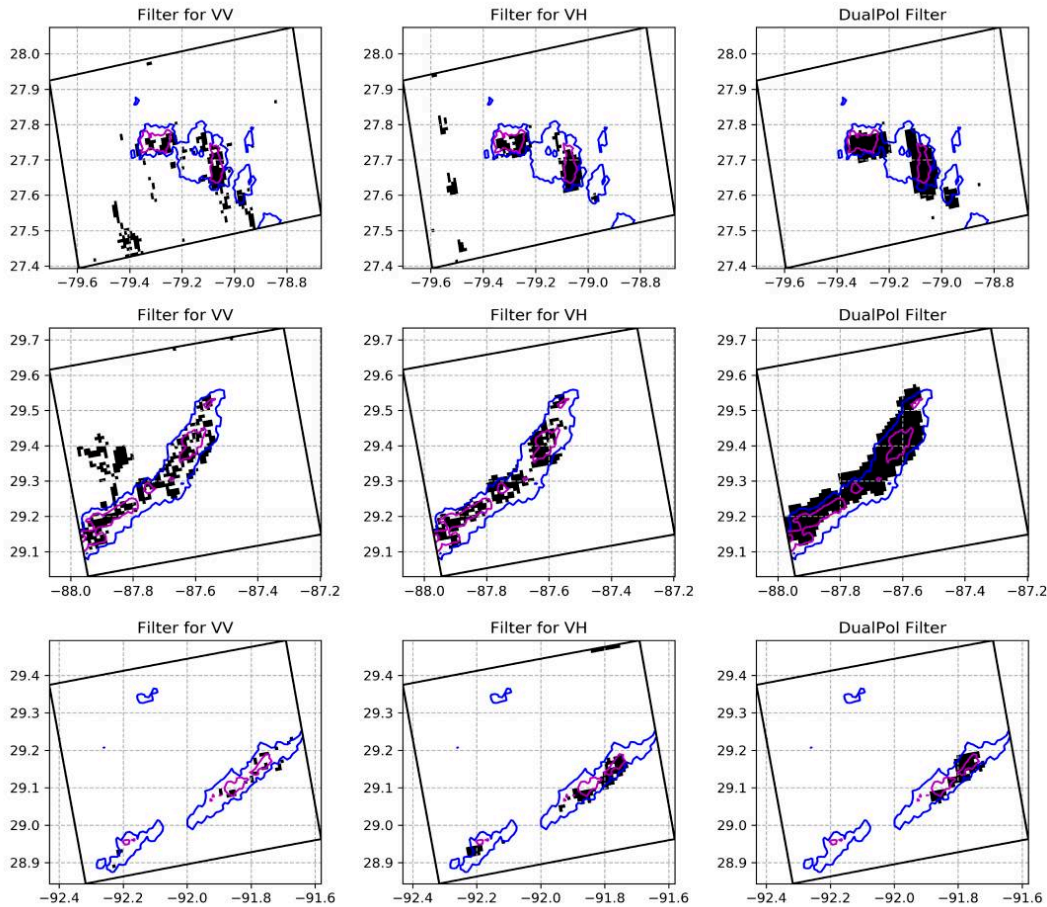


Figure 6.5: The first and second columns show the Koch filters generated with VV (400 m) and VH (800 m) channels respectively for the three cases in Figs. 4.1 ~ 4.3. The last column shows the proposed dual-pol filters correspondingly. The blue and purple contours mark the base reflectivity of 20 dBZ and 40 dBZ respectively.

the modulation in the azimuthal direction on the left hand side of the swath at low incidence angle. Furthermore, VV filters seem to capture signatures that do not correspond to high base reflectivity values such as the wind gust front on the first case and the area with low backscattered signal observed on the second case. The third case is more complex. VH and VV signatures have opposite signs and only the VH filter (positive rain signature) is able to capture the rain signature in the south area. The areas with the strongest rain rate are captured by all three filters. These three cases illustrate the capabilities of the dual polarization for filtering rain signatures.

As observed on Figure 6.3, our detection rate is not 100% , especially for low to medium rain rates and high wind speed regimes. Indeed, our approach can only detect area in SAR image where the

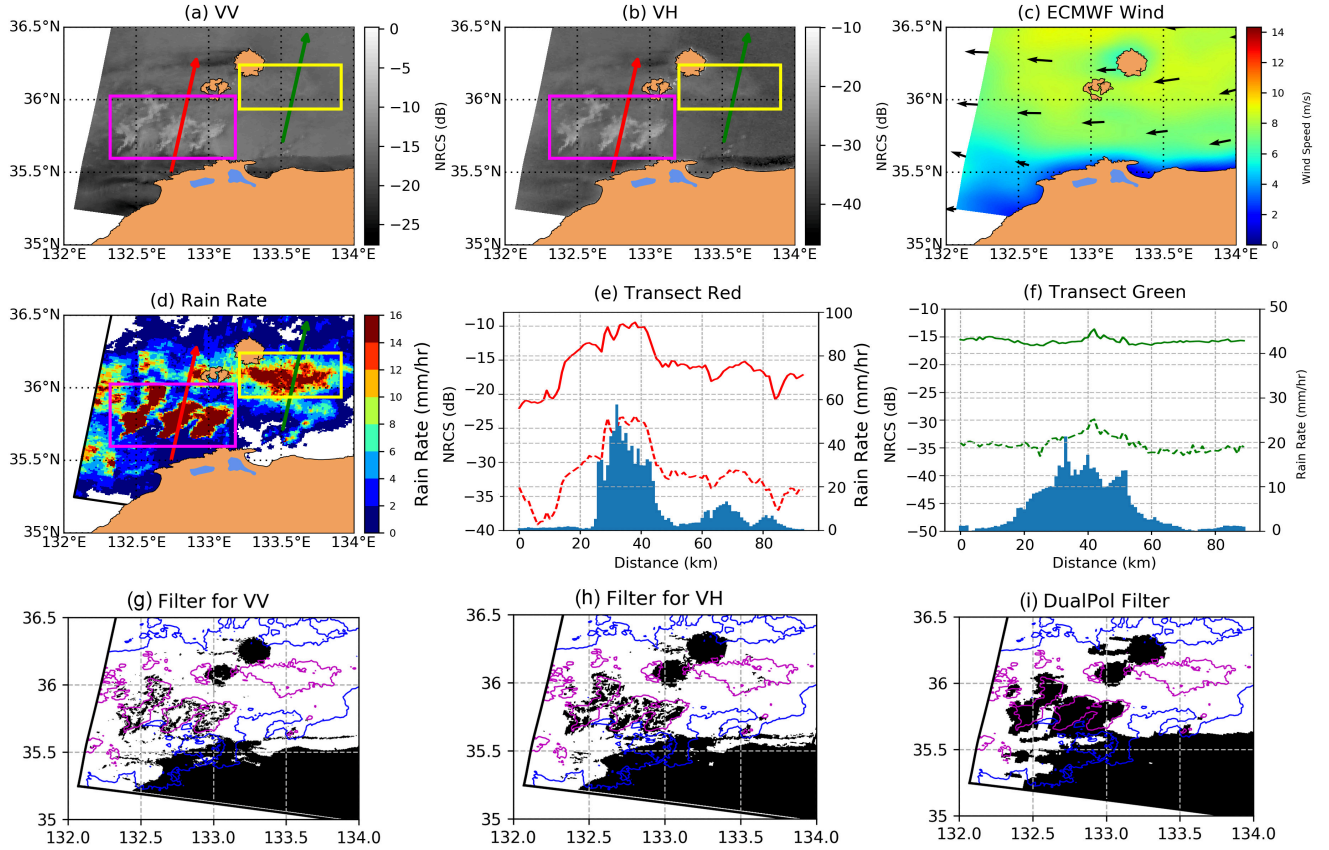


Figure 6.6: (a) and (b) Sentinel-1 VV and VH SAR images at 21: 08 UTC on 3 Sep 2019. (c) Wind speed and direction from ECMWF. (d) Rain rate provided by JMA. (e) (f) Transect of VV and VH NRCS and rain rate along the red and green lines of (a) and (b). (g) (h) (i) Masks generated only by single-pol VV/VH and by our proposed algorithm. The two rectangles overlaid on (a),(b),(d) outline the 2 areas with heavy rain.

backscattered signal is significantly affected by rain. Figure 6.6 illustrates such a case. Here the wind as given by ECMWF is about 9 m/s with two main areas exhibiting rain rates larger than 10 mm/hr, but occurring at different incidence angle ranges in the image. The first one in the south-west has a stronger rain rate ($RR \in [14 - 16]$ mm/hr) and corresponds to larger incidence angles ($\theta \in [41, 46]$ degrees) than the second one in the north-east ($RR \in [10 - 14]$ mm/hr; $\theta \in [38, 41]$ degrees). As observed, for the second area, the rain impact on the roughness is much less (see transects). Consequently, it is not captured by our detection algorithm. In this case, such a difference between the two signatures probably comes from the difference of incidence angle and rain rates, more favorable (higher incidence angle and stronger rain rate) in the south-west.

This case also illustrates the fact that our method does not only detect areas impacted by rain but also any area with non-wind related features that produce in-homogeneity in the SAR image. Indeed, as observed areas with low backscattered signal associated to low wind speed values such as in the lee of the island (middle) or close to the coast (south part of the area) are detected by our filter. This was already mentioned in the previous study by Koch (2004) as the detection is only based on edges or textural features analysis. As implemented here, the addition of a second channel of polarization as well as the optimisation of the detection parameters based on reflectivity measurements from high resolution radar is not enough for deciphering between various non-wind related phenomena.

Overall, the dual-pol methodology shows the better performance on the detection where the radar backscatter are affected by the precipitation, compared to the koch filter at single-pol. The detection percentage is strongly associated with the rain rate and the radar incidence angle. The heavier the precipitation is, the easier the rain-contaminated area is detected.

6.2 Rainband Filter in tropical cyclones

Rainbands in tropical cyclones are organized as spiral stripes around a rotation center. Through the case studies in Chapter 4, rainbands have different performance in SAR images, dependent on rain rate and wind speed. For eyewall, as rain rate is lower than 35 dBZ (5.4 mm/h), almost no apparent signatures are observed. In comparison, areas with rain rate exceeds 40 dBZ (12mm/h) are often shown as dark regions around the center for all the categories. For outer rainbands, the rain signatures are similar to observation of thunderstorms, shown as obvious bright patches surrounded by dark ones, which might differ at co- and cross-polarizations.

Up to now, people can get wind information from SAR images by taking advantage of empirical GMFs, i.e., CMOD4, CMOD5 for co-polarization observation and H13E, H14E for cross-polarization observation of cyclone cases. These GMFs have good applications with high accuracy of wind retrieval but only in very light rain area. Because the radar backscatter in rainbands is not only a function of wind speed but also modulated by the rain-induced structures, atmospheric volume scattering and attenuation, as well as gust fronts. In areas heavily contaminated by rainfall (obvious rainband signatures), the inversion errors can reach 50%. Generally, to improve the inversion accuracy, it is necessary to flag rainband signatures for cyclone cases. In addition, the rainband flag as a good indicator of cyclone structures could potentially demonstrate the some interior state of cyclone motion and help improve model on forecast in the future.

However, the dual-pol filter proposed above is not effective in detecting the rainbands. Fig. 6.7 shows

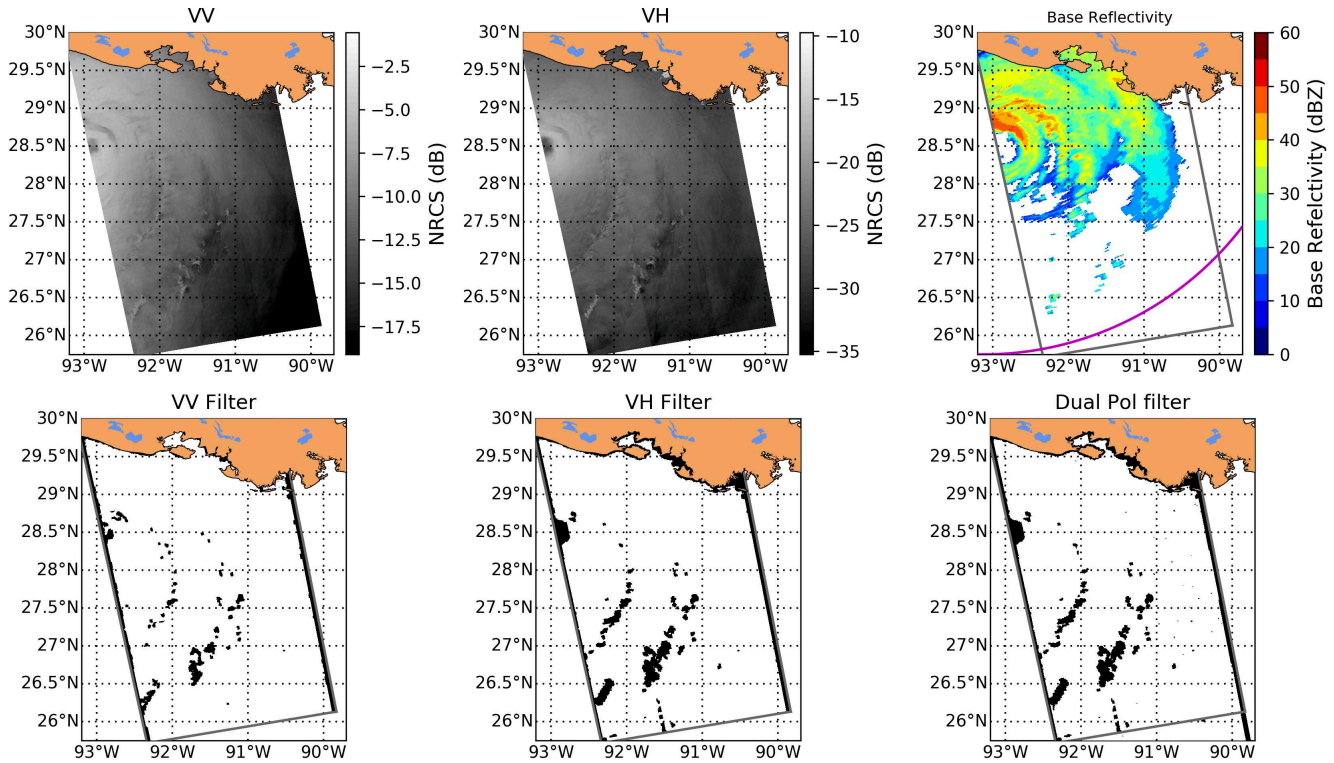


Figure 6.7: Tropical cyclone Laura captured by Sentinel-1 at 00:10 UTC at 27 Aug 2020.(a)(b) VV-pol and VH-pol images.(c) Base Reflectivity provided by NEXRAD at the same time. (d)(e) (f) VV, VH and dual (VV and VH) pol filter)

an example of TC Laura captured by sentinel-1 at co- and cross-polarizations, along with base reflectivity from NEXRAD and masks produced by koch filter and dual-pol filter. It is well known that the local gradient methods proposed by Koch (2004) aimed for masking all inhomogeneous features in SAR images, which of course has the potential of rain signatures detection. However, the rainband signatures around the center, colocated with the high base reflectivity more than 40 dBZ is not well detected in each polarization. And our proposed dual-pol filter does not successfully capture these variation around the center. Thus, a new approach needs to be proposed tailored for rain signature detection in cyclone cases.

6.2.1 NRCS Difference map

No matter the inner rainbands or outer rainbands, the radar backscatter shows the strong variation under precipitation in 1-km resolution SAR images. In terms of signal decomposition, the strong variant backscatter under precipitation is composed of signals at different frequencies. More high-frequency signals can be possibly extracted in heavy precipitation region. However, in low-resolution images at 20km or

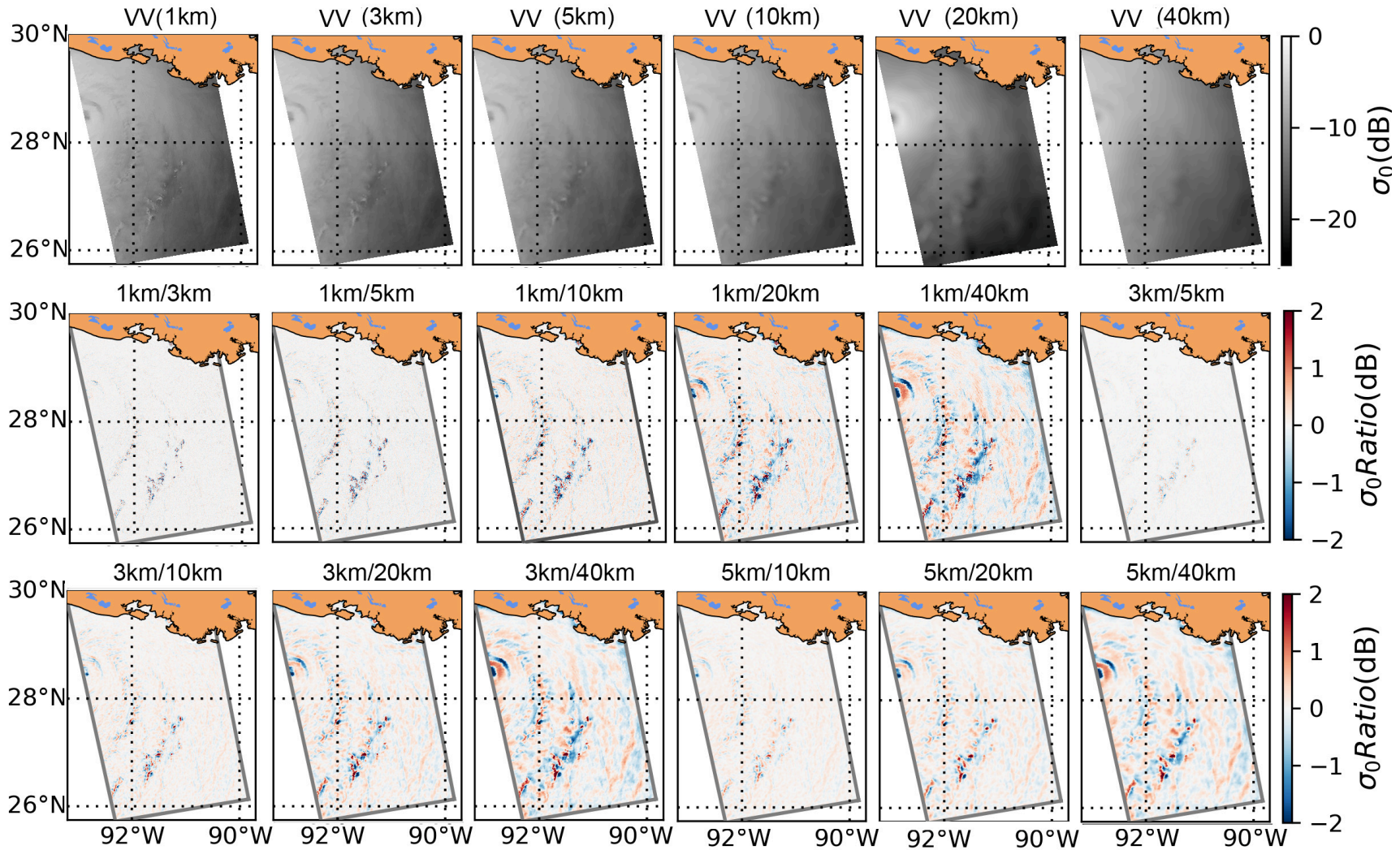


Figure 6.8: VV-pol image of TC Laura at multiple resolutions, i.e., 1km, 3km, 5km, 10km,20km, 40km (top panels) with $\sigma_{0,diff}$ combining different resolutions (middle and bottom panels).

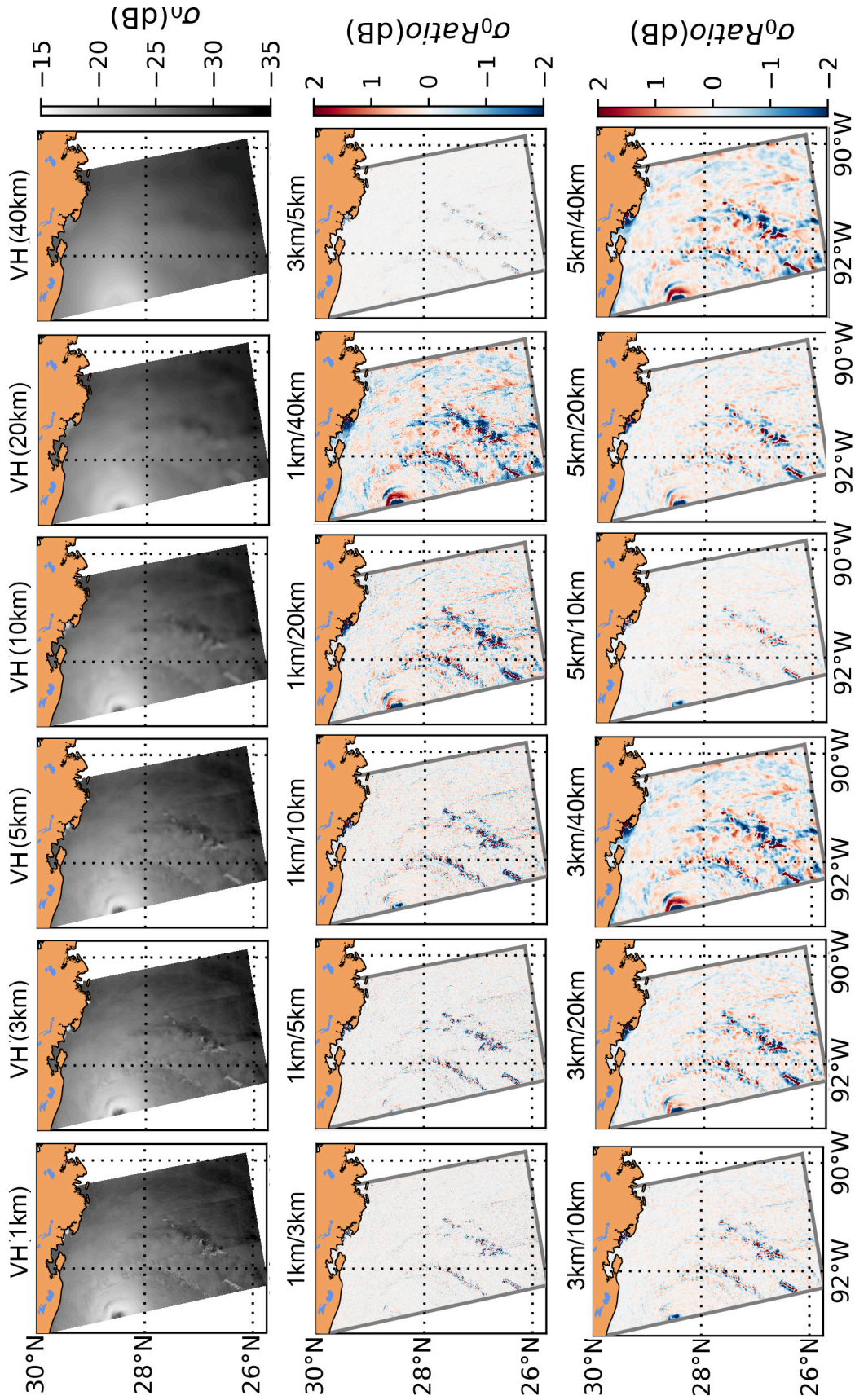


Figure 6.9: Same with Fig. 6.8 but for VH.

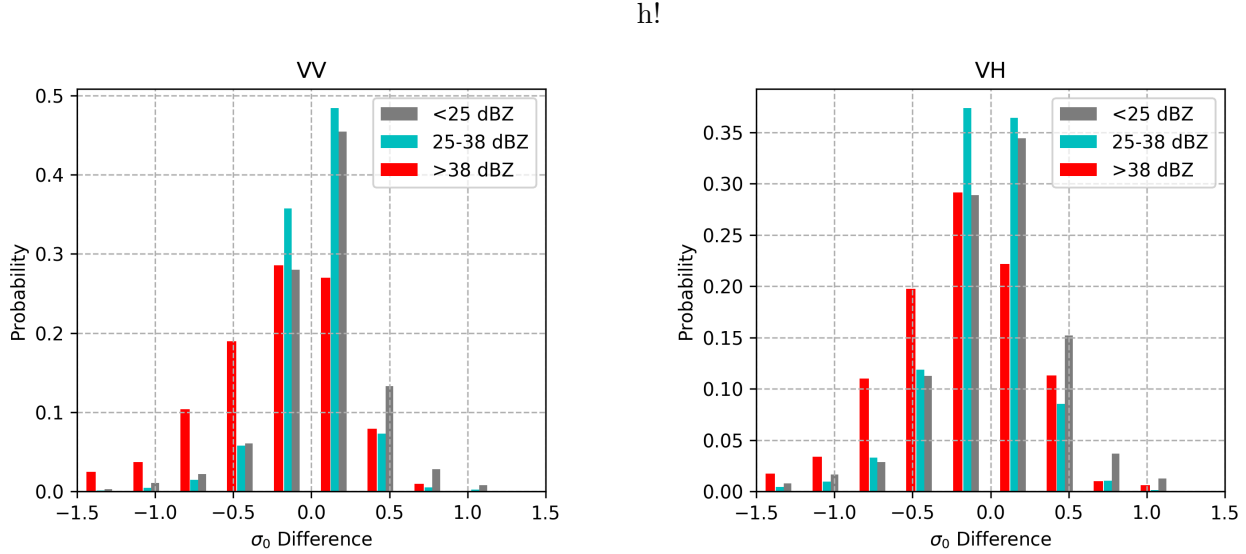


Figure 6.10: Pdf of $\sigma_{0,diff}$ between 5 km and 20 km with respect to base reflectivity in (a)VV and (b) VH.

40km, it is almost impossible to observe the rain signatures even where the heavy precipitation is detected by the weather radar close to the center. As seen in Fig. 6.8, with the resolution degrading, it becomes more and more difficult to identify the rainbands which are easy to recognize in 1-km-resolution image.

The difference of SAR images between 2 specific resolutions can manifest the rainband as shown. These maps in the center and lower panel in Fig. 6.8 are got by the equation $\sigma_{0,diff} = \sigma_{0,res1} - \sigma_{0,res2}$. For instance, the final map ($\sigma_{0,diff}$) at 1km/10km takes the *res1* as 1 km and *res2* as 10 km. This operation is did in the unit of dB. Apparently, the maps at 1km/10km , 1km/20km, 1km/40km, 3km/10km, 3km/20km, 3km/40km, 5km/20km, 5km/40km (referred as difference map in the following) shows the large variation in rainbands close to and far from the center. As seen, the difference map in 1km/40km shows strong negative/positive difference in rainbands. Yet the some patches associated with local winds also show large variations simultaneously. Thus, a smooth filter is necessary to weaken those features unrelated to rain, which shall be discussed next.

In addition, we note that the difference maps in VV and VH have shown distinct abilities to manifest rainbands due to the signal sensitivity to polarizations. As with the same combinations of *res1* and *res2*, the difference map in VH presents a larger variation in the far rainbands than VV. Because the bright patches in relation to rain is more pronounced in VH. It would be helpful to identify the rainbands if the differences at dual-polarizations are taken into account.

6.2.2 Non-local mean filter

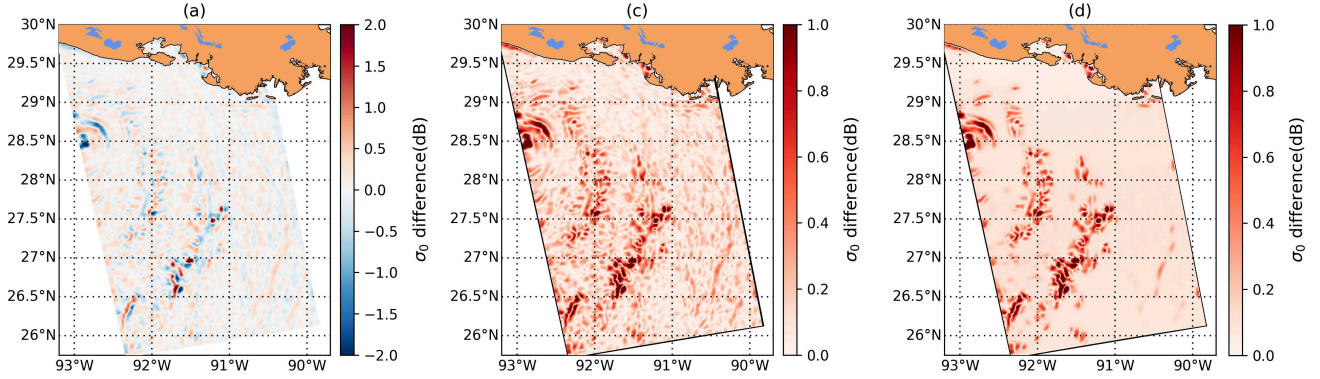


Figure 6.11: (a) $\sigma_{0,\text{diff}}$ between 5 km and 20 km. (b) Absolute value of $\sigma_{0,\text{diff}}$ of (a). (c) Final result after Non-Local Mean filter applied on (b).

The difference map also shows the some noises because of the local wind variation, as seen in 5km/20km difference map. Some filters such as Gaussian filter and median filter can help remove the small noises and but also weaken some useful details in images because the final value at each pixel is decided by a group of neighbors surrounding a target pixel. Unlike these traditional smooth filters, the non-local mean (NLM) filter gave a weight on the each neighbors depending on how similar these neighbors are to the target pixel.

Suppose v is the original image and j is the pixels belonging to I , the filtered value at location i can be calculated by Eq. 6.3

$$NL[v](i) = \sum_{j \in I} w(i, j)v(j) \quad (6.3)$$

where $w(i, j)$ is the weighting function between point i and j , which gives the similarity between the each pixel j to the target i defined as Eq. 6.4.

$$w(i, j) = \frac{1}{Z(i)} e^{-\frac{\|v(\mathcal{N}_i) - v(\mathcal{N}_j)\|_{2,\alpha}^2}{h^2}} \quad (6.4)$$

where $Z(i)$ is the normalizing constant

$$Z(i) = \sum_j e^{-\frac{\|v(\mathcal{N}_i) - v(\mathcal{N}_j)\|_{2,\alpha}^2}{h^2}} \quad (6.5)$$

With the involvement of similarity weight $w(i, j)$, this filter has the advantage of keeping the main structures in one image after the small noises has been cleaned up.

Before applying NLM filter to the difference map, it is necessary to split the negative or positive domain in difference map because the NLM filter has the best performance as applying in each domain. In Fig. 6.11, we simplify the processes and just take the absolute of $\sigma_{0,\text{diff}}$. After the this step, the rainband structures is clearly strengthened. Fig. 6.11 (b) shows that NLM filter keeps the large variation area in rainband and most irrelated features are removed. This example illustrates that NLM filter is beneficial to extract the rainbands precisely.

6.2.3 ROC curve

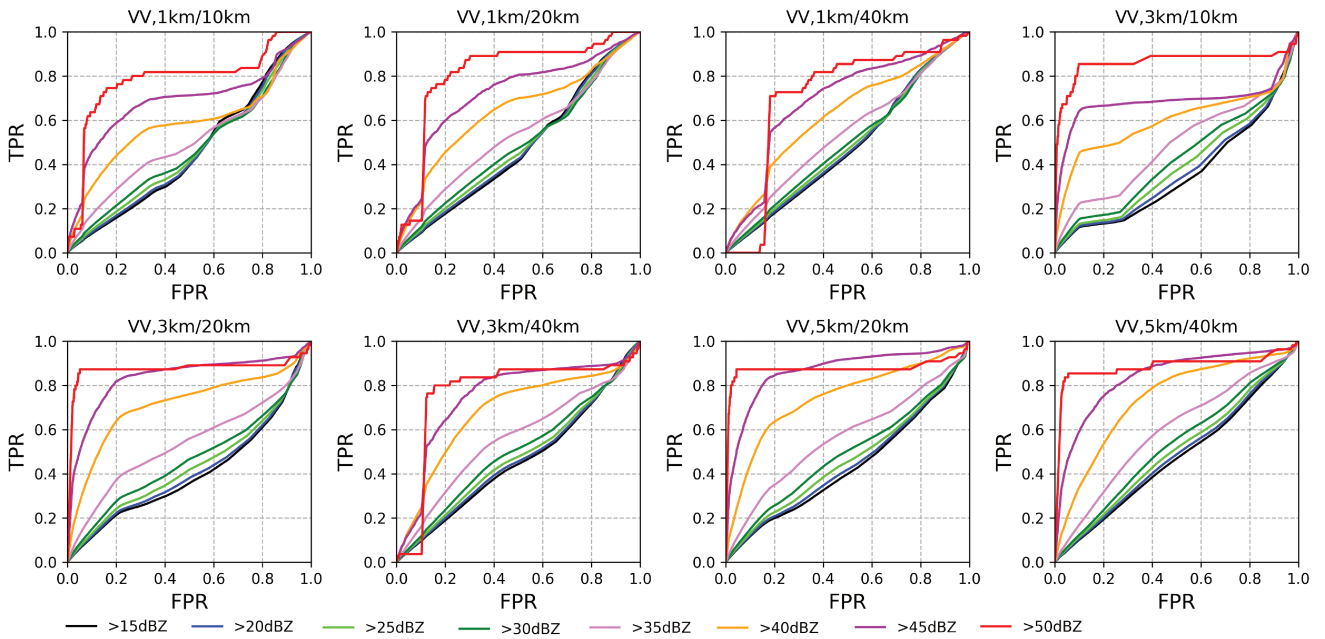


Figure 6.12: ROC curves for VV polarization at different resolution combinations.

To obtain the final rainband mask, a global threshold or adaptive thresholds can be applied on the difference map. The global threshold technique applies one single threshold on the whole image whereas the threshold at each pixel varies depending on the neighbor information in adaptive technique. Here we choose the global threshold because the difference map is generated locally by taking into account that surrounding signal. As illustrated in the optimization of dual-pol filter in generating the dual-pol rain mask, the agreement between the rainband mask and the base reflectivity is strongly dependent on the global threshold. In Fig. 6.12 and Fig. 6.13, we show ROC curves for VV-pol and VH-pol difference maps with different combination of $res1$ and $res2$, i.e., 1km/10km, 1km/20km, 1km/40km, 3km/10km, 3km/20km, 3km/40km, 5km/20km, 5km/40km. Here the base reflectivity groups are set over 15 dBZ, 20

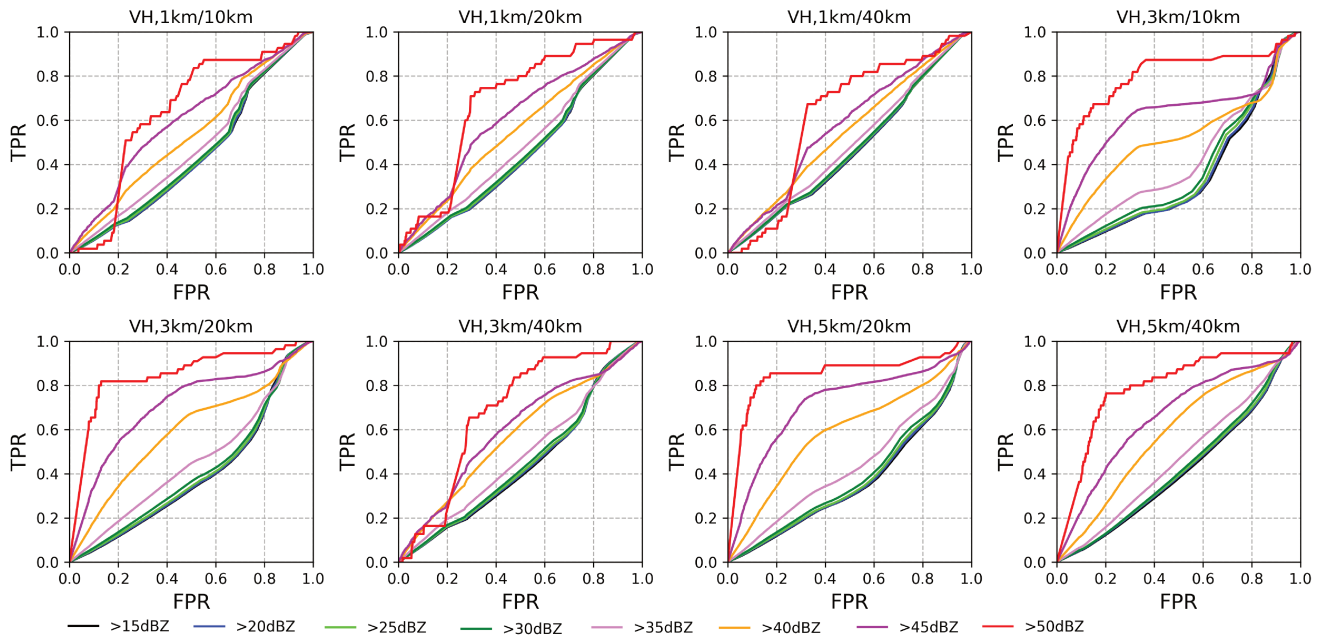


Figure 6.13: Same with Fig. 6.12 but for VH.

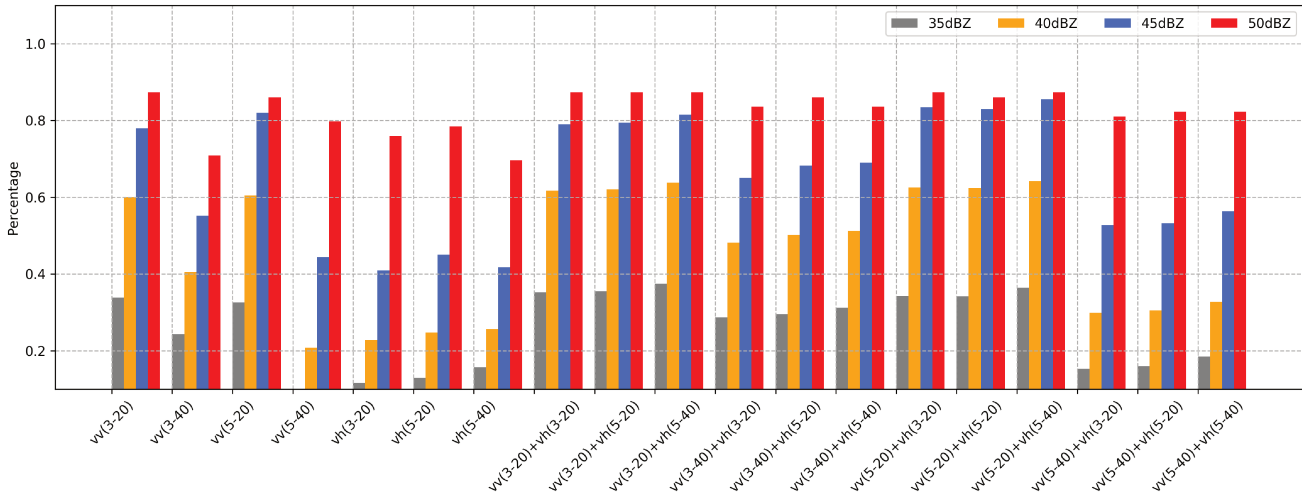


Figure 6.14: The detection percentage at different combination of *res1* and *res2*.

dBZ, 25 dBZ, 30 dBZ, 35 dBZ, 40 dBZ and 50 dBZ respectively.

In terms of VV polarization, the detection percentage generally increases with base reflectivity for all the difference maps, similar to the ROC results in regular cases. And as observed, the lower panel in Fig. 6.12 shows higher TPR than upper panel. It confirms that the signal in TCs can only be modified under very intense rainfall, generally higher than 40 dBZ. For VH, the agreement is generally lower than

VV with the same base reflectivity threshold. It can be explained that the signal reduction due to rain at VH is less pronounced than VV, for instance, the dark rainband closet to the center in Fig. 6.12 and Fig. 6.13. Even though the increase in far rainbands is more obvious in VH, the collected cases shows more dark rainbands especially near the cyclone center. For the ROCs in VH, apparently the maps at 3km/20km, 5km/20km and 5km/40km have higher agreement with base reflectivity and the former two is comparable in case of the 45 dBZ and 50 dBZ.

And the optimized thresholds are also variant in different reflectivity groups. Here we take the minimum distance to the top left corner as criteria for the threshold optimization as described in section 6.1.2. As for each difference map in VV, the optimized thresholds are 0.20, 0.43, 0.14 and 0.78 corresponding to the 3km/20km, 3km/40km, 5km/20km and 5km/40km maps respectively. For VH, we choose 3km/20km, 5km/20km and 5km/40km with optimized thresholds of 0.71, 0.49 and 0.64 due to their better detection.

Considering these multiple difference maps, a new mask combining VV and VH information can be generated. The different combination based on the above evaluation on ROCs is presented in Fig. 6.14. As can be seen, the masks only derived from VV polarization is better than VH but still lower than that in combination of dual-polarization. Summing up all the dual-polarization masks, we can see that the filter in (VV(5-20) + VH(5-40)) has a higher detection as reflectivity over 45 dBZ, even with close values to the joint mask in (VV(3-20) + VH(5-40)) at 35 dBZ, 40 dBZ and 50 dBZ.

6.2.4 Validation

Fig. 6.15 shows the new developed mask (referred as developed mask hereafter) based on dual-pol information targeted on cyclone cases captures more rainbands than the other algorithms. In upper panel, JMA radars shows very high rain rate up to 35 mm/h in the closet rainband to the center, which is collocated well with the dark circle in SAR images. The masks presented in the middle panel, including the single-pol mask based on original Koch algorithm and the dual-pol mask proposed for regular cases in section 6.1 do not capture this rainband effectively. In comparison, the developed mask captures not only the rainband closet to the center but also several rainbands far from the center. It is noticed that not all the area associated with heavy rain is detected because the the rain mask generated at VV and VH is only sensitive to strong variation with respect to local neighbors. Despite this, the main structures of rainbands is still clearly shown.

The developed filter is further validated as applied on all cyclone cases over Japan area against JMA rain measurements in terms of rain rate, wind speed and incidence angle in statistics. Here another

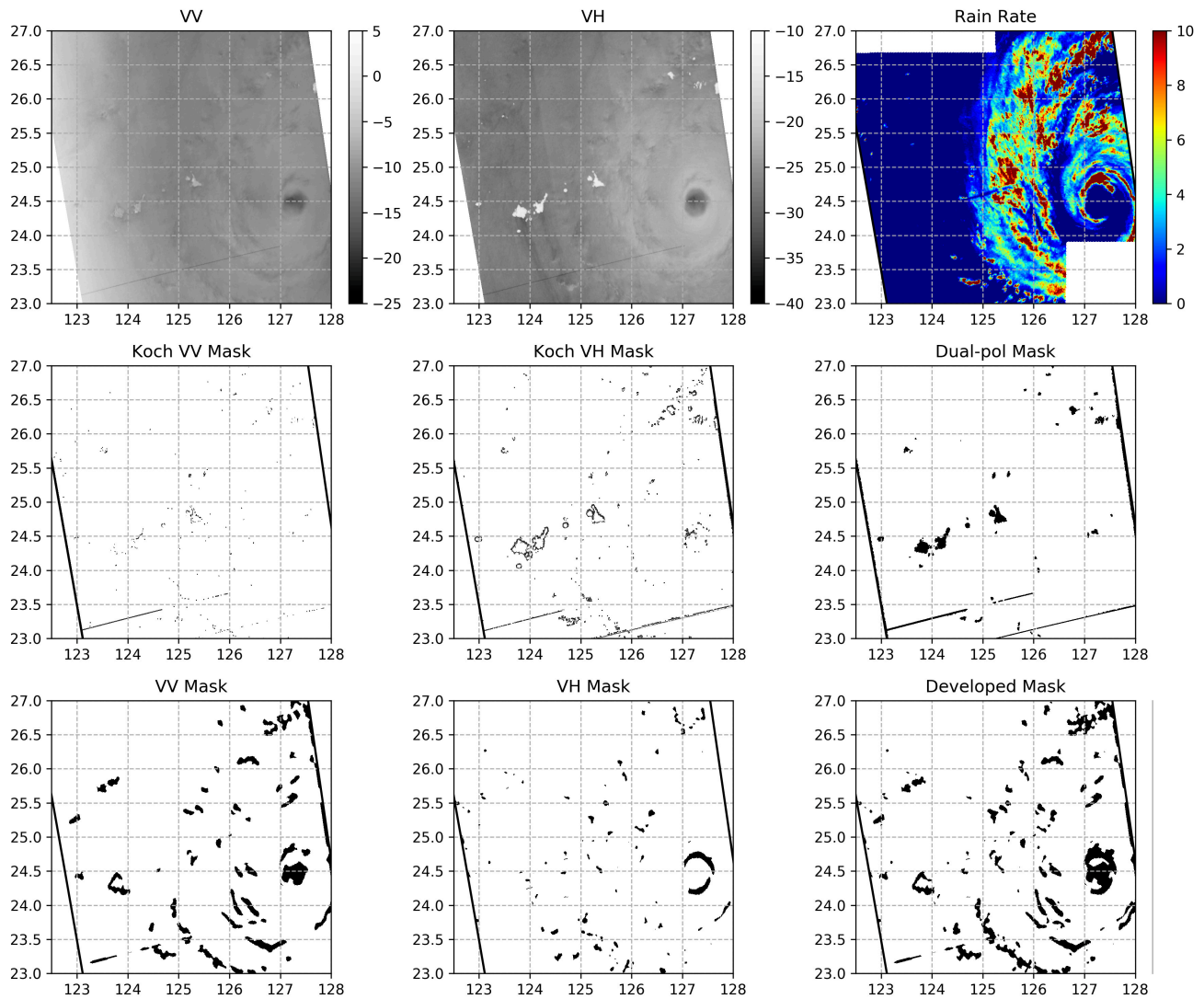


Figure 6.15: top panel: Typhoon Maysak captured by Sentinel-1 at VV and VH polarizations and the together with rain rate from JMA. Middle panel: The rain masks from Koch method at VV and VH respectively and the dual-pol filter we proposed. Bottom panel: rain masks from VV- and VH-pol $\sigma_{0,diff}$ along with our developed method.

three filter are compared with the developed filter, i.e., the Koch filters generated at VV and VH images respectively and the dual-pol filter. Wind speed here is from the ECWMF and rain rate is provided by JMA radars.

Fig. 6.16 assess the statistics of rain detection by the developed filter in comparison to the Koch filter and dual-pol filter as a function of rain rate and wind speed. Note that we included all the cyclone cases in different category so that the statistics here is only dependent on the surrounding wind speed. Similar to

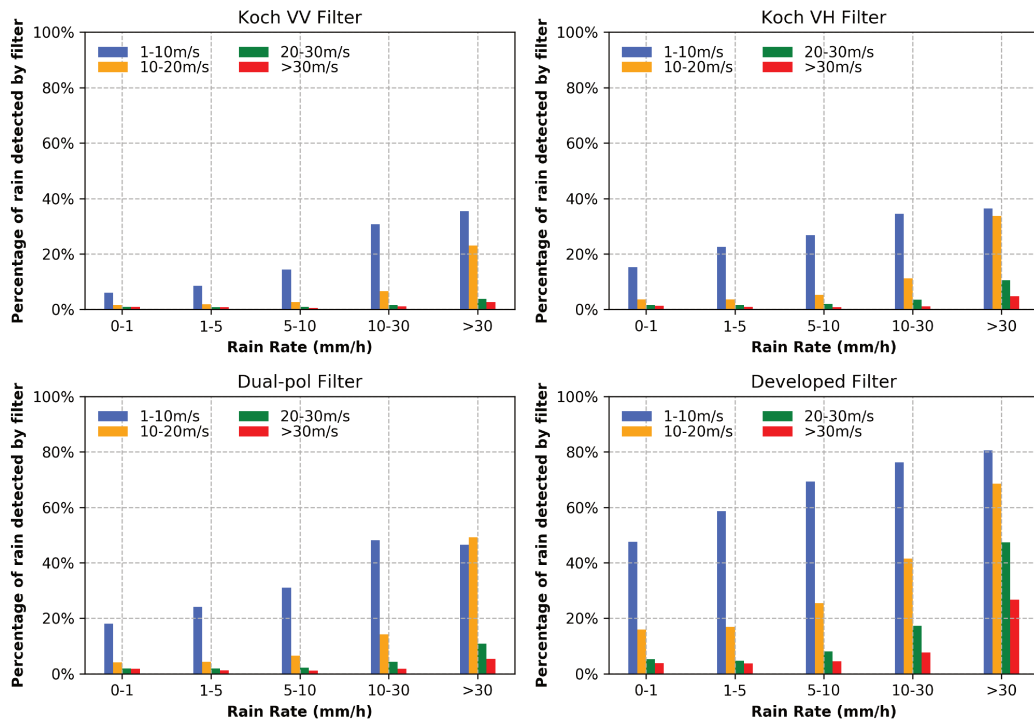


Figure 6.16: Rain detection from (a) VV-generated filter, (b) VH-generated filter, (c) dual-pol filter and (d) our developed filter as a function of rain rate for different wind speed regimes.

Fig. 6.3, there is an interaction between rain rate and wind speed impacting the detection efficiency for all the filters in cyclone cases. With rain rate increasing, the detection increases significantly. Meantime, the improvement of wind speed reduces the probability of all the rain filters at a given rain rate. Nevertheless, apparently the developed filter shows greater detection percentage compared with the Koch filters and dual-pol filter. Especially as rain rate becomes larger than 5 mm/hr, the developed filter can captures more than 70 % rainband. The wind speed has an obvious impact on rainband detection in SAR images. But with rain rate over 30 mm/h, the developed filter can still detect about 70 % for wind speed of 10-20 m/s and more than 40 % for wind speed of 20-30m/s, much higher than the other filters.

We also note that the percentage decreases to around 30 % as wind speed exceeds over 30 m/s. This value is not high as expected for the cyclone cases. But we should note that only 28 cases are involved in this statistical validation, indicating that the percentage might be largely reduced. In particular, as the heavy rain is quite close to the land, the low resolution SAR map is partially contaminated by the ambient backscatter from land as the fixed size footprint slides even though a land mask is applied. Fig. 6.17 presents two examples showing this impact. The first case Maysak only includes a small island

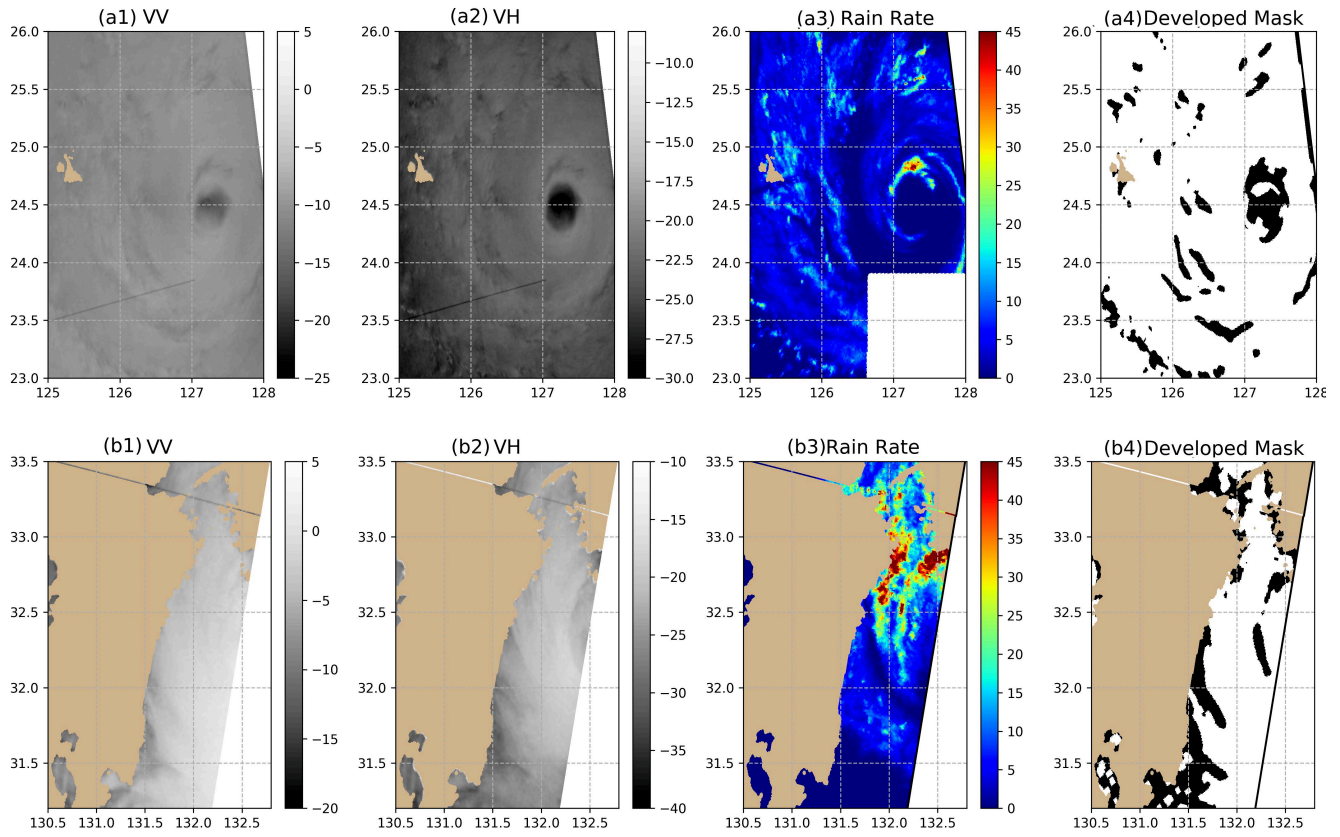


Figure 6.17: The upper panels show a zoom of cyclone Maysak case presented in Fig. 6.15. The lower panels are for Malakas on 19 Sep 2016 at 21:21 UTC.

and the filter thus detects the rainbands very well. Yet for the case Malakas, the cyclone center is really close to the land so that not all the area with rain rate over 30 mm/h is captured, for instance, the elongated rain region to the east of the island. It confirms that the developed filter can effectively detect the rainband in cyclone cases but it becomes more complicated once quite close to the land.

The detection rate is also analyzed with respect to incidence angle for the different filters in Fig. 6.18. As observed, the developed filter is less impacted by the swath border whereas the Koch filters and the dual-pol filter are more sensitive in the near incidence angle range less than 31° . In addition, with the incidence angle exceeding 31° , the rainband detection by the developed filter increases with incidence angle with the same trend as the others. This illustrates that the impact of incidence angle on rain detection for high wind regimes in cyclone cases can not be ignored as the regular ones.

Overall, the developed filter shows a better detection on the rainband in cyclone cases, much higher than the Koch filters and the dual-pol filter targeted on regular cases. However, this filter is still impacted

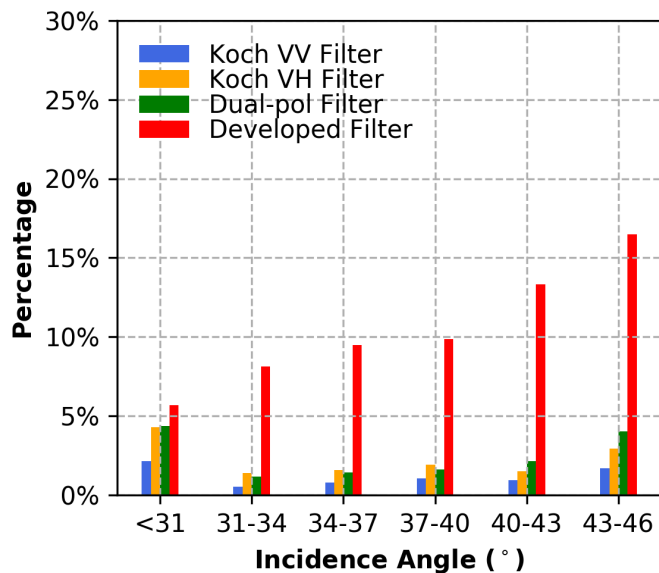


Figure 6.18: Rain detection as a function of incidence angles.

on the wind speed, rain rate and incidence angle to some extent. Also for some cases very close to land, the rainbands might be less captured due to the contamination of high backscatter from land.

6.3 Summary

This chapter described two separate algorithms in the purpose of rain detection in regular and cyclone cases. These two algorithms aim to provide an effective rain mask serving for improving accuracy of the wind inversion because the numerous studies have shown that the rain can biased the wind speed accuracy largely. Essentially, the signal received by SAR in rain area comes from a different scattering mechanisms from that without rain. Thus it leads to larger errors of wind speed in rain area after the application of GMFs on radar backscatter. Thus an efficient rain mask is beneficial to the wind inversion improvement by removing the involvement of backscatter in rain area.

In terms of regular cases, we develop the single-pol heterogeneity filter Koch (2004) and propose a dual-pol filter by taking advantage of dual-pol information in Sentinel-1. The reason for the dual-pol combination is based on the observation in Section 4 where the rain signatures in VH is more pronounced than in VV especially at low incidence angles and high winds. Thus, the dual-pol filter improves the rain detection by merging the filters generated from a VV image at a resolution of 400 m resolution and from a VH image at a resolution of 800 m respectively. This filter is validated against with the original Koch filters in different rain rates and wind speeds. In all the occasions, the new dual-pol filter show higher

detection than the others. Yet the detection becomes less sensitive with increasing wind speed.

Another developed filter targeted at cyclone cases is proposed, which can effectively capturing the spiral rainbands. This filter is fundamentally a local algorithm, based on the signal variation with respect to the surrounding. Even though this algorithm is trained by only 28 cyclone cases, it still shows better detection on rainbands compared to the Koch filter and the dual-pol filter proposed for regular cases. Impressively, as rain rate gets over 30 mm/h with a wind speed less than 10 m/s, about 80 % rainbands are detected by the developed filter whereas the dual-pol filter only detect about 50 %. This rainband filter has the potentials for the further cyclone translation prediction.

Inflow angle of tropical cyclone cases

Contents

7.1	Inflow angle from spiral rainbands	107
7.1.1	rainband shape	108
7.1.2	Inflow angle estimation	109
7.1.3	Inflow angle distribution	110
7.2	Inflow angle comparison for TC Michael	116
7.2.1	Translations of dropsondes and HWRF data	116
7.2.2	Wind directions compared with dropsondes	118
7.2.3	Comparison between wind streaks and rainbands	120
7.2.4	Comparison between HWRF data and rainbands	121
7.2.5	Comparison between wind streaks and HWRF data	123
7.3	Summary	125

This chapter investigates the inflow angles derived from spiral rainbands associated with normalized radial distance (R^*), storm translation speed (V_s) and the maximum wind speed (V_{max}). Inflow angles from rainbands are compared with that from in situ dropsondes, wind streaks analysis from SAR images, wind direction from HWRF model, in the case of TC Michael.

7.1 Inflow angle from spiral rainbands

Wexler (1947) noticed the inward spiral in hurricanes by weather radar observations. Senn et al. (1957) and Lahiri (1981) found that the spiral clouds in TCs generally fit with equiangular spirals. The equiangular spiral or logarithmic spiral is defined as a curve cutting all radial line by a constant angle. Thus the rainbands were assumed to be well arranged along streamlines with the same inflow angle, which was confirmed by Willoughby et al. (1984) and Willoughby (1988) through a comparison between radar and aircraft data. However, the inflow angle derived from the sea surface wind measurements from

dropsondes fits a normal distribution with a mean -22.6° (Zhang and Uhlhorn, 2012). In this subsection, we examine the inflow angle behavior of rainbands based on the rainband masks proposed in section 6.2.

7.1.1 rainband shape

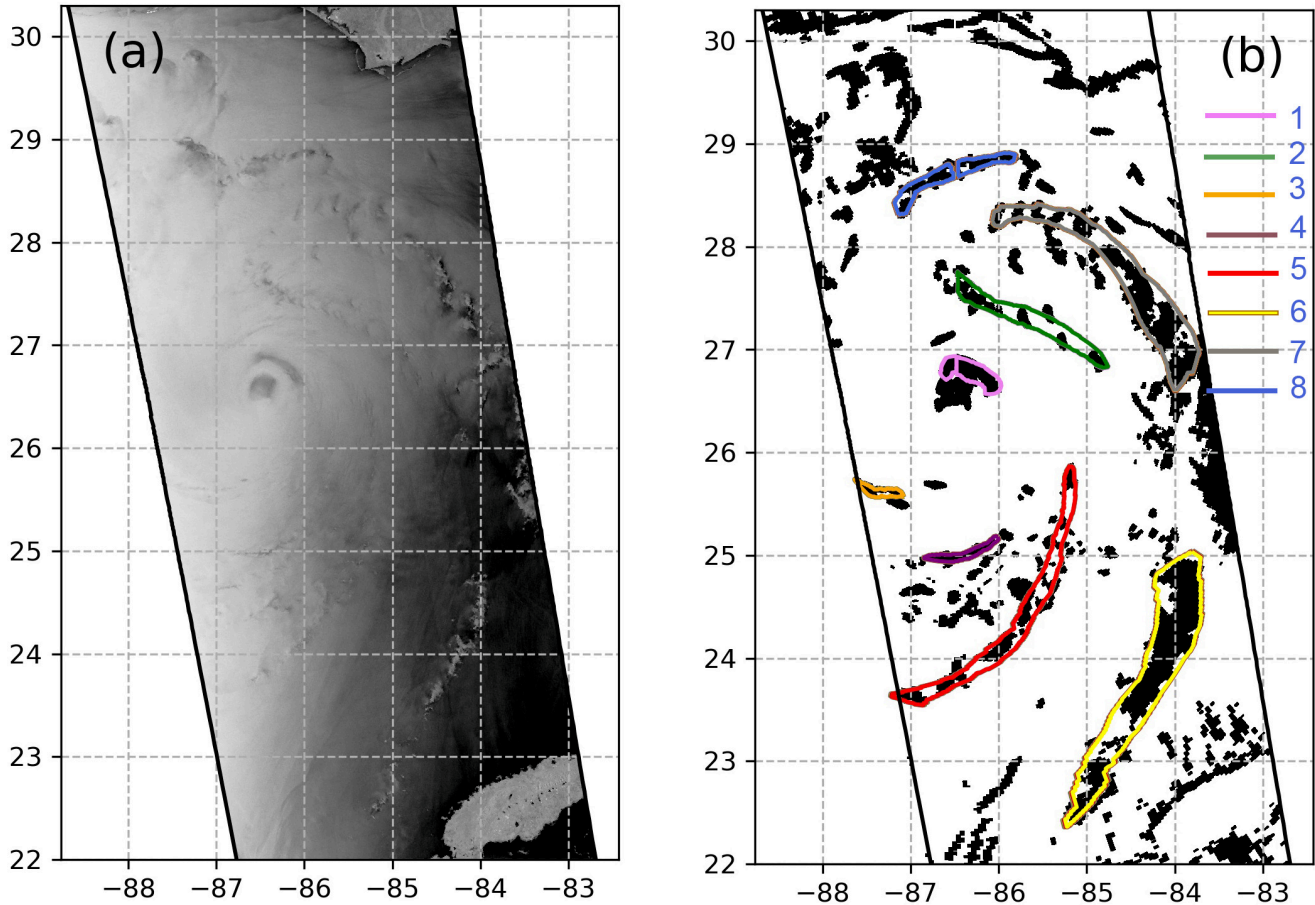


Figure 7.1: (a) TC Michael captured by Sentinel-1 at 9 Oct 2018 at 23:45. (b) Mask generated from dual-pol SAR images based on the method proposed in Section 6.2. The shape of rainbands are shown by colored lines.

The detection method in section 6.2 is used to mask the pixels in SAR images associated with rain and other phenomenon impacting the NRCS. As shown in Fig. 7.1, the mask for Micheal detects the inhomogenous area, some of which are apparently related to spiral rainbands. According to the mask, the shapes of rainbands could be extracted approximately. Thus we manually depict the shapes of 8 rainbands which are readily recognized by referring the mask to the SAR image. For instance, as for rainband 1, 3 and 4, the borders of the some patches are clearly shown, which are readily connected for the shapes.

However, for the other rainbands, many individual patches exist in the surrounding which gives rise to more difficulty for the shape extraction. In this situation, patches associated with the reduction or enhancement of NRCS are manually selected and connected for a rough shape.

7.1.2 Inflow angle estimation

To get the inflow angle for each individual rainband, it is necessary to fit in the shape by a streamline equation. Assuming the streamline ψ , the radial (v) and tangential (u) components at one given point (S) can be given:

$$\begin{aligned} u &= -\frac{d\psi}{dr} \\ v &= \frac{1}{r} \frac{d\psi}{d\varphi} \end{aligned} \quad (7.1)$$

where r and φ are radius and angle in polar coordinates respectively. The streamline equation is then derived

$$-r \frac{d\varphi}{u} = \frac{1}{v} dr \quad (7.2)$$

Considering $\frac{v}{u} = \tan \alpha$, where α is inflow angle, we can get the final form of the streamline

$$-d\varphi = \frac{dr}{r} \cdot \frac{1}{\tan \alpha} \quad (7.3)$$

Assuming the inflow angle is constant in a small segment of the streamline, we can get

$$-\varphi = \ln r \cdot \frac{1}{\tan \alpha} + \beta \quad (7.4)$$

$$r = e^{(\beta - \varphi) \cdot \tan \alpha} \quad (7.5)$$

In practice, the mask of rainbands based on proposed algorithm above has a certain width, which also varies with φ . Thus to get the streamline for each rainband, we assume that the small segment of rainband fit in the function of logarithm spiral. To be more specific, to get r of the streamline at given angle φ , all the points in the vicinity ($\varphi \pm 20^\circ$) are collected to fit in the spiral equation 7.5. Then r is derived by this fit strategy so that the point $S(\varphi, r)$ in the streamline is determined. According to this strategy, the streamline for one spiral rainband is extracted. Fig. 7.3(a) shows an example of Michael with rainband masks and derived streamlines.

Through the streamlines, we can see that the normalized radial distance (R^*) for each rainband decreases with increasing φ_r (Fig. 7.3(b)). Note that φ_r is relative angles starting from storm moving

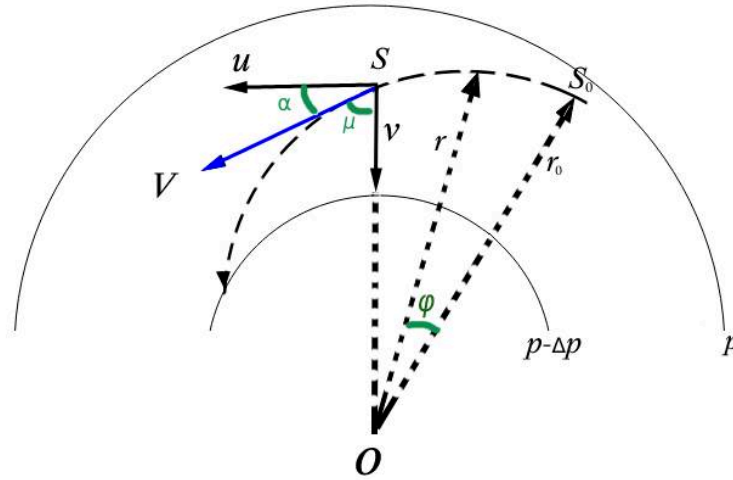


Figure 7.2: To the derivation of the streamline equation. α is the inflow angle and μ is complementary to α . The bold dashed curve is the streamline; solid curves designate p and $p-\Delta p$ isobars (p is the pressure, Δp is the pressure change between isobars); V is the wind speed in point S ; u and v are tangential and radial components of the wind speed V at point S , respectively; and ϕ is the polar angle of radius vector r counted off from arbitrary selected point S_0 .

direction (354° for this case) and increasing counter clockwise in north hemisphere. The inflow angles extracted from the rainband streamlines are then checked individually with respect to R^* and φ_r in Fig. 7.3(c)(d). $R^* = R/\text{RMW}$ where R is the radial distance from the center. For rainband 1 (pink) located at 1-2 RMW, α is around 0, which means the rainband has a shape close to a circle around the center. In comparison, rainband 2 (green), 5 (red) and 6 (yellow) far from the center have smaller inflow angles which decrease with R^* , suggesting that the inflow angle is radial distance distance dependent.

7.1.3 Inflow angle distribution

A total of 54 TC cases with storm center captured by Sentinel-1 or Radarsat-2 are collected to investigate the inflow angle distribution with respect to different physical parameters (e.g., normalized radial distance (R^*), maximum wind speed (V_{max}), storm translation speed (V_s)). As shown in Fig. 7.4, these cases are with V_{max} from 32 to 80 m/s and RMW ranging from 6 to 55 km. V_{max} for each case is extracted from the wind speed map retrieved from SAR images as explained in Section 4.2. Note that the radial profile of wind speed is very sensitive to TC center. Here the center position is defined as the centroid of the maximum wind gradient contour around the eye following the method proposed by

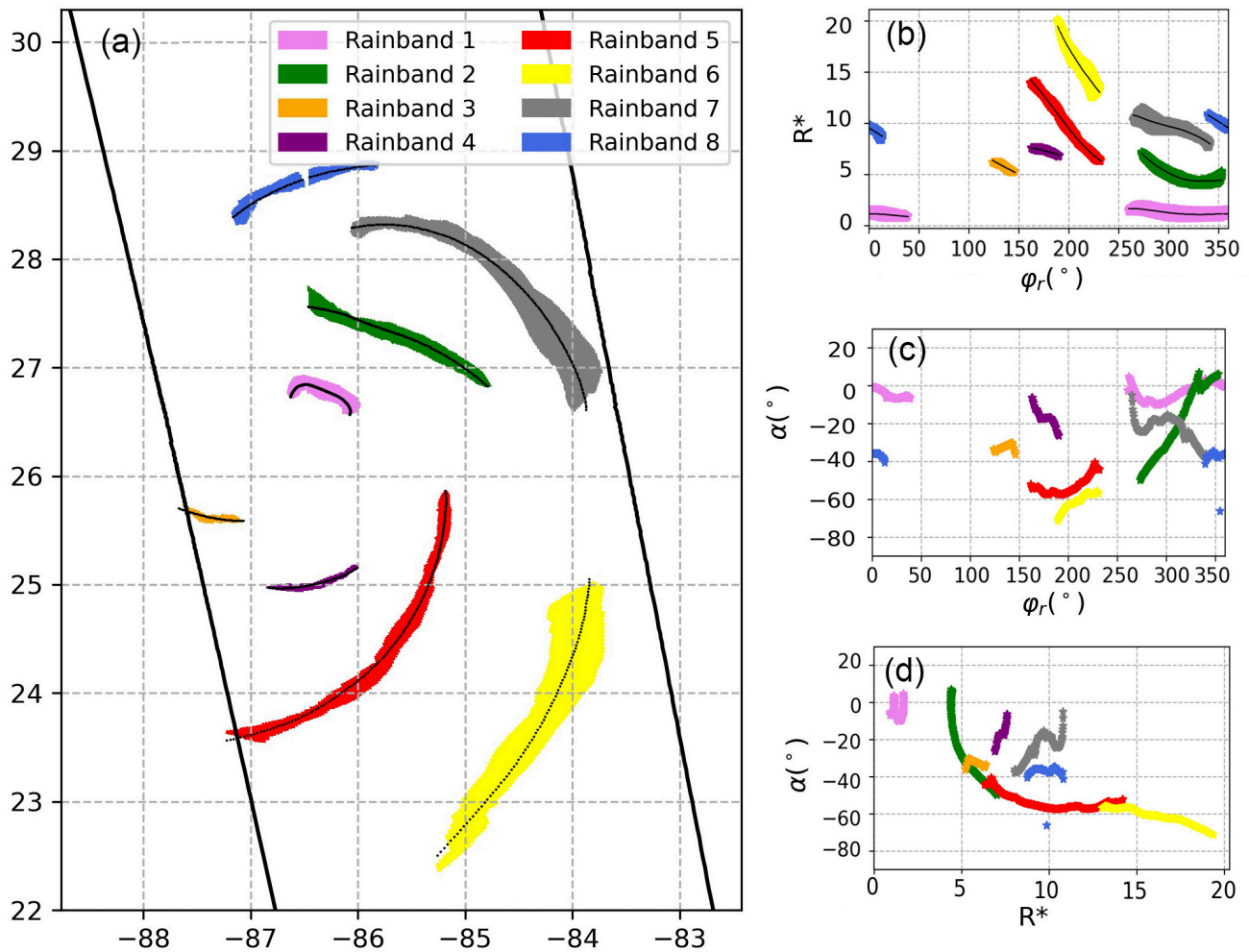


Figure 7.3: (a) the mask for each rainband along with the fitted streamline by equation 7.5. (b) The normalized radial distance (R^*) with respect to the relative angle φ_r for each rainband. Inflow angles for each rainband associated with φ_r (c) and R^* (d).

Vinour et al. (2021). From Fig. 7.5, TCs at low category are more prone to have a large RMW. The storm translation speed (V_s) here refers to best track product at the closest time to SAR acquisition time. The histogram of V_s has the maximum at 5 m/s while the maximum is over 11 m/s. These cases at different states allow us to dig into the inflow angle with respect to V_{max} , RMW and V_s .

Fig. 7.6(a) compares inflow angle with respect to the normalized radial distance (R^*) since RMW differs for each case. As observed, the mean of α decreases with R^* up to 11 and then fluctuates, mostly subject to the less data amount. As focusing on the histogram of α in Fig. 7.6(b), it can be seen that with increasing R^* , more data concentrates in bins less than -40° . As R^* is less than 2, inflow angles are

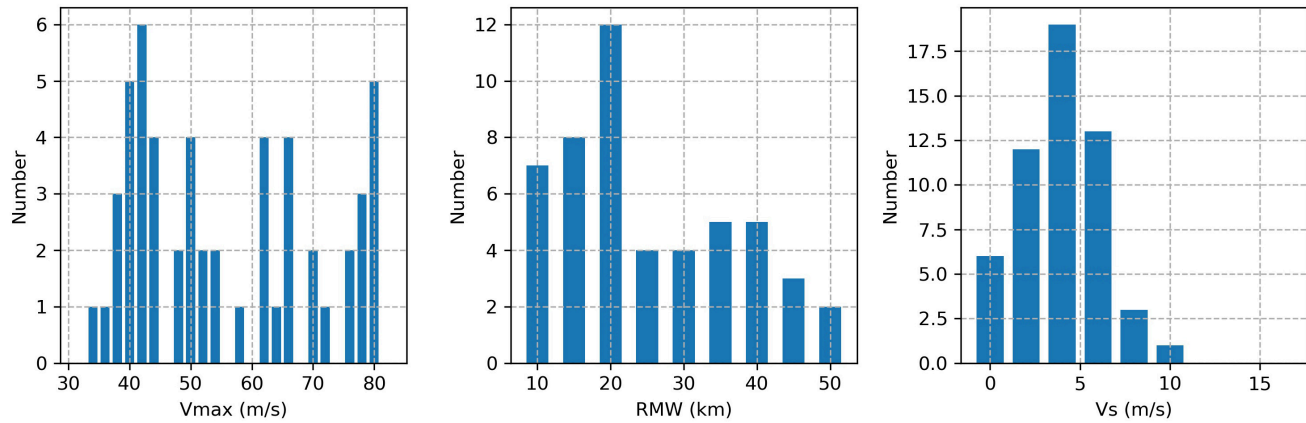


Figure 7.4: The histograms of maximum wind speed (V_{max}), the radius of V_{max} (RMW) and storm translation speed (V_s). V_{max} and RMW are extracted from SAR images.

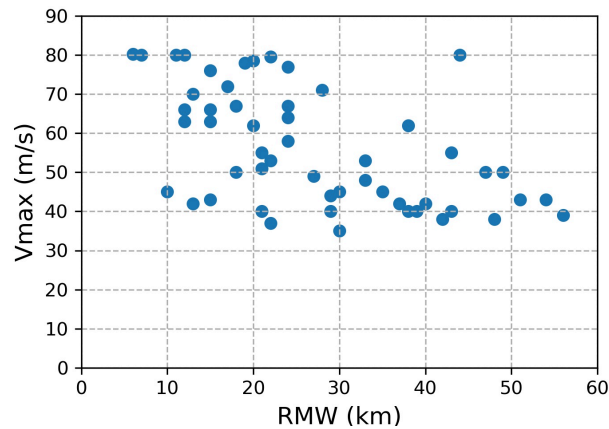


Figure 7.5: The radius of maximum wind as a function of maximum wind speed.

almost more than -20° with peak around -2° . With R^* between 2 and 6, 4.1% data is less than -40° and 30.5% is between -40° and -20° . As for R^* exceeding 6, more than a half data is lower than -20° with 20.7% less than -40° and 33.5% between -40° and -20° . The histogram shows that inflow angle α is prone to be zero for rainbands close to center, whereas it decreases with increasing radial distance. This displays a similar trend with Zhang and Uhlhorn (2012) but with a larger value as R^* is smaller than 6 probably because they estimated the inflow from sea surface winds collected by Dropsondes.

Further stratification of α among weak/strong, small/large, and fast/slow-moving storms is shown in Fig. 7.7 to check the inflow angle variation under different states. The dotted line is fitted by quadratic distribution in each group according to V_s , V_{max} and RMW. As observed, rainbands of TCs at higher

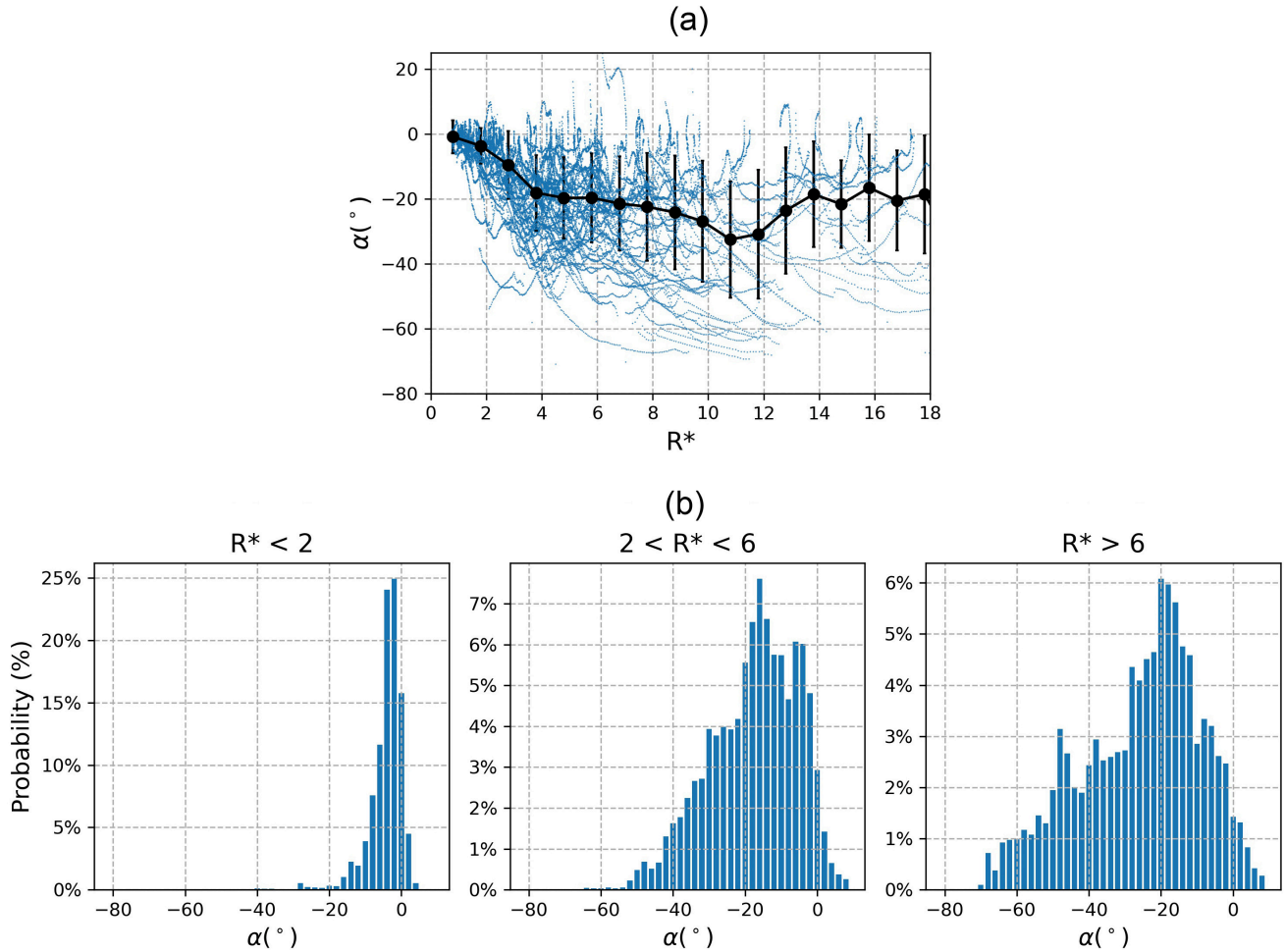


Figure 7.6: (a) The distribution of Inflow angle (α) with respect to the normalized radial distance (R^*). The black line shows the mean of α with errorbars.(b) The histograms of α at different radial distance ranges.

category have larger inflow angles at R^* from 0 to 11. This is contrary to the result in Zhang and Uhlhorn (2012), where the TCs at high category V_{max} have smaller inflow angles with radial distance increasing. In addition, TCs with smaller RMW and fast moving storms have larger α , in line with Zhang and Uhlhorn (2012). This is reasonable with Fig. 7.7(a) because TCs at high category are prone to have a smaller eye as shown in Fig. 7.5. Also, fast moving storms ($V_s > 5$ m/s) may be impacted heavily by wind shear, leading to the increase of inflows.

The decrease of inflow angle with R^* suggests its dependence on sea surface wind speed (U_{10}), which is examined in Fig. 7.8. U_{10} is retrieved from a combined information from co- and cross-polarization sea surface backscatter (Mouche et al., 2017), with a bias and standard deviation of 0.7 and 2.7 m/s. As

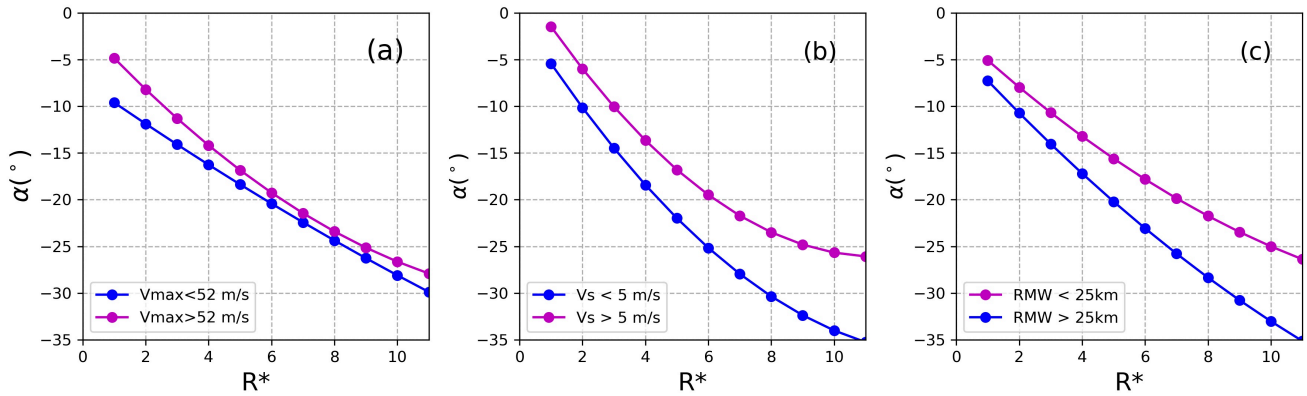


Figure 7.7: Inflow angle (α) versus R^* with maximum wind speed (V_{max}) stronger and weaker than 52 m/s (a), storm translation speed lower and higher than 5 m/s (b), RMW larger and smaller than 25 km (c).

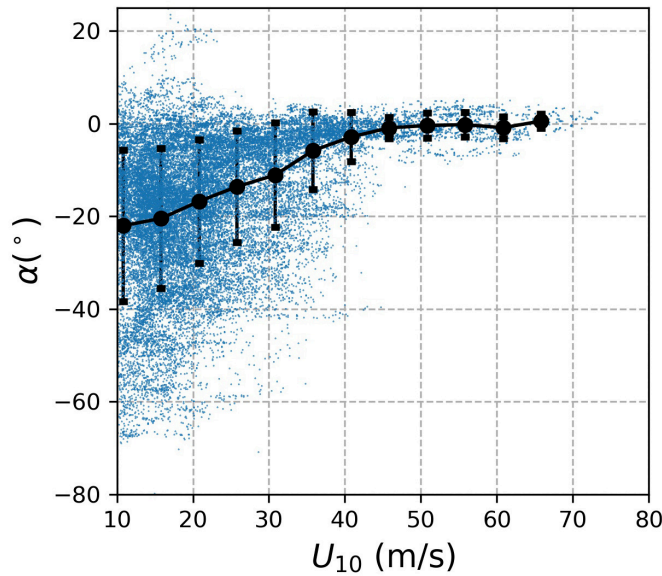


Figure 7.8: The scatter of Inflow angle (α) with respect to sea surface wind speed at 10 m (U_{10}). The mean and standard deviation α of are shown by the black lines.

shown, the mean of α increases with U_{10} up to 45 m/s and then almost stays around 0. The rainband in TCs with wind speed exceeding 45 m/s, commonly exist around the center. It is consistent with the Fig. 7.6(a) to some extent which shows the dependence of inflow angles on the radial distance. Combing the two analysis, we can infer that the rainband close to center in a high-category TC is only dependent on radial distance but less impacted by the sea surface wind speed. In comparison, the large variation in low wind region show more uncertainty of the inflow angles, indicating the impact of other parameters in

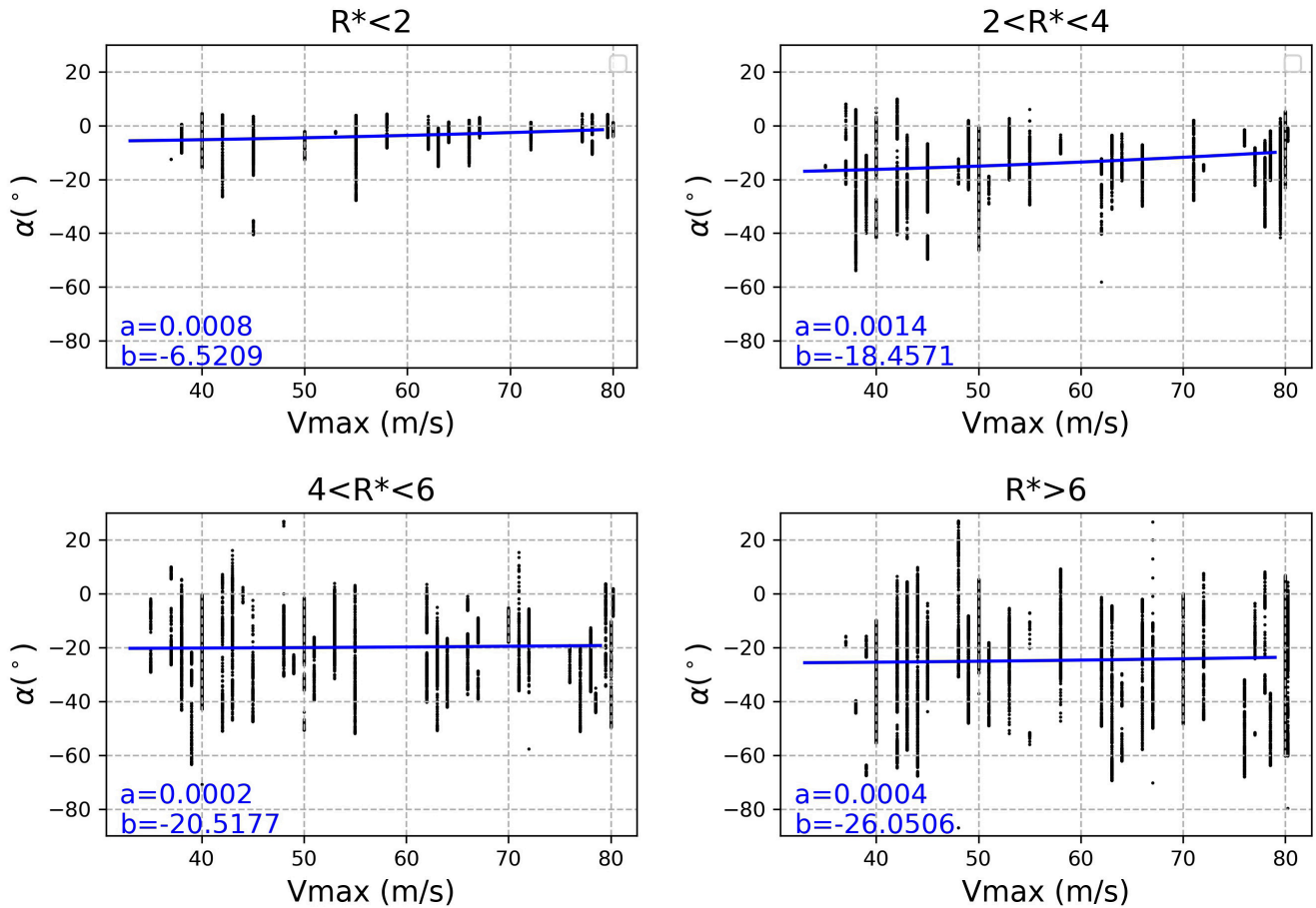


Figure 7.9: Inflow angle (α) against V_{max} under different normalized radial distance ranges. a and b are coefficients in linear regression $\alpha = a \times V_{max} + b$.

the far radial distance in addition to sea surface wind.

The inflow angle α against V_{max} is investigated at four R^* groups (0-2, 2-4, 4-6 and ≥ 6) in Fig. 7.9. Instead of taking the mean, a linear regression is applied on each group. The slope (a) and intercept (b) for each linear fit are denoted in each group. As observed, α slightly increases with V_{max} in R^* groups [0-2] and [2-4]. The latter shows more dependence on V_{max} , indicating the weakness of wind inflow in the inner core for a high-category TC. As R^* exceeds 4, α appears to have little relationship with V_{max} but strong dependence on radial distance. We also note that the variance of α increases with R^* for all categories, indicating the instability of outer rainband transformation. The inner and outer rainbands differing in the surrounding sea surface wind speed are also with different convergence layer depth. The net convergence in inner rainband region is below 2 km height but in outer rainbands is constrained below 7.5 km (Li and Wang, 2012). The convective process for far rainbands is close to the squall lines,

which is less impacted the Rossby waves in the inner core of TC.

7.2 Inflow angle comparison for TC Michael

Michael is a very powerful and destructive hurricane striking the contiguous U.S. in 2018. It originated near western Caribben and became a tropical depression in 7 Oct 2018 in the south of Mexico. Before landing, it was in category-5 with maximum sustained winds of 72 m/s and a minimum pressure of 919 millibars according to best track data. Several cases of Micheal was captured by Sentinel-1 in Gulf of Mexico. Here we only present the Micheal at 23:45 UTC on 9 Oct 2018 with multiple observations of wind directions. An intercomparison is conduted in terms of wind directions/inflow angles from SAR wind streaks analysis, Hurricane Weather Research and Forecasting (HWRF) model, in situ dropsondes, and SAR rainbands.

7.2.1 Translations of dropsondes and HWRF data

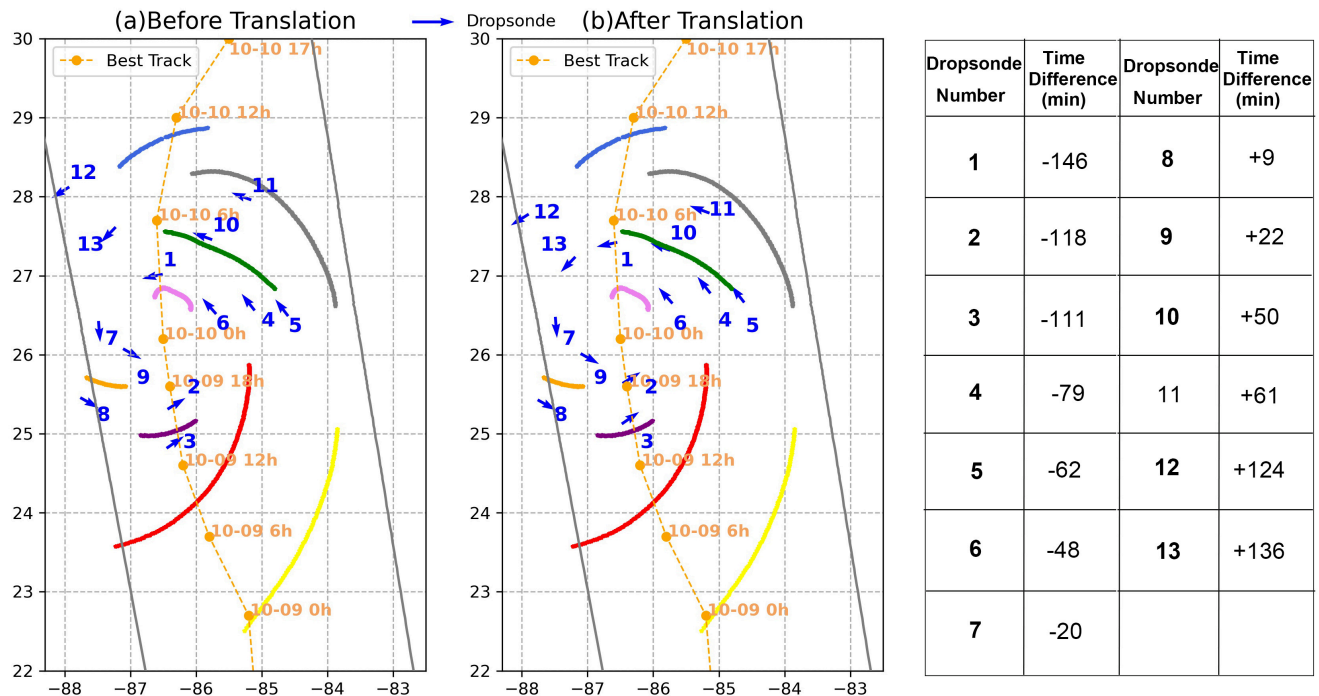


Figure 7.10: The dropsonde location before (a) and after translation (b). The orange dash line shows the TC track location at close times from best track. The time difference between dropsondes and SAR acquisition time is shown in the right table. T Inflow angle (α) with storm translation speed lower and higher than 5 m/s.

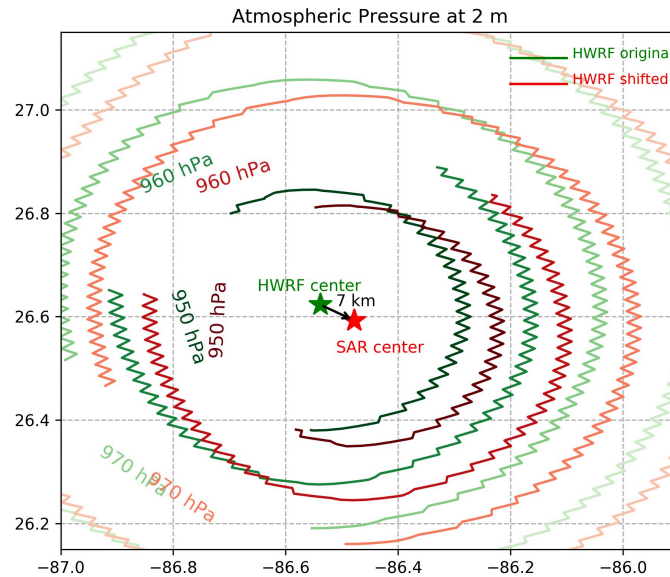


Figure 7.11: The contour of atmosphere pressure from HWRf before and after shift. The TC center distance between HWRf and SAR is 7 km.

For a more accurate comparison, we need to translate the locations of dropsonde and HWRf due to the variant time difference. As for dropsondes, the time difference between dropsondes and Sentinel-1 data is limited within ± 2.5 h as shown in the table in Fig. 7.10. Since dropsondes were probably translated in some distance for this period, a correction of dropsonde locations is made along the trajectory of TC referring to the best track data. To be more specific, for dropsondes 1-7, their locations are shifted to the north whereas dropsondes 8-13 are shifted towards south dependent on the time difference. The final locations of dropsondes are shown in Fig. 7.10(b).

The HWRf model developed by the Hurricane Research Division of the Atlantic Oceanographic and Meteorological Laboratory provides wind components at 74 levels from 10 m to 30 km at 0 UTC on 10 Oct 2018. Since wind components are first provided on a resolutions of 3 km, it is remapped on SAR grids with 1-km resolution for further comparison. Note that the HWRf data is provided around 15 mins after SAR acquisition time. Thus a translation of HWRf data is also proposed. To this end, the center of HWRf data is first shifted southeast to SAR center in 7 km, as depicted in Fig. 7.11(a). Since TC keeps rotating as moving towards the land, we also rotate HWRf data clockwise 4° after checking the NEXRAD measurements. One may notice that the inner and outer rainbands differ at different rotating velocity. Here we just selected the three rainbands in some distances for simplicity. As shown in Fig. 7.12,

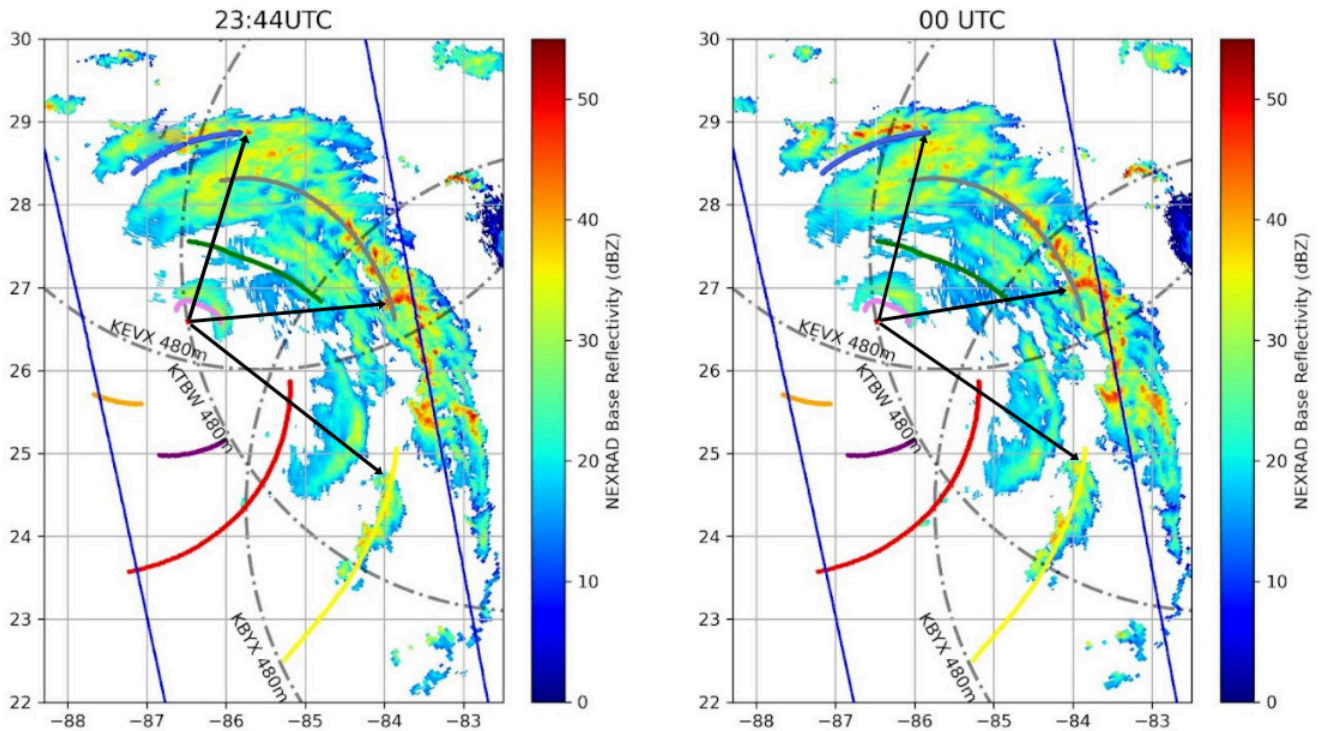


Figure 7.12: Base reflectivity from three NEXRAD stations, KEVX, KTBW and KBYX. The measurements were at 23:45 on 9 Oct 2018 and on 0 UTC on 10 Oct 2018 respectively. The dash line denotes the maximum detection range for each weather radar station. Colored lines are the extracted streamlines for each rainband. The black lines with arrows were intended for the estimating the degree of rotation.

rain cells in three rainbands shows apparent rotation as pointed by the black lines with arrows. Thus a mean rotation of $\sim 4^\circ$ is got and applied on HWRF after a shift.

7.2.2 Wind directions compared with dropsondes

As described in Section 7.1, the streamlines for rainbands can be extracted by assuming the partial rainband fit in the logarithm spiral. As shown in Fig. 7.12, the streamlines for rainband 6 (yellow), 7 (gray) and 8 (royalblue) are well collocated with NEXRAD base reflectivity shape at 23:44 UTC. The streamline for rainband 1 (pink) shows a little rotation with reflectivity due to a fast rotation of eyewall. Limited by the NEXRAD detection range, it is difficult to compare the other rainbands with the base reflectivity. But with the 4 collocated rainbands, we can see that the extracted streamlines have a good capability of presenting the spiral patterns of rainbands. Since the rainbands has some distance with the dropsondes,

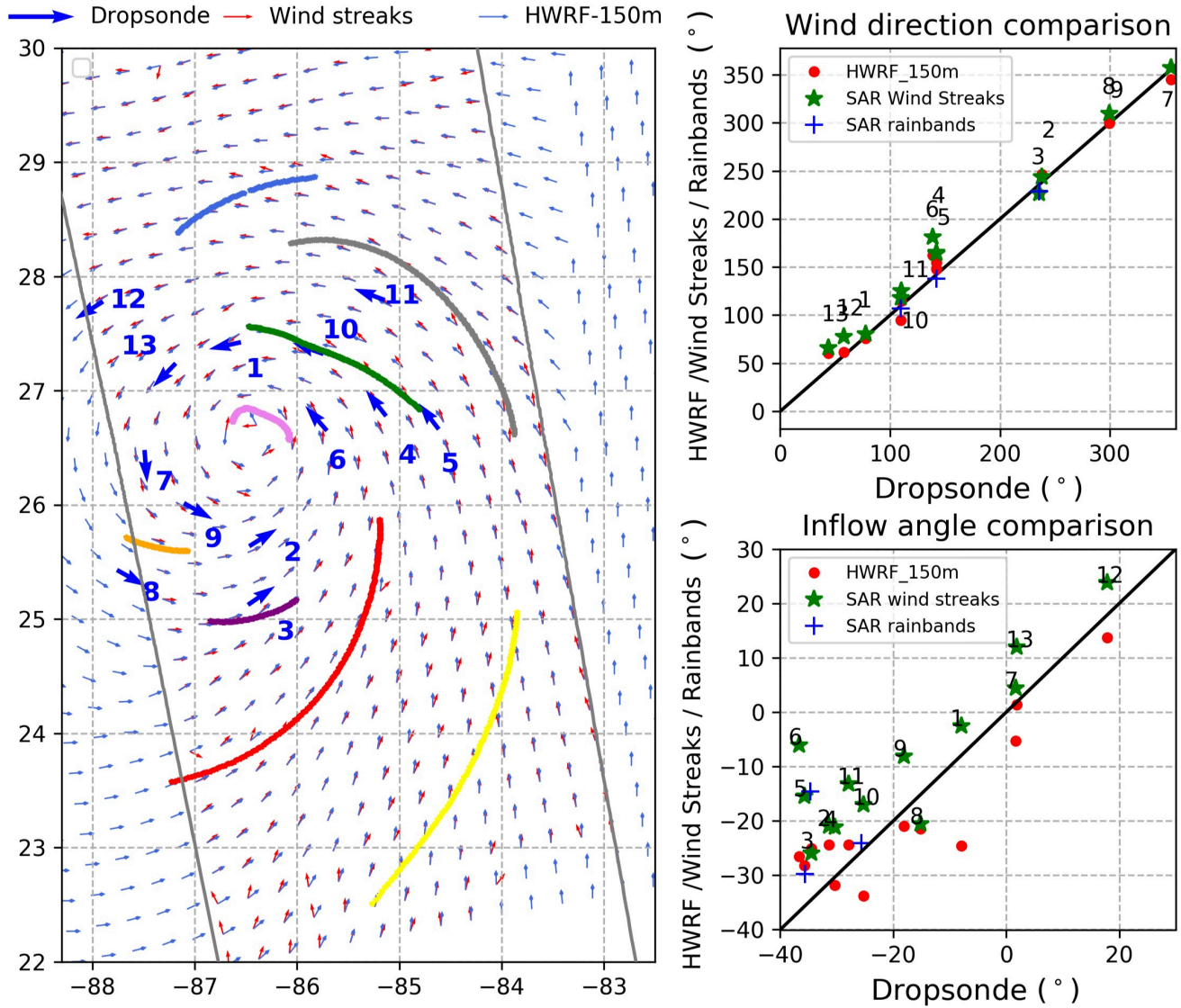


Figure 7.13: Left panel shows the wind direction from in situ dropsondes(bold blue arrow), wind streaks(thin red arrow) and HWRf data (thin blue arrow) at a height of 150 m. The colored lines denoted the streamlines of flagged rainbands in Fig. 7.3. The right panel compares inflow angle (α) and wind direction from HWRf data and wind streaks with dropsondes.

just dropsondes 3, 5, 10 close to the rainbands are collected for the comparison.

For the 3 dropsondes, three points in rainbands in closet distance are compared in terms of wind directions and inflow angles. The wind direction and inflow angle from rainband 2(green) and 5 (purple) are both in good agreement with the dropsondes 10 and 3 respectively. The inflow angles are computed by the difference between the unit vector u and the wind vectors from dropsondes in polar coordinates

similar to the estimation for rainbands in Fig. 7.2. For dropsonde 3, despite very close wind direction, the inflow angles are much larger than rainband, indicating an inflow pushing the rainband inward.

Koch (2004) proposed local gradient method to derive wind direction directly from wind streaks on SAR images. Fan et al. (2019) applied the local gradient method to SAR images with TCs and had a good estimation of wind direction from dual-pol Sentinel-1 data with a bias and RMSE of -0.54° and 14.78° . Also they removed the 180° ambiguity by assuming a threshold for each quadrant depending on the hemisphere. The gradient histogram for each single polarization were combined to uncover the direction of maximum gradient, serving for the final wind direction in TCs. For Micheal, the wind direction is extracted on the resolution 8 km in the eyewall and 25 km in the peripheral region, then interpolated on 1 km. It can be seen that in Fig. 7.13, the wind vectors derived from wind streaks (red arrows) display the cyclonic structures. But in area very close to center, the wind direction accuracy decreases with the opposite direction in local region (Fan et al., 2019).

The wind direction and inflow angles estimated from wind streaks are compared with dropsondes as shown in Fig. 7.13. Good agreement of wind direction is observed but the inflow angles from wind streaks are almost larger than dropsondes. As known, wind streaks are strongly associated with atmosphere boundary layer rolls whose axis is above the sea surface. The difference between the mean wind direction and the roll direction vary from approximately -30° to 10° with a mean of -4° reported by Foster (2005). Here the mean difference between them is about -10° , in line with the previous observation.

Given dropsonde measures wind directions at 150 m, wind directions and inflow angles from HWRF data at the same height are compared with dropsondes in Fig. 7.13. As observed, the inflow angle difference between HWRF data and dropsondes have a mean bias of -3.2° . Most inflow angles from HWRF are lower than dropsondes, more inward to the TC center. That might be impacted by the translation of dropsondes or an underestimation of dropsonde height due to an oblique path .

7.2.3 Comparison between wind streaks and rainbands

Fig. 7.14 compares the inflow angles and wind directions from wind streaks and derived rainband streamlines. As for the wind direction, the directions from rainbands and wind streaks show a high agreement, with the correlation coefficient of 0.89 and bias of -7.8. However, the correlation coefficient for inflow angles drops to 0.16 but the bias improves to 5.9 due to different coordinates. In particular, the inflow angles for rainband 1 (pink) have great bias (over 50°) compared with wind streaks, probably because the wind directions estimated from wind streaks around TC eye are not that accurate. It is known that the accuracy of wind direction estimation by gradient methods is very sensitive to the inhomogeneity

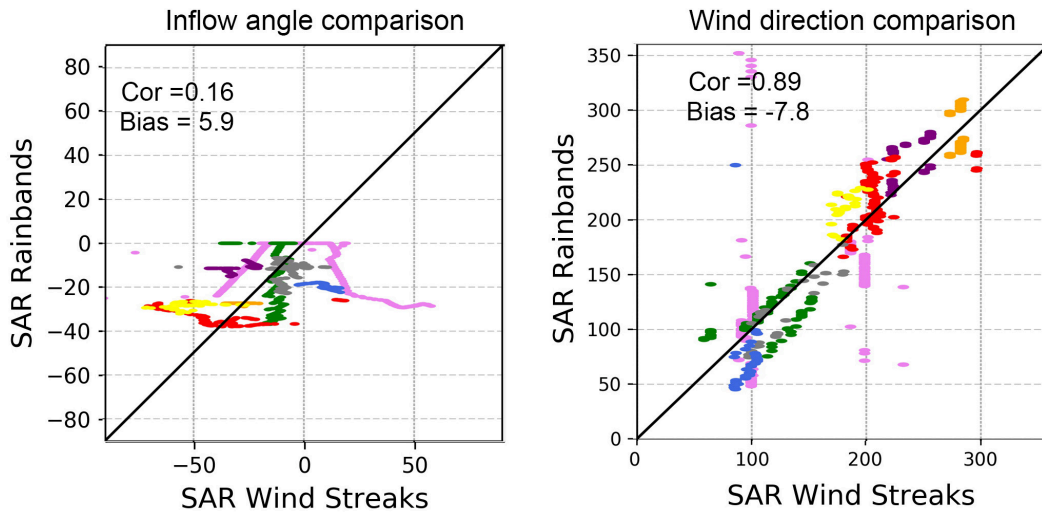


Figure 7.14: (a) Inflow angle (α) from SAR wind streaks are compared with that from the streamlines of rainbands. (b) wind direction comparison between SAR wind streaks and rainbands.

in the vicinity. The obscuration of wind streaks existing between the TC eye and the radius of maximum wind speed, would lead to great bias. Besides, other patterns in addition to wind streaks can also give rise to some errors in the estimation. Moreover, we need to note that the resolution of wind streaks are first estimated from 8 km, whereas the attenuation of rainband in eyewall is at a little larger scale (Fig. 4.15).

For rainband 5 (red), wind directions from rainbands are slightly larger than SAR wind streaks. And the inflow angles of rainbands almost keep consistent, around -35° , whereas wind streaks have the inflows from -70° to -2° . Similarly, the inflow angles of rainband 4 (purple), rainband 6 (yellow) and rainband 8 (royalblue) also have little variation, around -30° , -10° , -20° respectively yet corresponding to a large inflow variation from wind streaks. Rainbands with the same inflow angle give an evidence about equiangular spirals proposed by Senn et al. (1957) and Lahiri (1981). By comparison, the inflow angles of rainband 2 (green) and rainband 7 (gray) in the northeast of the eye have large variation but wind streaks have almost the constant inflow angles. The comparison shows the asymmetry of inflow angles of rainbands different from wind streaks, might associated with the direction of the wind shear.

7.2.4 Comparison between HWRF data and rainbands

HWRF provides the wind components at multiple layers at the height from 10 m to 63 km. Our analysis shows that the correlation coefficient and bias between HWRF and SAR derived rainbands also change with height before and after translation (Fig. 7.11). After the shift and rotation of HWRF data,

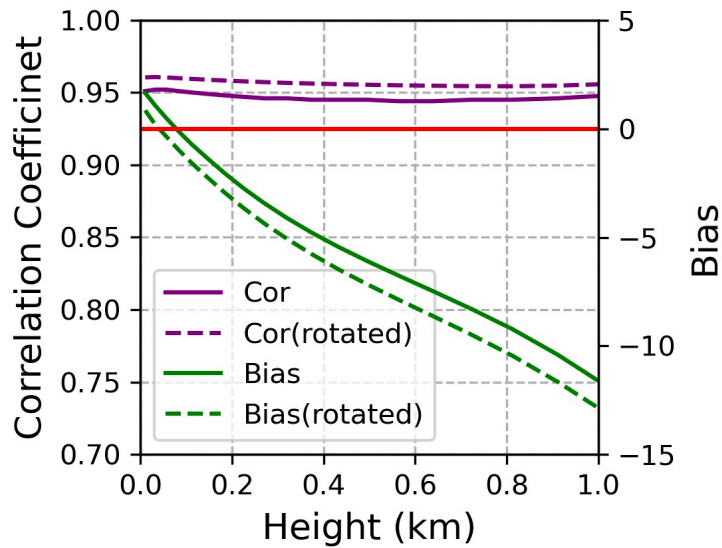


Figure 7.15: The correlation coefficient and bias of wind direction between SAR rainband streamlines and HWRP data at different heights are shown before (solid) and after (dash) HWRP data shift and rotation.

the correlation coefficient improves and the bias decreases, indicating the efficiency of the translation. And the bias crossing 0 at a lower height, about 100 m.

Fig. 7.16 shows the inflow angle and wind direction comparison between rainbands and HWRP wind components at 3 layers (10 m, 500 m, 1 km). As observed, the total bias in wind direction/inflow angle comparison improves with height due to the wind direction variation from HWRP at different layers. Meantime, it can be noted that the bias for different rainbands differ from each other. For rainband 1 (pink) around the TC center, the inflow angles from HWRP at layer 10 m have the best agreement with rainbands compared with other layers. Especially at 1 km, the inflow angles from HWRP are almost positive, indicating a strong outflow in the eyewall region. We can also observe that rainband 2 (green), rainband 4 (purple) and rainband 5 (red) have larger inflow angles than that from HWRP data at height of 10 m. But with height increasing, the inflow angles from HWRP gradually increase. It suggests that the inflow from winds becomes weaker at a higher altitude. Particularly for rainband 5 (red), the inflow angles from rainbands are almost larger than HWRP at 10 m but lower than HWRP at 1 km. Rainband 8 (royalblue) always has larger inflow angles than HWRP even at the lowest layer. This explains the apparent outward movement of the rainband in 15 mins from the continuous NEXRAD reflectivity observations (Fig. 7.12).

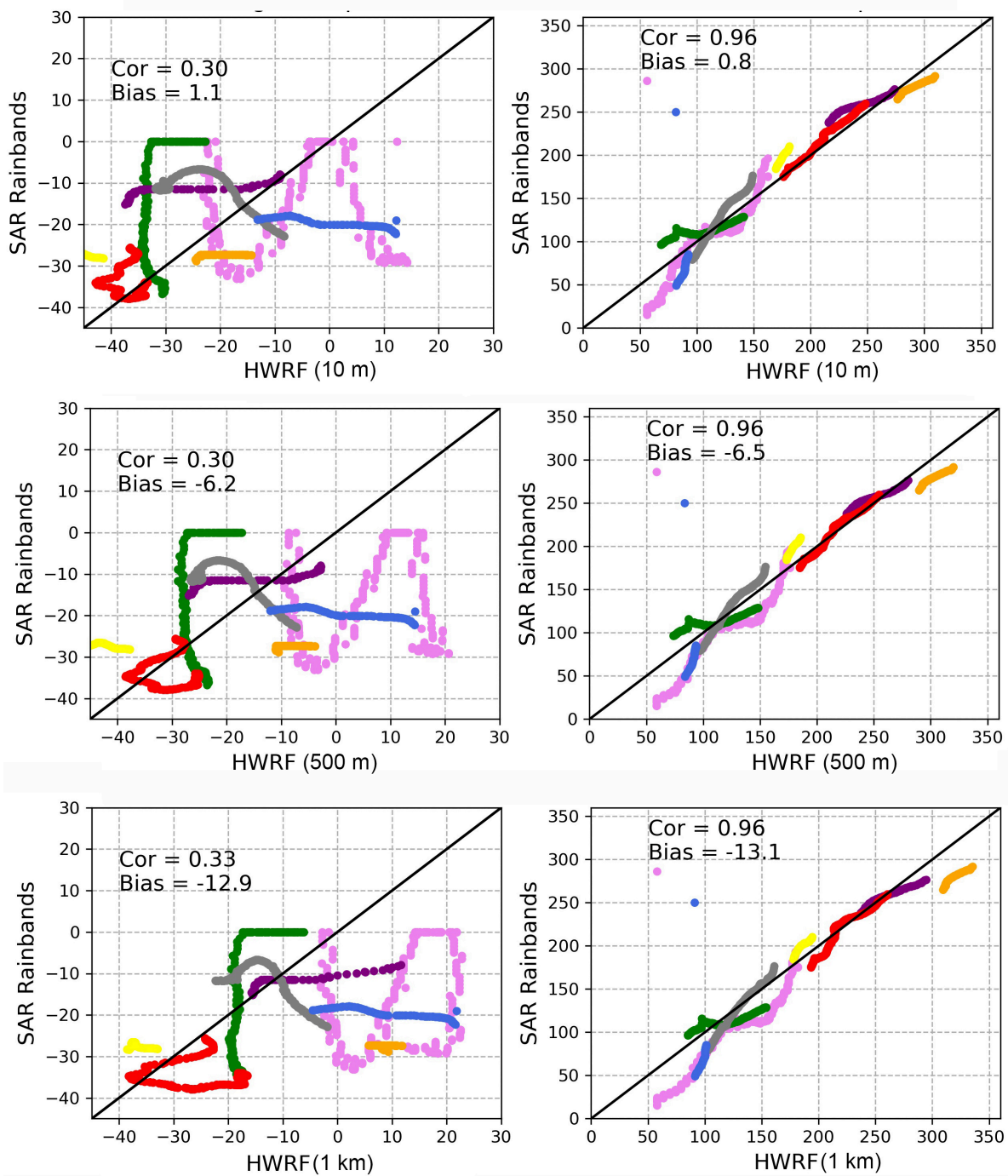


Figure 7.16: Inflow angle (left panel) and wind direction (right panel) from SAR rainbands are compared with HWRf data at three heights, 10 m, 500 m, and 1 km.

7.2.5 Comparison between wind streaks and HWRf data

As mentioned before, an estimation of wind direction in hurricane can be retrieved from the wind streaks in SAR images by the gradient method. The wind streaks are known associated with atmosphere

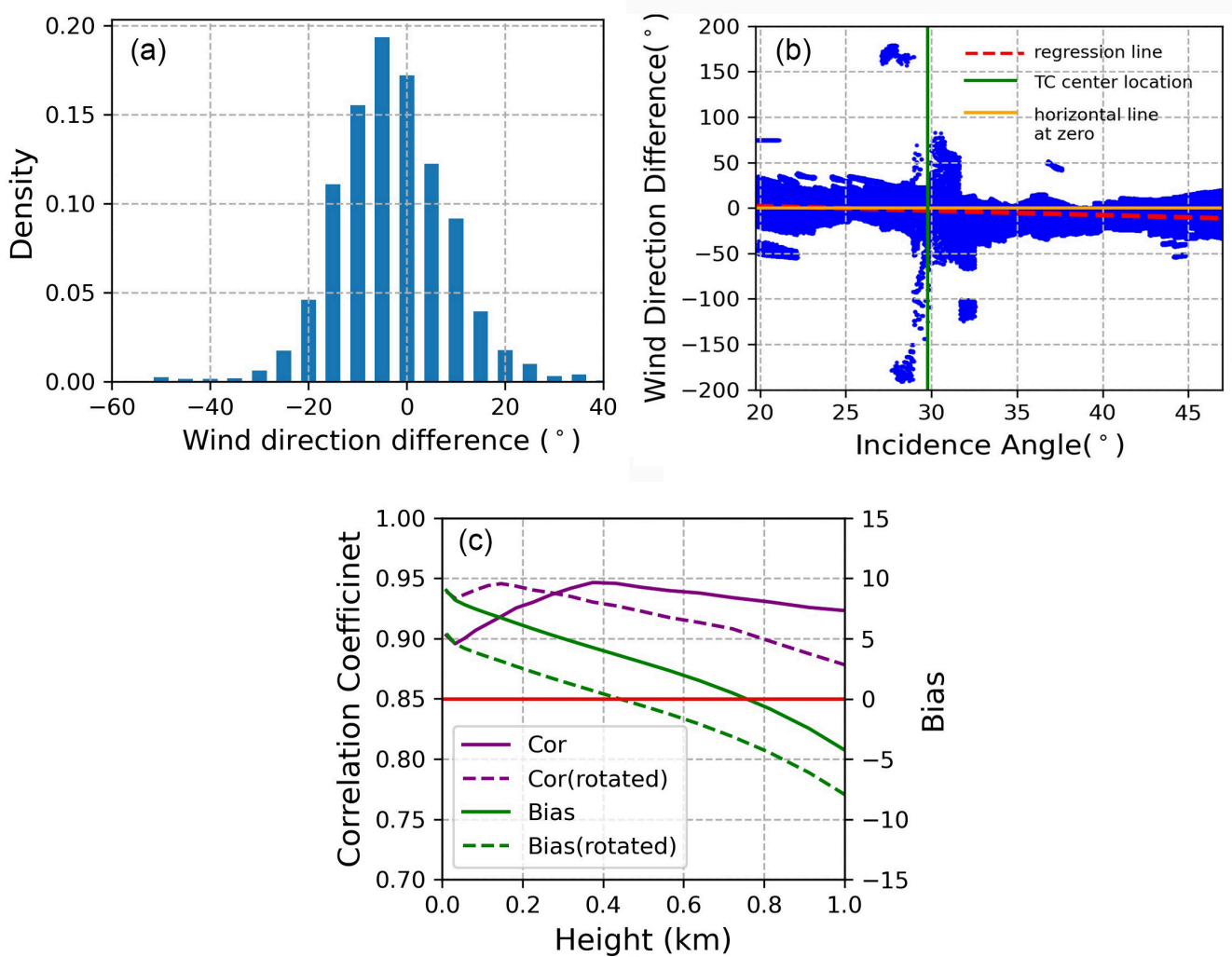


Figure 7.17: (a) The histogram of wind direction difference between HWRF (10 m) and wind streaks. (b) the wind direction difference against incidence angle. The dash red line is the regression fit on the scatter points. The green line marks the location of TC center. The orange line denotes the location of difference equal to 0. (c) The correlation coefficient and bias between SAR wind streaks and HWRF data are shown at increasing heights before (solid) and after (dash) HWRF data shift and rotation .

boundary rolls, which are prevalent in hurricanes. The turbulence away from the deep convection of rainbands helps to form the rolls due to the instability in the hurricane boundary layer, i.e., the inflection point present in vertical wind profiles (Foster, 2005). In previous observation, the rolls are oriented $\sim 4^\circ$ on average to the left of the mean wind direction, and with a mean depth of 660 m (Foster, 2005; Morrison et al., 2005). Here we compare the wind direction from wind streaks and HWRF data to check the characteristics of the rolls.

Fig. 7.17(a) shows a histogram of wind direction difference between HWRf data at 10 m and wind streaks. More than 90% data is located in the range from -20° to 10° with a mean of -5° , close to the mean of -4° in Morrison et al. (2005). And it is noticeable that the points with difference of $\pm 60^\circ$ are around center, as shown in Fig. 7.17(b). In the map of Fig. 7.13, we can observe the some difference between HWRf and wind streaks in the eyewall. The large difference is probably due to the different resolutions of wind streaks and HWRf data, on 8 km and 3 km, respectively. Also, we can see that the wind direction difference slightly decreases with incidence angle. That means the wind directions from wind streaks are overestimated in small incidence angles but underestimated in larger incidence angle.

Further comparison of wind direction is made between wind streaks and HWRf at different layers, leading to the variation of the corresponding correlation coefficient and bias. Similar to Fig. ??, the correlation coefficient and bias are shown before and after the shift and rotation in Fig. 7.17. As seen, the correlation coefficient first increases and then decreases whereas the bias keep decreasing with height. The bias decreases to 0 at 780 m and 420 m before and after translation. This suggests that the mean direction of atmospheric rolls existing in boundary layer is controlled by the wind direction at the height of several hundred meters.

7.3 Summary

This section shows the inflow angles and wind directions by using the rainband mask in TCs. The inflow angles are strongly dependent on normalized radial radius. In particular, in the region close to center, the inflow angles are close to zero, indicating a rough circular shape for the inner rainband. With the increasing radial distance, the mean of inflow angles decreases but with increasing standard deviation. Meantime, the rainband is also impacted by the translation speed, maximum wind speed, and its radius. A TC at high category with a fast translation speed and relative small eye are usually observed with higher inflow angles.

The wind directions and inflow angles from dropsondes, HWRf data, SAR derived wind streaks and rainbands are compared in the case of Michael. The intercomparison of wind directions among these dataset shows good agreement. But with the inflow angles, more difference is observed. Based on the difference between wind streaks and HWRf winds, the scale of rolls can be predicted below 1 km. Meantime, with the wind directions from HWRf, it can be seen the outwards in rainband of eyewall and more large inflows. It probably can be used to predict the intensification or depression of TCs by examining the inflow angle behavior.

Conclusions

Contents

8.1	Conclusions	126
8.2	Future work	128

8.1 Conclusions

This study takes benefit of the Sentinel-1 C-band SAR mission new capabilities that provides observations over the sea surface in both co- and cross-polarization and of the significant number of data now routinely acquired in coastal areas. With these advantages, we systematically analyze the precipitation signatures observed in Sentinel-1 images collocated with high-resolution measurements from ground-based radar from US and Japanese networks. The investigation, based on the collocated dataset, evaluates the impacts of the rain intensity on C-band radar backscatter, on which a transfer model is proposed to discuss the mechanisms of the signatures associated with rainfall. Those quantitative analyses not only help to develop the algorithms to detect the signatures of tropical rain cells and rainbands in TCs but are also favorable for understanding the interaction between the raindrops and microwaves and have the potential to predict the evolution of TC structures.

Upon evaluating the rain impact on radar backscatter, we found that heavy rainfall generally increases the radar backscatter under low to moderate wind regimes at co- and cross-polarization, although at C-band concurrent bright and dark patches are observed in many cases. Additionally, the radar backscatter contaminated by rain is also polarization and incidence angle dependent. The rain signature is found to be more pronounced at high incidence angles in VV but not in VH. Especially at low incidence angles, the rain signatures can be observed as dark areas in VV but bright areas in VH. For TCs, the inner rainband especially the eyewall appears as dark bands close to the center for cases from category-1 to category-4. The radial location of the heaviest precipitation in eyewall gets closer to the RMW as TC becomes intenser. Comparatively, the outer rainband especially distant rainbands are often bright patches surrounded by some dark spots and probably are bright in VH but dark in VV. Signatures of rainbands

is also dependent on the surrounding wind speed and incidence angles, similar to tropical rain cells.

A numerical model to analyze the signature of rain in SAR images has been developed to compute the radar backscatter under different rain rate. It is based on the transfer equation of electromagnetic wave through the atmosphere. The NRCS simulated by this model has a good agreement with observation, and proves that the effects of volume scattering and attenuation on raindrops are main contributor to the signatures apparent in SAR images. Also since rainbands can have a significant rotation within minutes, the validation on this model greatly benefits from the short time gap between SAR data and weather radar measurements.

According to the qualitative analysis in the first two chapters, the precipitation signatures are well known in different rain rates and wind speeds. As for rain cell detection, the filter as defined by Koch (2004) has been implemented on both co- and cross-polarization channels, for different resolutions. A threshold has been defined to maximize the rain detection based on the collocated dataset. The results we obtained show that the combination of the filters computed for each polarization channel at two different resolutions (VV: 400 m and VH: 800 m) significantly improves the rain detection capability in comparison of using only co- or cross-polarization filters.

Another method targeting on rainband detection in TCs is based on the difference of SAR data at multiple resolutions. Although limited TC cases are collected to train the best threshold for both polarizations, it still shows the good capability of locating rainbands in TCs, even better than the dual-pol filter above. However, similar to dual-pol filter, the detection of precipitation decreases with increasing wind speeds but increase with rainfall rate. This method helps locate the rainbands in TCs, serving for the further spiral pattern analysis of rainbands.

With the method above, we manually extract the shapes of rainbands for a total of 54 TC cases. The shape of rainbands display the spiral patterns and are applied to extract the streamlines by fitting a logarithmic spiral on each segment. The inflow angles from the SAR derived rainbands shows strong dependence on the radial distance, also with the impact of translation speed (V_s), maximum wind speed (V_{max}) and its radius(RMW). High-category TCs with small eye and fast translation speed are prone to have small inflow angles.

Meantime, the inflow angles and wind directions from SAR derived rainbands are compared with in situ dropsondes, HWRF data and SAR extracted wind streaks in the case of Michael. Good agreements are found in the intercomparison of wind directions whereas the inflow angles are observed with some difference. with the wind directions from HWRF, it can be seen the outwards in rainband of eyewall and more inflows in outer rainbands. In addition, the wind streaks extracted from SAR is in good line with

the wind direction from HWRF at 420 m. It reveals the rolls constrained in the atmosphere boundary layer below 1 km.

8.2 Future work

The present work was conducted based on the collocated C-band SAR data and weather radar measurements. Base reflectivity provided by NEXRAD is measured at an elevation angle of 0.5° . Yet since the weather radar can reach a maximum distance of 480 km, the weather radar beam can reach a height of 6 km close to the furthest detection distance. As known, the base reflectivity varies with height. In particular, the base reflectivity in stratiform precipitation usually displays the maximum around melting layer (4-5 km). Thus, rain rate derived from base reflectivity at 0.5° may not be the same with that reaching sea surface, depending on the beam height. This is also one of the factors leading to large errorbars in the statistics of $NRCS_{ratio}$ in Fig. 4.5. Despite this, the quantitative analysis about the NRCS under different rain rates shows a general trend about the NRCS and rain rate, which can help people to recognize the features of precipitation in SAR images as well as understand the different response of precipitation to polarizations.

As for the mechanisms of precipitation signatures, we refer to hydrometeor classification provided by NEXRAD L3 products. These products can only be provided at several elevation angles similar to base reflectivity. This leads to data deficiency at many heights, i.e., the discontinuity of hydrometer distribution over the vertical. For the furthest pixels, the product can be only available for the top elevation, above the melting layer. Comparatively, for rain cells close to the weather radar it can be available at all the elevations, depending on the distance between the rain cells and the radar. Even though we collected the classification results at all the levels, the statistics about the hydrometer distribution for bright patches needs further validation.

Jameson et al. (1997) noticed the strong signal returned at the melting layer only at cross-polarization. Our statistical results show that the NRCS at cross-polarization is more sensitive to heavy rainfall especially at high winds. Up to now, weather radar can only provide the classification product of hydrometers based on a fuzzy logic scheme but without any information about densities. This brings great challenge to simulate the different kind of hydrometeors in one volume. Given the local measurements about the concentration and density are provided, it is still possible to include multiple scattering on these different hydrometeors.

The dual-polarization filters proposed are hopefully applied on other C-band satellite data, i.e.,

RADARSAT-2, yet the incidence angle differing from Sentinel-1 might gave slightly different performance. The encouraging performance of a dual-polarization filter to detect rain signatures in SAR images seems to be applicable also to other, non-rain-related features visible on SAR images, such as roll vortices (C. Wang et al., 2020). Additionally, in the particular case of rain detection and segmentation, further work could be done to decipher between the various rain contributions (i.e., stratiform rain, convective rain) and the possible relationship of backscattered signal with lightning events by exploiting the full capability of SAR (for instance, by including phase information), including data from ground-based radars but also other ancillary products such as the Geostationary Global Lightning Mapper (GLM).

The spiral pattern of TC rainbands can be a good indicator of TC intensity and evolution with more co-analysis with models and in situ observations. In particular, with advantage of Satellite Hurricane Observation Campaign (SHOC), more TC cases are being collected continuously. The vertical structure of inflows can be further examined for TCs at different category by the collocation between SAR observation with dropsondes and HWRF. Besides, the inflow of inner rainbands and outer rainbands has the potential to identify the intensification or depression during the TC evolution's and to extract the maximum wind speed around TC eye.

References

- Allison, Lewis J, Edward B Rodgers, Thomas T Wilheit, and Robert W Fett (1974). “Tropical cyclone rainfall as measured by the Nimbus 5 electrically scanning microwave radiometer”. In: *Bulletin of the American Meteorological Society* 55.9, pp. 1074–1090.
- Alpers, Werner, Biao Zhang, Alexis Mouche, Kan Zeng, and Pak Wai Chan (2016). “Rain footprints on C-band synthetic aperture radar images of the ocean-Revisited”. In: *Remote Sensing of Environment* 187, pp. 169–185. ISSN: 0034-4257. DOI: <https://doi.org/10.1016/j.rse.2016.10.015>.
- Atlas, David (1994). “Footprints of storms on the sea: A view from spaceborne synthetic aperture radar”. In: *Journal of Geophysical Research: Oceans* 99.C4, pp. 7961–7969.
- Ban, Yifang and Osama Yousif (2016). “Change detection techniques: A review”. In: *Multitemporal Remote Sensing*, pp. 19–43.
- Battan, Louis J (1971). “Radar attenuation by wet ice spheres”. In: *Journal of Applied Meteorology* 10.2, pp. 247–252.
- Best, AC (1950). “The size distribution of raindrops”. In: *Quarterly Journal of the Royal Meteorological Society* 76.327, pp. 16–36.
- Black, Michael L, Robert W Burpee, and Frank D Marks Jr (1996). “Vertical motion characteristics of tropical cyclones determined with airborne Doppler radial velocities”. In: *Journal of Atmospheric Sciences* 53.13, pp. 1887–1909.
- Bliven, L. F. and J. P. Giovanangeli (1993). “An experimental study of microwave scattering from rain-and wind-roughened seas”. In: *International Journal of Remote Sensing* 14.5, pp. 855–869.
- Bliven, L. F., P. W. Sobieski, and C. Craeye (1997). “Rain generated ring-waves: measurements and modelling for remote sensing”. In: *International Journal of Remote Sensing* 18.1, pp. 221–228.
- Braun, N and M Gade (2006). “Multi-frequency scatterometer measurements on water surfaces agitated by artificial and natural rain”. In: *International Journal of Remote Sensing* 27.1, pp. 27–39. DOI: [10.1080/01431160500239214](https://doi.org/10.1080/01431160500239214).
- Browne, Ian C and NP Robinson (1952). “Cross-polarization of the radar melting-band”. In: *Nature* 170.4338, pp. 1078–1079.

- Cavaleri, Luigi, Luciana Bertotti, and Jean-Raymond Bidlot (2015). “Waving in the rain”. In: *Journal of Geophysical Research: Oceans* 120.5, pp. 3248–3260.
- Cheng, Jingjing and Qingqing Li (2020). “A numerical study of convective-scale downdrafts in the outer core of tropical cyclones in vertically varying environmental flows”. In: *Tropical Cyclone Research and Review* 9.3, pp. 143–161. ISSN: 2225-6032. DOI: <https://doi.org/10.1016/j.tcrr.2020.06.002>. URL: <https://www.sciencedirect.com/science/article/pii/S2225603220300357>.
- Contreras, Robert F and William J Plant (2006). “Surface effect of rain on microwave backscatter from the ocean: Measurements and modeling”. In: *Journal of Geophysical Research: Oceans* 111.C8. DOI: 10.1029/2005JC003356.
- Craeye, Christophe and Piotr W Sobieski (1995). “Numerical modelling of radar signatures of splashes produced by rain drops on water surfaces”. In: *1995 International Geoscience and Remote Sensing Symposium, IGARSS'95. Quantitative Remote Sensing for Science and Applications*. Vol. 1. IEEE, pp. 839–841.
- Craeye, Christophe, Piotr W Sobieski, Larry F Bliven, and Albert Guissard (1999). “Ring-waves generated by water drops impacting on water surfaces at rest”. In: *IEEE journal of oceanic engineering* 24.3, pp. 323–332.
- D’Amico, Michele MG, Anthony R Holt, and Carlo Capsoni (1998). “An anisotropic model of the melting layer”. In: *Radio Science* 33.3, pp. 535–552.
- Danklmayer, Andreas, Björn J Doring, Marco Schwerdt, and Madhu Chandra (2009). “Assessment of atmospheric propagation effects in SAR images”. In: *IEEE Transactions on Geoscience and Remote Sensing* 47.10, pp. 3507–3518.
- Dodge, Peter, Robert W Burpee, and Frank D Marks Jr (1999). “The kinematic structure of a hurricane with sea level pressure less than 900 mb”. In: *Monthly weather review* 127.6, pp. 987–1004.
- Draper, David W and David G Long (2004). “Evaluating the effect of rain on SeaWinds scatterometer measurements”. In: *Journal of Geophysical Research: Oceans* 109.C12.
- Dvorak, Vernon F (1975). “Tropical cyclone intensity analysis and forecasting from satellite imagery”. In: *Monthly Weather Review* 103.5, pp. 420–430.
- Fan, Shengren, Biao Zhang, Alexis A Mouche, William Perrie, Jun A Zhang, and Guosheng Zhang (2019). “Estimation of wind direction in tropical cyclones using C-band dual-polarization synthetic aperture radar”. In: *IEEE Transactions on Geoscience and Remote Sensing* 58.2, pp. 1450–1462.
- Fett, Robert W and Samson Brand (1975). “Tropical cyclone movement forecasts based on observations from satellites”. In: *Journal of Applied Meteorology and Climatology* 14.4, pp. 452–465.

- Foerster, Annette M, Michael M Bell, Patrick A Harr, and Sarah C Jones (2014). “Observations of the eyewall structure of Typhoon Sinlaku (2008) during the transformation stage of extratropical transition”. In: *Monthly Weather Review* 142.9, pp. 3372–3392.
- Foote, G Brant and PS Du Toit (1969). “Terminal velocity of raindrops aloft”. In: *Journal of Applied Meteorology* 8.2, pp. 249–253.
- Foster, Ralph C (2005). “Why rolls are prevalent in the hurricane boundary layer”. In: *Journal of the Atmospheric Sciences* 62.8, pp. 2647–2661.
- Fu, Lee-Leung and Benjamin Holt (1982). “Seasat views oceans and sea ice with synthetic-aperture radar”. In: 81.
- Green, T and DF Houk (1979). “The mixing of rain with near-surface water”. In: *Journal of Fluid Mechanics* 90.3, pp. 569–588.
- Hence, Deanna A and Robert A Houze Jr (2011). “Vertical structure of hurricane eyewalls as seen by the TRMM Precipitation Radar”. In: *Journal of the Atmospheric Sciences* 68.8, pp. 1637–1652.
- Houze Jr, Robert A (2010). “Clouds in tropical cyclones”. In: *Monthly Weather Review* 138.2, pp. 293–344.
- (2014). “Clouds and precipitation in tropical cyclones”. In: *International Geophysics*. Vol. 104. Elsevier, pp. 287–327.
- Iguchi, Toshio and Atlas, David and Okamoto, Ken’ichi and Sumi, Akimasa (1995). “Footprints of storms on the sea in the JERS-1 SAR image”. In: *IEICE transactions on communications* 78.12, pp. 1580–1584.
- Jameson, Arthur R, Fuk K Li, Stephen L Durden, Ziad S Haddad, Benjamin Holt, Tim Fogarty, Eastwood Im, and Richard K Moore (1997). “SIR-C/X-SAR observations of rain storms”. In: *Remote Sensing of Environment* 59.2, pp. 267–279.
- Jorgensen, David F (1984). “Mesoscale and convective-scale characteristics of mature hurricanes. Part I: General observations by research aircraft”. In: *Journal of Atmospheric Sciences* 41.8, pp. 1268–1286.
- Katsaros, Kristina B, Paris W Vachon, W Timothy Liu, and Peter G Black (2002). “Microwave remote sensing of tropical cyclones from space”. In: *Journal of Oceanography* 58.1, pp. 137–151.
- Koch, Wolfgang (2004). “Directional analysis of SAR images aiming at wind direction”. In: *IEEE Transactions on Geoscience and Remote Sensing* 42.4, pp. 702–710.
- Lahiri, Abhijit (1981). “A study of cloud spirals of tropical cyclones”. In: *Mausam* 32.2, pp. 155–158.
- Lemaire, David, LF Bliven, Christophe Craeye, and Piotr Sobieski (2002). “Drop size effects on rain-generated ring-waves with a view to remote sensing applications”. In: *International Journal of Remote Sensing* 23.12, pp. 2345–2357.

- Li, Qingqing and Yuqing Wang (2012). “A comparison of inner and outer spiral rainbands in a numerically simulated tropical cyclone”. In: *Monthly Weather Review* 140.9, pp. 2782–2805.
- Li, Xiaofeng, Jun A Zhang, Xiaofeng Yang, William G Pichel, Mark DeMaria, David Long, and Ziwei Li (2013). “Tropical cyclone morphology from spaceborne synthetic aperture radar”. In: *Bulletin of the American Meteorological Society* 94.2, pp. 215–230.
- Lin, I-I, Werner Alpers, Victor Khoo, Hock Lim, Tian Kuay Lim, and Dayalan Kasilingam (2001). “An ERS-1 synthetic aperture radar image of a tropical squall line compared with weather radar data”. In: *IEEE Transactions on Geoscience and Remote Sensing* 39.5, pp. 937–945.
- Lin, Wenming, Marcos Portabella, Ad Stoffelen, Antonio Turiel, and Anton Verhoef (2014). “Rain identification in ASCAT winds using singularity analysis”. In: *IEEE Geoscience and Remote Sensing Letters* 11.9, pp. 1519–1523. DOI: 10.1109/LGRS.2014.2298095.
- Liu, Xinan, Quanan Zheng, Ren Liu, Dan Wang, James H Duncan, and Shih-Jen Huang (2016). “A study of radar backscattering from water surface in response to rainfall”. In: *Journal of Geophysical Research: Oceans* 121.3, pp. 1546–1562. DOI: 10.1002/2015JC010975.
- Marks Jr, Frank D (1985). “Evolution of the structure of precipitation in Hurricane Allen (1980)”. In: *Monthly Weather Review* 113.6, pp. 909–930.
- Marshall, J. S. and W. M. K. Palmer (1948). “The distribution of raindrops with size”. In: *J. Meteorol.* 5.165-166.
- Maynard, Russell H (1945). “Radar and weather”. In: *Journal of Atmospheric Sciences* 2.4, pp. 214–226.
- Melsheimer, Christian, Werner Alpers, and Martin Gade (1998). “Investigation of multifrequency/multipolarization radar signatures of rain cells over the ocean using SIR-C/X-SAR data”. In: *Journal of Geophysical Research: Oceans* 103.C9, pp. 18867–18884. DOI: 10.1029/98JC00779.
- (2001). “Simultaneous observations of rain cells over the ocean by the synthetic aperture radar aboard the ERS satellites and by surface-based weather radars”. In: *Journal of Geophysical Research: Oceans* 106.C3, pp. 4665–4677. DOI: 10.1029/2000JC000263.
- Mitnik, L (1992). “Mesoscale coherent structures in the surface wind field during cold”. In: *La mer* 30, pp. 287–296.
- Molinari, John, Paul Moore, and Vincent Idone (1999). “Convective structure of hurricanes as revealed by lightning locations”. In: *Monthly weather review* 127.4, pp. 520–534.
- Moore, R, Y Yu, A Fung, D Kaneko, G Dome, and R Werp (1979). “Preliminary study of rain effects on radar scattering from water surfaces”. In: *IEEE Journal of Oceanic Engineering* 4.1, pp. 31–32. DOI: 10.1109/JOE.1979.1145408.

- Morrison, Ian, Steven Businger, Frank Marks, Peter Dodge, and Joost A Businger (2005). “An observational case for the prevalence of roll vortices in the hurricane boundary layer”. In: *Journal of Atmospheric Sciences* 62.8, pp. 2662–2673.
- Mouche, Alexis A, Bertrand Chapron, Biao Zhang, and Romain Husson (2017). “Combined co-and cross-polarized SAR measurements under extreme wind conditions”. In: *IEEE Transactions on Geoscience and Remote Sensing* 55.12, pp. 6746–6755.
- Nie, Congling and David G Long (2007). “A C-band wind/rain backscatter model”. In: *IEEE Transactions on Geoscience and Remote Sensing* 45.3, pp. 621–631. DOI: 10.1109/TGRS.2006.888457.
- Nystuen, Jeffrey A (1990). “A note on the attenuation of surface gravity waves by rainfall”. In: *Journal of Geophysical Research: Oceans* 95.C10, pp. 18353–18355.
- Oguchi, T. (Sept. 1983). “Electromagnetic wave propagation and scattering in rain and other hydrometeors”. In: *Proceedings of the IEEE* 71.9, pp. 1029–1078. ISSN: 0018-9219. DOI: 10.1109/PROC.1983.12724.
- Olsen, Rogers, D. V. Rogers, and D. Hodge (1978). “The aR b relation in the calculation of rain attenuation”. In: *IEEE Transactions on antennas and propagation* 26.2, pp. 318–329. DOI: 10.1109/TAP.1978.1141845.
- Otsu, Nobuyuki (1979). “A threshold selection method from gray-level histograms”. In: *IEEE transactions on systems, man, and cybernetics* 9.1, pp. 62–66.
- Phan, Anh, Duong N Ha, Chuc D Man, Thuy T Nguyen, Hung Q Bui, and Thanh TN Nguyen (2019). “Rapid assessment of flood inundation and damaged rice area in red river delta from sentinel 1A imagery”. In: *Remote Sensing* 11.17, p. 2034.
- Reppucci, Antonio, Susanne Lehner, and Johannes Schulz-Stellenfleth (2007). “Tropical Cyclones Features Inferred from SAR Images”. In: *ENVISAT Symposium 2007*. 2P1, pp. 1–6.
- Reynolds, Osborne (1875). “On the action of rain to calm the sea”. In: *Proc. Lit. Phil. Soc. Manchester* 14, pp. 1874–1875.
- Rodriguez, Francisco and Russell Mesler (1985). “Some drops don’t splash”. In: *Journal of colloid and interface science* 106.2, pp. 347–352.
- Senn, H.W. Hiser, and R.C. Bourret (1957). *Studies of hurricane spiral bands as observed on radar*. Tech. rep. MIAMI UNIV FLA MARINE LAB.
- Senn, HV and HW Hiser (1959). “On the origin of hurricane spiral rain bands”. In: *Journal of Atmospheric Sciences* 16.4, pp. 419–426.

- Sezgin, Mehmet and Bülent Sankur (2004). “Survey over image thresholding techniques and quantitative performance evaluation”. In: *Journal of Electronic imaging* 13.1, pp. 146–165.
- Shi, Jian, Jiachen Hu, Weizeng Shao, Xiaoqing Wang, Xinzhe Yuan, Liangbo Zhao, and Xiaofeng Li (2019). “The impact of rain to observed signal from Chinese Gaofen-3 synthetic aperture radar in typhoons”. In: *Acta Oceanologica Sinica* 38.11, pp. 121–133.
- Slack, JK, AR Holt, and V Brown (1994). “Workpackage WP 400: Implementation of direct algorithms”. In: *Rain radar retrieval algorithms*.
- Sobieski, P. W. and L. F. Bliven (1995). “Scatterometry of a drop impact on a salt water surface”. In: *International Journal of Remote Sensing* 16.14, pp. 2721–2726.
- Tournadre, J and Y Quilfen (2003). “Impact of rain cell on scatterometer data: 1. Theory and modeling”. In: *Journal of Geophysical Research: Oceans* 108.C7.
- Tsimplis, M and SA Thorpe (1989). “Wave damping by rain”. In: *Nature* 342.6252, pp. 893–895.
- Ulaby, F. T., R. K. Moore, and A. K. Fung (1981). “Microwave Remote Sensing: Fundamentals and Radiometry”. In: *Artech House*.
- Vinour, Léo, Swen Jullien, Alexis Mouche, Clément Combot, and Morgan Mangeas (2021). “Observations of Tropical Cyclone Inner-Core Fine-Scale Structure, and Its Link to Intensity Variations”. In: *Journal of the Atmospheric Sciences* 78.11, pp. 3651–3671.
- Wang, Chen, Douglas Vandemark, Alexis Mouche, Bertrand Chapron, Huimin Li, and Ralph C Foster (2020). “An assessment of marine atmospheric boundary layer roll detection using Sentinel-1 SAR data”. In: *Remote Sensing of Environment* 250, p. 112031.
- Wetzel, LB (1990). “On the theory of electromagnetic scattering from a raindrop splash”. In: *Radio science* 25.06, pp. 1183–1197. ISSN: 1944-799X. DOI: 10.1029/RS025i006p01183.
- Wexler, Harry (1947). “Structure of hurricanes as determined by radar”. In: *Annals of the New York Academy of Sciences* 48.8, pp. 821–845.
- Willoughby, H.E. (1988). “The dynamics of the tropical cyclone core”. In: *Aus. Meteor. Mag.* 36, pp. 183–191.
- Willoughby, H.E., F.D. Marks, and R.J. Feinberg (1984). “Stationary and moving convective bands in hurricanes”. In: *Journal of the Atmospheric Sciences* 41.22, pp. 3189–3211.
- Worthington, Arthur Mason (1908). *A study of splashes*. Longmans, Green, and Company.
- Xiao, Jing, Zhe-Min Tan, and Kim-Chiu Chow (2019). “Structure and formation of convection of secondary rainbands in a simulated typhoon Jangmi (2008)”. In: *Meteorology and Atmospheric Physics* 131.4, pp. 713–737.

- Xu, Feng, Xiaofeng Li, Peng Wang, Jingsong Yang, William G Pichel, and Ya-Qiu Jin (2015). “A backscattering model of rainfall over rough sea surface for synthetic aperture radar”. In: *IEEE Transactions on Geoscience and Remote Sensing* 53.6, pp. 3042–3054. DOI: 10.1109/TGRS.2014.2367654.
- Yikun, Cai (1988). “Collision of water drop on water”. In: *Acta Mechanica Sinica* 4.4, pp. 297–304.
- Yu, Fangjie, Wuzi Sun, Jiaojiao Li, Yang Zhao, Yanmin Zhang, and Ge Chen (2017). “An improved Otsu method for oil spill detection from SAR images”. In: *Oceanologia* 59.3, pp. 311–317.
- Zhang, Guosheng, Xiaofeng Li, William Perrie, Biao Zhang, and Lei Wang (2016). “Rain effects on the hurricane observations over the ocean by C-band Synthetic Aperture Radar”. In: *Journal of Geophysical Research: Oceans* 121.1, pp. 14–26. DOI: 10.1002/2015JC011044.
- Zhang and Eric W. Uhlhorn (2012). “Hurricane sea surface inflow angle and an observation-based parametric model”. In: *Monthly Weather Review* 140.11, pp. 3587–3605.

Résumé de la thèse "Observations et quantifications des signatures de fortes précipitations à partir de mesures SAR à double polarisation en bande C"

Le radar à synthèse d'ouverture, fréquemment utilisé comme SAR (Synthetic Aperture Radar) spatial a la capacité de capturer divers phénomènes océaniques et atmosphériques, y compris les cellules de pluie tropicale et les bandes de pluie dans les cyclones tropicaux (TC). En 1978, Seasat a documenté les premières signatures de cellules de pluie tropicale et de TC dans des images SAR. Depuis lors, de nombreux efforts ont été consacrés à comprendre les mécanismes des signatures de pluie dans les images SAR. Cependant, il existe encore des points de vue contradictoires et des limites sur la recherche concernant l'ampleur de l'impact de la pluie sur la rétrodiffusion radar et la manière de reconnaître ces signatures de pluie dans les images SAR ainsi que la manière dont la direction du vent se répartit autour des bandes de pluie dans les TC. Ces incertitudes sont principalement dues aux jeux de données limités disponibles et aux grandes résolutions spatiales du passé. Cette recherche vise à découvrir et à expliquer la modification par la pluie de la rétrodiffusion radar en bande C et à proposer des algorithmes améliorés pour détecter les signatures de pluie dans les images SAR sous différents régimes de vent. En particulier, détecter les signatures des bandes de pluie dans les TC pourrait aider à comprendre les structures du vent en relation avec les rouleaux aux limites de l'atmosphère dans les TC. Ce chapitre fournira une introduction à l'étude en discutant d'abord de l'arrière-plan et du contexte, suivi du problème de recherche, des objectifs et de la signification de la recherche ainsi que de l'organisation générale de cette thèse.

Les signatures des précipitations dans les images SAR dépendent de la configuration instrumentale SAR (angle d'incidence, polarisation, fréquence), de la modification de la surface de la mer par la pluie (ondes circulaires, éclaboussures et amortissement des vagues) ainsi que des effets atmosphériques (diffusion volumique et atténuation).

Melsheimer(1998) a montré que les signatures de pluie étaient dépendantes de la fréquence en utilisant les données de la mission SIR-C/X-SAR (Spaceborne Imaging Radar-C/X-band SAR) en 1994. Ils ont comparé les signatures de pluie simultanément à L Bandes -, X et C basées sur les données SIR-C/X-SAR. Les signatures de précipitations en bande, C sont les plus compliquées à interpréter des trois fréquences, car la rétrodiffusion radar peut être améliorée ou réduite à cette fréquence, résultant des effets entrelacés de la modification de surface et des effets atmosphériques. De nombreux chercheurs se sont concentrés sur les structures de surface induites par la pluie pour comprendre les mécanismes des signatures de pluie, puisque les structures de surface (ondes annulaires, produites d'éclaboussures) sont couramment observées et peuvent être facilement créées en laboratoire. Ces structures modifient apparemment la rugosité de la surface de la mer et sont également des diffuseurs potentiels de micro-ondes incidentes. Quant aux effets atmosphériques, les gouttes de pluie peuvent diffuser et absorber les micro-ondes incidentes. L'atténuation et la diffusion sont assez importantes à haute fréquence (par exemple, bande Ku, bande X) mais ne peuvent pas être considérées comme négligeables en bande C, en particulier dans les fortes précipitations.

Les études existantes sur les signatures de pluie dans les images SAR en bande s'indiquent que la rétrodiffusion radar dans la zone de pluie est le résultat de plusieurs facteurs. Compte tenu des mécanismes complexes impliqués, il est difficile d'évaluer comment la section efficace radar normalisé (NRCS) répond au taux de précipitations et de séparer les contributions des différents processus. Sur ce, quelques études se sont concentrées sur des études de cas ou des modèles conceptuels explicatifs de l'impact de la pluie. Cependant, leurs résultats présentent des points de vue contradictoires sur la sensibilité du NRCS au taux de pluie et les modèles ne peuvent pas toujours être appliqués qualitativement aux images SAR. Par exemple, Lin(2014) a montré que le NRCS VV-pol augmente significativement avec le taux de pluie, même sous une pluie légère, tandis que Liu et al. (2016) a constaté que le NRCS

augmente avec la réflectivité de base jusqu'à 45 dBZ, puis diminue progressivement. Comme pour les modèles proposés, les facteurs pris en compte diffèrent ce qui rend difficile la compréhension des mécanismes impliqués.

La détection/reconnaissance des signatures de pluie dans les images SAR n'a pas été largement étudiée, principalement en raison du manque de mesure coïncidente du taux de précipitations. Au lieu de cela, de nombreux algorithmes ont été proposés pour la détection d'hétérogénéité dans les images SAR, que ce soit dans le domaine spectral ou spatial. Ces méthodes montrent une efficacité dans la détection d'objets, mais avec un défaut dans la reconnaissance de la signature de la pluie. Avec les avantages des informations à double polarisation de Sentinel-1, on peut s'attendre à ce qu'il serve grandement au développement de la détection de signature de pluie, en particulier la reconnaissance des bandes de pluie dans les TC qui pourraient non seulement aider à éliminer la zone contaminée par la pluie, mais aussi révéler la structure du cyclone et son développement potentiel.

Compte tenu des points de vue contradictoires et de la limitation de l'impact des précipitations sur la rétrodiffusion radar, cette étude tire parti des nouvelles capacités de la mission SAR en bande C Sentinel-1 qui fournit des observations sur la surface de la mer en co-polarisation et en polarisation croisée et de l'important nombre de données désormais acquises en routine dans les zones côtières. Avec ces avantages, nous analysons systématiquement les signatures de précipitations observées dans les images Sentinel-1 colocalisées avec les mesures haute résolution des radars au sol des réseaux américains et japonais. L'enquête, basée sur le jeu de données colocalisé, évalue les impacts de l'intensité de la pluie sur la rétrodiffusion radar en bande C, sur laquelle un modèle de transfert est proposé pour discuter des mécanismes des signatures associées à la pluie. Ces analyses quantitatives aident non seulement à développer les algorithmes pour détecter les signatures des cellules de pluie tropicales et des bandes de pluie dans les TC, mais sont également favorables à la compréhension de l'interaction entre les gouttes de pluie et les micro-ondes et ont le

potentiel de prédire l'évolution des structures des TC.

Pour être plus précis, les objectifs de cette étude sont : 1) Quantifier l'impact du taux de précipitations sur la rétrodiffusion radar en bande C sous différents régimes de vent et la différence entre la copolarisation et la polarisation croisée ; 2) Proposer un modèle pour évaluer la contribution de la diffusion volumique et de l'atténuation sur la rétrodiffusion radar lors de fortes pluies ; 3) Proposer les méthodes de reconnaissance des amas de cellules de pluie et des bandes de pluie dans les TC ; 4) Évaluer l'angle d'afflux et la direction du vent dérivés des bandes de pluie TC, des traînées de vent et de différents modèles. Cette étude vise à mieux comprendre la modification de la rétrodiffusion radar par les précipitations, en bénéficiant d'un grand ensemble de données colocalisées entre le SAR en bande C et le radar météorologique. Cet ensemble de données unique pourrait être largement utilisé pour d'autres études sur les précipitations et/ou comme données auxiliaires pour soutenir davantage d'enquêtes sur des sujets atmosphériques ou océaniques. Cependant, bien que l'ensemble de données soit considérablement volumineux, l'observation des TC est encore limitée en raison de l'occurrence limitée des TC. Ainsi, l'algorithme de détection de la bande de pluie nécessitera encore une validation supplémentaire en utilisant davantage de cas de TC. Les angles d'afflux autour des bandes de pluie dans les TC offrent une attention unique sur les structures des cyclones. En raison du nombre limité de TC, une analyse plus complète des angles d'afflux est nécessaire pour révéler la variation des vents de surface. De plus, comme le modèle proposé dans cette étude se concentre sur la transmission atmosphérique, il a de bons potentiels pour être intégré dans des modèles plus complexes à l'avenir.

Cette thèse est organisée en 8 chapitres. Dans le premier chapitre, l'historique et le contexte de l'étude sont présentés. Il présente également les objectifs de recherche et les questions suivies. En même temps, nous proposons les valeurs d'une telle recherche et quelques limites. Le deuxième chapitre résume la littérature existante

concernant l'observation des précipitations dans les données SAR et certaines expériences de laboratoire menées pour comprendre les structures induites par la pluie et la transmission atmosphérique lorsque les précipitations se produisent. Certaines méthodes de traitement d'images telles que la détection de cibles (méthodes de gradient local et de seuillage) déjà utilisées pour l'analyse d'images SAR est présentée.

Le chapitre trois décrit en détail les différents ensembles de données utilisés dans cette étude, y compris les images SAR, la mesure des précipitations par radar météorologique, le produit vent du Centre européen pour les prévisions météorologiques à moyen terme (ECMWF). Les données SAR sont acquises par Sentinel-1 et RadarSAT-2. Les données du radar météorologique proviennent des stations de radar météorologique de nouvelle génération (NEXRAD) et de l'Agence météorologique japonaise (JMA). Les données radars météo et le vent ECMWF sont colocalisés sur des grilles SAR temporairement et spatialement à la résolution de 1 km. La différence de temps entre les images SAR et le radar météorologique est inférieure à 10 min.

Dans le chapitre quatre, les statistiques de NRCS de polarisation VV et VH sont données avec des angles d'incidence et des vitesses de vent croissants en cas de cellules de pluie tropicales et de cyclones tropicaux respectivement . Lors de l'évaluation de l'impact de la pluie sur la rétrodiffusion radar, nous avons constaté que les fortes pluies augmentent généralement la rétrodiffusion radar dans des régimes de vent faible à modérés à co- et à polarisation croisée, bien qu'en bande C, des taches lumineuses et sombres simultanées soient observées dans de nombreux cas. De plus, la rétrodiffusion radar contaminée par la pluie dépend également de la polarisation et de l'angle d'incidence. La signature de la pluie est plus prononcée aux angles d'incidence élevés en VV, mais pas en VH. En particulier aux faibles angles d'incidence, les signatures de pluie peuvent être observées sous forme de zones sombres en VV, mais de zones claires en VH.

Les observations sur les TC sont analysées en termes de bandes de pluie en mur oculaire et en spirale. La précipitation dans le mur de l'œil induit une forte atténuation de la rétrodiffusion radar, représentée par une bande sombre autour du centre. En comparaison, les bandes de pluie en spirale sont représentées par des motifs différents avec une distance croissante par rapport au centre. Pour les bandes de pluie proches du mur de l'œil, on l'observe avec une région sombre en VV et VH, tandis que les bandes de pluie éloignées du centre peuvent être observées comme sombres en VV et lumineuses en VH, ou lumineuses avec des taches sombres dans les environs dans les deux polarisations. Les signatures des précipitations dans les TC dépendent également du taux de pluie, de la vitesse du vent et des angles d'incidence, comme dans le cas des cellules de pluie. En particulier, l'atténuation du mur oculaire est liée à l'amélioration de la catégorie de VV. De plus, les précipitations maximales se situent dans 1-2 RWM. Et avec l'augmentation du RMW, le RMRR s'éloigne du RMW, indiquant une dispersion des précipitations et un processus d'affaiblissement des TC.

Le chapitre cinq présente un modèle numérique qui a la capacité de simuler la rétrodiffusion radar sous différents taux de pluie. Dans ce mode, l'atténuation et la rétrodiffusion par les gouttes de pluie sont prises en compte et simultanément, les effets de surface sont négligés. Ce modèle est basé sur l'équation de transfert des ondes électromagnétiques à travers l'atmosphère. Le NRCS simulé par ce modèle est en bon accord avec l'observation, et prouve que les effets de la diffusion volumique et de l'atténuation sur les gouttes de pluie sont les principaux contributeurs aux signatures apparentes dans les images SAR. De plus, étant donné que les bandes de pluie peuvent avoir une rotation importante en quelques minutes, la validation de ce modèle bénéficie grandement du court intervalle de temps entre les données SAR et les mesures radar météorologique.

Dans le chapitre six, deux méthodologies avec la capacité de filtrer les cellules de pluie et les bandes de pluie dans les TC dans les images SAR sont présentées. Les nouveaux filtres sont développés à l'aide des données colocalisées sur les zones

côtières américaines et sont ensuite validés indépendamment à l'aide des données colocalisées sur l'archipel japonais. Comme pour la détection des cellules de pluie, le filtre tel que défini par Koch (2004) a été mis en œuvre sur les deux canaux de co-polarisation et de polarisation croisée, pour différentes résolutions. Un seuil a été défini pour maximiser la détection de pluie en fonction du jeu de données colocalisé. Les résultats que nous avons obtenus montrent que la combinaison des filtres calculés pour chaque canal de polarisation à deux résolutions différentes (VV : 400 m et VH : 800 m) améliore considérablement la capacité de détection de la pluie par rapport à l'utilisation uniquement de filtres de co-polarisation ou de polarisation croisée.

Une autre méthode ciblant la détection de la bande de pluie dans les TC est basée sur la différence des données SAR à plusieurs résolutions. Bien que des cas limités de TC soient collectés pour former le meilleur seuil pour les deux polarisations, cela montre toujours la bonne capacité de localisation des bandes de pluie dans les TC, encore mieux que le filtre à double polarité ci-dessus. Cependant, comme pour le filtre à double polarité, la détection des précipitations diminue avec l'augmentation de la vitesse du vent mais augmente avec le taux de précipitations. Cette méthode aide à localiser les bandes de pluie dans les TC, servant à l'analyse ultérieure du motif en spirale des bandes de pluie.

Dans le chapitre sept, les angles d'afflux et les directions du vent dérivés des bandes de pluie, des dropsondes in situ, des stries de vent et des données HWRF sont analysés dans TC Michael. Avec la méthode ci-dessus, nous extrayons manuellement les formes des bandes de pluie pour un total de 54 cas TC. La forme des bandes de pluie affiche les motifs en spirale et est appliquée pour extraire les lignes de courant en ajustant une spirale logarithmique sur chaque segment. Les angles d'afflux des bandes de pluie dérivées du SAR montrent une forte dépendance à la distance radiale, également avec l'impact de la vitesse de translation (V_s), de la vitesse maximale du vent (V_{max}) et de son rayon (RMW). Les TC de haute catégorie avec un petit œil et

une vitesse de translation rapide sont susceptibles d'avoir de petits angles d'entrée.

Entre-temps, les angles d'afflux et les directions du vent à partir des bandes de pluie dérivées du SAR sont comparés aux dropsondes in situ, aux données HWRF et aux stries de vent extraites du SAR dans le cas de Michael. De bons accords sont trouvés dans l'intercomparaison des directions du vent alors que les angles d'afflux sont observés avec une certaine différence. avec les directions du vent de HWRF, on peut voir l'extérieur dans la bande de pluie du mur oculaire et plus d'afflux dans les bandes de pluie extérieures. De plus, les stries de vent extraites de SAR sont bien alignées avec la direction du vent de HWRF à 420 m. Elle révèle les rouleaux contraints dans la couche limite de l'atmosphère en dessous de 1 km.

Dans cette thèse, nous étudions le potentiel des nouvelles capacités des récentes missions SAR pour localiser la signature de la pluie et en déduire les propriétés dans le cas particulier des cyclones tropicaux. En particulier, nous avons construit pour la première fois un ensemble de données complet avec à la fois des images SAR à haute résolution et des mesures de pluie à haute résolution à partir d'un radar de pluie au sol, y compris des cas extrêmes tels que TC. Cela fournit un ensemble de données unique pour améliorer notre compréhension de la signature de la pluie sur les images SAR. En outre, nous avons caractérisé la signature de la pluie (modulation du signal) sur les images SAR en polarisation VV et VH, en fonction de l'angle d'incidence, de la polarisation, de la vitesse du vent environnant et du taux de précipitations. Nous avons développé un modèle analytique pour expliquer les observations SAR lors d'événements pluvieux. Le modèle reproduit très bien le NRCS mesuré en cas de précipitations. La diffusion volumique et l'atténuation dans l'atmosphère sont les principaux mécanismes d'amélioration ou de réduction de la rétrodiffusion radar. De plus, des méthodes de signalisation des cellules de pluie et des bandes de pluie dans les TC ont été développées pour détecter efficacement la pluie qui a un impact significatif sur la rétrodiffusion de la surface de la mer. L'orientation de la bande

pluviale et les directions du vent obtenues à partir de l'analyse des stries de vent se sont avérées très cohérentes, mais conduisent à des estimations différentes de l'angle d'afflux. Cette étude montre que l'angle d'afflux pour la bande de pluie TC dépend de la distance radiale, des vents de surface de la mer, de RMW et de V_{max} .

Sur la base du modèle d'atmosphère, il est possible de récupérer le taux de pluie à partir des images SAR. Et il est possible de s'appliquer aux données SAR globaux, comme le mode WV. Des efforts supplémentaires sont nécessaires pour modéliser la rétrodiffusion radar sous une autre polarisation, en particulier pour la polarisation croisée. Avec l'observation des données GPM et radars météorologiques, le modèle peut être potentiellement appliqué sur un taux de pluie 3D. Les bandes de pluie de TC peuvent nous donner plus d'informations sur la dynamique de TC et ont le potentiel de prédire l'état de TC et son évolution. Avec la mission suivante SA Earth Explorer 10, nous pouvons avoir plus d'opportunités d'étudier le développement des nuages par rapport aux paramètres de surface. Surtout, il présente des avantages avec différents angles de vision radar et un capteur optique pour le mouvement des nuages.

Titre : Observations et quantifications des signatures de précipitations à partir des mesures SAR à double polarisation en bande C

Mots clés : Radar à synthèse d'ouverture, précipitations, vents de surface océaniques, cyclone tropical

Résumé : Les signatures de pluie sont des phénomènes très courants observés sur les images radar à synthèse d'ouverture (SAR) en bande C acquises au-dessus de l'océan. Généralement, les signatures apportent des obstacles à l'application maritime et perturbent le signal reçu de la surface de la mer. Cette étude s'appuie sur des acquisitions SAR en bande C et sur des mesures à haute résolution d'un radar météorologique au sol pour documenter l'impact de la pluie sur le signal rétrodiffusé par le radar dans les canaux de co-polarisation et de polarisation croisée pour les cellules et les bandes de pluie au sein des cyclones tropicaux (TC).

À l'aide de mesures colocalisées, un modèle numérique est développé et calibré. De nouvelles méthodes sont ensuite proposées pour signaler les signatures de pluie, améliorant la détection de la bande de pluie dans les TC. Les bandes de pluie détectées sont ensuite utilisées pour fournir de nouvelles informations pour décrire et comprendre les structures du vent TC, en plus par rapport aux Dropsondes in situ, aux traînées de vent détectées par SAR et aux simulations numériques HWRF haute résolution.

Title : Observations and Quantifications of Precipitation Signatures from C-band dual-polarized SAR measurements

Keywords : Synthetic aperture radar, precipitation, ocean surface winds, tropical cyclone

Abstract : Rain Signatures are very common phenomena observed on C-band Synthetic Aperture Radar (SAR) images acquired over ocean. Generally, the signatures bring obstacles to the maritime application and disturb the signal received from the sea surface. This study relies on C-band SAR acquisitions and high-resolution measurements from ground-based weather radar to document the rain impact on the radar backscattered signal in both co- and cross-polarization channels for rain cells and bands within tropical cyclones (TCs). Using co-located measurements, a numerical model is developed and calibrated. New methods are then proposed for flagging the rain signatures, improving rainband detection in TCs.

Detected rainbands are then used to provide new insights to describe and understand the TC wind structures, further compared with in situ Dropsondes, SAR detected wind streaks and high-resolution numerical HWRF simulations.